CHEMICAL SOLUTION DEPOSITION OF MOLYBDENUM SULFIDE ON TWO DIMENSIONAL TITANATE AND NIOBATE NANOSHEETS FOR PHOTOCATALYTIC DYE DEGRADATION

THESIS SUBMITTED TO

D. Y. PATIL EDUCATION SOCIETY (DEEMED TO BE UNIVERSITY), KOLHAPUR

FOR THE DEGREE OF

DOCTOR OF PHILOSOPHY
IN
PHYSICS

BY

Mr. VIKAS VIJAY MAGDUM

M. Sc.

UNDER THE SUPERVISION OF

Dr. JAYAVANT LAXMAN GUNJAKAR

M. Sc., Ph. D.

ASSOCIATE PROFESSOR,
CENTRE FOR INTERDISCIPLINARY RESEARCH,
D. Y. PATIL EDUCATION SOCIETY
(DEEMED TO BE UNIVERSITY),
KOLHAPUR- 416 006, MAHARASHTRA, (INDIA)

2024

CHEMICAL SOLUTION DEPOSITION OF MOLYBDENUM SULFIDE ON TWO DIMENSIONAL TITANATE AND NIOBATE NANOSHEETS FOR PHOTOCATALYTIC DYE DEGRADATION

A THESIS SUBMITTED TO

D. Y. PATIL EDUCATION SOCIETY (DEEMED TO BE UNIVERSITY), KOLHAPUR

FOR THE DEGREE OF

DOCTOR OF PHILOSOPHY

IN

PHYSICS

UNDER THE FACULTY OF

INTERDISCIPLINARY STUDIES

BY

Mr. VIKAS VIJAY MAGDUM

M. Sc.

UNDER THE SUPERVISION OF

Dr. JAYAVANT LAXMAN GUNJAKAR

M. Sc., Ph. D.

CENTRE FOR INTERDISCIPLINARY RESEARCH,

D. Y. PATIL EDUCATION SOCIETY (DEEMED TO BE UNIVERSITY),

KOLHAPUR- 416 006, MAHARASHTRA, (INDIA)

2024

DECLEARATION

I hereby declare that the thesis entitled "CHEMICAL SOLUTION DEPOSITION OF MOLYBDENUM SULFIDE ON TWO DIMENSIONAL TITANATE AND NIOBATE NANOSHEETS FOR PHOTOCATALYTIC DYE DEGRADATION" submitted for the degree of **Doctor of Philosophy (Ph.D.)** in **Physics** under the faculty of **Centre for Interdisciplinary Research** of D. Y. Patil Education Society (Deemed to be University), Kolhapur is completed and written by me, has not before made the basis for the award of any other higher education institute in India or any other country to the best of my knowledge. Further, I declare that I have not violated any of the provisions under the Copyright and Piracy/Cyber/IPR Act amended from time to time.

Place: Kolhapur

Research Student

Date: 22/12/2024

Mr. Vikas Vijay Magdum

CERTIFICATE OF GUIDE

This is to certify that the thesis entitled "CHEMICAL SOLUTION DEPOSITION OF MOLYBDENUM SULFIDE ON TWO DIMENSIONAL TITANATE AND NIOBATE NANOSHEETS FOR PHOTOCATALYTIC DYE DEGRADATION" which is being submitted herewith for the award of the Degree of **Doctor of Philosophy (Ph.D.)** in **Physics,** Faculty of Interdisciplinary Studies, under the guidance of Dr. Jayavant L. Gunjakar, Centre for Interdisciplinary Research (CIR), D. Y. Patil Education Society (Deemed to be University), Kolhapur, is the result of the original research work completed by **Mr. Vikas Vijay Magdum** under my supervision and guidance and to the best of my knowledge and belief the work embodied in this thesis has not formed earlier the basis for the award of any degree or similar title of this or any other university or examining body.

Place: Kolhapur

Research Guide

Date: 22/12/2024

Dr. Jayavant Laxman Gunjakar

Associate Professor,
D. Y. Patil Education (Deemed to be University), Kolhapur-416006.

Forwarded through,

Prof. C. D. Lokhande

Dean and Research Director,
Centre for Interdisciplinary Research
D. Y. Patil Education (Deemed to be University),
Kolhapur-416006.

ACKNOWLEDGEMENT

*I would like to thank my colleague, **Mr. Yogesh Chitare**, for his continuous assistance and support in my research endeavors. I would like to express sincere thanks to my seniors, **Dr. Shrikant Sadavar, Dr. Navanath Padalkar, Dr. Rohini Shinde, Dr. Pranv. Katkar, Dr. Supriya Marje, Dr. Shital Kale, Dr. Sachin Pujari, Dr. Shivaji Ubale, Dr. Suraj Khalate, Dr. Vikas Mane** and **Dr. Satish Jadhav**, for their insightful guidance, scientific discussions, and valuable suggestions on the present work.*

*I would like to express my heartfelt gratitude towards the teachers who made me capable of completing my masters and encouraged for Ph.D. I would like to thank **Dr. Pravin Walke, Dr. Rajendra Kale and Mr. Tushar More,** sir, for teaching me science and making me walk on this endless journey of scientific research.*

*To my dear friends **Swapnil Nardekar, Pooja Nardekar, Yogesh Patil, Rakesh Mohite, Shraddha Pawar, Akash Patil** and **Vinod Patil,** I extend my heartfelt gratitude for always being there for me in every situation and for your unwavering support and assistance. I would like to acknowledge my labmates and other lab members at the Centre for Interdisciplinary Research, **Sambhaji Kumbhar, Shraddha Bhosale, Rushiraj Bhosale, Shirin Kulkarni, Prashant Sawant, Shweta Talekar, Sayali Kulkarni, Mayura Medhekar, Ganesh Khande, Sohel Shaikh, Sambhaji Khot, Dr. Prity Bagwade, Ranjit Nikam, Satish Phalke, Manohar Lad, Ketaki Kadam, Ajinkya Bagade, Jyoti Thorat, Sumita Patil, Kuldip Belekar, Ganesh Jadhav, Dhanashri Phadatare, Vinay Nimat, Suhasini Yadav, Shivprasad Jadhav, Anil Sutar, Arti Patil, Sagar Patil, and Dilip Patil** for*

their wonderful collaboration. I want to thank them for their support and valuable suggestions during research work.

*It is my duty to acknowledge and express my most sincere gratitude to the people who helped me financially during this most crucial period of my life. I am most thankful to **Dr. J. L. Gunjakar, Mr. Rakesh Mohite, Miss. Shraddha Pawar, Mr. Vaibhav Charanti, Mr. Pravin Bone, Mr. Prajyot Patil, Dr. Prity Bagwade, Dr. Navnath Padalkar, Dr. Shrikant Sadavar, Dr. Rohini Shinde, Dr. Dhanaji Malavekar, Dr. Supriya Marje,** and many others who helped me financially during my Ph.D. journey.*

I am also thankful to all teaching and non-teaching staff of the Centre for Interdisciplinary Research for their cooperation.

*Last but not least, I hereby express my most profound appreciation and regards to my beloved parents (**Mom and Dad**), Brothers (**Vipul Dada and Sumit**), sister (**Varsha Tai, Niya Tai and Shubha Tai**), Sister in laws (**Aarti Vahini and Poonam**) uncle and aunty (**Kaka and Kaku**), **Mr. Anup Jujare** and all of the family members who despite their hard times and sufferings, continuously supported and encouraged me to complete my research. I am thankful to our newest family members, **Arjavi, Arnav, Anvit, Vrushadhish, Vihani** and **Swasti,** for being the reason behind my smile.*

<div align="right">

*~**Vikas***

</div>

Place: Kolhapur

LIST OF ABBREVIATIONS

- ❖ **2D** — 2-dimensional
- ❖ **2DMON** — 2-dimensional metal oxide nanosheets
- ❖ **AOP** — Advanced oxidation process
- ❖ **BE** — Binding energy
- ❖ **BOD** — Biological oxygen demand
- ❖ **CBD** — Chemical bath deposition
- ❖ **CB** — Conduction band
- ❖ **COD** — Chemical oxygen demand
- ❖ **CR** — Congo red
- ❖ **DDW** — Double distilled water
- ❖ **EDS** — Energy dispersive X-ray spectroscopy
- ❖ **EPD** — electrophoretic deposition
- ❖ **FE-SEM** — Field emission-scanning electron microscopy
- ❖ **FTIR** — Fourier transform infrared spectroscopy
- ❖ **HER** — Hydrogen evolution reaction
- ❖ **LbL** — Layer by layer
- ❖ **LB** — Langmuir Blodgett
- ❖ **LUMO** — Lower unoccupied molecular orbit
- ❖ **MB** — Methylene blue
- ❖ **MCSD** — Modified chemical solution deposition
- ❖ **MO** — Methyl orange
- ❖ **Modified SILAR** — Modified successive ionic layer adsorption and reaction
- ❖ **NHE** — Normal hydrogen electrode
- ❖ **RhB** — Rhodamine B
- ❖ **RT** — Room temperature
- ❖ **SILAR** — Successive ionic layer adsorption and reaction
- ❖ **TMDs** — Transition metal dichalcogenides
- ❖ **TOC** — Total organic carbon
- ❖ **UV** — Ultraviolet

- ❖ **UV-Vis** Ultraviolet visible spectrophotometer
- ❖ **UV-Vis DRS** Ultraviolet diffuse reflectance spectroscopy
- ❖ **XPS** X-ray photoelectron spectroscopy
- ❖ **XRD** X-ray diffraction
- ❖ **VB** Valance band
- ❖ **WHO** World Health Organization

List of Figures

List of Tables and Charts

SUMMARY OF RESEARCH WORK

Granted/Published (Indian) Patents

1) Liquid column based optical infrared filter, J. L. Gunjakar, A. S. Patil, **V. V. Magdum**, Y. M. Chitare, A. S. Patil (Patent No: 501334).

2) Infrared (IR) cut-off water filter assembly, D. Y. Patil Education Society, J. L. Gunjakar, Y. M. Chitare, **V. V. Magdum**, S. P. Kulkarni, A. S. Patil, A. S. Patil (Patent No: 407337-001).

3) A method for depositing uniform coating of 2D titanate nanosheets, D. Y. Patil Education Society, J. L. Gunjakar, **V. V. Magdum**, Y. M. Chitare, S. P. Kulkarni, (Application No: 202421035776).

Papers Accepted at International Journals

1) **Vikas V. Magdum,** Yogesh M. Chitare, Shirin P. Kulkarni, Prashant D. Sawant, Shraddha A. Pawar, Shweta V. Talekar, Chandrakant D. Lokhande, Umakant M. Patil, Sharad B. Patil, Jayavant L. Gunjakar, Versatility of group VI layered metal chalcogenide thin films synthesized by solution-based deposition methods, Journal of Materials Chemistry C, 11 (2023) 9768-9786 **(I.F- 6.4)**.

2) **Vikas V. Magdum**, Yogesh M. Chitare, Shirin P. Kulkarni, Dhanaji B. Malavekar, Jin H. Kim, Jayavant L. Gunjakar, Development of MoS_2 anchored 2D exfoliated titanate nanosheets thin film for Efficient photocatalytic degradation of organic pollutants, Materials Science and Engineering B, 313 (2025) 117892 **(I.F.-3.9)**.

3) **Vikas V. Magdum**, Yogesh M. Chitare, Shirin P. Kulkarni, Dhanaji B. Malavekar, Amol U. Pawar, Ravindra N. Bulakhe, Chandrakant D. Lokhande, Umakant M. Patil, Sharad B. Patil, Jayavant L. Gunjakar, Tailoring the physicochemical properties of chemically deposited MoS_2 thin films for photocatalytic dye and TC degradation: effect of different cationic precursors, Journal of Materials Science: Materials in Electronics, 35 (2024) 1433 **(I.F.-2.8)**.

4) Shirin P. Kulkarni, **Vikas V. Magdum**, Yogesh M. Chitare, Dhanaji B. Malavekar, Jin H. Kim, Sultan Alshehri, Jayavant L. Gunjakar, Shashikant P. Patole, 2D porous hexaniobate-bismuth vanadate hybrid photocatalyst for

photodegradation of aquatic refractory pollutants, Heliyon, 10 (2024) e39235 **(I.F.-3.4)**.

5) Yogesh M. Chitare, **Vikas V. Magdum**, Shirin P. Kulkarni, Shweta V. Talekar, Shraddha A. Pawar, Prashant D. Sawant, Dhanaji B. Malavekar, Umakant M. Patil, Chandrakant D. Lokhande, Jayavant L. Gunjakar, Preferentially oriented m-tuned WO_3 thin-films photocatalysts for the multitargeted degradation of organic molecules, Applied Surface Science Advances, 19 (2024) 100573 **(I.F- 6.7)**.

6) Yogesh M. Chitare, Vikas V. Magdum, Shirin P. Kulkarni, Shweta V. Talekar, Shraddha A. Pawar, Prashant D. Sawant, Dhanaji B. Malavekar, Umakant M. Patil, Jin H. Kim, Sabah Ansar, Jayavant L. Gunjakar, Vertically aligned interlocked tungsten oxide nanosheet thin film for photocatalytic application: effect of deposition cycles, Journal of Materials Science: Materials in Electronics, 35 (2024) 1436 **(I.F.-2.8)**.

7) Prity P. Bagwade, **Vikas V. Magdum**, Dhanaji B. Malavekar, Yogesh M Chitare, Jayavant L. Gunjakar, Umakant M. Patil, Chandrakant D. Lokhande, Synthesis, characterization and visible light driven dye degradation performance of one-pot synthesized amorphous $CoWO_4$ powder, Journal of Materials Science: Materials in Electronics, 33 (2022) 24646-24662 **(I.F-2.8)**.

8) Shirin P. Kulkarni, **Vikas V. Magdum**, Yogesh M. Chitare, Prashant D. Sawant, Shweta V. Talekar, Shraddha A. Pawar, Amol U. Pawar, Dhanaji B. Malavekar, Shrikrishna D. Sartale, Ayman A. Ghfar, Jayavant L. Gunjakar, Modified successive ionic layer adsorption and reaction for interconnected bismuth vanadate nanograins: Highly active visible light harvesting photoanodes, Journal of Photochemistry and Photobiology A: Chemistry, 454 (2024) 115737 **(I.F.-4.1)**.

9) Shraddha A. Pawar, Shweta V. Talekar, Prashant D. Sawant, **Vikas V. Magdum**, Shirin P. Kulkarni, Yogesh M. Chitare, Chandrakant D. Lokhande, Hemraj M. Yadav, Jayavant L. Gunjakar, Aqueous Exfoliated 2D Cobalt-Iron-Layered Double Hydroxide Nanosheets: Effect of Co: Fe Ratio on Electrocatalytic Oxygen Evolution Reaction, Colloids and Surfaces A: Physicochemical and Engineering Aspects, 706 (2025) 135793 **(I.F.-4.9)**.

10) Shirin P. Kulkarni, Yogesh M. Chitare, **Vikas V. Magdum**, Prashant D. Sawant, Shweta V. Talekar, Shraddha A. Pawar, Dhanaji B. Malavekar, Sabah Ansar, Jin H. Kim, Jayavant L. Gunjakar, Nanohybrids of layered titanate and bismuth vanadate as visible-light-driven photocatalysts for the degradation

of dyes and antibiotic, ACS Applied Nano Materials, 10 (2024) 11411–11422 **(I.F- 5.9)**.

11) Harishchandra S. Nishad, Shobhnath P. Gupta, Vishal Kotha, **Vikas V. Magdum**, Vinayak V. Gawade, Shashikant P. Patole, Ankush V. Biradar, Pravin S. Walke, Sodium-substituted tungsten oxide nanoflowers: an efficient electrode enhancing the pseudocapacitive storage in aqueous asymmetric supercapacitors, ChemNanoMat, 10 (2024) e202300463, **(I.F- 6.8)**.

12) Navnath S. Padalkar, Chae H. Cho, **Vikas V. Magdum**, Yogesh M. Chitare, Shirin P. Kulkarni, Umakant M. Patil, Jong P. Park, Jayavant L. Gunjakar, Self-assembled architecture of 2D layered double hydroxide pillared with 0D polyoxomolybdate anions: High-performance redox-type cathode for solid-state hybrid supercapacitor, Journal of Energy Storage, 74 (2023) 1109538 **(I.F- 9.4)**.

13) Shirin P. Kulkarni, Yogesh M. Chitare, **Vikas V Magdum**, Prashant D. Sawant, Shweta V. Talekar, Shraddha A. Pawar, Umakant M. Patil, Kishor V. Gurav, Dhanaji B. Malavekar, Amol U. Pawar, Jayavant L. Gunjakar, Chemically synthesized facet-controlled visible light active $BiVO_4$ thin films for photoelectrochemical water splitting, Applied Physics A, 129 (2023) 876 **(I.F- 2.7)**.

14) Dhanaji B. Malavekar, **Vikas. V. Magdum**, Sambhaki D. Khot, Jeon H. Kim, Chandrakant D. Lokhande, Doping of rare earth elements: Towards enhancing the electrochemical performance of pseudocapacitive materials, Journal of Alloys and Compounds, 960 (2023) 170601 **(I.F- 6.371)**.

15) Prity P. Bagwade, Dhanaji B. Malavekar, **Vikas V. Magdum**, Sambhaji D. Khot, Ranjit P. Nikam, Dilip J. Patil, Umakant M. Patil, Chandrakant D. Lokhande, Nanocrystalline cobalt tungstate thin films prepared by SILAR method for electrocatalytic oxygen evolution reaction, International Journal of Hydrogen Energy, 48 (2023) 8465-8477 **(I.F-7.2)**.

16) Navnath S. Padalkar, Shrikant V. Sadavar, Rohini B. Shinde, Akash S. Patil, Umakant M. Patil, **Vikas V. Magdum**, Yogesh M. Chitare, Shirin P. Kulkarni, Ravindra N. Bulakhe, Vinayak G. Parale, Jayavant L. Gunjakar, 2D-2D nanohybrids of Ni–Cr-layered double hydroxide and graphene oxide nanosheets: Electrode for hybrid asymmetric supercapacitors, Electrochimica Acta, 424 (2022) 140615 **(I.F- 6.6)**.

17) Rutuja P. Gambhir, Arun K. Parthasarathy, Shimpa Sharma, Shital Kale, **Vikas V. Magdum**, Arpita P. Tiwari, pH-responsive glycine functionalized

magnetic iron oxide nanoparticles for SARS-CoV-2 RNA extraction from clinical sample, Journal of materials science, 57 (2022) 13620-13631 **(I.F- 4.5)**.

18) Rohini B. Shinde, Navnath S. Padalkar, Shrikant V. Sadavar, Shital B. Kale, **Vikas V. Magdum**, Yogesh M. Chitare, Shirin P. Kulkarni, Umakant M. Patil, Vinayak G. Parale, Hyung-Ho Park, Jayavant L. Gunjakar, 2D–2D lattice engineering route for intimately coupled nanohybrids of layered double hydroxide and potassium hexaniobate: Chemiresistive SO_2 sensor, Journal of Hazardous Materials, 432 (2022) 128734 **(I.F- 14.2)**.

19) Shrikant V. Sadavar, Navnath S. Padalkar, Rohini B. Shinde, Akash S. Patil, Umakant M. Patil, **Vikas V. Magdum**, Yogesh M. Chitare, Shirin P. Kulkarni, Shital B. Kale, Ravindra N. Bulakhe, Deu S. Bhange, Saji T. Kochuveedu, Jayavant L. Gunjakar, Lattice engineering exfoliation-restacking route for 2D layered double hydroxide hybridized with 0D polyoxotungstate anions: cathode for hybrid asymmetric supercapacitors, Energy Storage Materials, 48 (2022) 101-113 **(I.F- 20.88)**.

20) Rohini B. Shinde, Navnath S. Padalkar, Shrikant V. Sadavar, Akash S. Patil, Shital B. Kale, **Vikas V. Magdum**, Yogesh M. Chitare, Shirin P. Kulkarni, Umakant M. Patil, Vinayak G. Parale, Jayavant L. Gunjakar, Lattice engineering route for self-assembled nanohybrids of 2D layered double hydroxide with 0D isopolyoxovanadate: Chemiresistive SO_2 sensor, Materials Today Chemistry, 24 (2022) 100801 **(I.F- 8.2)**.

21) Shrikant V. Sadavar, Navnath S. Padalkar, Rohini B. Shinde, Akash S. Patil, Umakant M. Patil, **Vikas V. Magdum**, Yogesh M. Chitare, Shirin P. Kulkarni, Ravindra N. Bulakhe, Vinayak G. Parale, Jayavant L. Gunjakar, Graphene oxide as an efficient hybridization matrix for exploring electrochemical activity of two-dimensional cobalt-chromium-layered double hydroxide-based nanohybrids, ACS Applied Energy Materials, 5 (2022) 2083-2095 **(I.F- 6.4)**.

22) Rohini B. Shinde, Akash S. Patil, Shrikant V. Sadavar, Yogesh M. Chitare, **Vikas V. Magdum**, Navnath S. Padalkar, Umakant M. Patil, Saji T. Kochuveedu, Vinayak G. Parale, Hyung-Ho Park, Chandrakant D. Lokhande, Jayavant L. Gunjakar, Polyoxotungstate intercalated self-assembled nanohybrids of Zn-Cr-LDH for room temperature Cl_2 sensing, Sensors and Actuators B: Chemical, 352 (2022) 131046 **(I.F- 9.2)**.

23) Yogesh M. Chitare, Satish B. Jadhav, Padamaja N. Pawaskar, **Vikas V. Magdum**, Jayavant L. Gunjakar, Chandrakant D. Lokhande, Metal oxide-

based composites in nonenzymatic electrochemical glucose sensors, Industrial & Engineering Chemistry Research, 60 (2021) 18195-18217 **(I.F- 4.2)**.

24) Shobhnath P. Gupta, Harishchandra Nishad, **Vikas V. Magdum**, Pravin S. Walke, High-performance supercapacitor electrode and photocatalytic dye degradation of mixed-phase WO3 nanoplates, Materials Letters, 281 (2020) 128639 **(I.F- 3.5)**.

Book Chapter

1) Yogesh M. Chitare, **Vikas V. Magdum**, Satish B. Jadhav, Shirin P. Kulkarni, Chandrakant D. Lokhande, Jayavant L. Gunjakar, Rare Earth Element-Based Nonenzymatic Glucose Sensor, Chemically deposited metal chalcogenide-based carbon composites for versatile applications, Springer International Publishing, (2023) 393-410.

Attended/ Presented, National/International Conference, Workshop and Seminar

1) Poster presentation in the National Conference on "Recent Trends in Functional Materials and Their Applications-2024 (RTFMA-2024)" held at Shardabai Pawar Mahila Arts, Commerce and Science College, Shardanagar, Malegaon BK, Baramati, Pune, from 13th to 14th March 2024.

2) Oral presentation at the "International Conference on Nanotechnology Addressing the Convergence of Materials Science, Biotechnology, and Medical Science (IC-NACMBM-2024)" held at D. Y. Patil Education Society, Kolhapur, from 12th -14th February 2024.

3) Poster presentation at the DNYANSHODH-2023 (Search for Knowledge) held at D. Y. Patil Education Society, Kolhapur, on 9th March 2023.

4) Poster presentation at the "International Conference on Advanced Materials Synthesis, Characterization and Applications (AMSCA Maverick-2022)" held at Department of Physics, Savitribai Phule Pune University, Pune from 18th - 20th October 2022.

5) Poster presentation at the DNYANSHODH-2022 (Search for Knowledge) held at D. Y. Patil Education Society, Kolhapur, on 22th February 2022.

6) Attended International Conference on "Cancer Biology: Basic Science to Translational Research (CBTR-2020)" held at D. Y. Patil Education Society, Kolhapur, on 17th – 18th January 2020.

CONTENTS

1.1 General Introduction

1.1.1 Pollution

The 21st century has brought about remarkable industrial advancements worldwide, transforming human perspectives through groundbreaking scientific discoveries and innovations. Notable progress in material science, including the development of graphene, light-emitting diodes and semiconductors, has opened new avenues for human development [1]. However, this industrialization has also led to the environmental challenge of pollution. This has caused severe environmental problems with widespread impacts. For example:

➢ According to the Green Schools Alliance, Americans manufacture 1.8 billion disposable diapers, 220 million tires, and 30 billion foam cups each year.

➢ World Health Organization (WHO) states that ambient air pollution is responsible for 6.7% of global deaths.

➢ Approximately 1.5 million metric tons of nitrogen pollution are carried into the Gulf of Mexico annually by the Mississippi River in the United States, resulting in a dead zone the size of New Jersey every summer.

➢ WHO estimates that air pollution is linked to more than 7 million premature deaths each year, equating to one in eight global deaths.

These facts highlight the global nature of pollution and its significant impact on economic, human health and environmental aspects [2]. Various pollutants have decay times ranging from a few days to several centuries, as shown in **Table 1.1**.

Table 1.1: Different materials and their decay time.

Material	Decay time
Paper	2-4 weeks
Orange peels	6 months
Milk carton	5 years
Plastic bag	15 years
Tin can	100 years
Plastic bottles	450 years
Glass bottle	500 years
Styrofoam	Never

Pollution affects all forms of life, including humans, insects, aquatic creatures, and plants. Pollution stretches back to prehistoric times, evidenced by polluted layers found in cave ceilings and pollution from early metal forging **[3]**. Despite being predominantly generated in urban areas, pollution can spread to remote regions. For instance, pollutants like chemicals and pesticides have been detected in Antarctica's ice sheets, and massive amounts of plastic have accumulated in the Great Pacific Garbage Patch. These alarming facts underscore the urgent need for effective pollution control solutions. Water pollution is a particularly severe issue among several types of pollution due to its detrimental effects on ecosystems.

1.1.2 Water pollution

Water (H_2O) is the most essential thing for the existence of life. Though our planet Earth is covered by around 71% of water, 97% of available water is in the ocean (saline solution), which is not useful for drinking. From the remaining 3%, 2.15% of water is in the form of icebergs (Glaciers), and 0.61% is underground. Thus, a tiny fraction of the available water on Earth is useful for drinking in the form of freshwater lakes, rivers and inland seas. The rapid growth in industrialization and negligence of pollution-controlling measures are causing tremendous water pollution and constantly degrading these water sources.

Water pollutants are categorized as point source pollution and nonpoint source pollution. When the water source is polluted by direct inputs, such as a factory or sewage treatment plant, that source is categorized as point source pollution. On the other hand, when it is polluted by unidentifiable/ widespread /diffuse inputs such as farm runoff, construction sites, other land disturbances and air pollutants released by industries, which then fall back to land and sea, that source is categorized as nonpoint source pollution. Point source pollution is mainly caused by sewage, wastewater treatment, and industrial effluents. In contrast, nonpoint source pollution is produced by farming and fossil fuel power plants (via the air).

There are many reasons for water pollution. The increased population and industrialization have amplified the demand for water to a greater extent for industrial and household purposes. Also, such water usage releases many pollutants in wastewater, such as industrial dyes, pesticides, heavy metal ions etc. The changing pattern of farming increases the uncontrolled utilization of hazardous pesticides and herbicides that

ultimately mix in the groundwater and contaminate it. The textile industries use various organic dyes for textile dying and expel unused dye effluents in mainstream water bodies, thereby becoming one of the significant causes of water pollution. These contaminants cause cancer and a host of other health problems, including vertigo, facial, neck, and pharyngeal oedema, acute tubular necrosis, vomiting gastritis, and hypertension.

1.1.3 Water pollution due to organic dyes
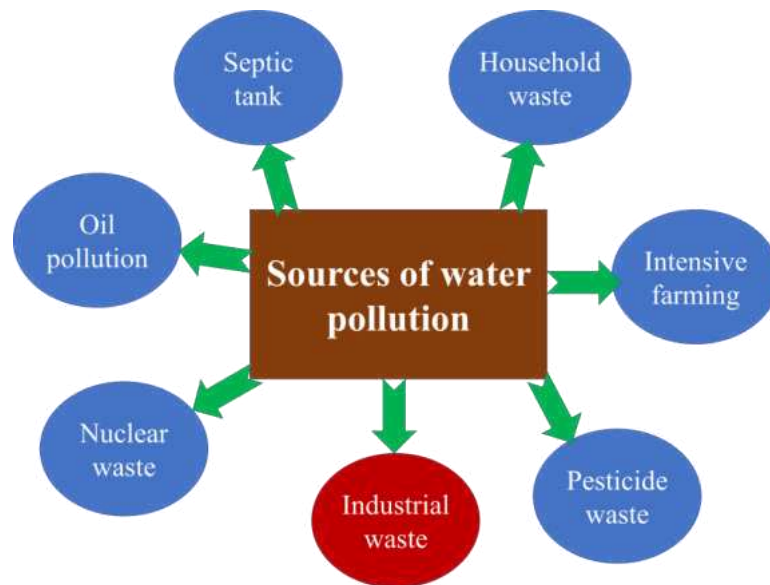
Figure. 1.1: Various water pollution sources **[4]**.

Water pollution has become a global concern due to its harmful environmental effects. Many industrial and household reasons are responsible for water pollution. **Fig. 1.1** shows various water-polluting agents that contribute to water pollution to a greater extent. Among them, water pollution caused by organic dyes from textile industries is one of the major reasons. It is found that effluents from the textile industry contain higher amounts of chemical oxygen demand (COD) and biological oxygen demand (BOD) than other industries. From an untreated industrial effluent, 80 % comes from the textile industry **[5]**. In textile industries, approximately 1-2 % of dyes are lost during production, and about 10-15% of this loss is discharged as effluent during dye applications **[6]**. These statistics reflect the vastly increased usage and discharge of harmful organic dyes. According to a report, the dye industry has become a 3.67 billion USD market in 2021 and is expected to reach a 5.12 billion USD value by 2027. According to a report by UNESCO, only 20% of dye wastewater is appropriately treated,

and the rest is disbursed without treatment **[7]**. The increased presence of colors in wastewater, even in small concentrations (less than 1 mg/dm3 for some dyes), is notably repulsive and unwanted, indicating the severity of pollution caused by organic dyes **[8].** All these facts highlight the impact of organic dyes on the global level.

1.1.4 Adverse effect of dyes

As mentioned above, less than 1 mg/dm^3 of dye contamination is objectionable and can cause severe problems to living organisms and the environment. It is seen that the use of toxic dyes causes changes in the physical and chemical properties of soil, causing severe damage to the environment and thereby affecting the flora and fauna of the ecosystem. These dyes are responsible for increasing BOD and COD, which are harmful to lives dependent on water. Water pollution, algal depletion, and chemical toxicity kill aquatic life, destroy soil, and contaminate drinking water **[9]**. The majority of organic dyes, including azo dyes, that are used to color food items contain aromatic centers in their molecular structures. Their breakdown and metabolic byproducts, such as benzidines, benzene sulphonic acids, and aromatic amines (anilines), are known carcinogens, mutagens, and DNA adducts, which cause later fatal consequences in cells.

Additionally, dyes can color water, which lowers the water body's transparency (sunlight penetration) and aeration. This negatively impacts the effectiveness of the critical process of photosynthesis, which in turn lowers the water's dissolved oxygen levels **[10, 11]**. Apart from this, these dyes can cause various biological disorders like skin irritation, contact dermatitis, chemosis, lacrimation, and respiratory distress **[12]**. This provides a significant reason for finding an effective method for dye removal from the wastewater.

1.1.5 Dyes

1.1.5.1 General facts

Dyes are staining or coloring substances or pigments used for the coloring process. More than 1,00,000 dyes are available commercially, producing around 8,00,000 tons annually. A mordant may be needed to increase the dye's fastness on the fiber. The dyes are typically applied in an aqueous solution. Unlike most organic compounds, dyes possess color because they

- absorb light in the visible spectrum (400-700 nm),

- have at least one chromophore (color-bearing group),
- possess a conjugated system, meaning that their double and single bonds alternate [13]

These dyes are classified into various types according to their characteristics. The various types of dye are given below.

Classification of dyes:

Organic dyes are widely used at the industrial level for various applications, including fabric coloring, leather tanning, food processing, etc. In this process, a considerable amount of dye wastewater is discharged into the mainstream water flow, causing harmful effects on the aquatic life. More than 1,00,000 dyes are available commercially, and they are being used as per their applicability for respective applications. However, these dyes are classified into different categories depending on different criteria. For instance, according to origin, dyes are classified into natural and synthetic dyes. The chemical structure divides the dyes into various types, such as direct, mordant, acidic, basic or reactive dyes.

Among these dyes, methylene blue (MB) and rhodamine B (RhB) have received considerable attention due to their excess use, highly toxic nature and property to adhere to any substance. Therefore, many scientists are working to degrade these dyes. The below section describes the properties of MB and RhB in detail.

1.1.5.2 Methylene blue:

MB with molecular formula $C_{16}H_{18}ClN_3S$, also known as methylthioninium chloride, is a salt widely used as a dye for coloring purposes [14]. MB is an aromatic heterocyclic basic dye. It is a widely recognized cationic, primary thiazine dye. It has a maximum absorption at 663 nm. It is highly soluble in water, forming a stable solution at room temperature. MB is a positively charged compound that contains an amino autochrome group [15]. The structural formula of MB is shown in **Fig. 1.2**.
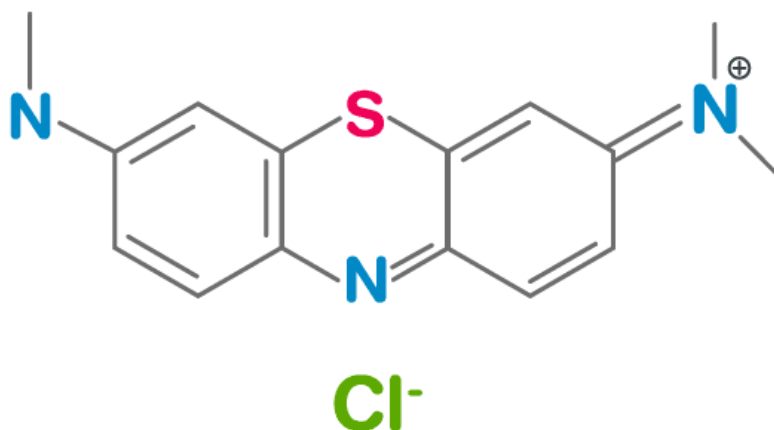
Figure 1.2: Structure of MB **[16]**.

1.1.5.3 Rhodamine B:

RhB, having molecular formula $C_{28}H_{31}ClN_2O_3$, is also one of the widely used dyes in industries, creating considerable water pollution when mixed with water due to its toxic nature. As far as toxicity is concerned, RhB is more toxic than MB. It quickly gets adsorbed on plastic and must be stored in glass containers **[17]**. It possesses strong absorption at 553 nm. It exhibits a dark pink color upon mixing in water with strong fluorescence. It is reported that RhB irritates the eyes and skin. In addition, it can damage internal organs upon ingestion. The structural formula of RhB is shown in **Fig. 1.3**.
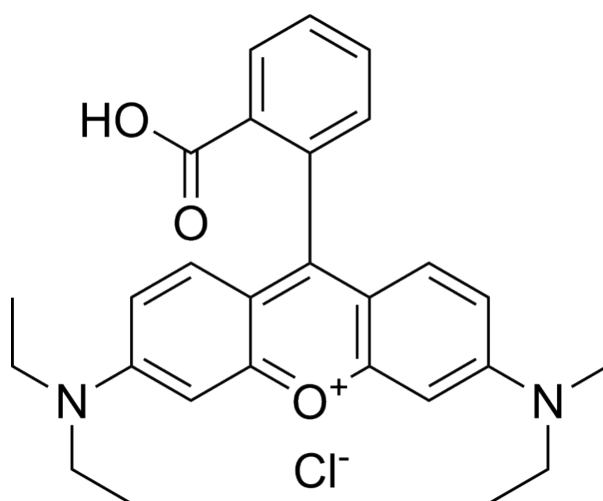
Figure 1.3: Structure of RhB **[18]**.

1.1.6 Dye removal techniques

The increased usage of organic dyes has made water pollution a severe global problem. Industrialization and globalization have increased the production of organic dyes due to their demand for final products and raw materials. The increased demand and usage of these dyes ultimately increase water pollution. Though dyes contribute to water pollution, scientists are working to reduce the concentration of dyes in wastewater. For this purpose, different techniques have been developed that are helpful in either reducing or degrading the dye concentration. The dye removal techniques can be broadly classified into the following categories:

1. Physical methods
2. Chemical methods
3. Biological methods.

Every method has its advantages as well as disadvantages. Every technique works on a different mechanism and has different efficiency and reusability. Therefore, a brief review of these methods is necessary to understand the advantages and disadvantages of each technique.

1.1.6.1 Physical methods

Adsorption:

It is a well-known process used to treat the dissolved organic dyes from industrial wastewater. Adsorption is the adhesion of particles from a gas, liquid or dissolved solid to a surface. Adsorption is a surface phenomenon that deals primarily with surface forces. Liquid-solid intermolecular forces of attraction result in the solute being concentrated at the solid surface when an adsorbate solution comes into contact with an adsorbent surface with a highly porous surface structure. Adsorption is one of the most popular chemical engineering techniques for extracting contaminants from industrial effluent. Adsorbents are mainly derived from zeolites, charcoal, clays, ores, and other waste resources. Zeolites, charcoal, clays, ores, and other waste materials are the primary sources of adsorbents. Seedust, fertilizer wastes, fly ash, coconut shell, rice husk, petroleum wastes, tannin-rich materials, sugar industry wastes, blast furnace slag, chitosan and seafood processing wastes, seaweed and algae, peat moss, scrap tires, fruit wastes etc. are examples of adsorbents made from waste resources. **[19]**.

Ion exchange:

Ion exchange has not been widely used to treat dye-containing effluents, mainly because ion exchangers cannot accommodate a wide range of dyes. In this process, wastewater is passed over the ion exchange resin until the available exchange sites are saturated. Both cationic and anionic dyes can be removed from dye-containing effluent this way. The advantages of this method include the lack of loss of adsorbent during regeneration, the recovery of solvent after use, and the removal of soluble dyes. A significant disadvantage of this method is its high cost. Organic solvents are expensive, and the ion exchange method is ineffective for dispersed dyes [20].

1.1.6.2 Chemical methods

Coagulation:

The process of removing suspended particles, contaminants, and colloidal elements from water by adding chemicals (coagulants) is known as coagulation. Coagulation destabilizes the electrostatic interactions between the molecules of reactive hydrolyzed dyes and the water by adding a coagulant. Locron or $FeCl_3$ are typically employed as coagulants in practice. The coagulating agents are generally high molecular weight compounds such as synthetic polymers having a linear structure. Since the contaminants are tiny particles and cannot settle by themselves, they are coagulated or bound together using a coagulant. The advantage of the coagulation and flocculation methods is the excellent elimination of insoluble dyes. However, extra costs for sludge treatment are required [21].

Membrane Filtration:

Membrane-based technologies, such as reverse osmosis, microfiltration, and nanofiltration, do not require chemical reagents. They are regarded as time- and money-saving techniques. According to recent studies, wastewater contaminated with dyes can be entirely decolored by nanofiltration membrane treatment, which may also lower the overall dye concentration above 72%. The dyes with molecular sizes between 600 and 1000 Da showed the best colorant removal performance. Numerous natural or waste-adsorptive materials, such as alginates, silicate, clay, natural polymeric materials, activated carbons, zeolites, and agricultural waste, can be readily added to membranes [22].

Advanced Oxidation Process:

The oxidation process, also referred to as the advanced oxidation process (AOP), is widely used among the different chemical processes used in wastewater treatment. In this process, an adequate amount of generated oxidative reactive species such as hydroxyl (OH^{*-}) and superoxide (O_2^{*-}) radicals are used for water purification. AOPs have been investigated for the inactivation of pathogens and pathogenic markers in addition to their ability to degrade organic and inorganic contaminants. The strong oxidants can swiftly degrade the recalcitrant organic pollutants present in the wastewater; hence, AOPs have been considered potential wastewater treatment technologies [23].

Highly reactive hydroxyl radical (OH^{*-}) species can be produced by a variety of mechanisms. Combinations of ultraviolet (UV), hydrogen peroxide (H_2O_2), and ozone (O_3) are the most prevalent. Certain catalysts (TiO_2, ZnO, etc.) and UV irradiation may also be used in conjunction with these processes. These procedures may also be combined with UV irradiation and specific catalysts (TiO_2, ZnO, etc). AOP offers a powerful water and wastewater treatment solution for reducing (removing) residual organic compounds as measured by COD, BOD or total organic carbon (TOC). Hydroxyl radicals are the end outcome of every AOP. The AOP process aids in the removal of nonbiodegradable or biologically hazardous substances from wastewater, including volatile organic compounds, insecticides, petroleum components, and aromatics. The contaminant materials are mainly converted into stable inorganic compounds such as water, carbon dioxide, and salts, which undergo mineralization. Reducing chemical pollutants and toxicity to a level that allows the cleansed wastewater to be reintroduced into receiving streams or, at the very least, into conventional sewage treatment is one of the objectives of wastewater purification using AOP techniques. Without creating more dangerous byproducts or sludge that need to be handled further, the AOP effectively breaks down a number of hazardous chemical compounds to acceptable levels.

Advantages of AOP

| | Fast reaction rates.

| | Potential to mitigate toxicity and perhaps even fully mineralize the treated organics.

ΙΙ Materials that need additional processing, like "spent carbon" from activated carbon absorption, are not produced in AOP.

ΙΙ Unlike biological or physical-chemical processes, it does not produce sludge (wasted biological trash).

Disadvantages AOP

ΙΙ Complex chemistry needs to be tuned for certain applications.

ΙΙ Excess peroxide must be required for some applications.

Fenton Process:

Fenton reagent is a suitable chemical for treating wastewater that is resistant to biological treatment or poisonous to live biomass. Chemical separation effectively decolorizes both soluble and insoluble colors by removing dissolved dyes from wastewater through sorption or bonding. This method's primary drawback is the creation of sludge due to the reagent and dye molecules flocculating. Even with its concentrated contaminants, the sludge still needs to be disposed of. Traditionally, it has been burned to generate electricity, but some people believe that this method of disposal is not environmentally friendly. Although cationic dyes do not coagulate, the performance depends on the ultimate floc formation and its settling quality. Reactive, acid, direct, vat, and mordant dyes typically coagulate, but the floc that develops is of low quality and settles poorly, producing mediocre results **[20]**.

1.1.6.3 Biological methods

Despite their ease of use, physicochemical wastewater treatment techniques aren't necessarily economical or ecologically benign. Because much of the sludge and leftovers from high electricity usage cannot be recycled, less production is needed. These techniques require a multi-stage treatment process with a lengthy retention period; they are not single-step.

Biological procedures, which involve the degradation of dyes by biological phenomena like bioremediation, are environmentally friendly ways to extract dye from textile wastewater at the lowest possible cost and with the longest possible operational time. Many synthetic dyes can be absorbed and broken down by biological things such as yeasts, bacteria, fungi, and algae. Some of the methods are discussed below.

Various fungi have been identified and have been tested for wastewater treatment. Potential outcomes for the biological degradation of textile dyes released from dying businesses have been demonstrated by combinations of aerobic and anaerobic treatment by various bacteria. *Phanerochaete chrysosporium, Phanerocheate chrysosporium, Trichoderma harzianum* and *Aspergillus* have been successfully applied for the biodegradation of various organic dyes.

Numerous microorganisms have been investigated; however, few dye-degrading bacteria have been found. Microbes used as pollution indicators for various toxicants in wastewater and crucial in the cleanup of organic pollutants need further study. The primary benefit of dealing with bacteria is their ease of culture and faster growth rate compared to other microorganisms. Molecular genetic manipulation can easily enhance the ability of bacteria to degrade dye. Bacteria may oxidize sulfur-based textile dyes (Sulfur Blue 15) to sulphuric acid and catabolize organic pollutants based on chlorinated and aromatic hydrocarbons, which can be broken down by using them as a carbon source. Numerous studies have shown microbes that can quickly break down certain azo-based dyes **[24]**.

Anaerobic method:

Azo dyes make up 60-70% of all textile dyestuffs. Azo dyes are soluble in solution and are not removed via conventional biological treatments. Reactive dyes are the most problematic compounds in textile dye effluents. Besides the decolorization of soluble dyes, biogas production is a significant advantage of this anaerobic system. Biogas can be reused to provide heat and power and will reduce energy costs **[20]**.

1.1.7 Semiconductor photocatalysis:

Typically, photocatalysis is a process in which catalysts absorb photons to create electrons and holes to initiate reduction and oxidation reactions. This process is also known as heterogeneous photocatalysis. The catalyst and reactants are in distinct phases during heterogeneous catalysis **[25]**. The field of heterogeneous photocatalysis encompasses a wide range of reactions, such as metal deposition, water purification, gaseous pollutant elimination, hydrogen transfer, dehydrogenation, mild or complete oxidations, and deuterium-alkane isotopic exchange **[26]**. The possibility of using solar light for various heterogeneous photocatalysis makes this process a promising tool for green chemistry applications. Due to their distinct properties, semiconductors and

transition metal oxides are the most widely used heterogeneous photocatalysts. In contrast to metals, semiconductors have an empty energy zone in which there are no available energy levels to encourage the recombination of an electron and hole created by photoactivation in the solid. The band gap is the empty space that lies between the top of the full valance band (VB) and the bottom of the unoccupied conduction band (CB) [25]. The three main components of a photocatalytic process are the catalytic reaction, charge creation and separation, and light harvesting. Thus, the balance of thermodynamics and kinetics of these three crucial reaction steps determines the overall efficiency of a photocatalytic system. Therefore, extensive research has been conducted over the past few decades to investigate sophisticated photocatalysts with enhanced light harvesting capabilities, high charge carrier separation efficiency, and effective catalytic reactivity. An electron is stimulated from the VB to the CB, creating a positive hole in the VB when the semiconductor absorbs a photon with energy equal to or greater than the material band gap. An exciton is a type of photogenerated electron-hole pair. The energy obtained from the excitation of the electron can be released as a photon by the excited electron and hole recombining. However, the selectivity for the intended product of photocatalysis and the efficiency of solar-to-chemical energy conversion is still inadequate. To satisfy these requirements, it is crucial to look for the appropriate materials to use as photocatalysts [27].

Advantages of heterogeneous photocatalysis

➢ The catalyst is in the solid phase, while the reactants are in the liquid or gas phase. This allows easier separation and recovery of the catalyst, making the process economical and sustainable.

➢ The photocatalyst absorbs light and generates an electron-hole pair, which is further utilized for the redox reactions.

➢ The catalyst does not get consumed during reactions, making it recyclable.

➢ The stability and reusability of heterogenous photocatalysts are the key advantages in industrial and environmental applications, as they reduce the cost and waste.

Considering these advantages, efforts were taken to develop efficient photocatalysts with extended exciton lifetime. Such efforts rely on structural modifications of photocatalysts by tuning synthesis conditions or doping appropriate dopant elements. Such strategies can modify the electronic structure and induce

intraband energy between VB and CB. Also, coupling the pure semiconductors photocatalyst with narrow-bandgap semiconductor nanostructures or, noble-metal nanoparticles or silicon nanowires can effectively suppress exciton recombination [28]. Facilitating interactions between excited electrons and oxidants to produce reduced products or between produced holes and reductants to produce oxidized products is the ultimate goal of photocatalyst design. At the semiconductor surface, oxidation-reduction reactions occur due to the production of negatively charged electrons and positively charged holes [29]. The ability of semiconductors to produce charge carriers when exposed to light, followed by the production of free radicals like OH^{*-}, which trigger further reactions and ultimately result in the formation of CO_2 and H_2O, is the primary mechanism underlying heterogeneous photocatalysis [30, 31]. Thus, the most appealing aspects of heterogeneous photocatalysis include [32-35],

- The process takes place at ambient conditions.
- The only requirements for the reaction to initiate are oxygen and photons, which can be obtained directly from the air and sun.
- A variety of inert matrices, including glasses, polymers, carbon nanotubes, and graphene oxides, can support the catalyst.

1.1.7.1 Dye degradation mechanism:

The photocatalytic dye degradation mechanism can be explained by two different methods: the direct and indirect dye degradation mechanisms. These mechanisms are briefly discussed below.

   a) **Direct mechanism for dye degradation:**

   This mechanism involves the dye excitation under visible light photons from the ground to the excited state. These excited dye species are further converted into semi-oxidized cations (Dye^+) by electron injection into the CB of the semiconductor. The reaction between trapped electrons and dissolved oxygen results in the formation of O_2^{*-} and OH^{*-} radicals. These radicals are mainly responsible for the oxidation of organic compounds, represented by the equation below [36].

$$Dye + h\upsilon \rightarrow dye* \qquad (1.1)$$

$$Dye* + semiconductor \rightarrow dye^+ + semiconductor^- \qquad (1.2)$$

b) Indirect mechanism for dye degradation:

The indirect mechanism for dye degradation can be explained in four different steps.

i) Photoexcitation: A photocatalytic reaction is initiated when photoelectrons are promoted from the filled VB to the CB of a semiconductor photocatalyst. The excitation process leaves behind a hole in the VB, which forms an electron-hole pair indicated by the following equation.

$$\text{Semiconductor} + h\upsilon \rightarrow \text{semiconductor} [e^- (CB) + h^+ (VB)] \qquad (1.3)$$
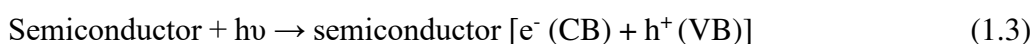
ii) Ionization of water: The photogenerated holes at the VB then react with water to produce OH^{*-} radical.

$$H_2O \text{ (ads)} + h^+ (VB) \rightarrow OH^{*-} \text{ (ads)} + H^+ \text{ (ads)} \qquad (1.4)$$
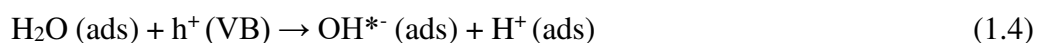
The OH^{*-} radicals formed on the irradiated semiconductor surface are potent oxidizing agents that attack organic molecules non-selectively to mineralize them to an extent.

iii) Oxygen ionosorption: Electrons in the CB are taken up by oxygen to generate anionic superoxide radicals (O^{2*-}).

$$O_2 + e^- (CB) \rightarrow O_2^{*-} \text{ (ads)} \qquad (1.5)$$

These superoxide ions prevent electron-hole recombination, thus maintaining electron neutrality.

iv) Protonation of superoxide: The superoxide O_2^{-*} radicals gets protonated which forms hydroperoxyl radical (HO_2^*) and then subsequently, H_2O_2. Further highly reactive hydroxyl radicals (OH^{*-}) are formed by the dissociation of H_2O_2.

$$O_2^{*-}\text{(ads)} + H^+ \rightarrow HOO^* \text{ (ads)} \qquad (1.6)$$

$$2HOO^* \text{ (ads)} \rightarrow H_2O_2 \text{ (ads)} + O_2 \qquad (1.7)$$

$$H_2O_2 \text{ (ads)} \rightarrow 2OH^{*-} \text{ (ads)} \qquad (1.8)$$

$$\text{Dye} + OH^{*-} \rightarrow CO_2 + H_2O \text{ (dye intermediates)} \qquad (1.9)$$

$$\text{Dye} + h^+ (VB) \rightarrow \text{Oxidation products} \qquad (1.10)$$

$$\text{Dye} + e^- \text{(CB)} \rightarrow \text{Reduction products} \hspace{4cm} (1.11)$$

1.1.7.2 Hybrid semiconductor photocatalysts for dye degradation:

Though various semiconductor photocatalysts are explored for photocatalytic dye degradation, most of the work is focused on the wide band gap semiconductors like TiO_2, Nb_2O_5 and ZnO **[37]**. The high stability and appropriate electronic band positions required for the redox reactions of H_2O are the reasons for their high interest. However, their photocatalytic activity is highly restricted due to their wide band gap (<4 % of the solar spectrum) and extremely high recombination rate of excitons. Thus, efforts are put into exploring narrow-band gap semiconductors to utilize the solar spectrum efficiently. Various narrow-band gap semiconductors, like transition metal -oxides, -sulfides, -nitrides etc., are used for photocatalytic dye degradation **[38]**. Still, their efficiency is limited by the high recombination rate of excitons.

Consequently, researchers are developing new strategies to suppress exciton recombination and improve photocatalysis performance. These efforts include doping foreign elements, coupling with other nanostructures, using Z-scheme, structural and morphological modifications, surface area tuning, etc. Recently, layered transition metal oxides and sulfide materials attracted more attention as photocatalysts due to their unique layered structure, ion-exchange properties, the possibility of achieving constituent 2D nanosheets via exfoliation, highly flexible chemical composition and versatile anisotropic properties **[39]**. In this regard, the layered titanate, niobate, and molybdenum sulfide (MoS_2) have attracted considerable consideration as potential materials for photocatalytic dye degradation. The nanosheets obtained from the exfoliation of these layered inorganic solids pave the way for developing intimately coupled photocatalytic systems.

1.2 A review of the literature

1.2.1 Literature survey of MoS_2 and its hybrid for photocatalytic dye degradation

The layered transition metal dichalcogenides (TMDs), including MX_2 (M = Mo, W; X = S, Se, Te) and their constituent nanosheets, have recently attracted considerable attention due to their novel physical phenomena in reduced dimension and the spatially confined electronic and optical properties **[40]**. In particular, MoS_2 is highly attractive as a heterogeneous photocatalyst due to its high activity for hydrogen evolution reactions

(HER) in water. Molybdenum is a relatively abundant non-precious metal. It can be prepared with different starting reagents, leading to tunable stoichiometry, structure and morphology. The recent discoveries about these materials as heterogeneous catalysts leave an open and wide field for research activity.

In one instant, 3D $TiO_2-MoS_2-TiO_2$ sandwiched material was prepared by mechano-chemical process and tested for photocatalytic activity for methyl orange (MO) dye degradation [41]. 3D $TiO_2-MoS_2-TiO_2$ sandwiched material showed 89.86 % MO degradation after 120 minutes upon the irradiation of light (wavelength range of 200-800 nm). MoS_2-TiO_2 hybrid was synthesized using a modified hydrothermal method to study phenol degradation under UV light irradiation [42]. Complete degradation of phenol was obtained by MoS_2-TiO_2 hybrid in 25 minutes. The solvothermal method was employed to prepare MoS_2-TiO_2 hybrids and used to degrade RhB [43]. The MoS_2-TiO_2 hybrid demonstrated 80 % RhB degradation upon 60 minutes of visible light irradiation. The thermal polymerization method was used to synthesize the MoS_2/C_3N_4 hybrid for the degradation of RhB [44]. Enhanced photocatalytic activity with 98 % degradation of RhB was observed for the MoS_2/C_3N_4 hybrid under visible light irradiation. $TiO_2@MoS_2$ hybrid was prepared using the hydrothermal method and examined for the degradation of RhB under the irradiation of wavelength range $280-700$ nm [45]. The $TiO_2@MoS_2$ composite displayed 100 % RhB degradation within 20 minutes. The sol-gel method was employed to prepare N-doped MoS_2, and the $N-MoS_2$ was used to degrade RhB [46]. 40 % of RhB degradation was obtained with N-doped MoS_2 after 80 minutes under visible light irradiation. $RGO/K_4Nb_6O_{17}$ was synthesized using a chemical method for application in the photodegradation of RhB [47]. 68.3% of RhB degradation was observed after 30 minutes upon the irradiation of a wavelength of 200- 700 nm. MoS_2-TiO_2 nanocomposites were synthesized using the hydrothermal method and used for MB degradation [48]. The nanocomposite exhibited 93 % MB degradation after 12 minutes of visible light irradiation. Ag/hybridized 1T-2H MoS_2/TiO_2 heterostructure was prepared by microwave-assisted hydrothermal method and employed for MB degradation [49]. The resultant hybrid displays 97 % degradation with a 12 times higher rate constant than pristine TiO_2. MoS_2-TiO_2 nanocomposites were synthesized by the mechanochemical route and employed for the degradation of MO dye [50]. It showed 93 % MO degradation in 80 minutes of UV irradiation. MoS_2/TiO_2 heterostructures were synthesized by hydrothermal method and used to degrade MB dye under visible light irradiation [51]. The heterostructure showed complete MB

degradation in 120 minutes of visible light irradiation. MoS_2/TiO_2 heterostructures were prepared with different concentrations of KBr using the hydrothermal method [52]. The prepared heterostructures are employed for the RhB degradation. The optimized heterostructure showed 95 % RhB degradation after 120 minutes. $TiO_2@MoS_2$ heterojunction nanostructures were synthesized using the hydrothermal method [53]. The optimized heterojunction degrades 97 % of Congo red (CR) dye in 120 minutes. Few-layer $MoS_2@TiO_2$ hollow spheres heterostructures were synthesized by hydrothermal method and used to degrade RhB dye [54]. It degrades 95 % of RhB in 120 minutes of visible light irradiation. TiO_2–MoS_2 samples were synthesized using the solvothermal method to degrade MB, which showed 65 % degradation in 100 minutes [55]. MoS_2/TiO_2 heterostructures were synthesized using photo-assisted deposition, which showed 94 % MB degradation [56]. Ag/Nb_2O_5 was prepared using the impregnation method and employed for the degradation of dark blue neutracyl, which shows 94 % degradation [57]. Nb_2O_5/MoS_2/Graphene ternary composite was prepared using hydrothermal, which showed 95 % MO degradation under visible light irradiation [58]. Niobium oxide heterogeneous catalyst was prepared using a chemical method, which showed 87 % MB degradation [59]. **Table 1.2** shows a brief review of the literature.

Table 1.2: A literature survey of MoS_2 and 2D metal oxide nanosheets with their performance.

Sr. No.	Hybrid Photocatalyst	Method of Synthesis	Wavelength used (nm)	Dye used	% dye removal	References
1	3D TiO_2- MoS_2- TiO_2	Mechano-chemical process	200-800	MO	89.86	42
2	MoS_2/ TiO_2	Modified Hydrothermal	UV irradiation	phenol	100	43
3	MoS_2/ TiO_2	solvothermal	370- 730	RhB	80	44
4	MoS_2/C_3N_4	Thermal polymerization	420-780	RhB	98	45
5	TiO_2@MoS_2	Hydrothermal	280-700	RhB	100	46
6	N-doped MoS_2	Sol-gel	553	RhB	40	47
7	RGO/$K_4Nb_6O_{17}$	Chemical method	200-700	RhB	68.3	48
8	MoS_2–TiO_2	Hydrothermal	420-780	MB	93	49
9	Ag/hybridized 1T-2H MoS_2/TiO_2	Microwave-assisted hydrothermal method	420-780	MB	97	50
10	MoS_2−TiO_2	Mechanochemical route	365	MO	93	51
11	MoS_2/TiO_2	Hydrothermal	420-780	MB	100	52
12	MoS_2/TiO_2	Hydrothermal	350-1100	RhB	95	53
13	TiO_2@MoS_2	Hydrothermal	420-780	(CR	97	55
14	MoS_2/TiO_2	Hydrothermal	400-800	RhB	95	56
15	TiO_2 –MoS_2	Solvothermal	UV light	MB	65	57

16	MoS$_2$/TiO$_2$	photo-assisted deposition method	420-780	MB	94	58
17	Ag/Nb$_2$O$_5$	impregnation method	UV light	Dark blue neutracyl	99	59
18	Nb$_2$O$_5$/MoS$_2$/ Graphene	Hydrothermal	420-780	MO	95	60
19	Niobium oxide	Chemical method	-	MB	87	61

The above literature survey clearly indicated that the MoS_2 demonstrated enhanced photocatalytic activity when coupled with the wide bandgap semiconductors. The TiO_2 is one of the highly suitable wide bandgap semiconductor materials for the coupling with MoS_2. Along with TiO_2, $K_4Nb_6O_{17}$ is another wide bandgap semiconductor for coupling with various narrow bandgap semiconductor photocatalysts. However, the efficient photocatalyst based on MoS_2 has not been realized in practical application.

1.3 Orientation and purpose of the thesis

The unprecedented growth of industrialization has led to enormous pollution around the globe. Wastewater released from various industries, such as the textile, pharmaceutical, and agriculture sectors, releases numerous toxic pollutants that are harmful to aquatic and human life. The dyes present in the wastewater are carcinogenic and cause unfavourable ecosystem changes. Therefore, an efficient and eco-friendly process for dye effluent degradation is essential. Among numerous wastewater treatment methods, heterogeneous photocatalysis has emerged as one of the most promising technologies for wastewater purification. Though many techniques are used to degrade these organic pollutants, an advanced oxidation process in the presence of a photocatalyst is an effective way to degrade and remove organic pollution in water bodies. Many low-dimensional semiconducting materials have been developed and explored as photocatalysts. This process has received increased research attention due to its environmentally benign nature and dependence on renewable energy resources. Earth's surface receives around 4 % of UV and 45 % of visible light, which shows the need to develop visible light-active photocatalysts to achieve maximum photocatalytic efficiency.

Thus, efforts were devoted to developing visible light-active photocatalysts. However, most visible light active photocatalysts possess high electron-hole recombination rates, poor photostability, low efficiency and inappropriate band positions to reduce protons and oxidize oxide ions. Consequently, various strategies were employed to enhance the photocatalytic performance by morphology and porosity tuning, doping, nanostructure formation, structural engineering and hybridizing with suitable photocatalysts. Nanostructured hybridization with strong electronic coupling can enable maximum solar spectrum absorption, thereby increasing the overall photocatalytic performance of the semiconducting material.

Recently, 2-dimensional (2D) materials have gained significant research attention owing to their obvious advantages, such as inherent surface charge, the presence of functional groups and the possibility of hybridizing with other inorganic species. In particular, wide bandgap 2D exfoliated titanate nanosheets (titanate-NS) and niobate nanosheets (niobate-NS) show excellent potential for photocatalytic applications due to their large surface area, ultrathin thickness, macromolecule nature, and negative surface charge. In addition, the titanate-NS and niobate-NS can act as a basic building block for hybridization with numerous guest species. On the other hand, various oxide, sulfide and phosphide-based materials have been employed as narrow bandgap semiconductors. Among them, MoS_2 is a promising narrow bandgap material with a layered structure and high surface area.

Consequently, the hybridization of MoS_2 with titanate-NS and niobate-NS can improve photocatalytic properties through strong electronic coupling between the hybridized species, enhanced surface area, increased visible light response and depressed electron-hole recombination rate. In addition, titanate-NS and niobate-NS can act as macromolecules with negative surface charge, and they can be used as precursors for deposition using the dip-coating method. On the other hand, the modified chemical solution deposition (MCSD) method found multiple advantages for the deposition of MoS_2 over titanate-NS and niobate-NS thin films, such as low-cost, binder-free approach and control over deposition parameters. Thus, hybridizing titanate-NS and niobate-NS with MoS_2 can produce a high surface area morphology with enhanced visible light activity.

From these perspectives, we fabricated $MoS_2@TiO_2$ hybrid thin films using a combination of dip-coating and MCSD methods. This kind of heterostructure formation has not been reported yet. The physicochemical properties of the $MoS_2@TiO_2$ hybrid thin films were thoroughly explored using various analytical techniques. Further, the prepared thin films were employed for the photocatalytic degradation of RhB and MB dyes under visible light irradiation. The degradation kinetics were studied by applying pseudo-first-order kinetics.

Various physicochemical characterization techniques are applied to investigate the different properties of synthesized hybrid thin films. The crystal structure (phase identification) of the pristine MoS_2, titanate-NS, niobate-NS and their hybrids is analyzed using the X-ray diffraction (XRD) technique. The optical properties of pristine

and nanohybrid materials are investigated with Ultraviolet-visible diffuse reflectance spectroscopy (UV-Vis DRS). The chemical bonding nature of the present nanohybrids is examined with Fourier-transform infrared (FTIR) and Micro-Raman spectroscopy analysis. The surface morphologies of pristine and hybrid thin films are scrutinized with Field emission scanning electron microscopy (FE-SEM). The elemental composition and distribution of the elements present in hybrids are examined with energy-dispersive X-ray spectroscopy (EDS) and elemental mapping analysis. The chemical oxidation states of the elements are probed with the X-ray photoelectron spectroscopy (XPS) technique.

The photoactivity of the pristine MoS_2 and MoS_2-based hybrid thin films for the photodegradation of dyes is evaluated with UV-Vis absorption spectroscopy analysis. MB and RhB are used as target dyes for the decomposition. The photocatalytic performance of synthesized nanohybrids is measured with a percentage degradation study using the formula,

$$\text{dye degradation (\%)} = \frac{C_0 - C_t}{C_0} \times 100 \tag{1.13}$$

where C_0 denotes the initial absorption and C_t denotes the absorption at time t.

Furthermore, a recyclability study was conducted to check the industrial usefulness of hybrid materials.

1.4 References

[1] J. Wood, Mater. Today, 11 (2008) 40.

[2] K. J. Maji, A. K. Dikshit, M. Arora, A. Deshpande, Sci. Total Environ., 612 (2018) 683.

[3] S. Hong, J.-P. Candelone, C. C. Patterson, C. F. Boutron, Science, 272 (1996) 246.

[4] H. A. Antwi, L. Zhou, X. Xu, T. Mustafa, Sustainability, 13 (2021) 3664.

[5] B. Lellis and C. Z. Fávaro-Polonio, J. A. Pamphile, J. C. Polonio, Biotechnol. Res. Innov., 3 (2019) 275.

[6] Q. Husain, Crit. Rev. Biotechnol., 26 (2006) 201.

[7] S. Rafaqat, N. Ali, C. Torres, B. Rittmann, RSC Adv., 12 (2022) 17104.

[8] T. Robinson, G. McMullan, R. Marchant, P. Nigam, Bioresour. Technol., 77 (2001) 247.

[9] S. O. Akinnawo, Environ. Chall., 12 (2023) 100733.

[10] R. Lachheb, E. Puzenat, A. Houas, M. Ksibi, E. Elaloui, C. Guillard, J.-M. Herrmann, Appl. Catal. B, 39 (2002) 75.

[11] G. A. R. de Oliveira, D. M. Leme, J. de Lapuente, L. B. Brito, C. Porredón, L. de B. Rodrigues, N. Brull, J. T. Serret, M. Borràs, G. R. Disner, M. M. Cestari, D. P. de Oliveir, Chem-Biol. Interact., 291 (2018) 171.

[12] M. A. Hassaan and A. E. Nemr, Am. J. Environ. Sci., 1 (2017) 64.

[13] E. N. Abrahart, Dyes and their intermediates, 2nd edition, New York Chemical Pub., 1977.

[14] I. Khan, K. Saeed, I. Zekker, B. Zhang, A. H. Hendi, A. Ahmad, S. Ahmad, N. Zada, H. Ahmad, L. A. Shah, T. Shah, I. Khan, Water, 14 (2022) 242.

[15] I. S. Aldabagh, D. N. Saad, E. I. Ahmed, Chem. Eng. J. Adv., 18 (2024) 100608.

[16] L. H. Pinto, S. Z. Bez, J. C. Soares, B. Bonfim, Q. Alzahrani, J. Environ. Prot., 11 (2020) 1015.

[17] H. Du, Y. Zhang, H. Jiang, H. Wang, Environ. Technol. Innov., 27 (2022) 102495.

[18] S. Liu, Z. Wang, T. Han, T. Fei, T. Zhang, H. Zhang, J. Porous Mater., 26 (2019) 941.

[19] R. V. Kandisa, N. Saibaba, K. B. Shaik, R. Gopinath, J. Bioremediat. Biodegrad., 7 (2016) 1.

[20] A. R. Warade, R. W. Gaikwad, R. S. Sapkal, V. S. Sapkal, Int. J. Adv. Res. Innov. Ideas Educ., 3 (2016) 3851.

[21] S. Mondal, Environ. Eng. Sci., 25 (2008) 383.

[22] K. Piaskowski, R. Świderska-Dąbrowska, P. K. Zarzycki, J. AOAC Int., 101 (2018) 1371.

[23] N. Y. Donkadokula, A. K. Kola, I. Naz, D. Saroj, Rev. Environ. Sci. Biotechnol., 19 (2020) 543.

[24] D. Bhatia, N. R. Sharma, J. Singh, R. S. Kanwar, Crit. Rev. Environ. Sci. Technol., 47 (2017) 1836.

[25] A. O. Ibhadon, P. Fitzpatrick, Catalysts, 3 (2013) 189.

[26] A. L. Linsebigler, G. Lu, J. T. Yates Jr., Chem. Rev., 95 (1995) 735.

[27] C. Gao, J. Low, R. Long, T. Kong, J. Zhu, Y. Xiong, Chem. Rev., 120 (2020) 12175.

[28] S. Karvinen, P. Hirva, T. A. Pakkanen, J. Mol. Struct. THEOCHEM., 626 (2003) 271.

[29] K. Maeda, J. Photochem. Photobiol. C: Photochem. Rev., 12 (2011) 237.

[30] A. Trapalis, N. Todorova, T. Giannakopoulou, N. Boukos, T. Speliotis, D. Dimotikali, Jiaguo Yu, Appl. Catal. B, 180 (2016) 637.

[31] S. Malato, P. Fernández-Ibáñez, M. I. Maldonado, J. Blanco, W. Gernjak, Catal. Today, 147 (2009) 1.

[32] J. Low, J. Yu, M. Jaroniec, S. Wageh, A. A. Al-Ghamdi, Adv. Mater., 29 (2017) 1601694.

[33] S. Malato, M. I. Maldonado, P. Fernández-Ibáñez, I. Oller, I. Polo, R. Sánchez-Moreno, Mater. Sci. Semicond. Process., 42 (2016) 15.

[34] B. Srikanth, R. Goutham, R. B Narayan, A. Ramprasath, K. P. Gopinath, A. R. Sankaranarayanan, J. Environ. Manage., 200 (2017) 60.

[35] S. N. Ahmed, W. Haider, Nanotechnology, 29 (2018) 342001.

[36] A. Ajmal, I. Majeed, R. N. Malik, H. Idriss, M. A. Nadeem, RSC Adv., 4 (2014) 37003.

[37] V. V. Magdum, Y. M. Chitare, S. P. Kulkarni, D. B. Malavekar, J. H. Kim, J. L. Gunjakar, Mater. Sci. Eng. B, 313 (2025) 117892.

[38] V. V. Magdum, Y. M. Chitare, S. P. Kulkarni, D. B. Malavekar, A. U. Pawar, R. N. Bulakhe, C. D. Lokhande, U. M. Patil, S. B. Patil, J. L. Gunjakar, J. Mater. Sci.: Mater. Electron., 35 (2024) 1433.

[39] S. P. Kulkarni, Y. M. Chitare, V. V. Magdum, P. D. Sawant, S. V. Talekar, S. A. Pawar, D. B. Malavekar, S. Ansar, J. H. Kim, J. L. Gunjakar, ACS Appl. Nano Mater., 7 (2024) 11411.

[40] W. Choi, N. Choudhary, G. H. Han, J. Park, D. Akinwande, Y. H. Lee, Mater. Today, 20 (2017) 116.

[41] X. Liu, Z. Xing, H. Zhang, W. Wang, Y. Zhang, Z. Li, X. Wu, X. Yu, W. Zhou, chemsuschem., 9 (2016) 1118.

[42] B. Pourabbas and B. Jamshidi, Chem. Eng. J., 138 (2008) 55.

[43] K. K. Paul, N. Sreekanth, R. K. Biroju, T. N. Narayanan, P. K. Giri, Sol. Energy Mater Sol. Cells, 185 (2018) 364.

[44] Q. Li, N. Zhang, Y. Yang, G. Wang, D. H. L. Ng, Langmuir, 30 (2014) 8965.

[45] W. Zhou, Z. Yin, Y. Du, X. Huang, Z. Zeng, Z. Fan, H. Liu, J. Wang, H. Zhang, Small, 9 (2013) 140.

[46] P. Liu, Y. Liu, W. Ye, J. M. D. Gao, Nanotechnology, 27 (2016) 225403.

[47] X. Li, T. Zhang, S. Gu, S.-Z. Kang, G. Li, J. Mu, Sep. Purif. Technol., 108 (2013) 139.

[48] M. Sabarinathan, S. Harish, J. Archana, M. Navaneethan, H. Ikeda, Y. Hayakawa, RSC Adv., 7 (2017) 24754.

[49] J. P. M. Alido, F. N. I. Sari, J.-M. Ting, Ceram. Int., 45 (2019) 23651.

[50] S. V. Kite, A. N. Kadam, D. J. Sathe, S. Patil, S. S. Mali, C. K. Hong, S.-W. Lee, K. M. Garadkar, ACS Omega, 6 (2021) 17071.

[51] S. Mutyala, M. M. J. Sadiq, M. Gurulakshmi, C. Suresh, D. K. Bhat, K. Shanthi, J. Mathiyarasu, J. Nanosci. Nanotechnol., 20 (2020) 1118.

[52] Z. A. Thiehmed and T. M. Altahtamouni, Nanomaterials, 12 (2022) 2904.

[53] R. Gopal, M. M. Chinnapan, A. K. Bojarajan, N. K. Rotte, J. S. Ponraj, R. Ganesan, I. Atanas, M. Nadarajah, R. K. Manavalan, J. Gaspar, Sci. Rep., 10 (2020) 21625.

[54] J. Su, S. Yu, M. Xu, Y. Guo, X. Sun, Y. Fan, Z. Zhang, J. Yan, W. Zhao, Mater. Res. Bull., 130 (2020) 110936.

[55] I. Tacchini, E. Terrado, A. Anso´n, M. T. Martı´nez, Micro & Nano Letters, 6 (2011) 932.

[56] W. Teng, Y. Wang, Q. Lin, H. Zhu, Y. Tang, X. Li, J. Nanosci. Nanotechnol., 19 (2019) 3519.

[57] M. K. Silva, R. G. Marques, N. R. C. F.Machado, O. A. A. Santos, Braz. J. Chem. Eng., 19 (2002) 359.

[58] M. I. Ghouri, E. Ahmed, Ceram. Int., 45 (2019) 23196.

[59] N. P. de Moraes, F. Na. Silva, M. L. C. P. da Silva, T. M. B. Campos, G. P. Thim, L. A. Rodrigues, Mater. Chem. Phys., 214 (2018) 95.

2.1 Introduction

Increasing water pollution has been considered one of the significant problems for marine life as well as human beings. There are several reasons for water pollution, out of which the toxification of water by organic dyes has a significant contribution. Various organic dyes are primarily used in textile industries to color fabrics. Also, synthetic dyes are widely used in many fields of advanced technology, e.g., in various textile, paper, leather tanning, food processing, plastics, cosmetics, rubber, printing and dye manufacturing industries. Their discharge into the hydrosphere causes a significant source of pollution due to their recalcitrant nature [1]. It has been reported that more than 1,00,000 dyes are available commercially, and around 8,00,000 tonnes of dyes are produced annually. About 10-15% of dyes are lost during various processes in the textile industry [2]. Many of these dyes have adverse effects on the environment. Some of them are carcinogenic and give rise to various biological disorders. These dyes can cause various biological disorders, as mentioned in **Chapter 1, section 1.1.4 [3]**. Various processes like adsorption on activated carbon, ultrafiltration, reverse osmosis, coagulation by chemical agents, ion exchange on synthetic adsorbent resins, etc., have been used to reduce water contamination. Nevertheless, they are non-destructive since they transfer organic compounds from water to another phase, thus causing secondary pollution [4]. In this context, heterogeneous photocatalysis has emerged as one of the best solutions for degrading organic dye pollutants from the water using sunlight in the presence of semiconductors.

Solution deposition techniques like chemical bath deposition (CBD) and successive ionic layer adsorption and reaction (SILAR) demonstrated the advantages of low-cost fabrication, large-area deposition and better orientation of crystallites with pinhole-free homogeneous and uniform deposition. Narrow band gap MoS_2 has proved its ability to harvest visible light for photocatalytic applications with unique crystal structure, chemical stability, low toxicity, low cost, high optical absorption coefficient, well-suited band structure and favorable flat band potential positive to hydrogen evolution reaction [5].

Photocatalysis includes a broad range of applications like solar-assisted H_2 production via water splitting, dye adsorption/degradation of organic dyes to reduce water pollution and conversion of carbon dioxide into gaseous hydrocarbons using

semiconductor photocatalyst. Various semiconductor materials have been exploited for photocatalysis. However, most photocatalysts ever developed are inappropriate for visible light photocatalysis because of their wide bandgap energy and unsuitable band positions for reducing protons and oxidizing oxide ions. Therefore, much effort is put into hybridizing two kinds of photocatalysts with suitable band positions. Such a hybridization strategy can enable exciton separation via strong electronic coupling between the coupled semiconductors. Especially nanostructures of wide bandgap TiO_2, Nb_2O_5 and ZnO are used for the coupling with narrow bandgap semiconductors like CdS, WO_3, $BiVO_4$, MoS_2, WS_2, etc **[6-8].** MoS_2 has shown promising application as an effective photocatalyst owing to its narrow bandgap and layered structure that facilitates photocatalytic performance. MoS_2 belongs to the transition metal chalcogenide group with the general formula MX_2, where M is a transition metal and X is a chalcogen. Its layered structure provides higher access to target organic molecules for adsorption, enhancing degradation efficiency. In addition, the sulfur sites in the MoS_2 are catalytically active sites that enhance the degradation performance. Recently, 2D metal oxide nanosheets (2DMON) have emerged as basic building blocks for synthesizing hybrid materials. These materials are unique because they have unusually high anisotropy in their crystal structure and morphology, large surface area, and ultrathin thickness of the exfoliated nanosheets **[9]**. These 2DMON can be synthesized using the soft-chemical exfoliation process of the pristine layered materials **[10]**. 2DMON demonstrated the excellent photocatalytic performance when hybridized with nanostructures of Fe_2O_4, ZnO, CdS, MoS_2, ZnCr-LDH and WO_3 **[9, 11-14]**. Still, the hybrid photocatalyst based on 2DMON is at the nascent stage.

Therefore, titanate nanosheets (Titanate-NS) and niobate nanosheets (Niobate-NS) derived from the exfoliation of parent layered crystals of $Cs_{0.7}Ti_{1.825}\square_{0.175}O_4$ and $K_4Nb_6O_{17}$, respectively, are suitable wide bandgap materials for the hybridization with narrow bandgap MoS_2. Due to the apparent advantages of chemical methods, they are the best choice for coupling MoS_2 with titanate-NS and niobate-NS. The coupling of MoS_2 with titanate-NS and niobate-NS can be expected to unveil enhanced photocatalytic activity through effective electron-hole pair separation via strong electronic coupling between the hybridized species.

2.2 Chemical solution deposition methods

It is well known that deposition techniques are broadly divided into two major categories: chemical and physical. Chemical deposition techniques are efficient in terms of low power consumption and temperature requirement, whereas physical deposition methods become way costlier, making the synthesis process inefficient. The performance of the material is mainly dependent on its properties, which can be tuned by synthesis methods. The chemical deposition methods offer easily controllable preparative parameters that can effectively alter reaction conditions and tune materials' properties. This section briefly describes the chemical deposition methods employed for the deposition of thin films.

2.2.1 CBD:
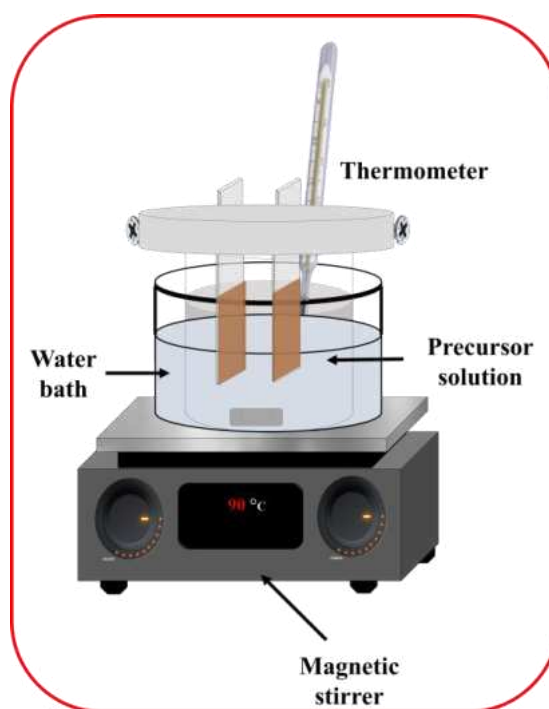
Figure 2.1: Schematic representation of CBD method.

CBD (**Fig. 2.1**) method is well employed for synthesizing various nanostructured semiconductors. It involves controlled precipitation that initiates the heterogeneous nucleation on the surface of the substrate immersed in the chemical bath.

Principle:

Precipitation occurs when the ionic product of the reactants exceeds the solubility product of the solution. With this process, ions combine on the substrate, which initiates film formation **[15]**.

Working:

A precursor solution is made with metal salts. Complexing or reducing agents may also be added to the solution to regulate the deposition rate and avoid undesirable side effects. The well-cleaned substrate is immersed in the solution. The substrate can be heated or kept directly at room temperature (RT), depending on the required film qualities. The metal ions are attracted to the substrate's surface, where they undergo reduction and create a thin layer. The reducing agents' pH, temperature and concentration affect how quickly the reduction happens **[16]**.

It is evident that the solubility product depends on several factors, such as the temperature of the solution, solvent and particle size **[17]**. So, optimizing the deposition parameters to obtain good quality and adherent thin films is important. The quality of thin films depends on several parameters like pH, the concentration of precursor, complexing agent, temperature of the solution, deposition time and type of substrate **[18]**. The importance of this deposition technique is that one can easily control preparative parameters to alter the material properties.

Advantages:

Cost-effective: Compared to other deposition methods like sputtering or chemical vapor deposition, CBD is a cost-effective option since it uses low-temperature processes and an affordable experimental setup.

Easy setup: The method works well in laboratory and industrial firms because it often only needs a beaker, heating plate and stirrer.

Large-area deposition: CBD has the ability to evenly cover large substrates, which is advantageous for applications such as large-area electronics and solar cells.

Versatility: An extensive range of materials, including metals, metal oxides and semiconductors, can be deposited on various types of substrate using this technique **[19]**.

2.2.2 SILAR:
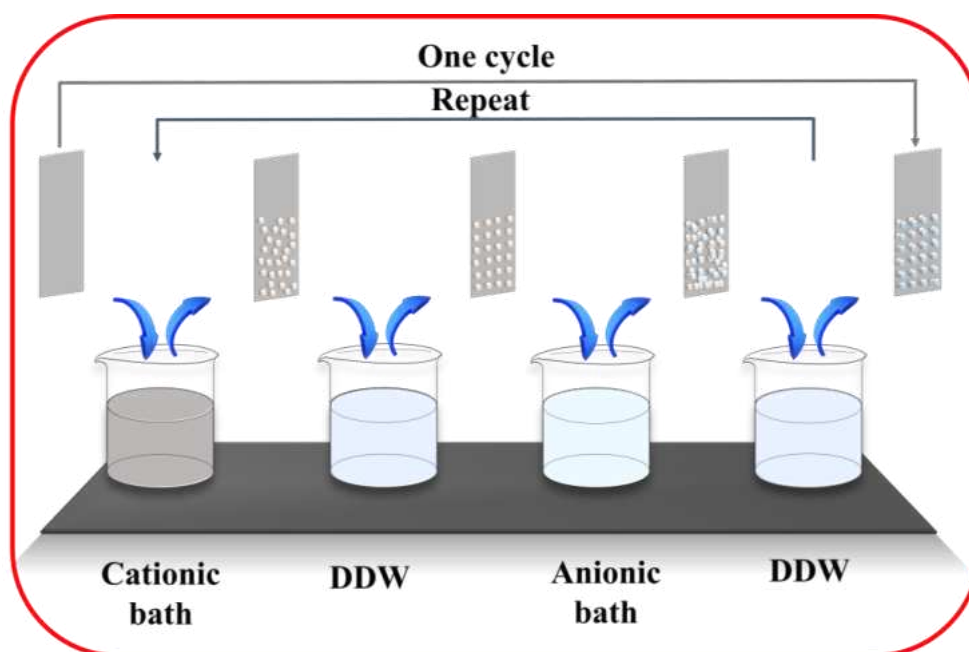
Figure 2.2: Schematic representation of the SILAR method.

SILAR is a modified version of the CBD method, which is one of the useful synthesis methods for depositing nanocrystalline semiconductor thin films. In CBD, when the ionic product exceeds the solubility product, the precipitation takes place. In this process, both homogeneous and heterogeneous precipitates are formed. The homogeneous precipitate can generate a bulk powder of semiconductors and lead to the wastage of precursor chemicals. This problem is resolved in the SILAR method by separating cationic and ionic solutions, thereby avoiding precipitation, as shown in **Fig. 2.2 [20]**.

Principle:

The alternating adsorption and reaction of ionic species on the substrate surface is the basis for the SILAR technique. The fundamental idea is that material is deposited in layers, with each layer being formed by a distinct immersion process in a different precursor solution **[21]**.

Working:

The SILAR method involves four steps: adsorption, first rinsing, reaction and second rinsing. One can employ a 2-beaker or 3-beaker system instead of the 4-beaker system by removing rinsing steps as per convenience. Dipping and rinsing times can be

optimized to obtain good-quality adherent thin films. Most importantly, the thickness of the film can be well controlled by varying deposition cycles. The concentration of the cationic and anionic solutions, pH, dipping and rinsing times and number of deposition cycles affect the film formation [22]. The SILAR method is advantageous in terms of its low cost, large-area deposition, use of a variety of substrates and RT deposition [20]. As a result, several metal-chalcogenides and -oxides have been deposited using the SILAR method. A brief discussion of the stepwise SILAR process is given below.

First immersion: The substrate is immersed in the first beaker (cationic solution), which contains the metal ions or precursor ions that will be utilized in the film.

First rinsing: To remove any excess precursor ions not attached to the surface, the substrate is removed and washed in DDW. This guarantees that only the ions attached to the surface remain on the substrate.

Second immersion: The substrate is subsequently dipped in a second solution, known as an anionic solution, which contains the reactants or counter ions that will react with the metal ions from the first solution.

Second rinsing: The substrate is removed from the second solution and rinsed again with DDW to eliminate unreacted ions.

Advantages:

Precise control of film thickness: Since the deposition is done layer by layer, SILAR enables exact control over the film thickness. The resulting film's thickness may be precisely controlled by varying the number of deposition cycles, which is essential for numerous applications in optoelectronics, solar cells and sensors.

Low-temperature process: The low-temperature deposition using the SILAR method makes it suitable for substrates that can not withstand high temperatures, such as glass or plastic.

High uniformity: The simplicity of deposition helps achieve high uniformity throughout the substrate surface. Therefore, this method can be used for large-area deposition [24].

2.2.3 Hydrothermal:

Figure 2.3: Schematic representation of the hydrothermal method.

The hydrothermal method resembles the chemical reaction carried out in a closed vessel at high temperature and pressure. This method offers controlled diffusivity in a closed chamber, as shown in **Fig. 2.3 [25]**. Hydrothermal is best known for obtaining various types of morphologies. Different surfactant-assisted chemical reactions result in distinct surface energies for the material. The main advantage of this method is that the materials with high vapor pressure can be synthesized using the hydrothermal method **[26]**.

Principle:

This method involves a heterogeneous chemical reaction in aqueous media above room temperature (over 100°C) and higher pressure levels (over 1 bar), generally achieved using an autoclave oven **[27]**.

Working:

The first step in the process is making a precursor solution. In this process, appropriate chemical reagents are dissolved in water. Additional reagents may be added to the solution to modify the concentration of particular ions or alter pH. The precursor solution is then transferred into a sealed container, typically a Teflon-lined autoclave (a high-pressure vessel). A Teflon container placed inside a sealed steel chamber is used for hydrothermal synthesis. This system is then put in an autoclave or furnace to heat at the desired temperature **[28]**.

Temperatures within the autoclave are usually between 100°C and 300°C. The water stays superheated in these circumstances, enabling the precursors to react and create the intended solid product, usually in the form of thin films, crystals, or nanoparticles. The high temperature and pressure during the reaction speed up chemical reactions, improve the chemicals' solubility and encourage crystal nucleation and development **[29]**.

Advantages:

Synthesis of high-purity materials: Highly pure materials can be synthesized using the hydrothermal process. For high-quality materials, the combination of high temperature and high pressure minimizes the production of undesirable byproducts.

Control over material properties: The hydrothermal process offers precise control over the material's size, shape, and crystallinity by varying synthesis parameters such as temperature, pressure, precursor concentration, and reaction time. This makes it perfect for electronics, optics, and catalysis, which require exact control over material properties.

Environmentally friendly: Since water is a commonly available and non-toxic solvent, the hydrothermal process is frequently seen as environmentally friendly. Additionally, the technique usually does not include hazardous organic solvents, which lowers the adverse environmental effects **[26]**.

2.2.4 Electrodeposition:

Electrodeposition is a renowned method for depositing thin films of material by providing electrical bias to a conducting substrate immersed in the solution containing a salt of that material **[30]**. This technique has recently gained enormous attention due to its simplicity of deposition mechanism.

Principle:

When the conducting substrate is immersed in the electrolyte containing cations and anions to be coated and potential is applied across the electrode-electrolyte interface, charge transfer occurs, followed by film deposition. For electrodeposition, a DC power source or electrochemical workstation can be used that benefits excellent control over

deposition potential, which is the driving force of the electrodeposition reaction **[31]**. The schematic illustration of the electrodeposition method is displayed in **Fig. 2.4**.
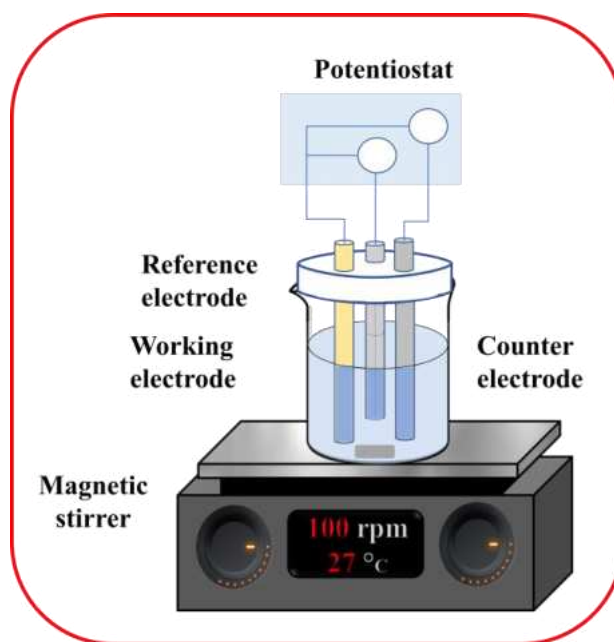
Figure 2.4: Schematic representation of the electrodeposition method.

Working:

The cleaned substrate is connected to the negative terminal (cathode) of a DC power supply, and the anode is connected to the positive terminal. The electrolyte solution is placed in the bath and the electrodes (anode and cathode) are immersed in the solution. The anode and cathode are subjected to a potential difference. While the anode supplies metal ions to the electrolyte, the metal cations from the electrolyte solution are drawn to the cathode (substrate) and undergo reduction **[32]**. The metal is deposited to the substrate's surface layer by layer. The metal ions undergo reduction at the cathode before being deposited on the surface. The applied current, the concentration of metal ions in the solution and the bath's temperature determine the rate of deposition **[33]**.

Advantages:

Excellent adhesion: The deposited metal usually adheres strongly to the substrate after electrodeposition. Additionally, the method yields highly consistent, smooth coatings, which is crucial for use in sensors, electronics and other precision sectors.

Alloy deposition: Electrodeposition can be utilized to produce alloy coatings through the simultaneous reduction of metal ions from several metal sources. This makes it

possible to deposit alloys with a regulated composition, which is advantageous for uses that are required for particular material qualities like electrical conductivity, hardness or corrosion resistance.

Ability to deposit on complex shapes: Since electrodeposition relies on electrochemical reactions, it can coat substrates with sophisticated types, holes, and cavities. Because of this, it is suitable for coating printed circuit boards, connections, and electronic components **[34]**.

2.2.5 Dip-coating:
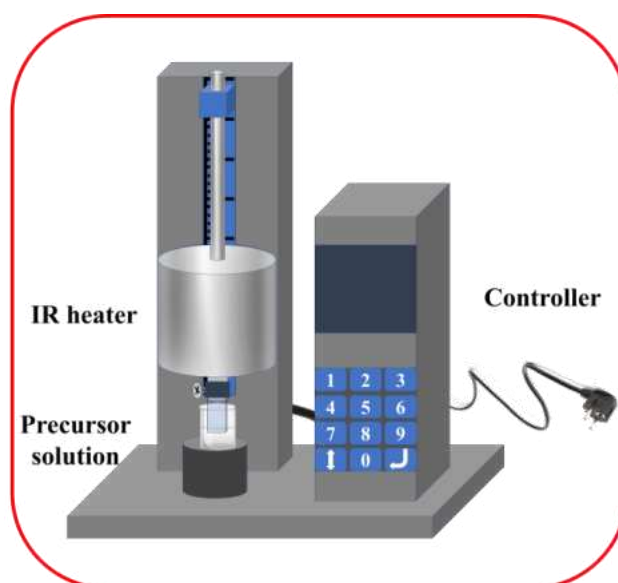
Figure 2.5: Schematic representation of the dip-coating method.

Fig. 2.5 shows a schematic of the dip-coating technique, which is being used worldwide at the industrial scale due to its simple and straightforward application for the deposition of various nanostructured thin films.

Principle:

The dip coating process involves dipping a substrate at a controlled speed in the colloidal suspension containing the material to be deposited. Another critical factor in the dip-coating is the retrieval speed of the substrate from the solution **[35]**. Capillary action helps draw the coating solution onto the substrate's surface as it is removed from the solution, creating a thin layer. Once optimized, this method can be used to deposit highly uniform and adherent thin films.

Working:

Depending on the desired coating area, the substrate is either fully or partially submerged after being dipped into the prepared solution. The substrate is removed from the solution at a regulated pace following immersion. This phase is crucial as it determines the coating's thickness and homogeneity **[36]**. A few millimetres per second to several centimetres per second is the usual range for the withdrawal speed. After retrieval, the film is subjected to the infrared heating chamber, where the coating solution starts to evaporate. The volatility of the solvent and the temperature of the IR chamber both affect the rate of evaporation. The thickness of the film can be controlled by repeating the number of dip cycles **[37]**.

Atmospheric temperature, airflow, and surrounding cleanliness are the factors that influence the deposition carried out using the dip coating method. This method is beneficial for materials with thickness-dependent properties as it favors thickness control.

Advantages:

Scalability: Applications for dip-coating can be readily expanded from laboratory to industrial scale. Because of its scalability, it is perfect for producing coated goods in large quantities, including circuit boards, optical devices or automobile parts.

Low material waste: When it comes to material utilization, the dip-coating method is comparatively efficient. By recovering and reusing the extra solution, waste can be minimized and material costs can be decreased overall.

Thickness control: When several layers of the material are required, dip-coating offers excellent control over film thickness. The the rate of withdrawal and the number of dips can be changed to alter the thickness **[38]**.

2.3 Solid-state synthesis:

Solid-state synthesis is one of the nanomaterial synthesis methods used to produce highly crystalline materials. This reaction mainly involves mixing two or more solid reactants and their decomposition at moderately higher temperatures (typically 1000-1500 °C). Fine-grained compounds are crushed, pelletized and heated for a given time at higher temperatures. Many of the oxide precursors require a specific temperature and pressure in order to initiate chemical reactions, which can be fulfilled by this

method. As usual, various factors affect the material formation, such as precursors, annealing temperature, ramp rate, annealing time, surface area and free energy associated with the reaction **[39]**.

Experimental procedure:

> **Reagents**

The fine-grained powder precursors are preferred for the solid-state synthesis method. The selection of reagents is also based on the feasibility and the reaction rate. Also, the atmosphere for the reaction should be taken into consideration. An inert, oxidizing or reducing atmosphere can directly affect the composition of the final product.

> **Reaction**

Once precursors are weighed appropriately, they are mixed, usually in mortar and pestle (for small-scale synthesis). These precursors are then intimately crushed to form a homogenous mixture. One can add volatile solvents such as acetone or ethanol to form a slurry and convert them into pellets upon evaporation of volatile content.

> **Heat treatment**

The heat treatment is the most crucial part of the solid-state synthesis method, as it determines the phase formation of the resultant material. The temperature required for the reaction is determined by the precursors used and their melting points. While synthesizing a new material, several reactions should be carried out to optimize the temperature. Some materials can be formed in a couple of hours, while some may take weeks. Nowadays, programmable furnaces are being used, allowing one to adjust heating and cooling rates with multiple steps. The homogenous mixture is first placed in a suitable container, such as a crucible or boat and then put in the furnace. Various types of crucibles and boats in the market have different temperature ranges. Materials like quartz, porcelain, alumina, etc., can be used depending on the temperature **[40].**

2.4 Exfoliation:

Exfoliation is one of the important aspects of the material engineering process. 2D material exfoliation is a technique used to isolate individual layers of 2D materials from their bulk counterparts to harness their unique properties. This process is crucial

for materials like graphene, TMDs, and black phosphorus, which exhibit extraordinary electrical, mechanical and optical characteristics in their monolayer forms **[41]**. Exfoliation typically involves mechanical methods, such as using adhesive tapes to peel off layers, or chemical methods, like liquid-phase exfoliation, where materials are dispersed in a solvent and then separated into thinner layers through sonication or other techniques **[42]**. This technique allows researchers and engineers to explore and utilize the exceptional properties of 2D materials for various applications, including in advanced electronics, photonics and energy storage systems **[43]**. By producing high-quality monolayers and few-layer materials, exfoliation paves the way for innovations in nanoscale technology and the development of next-generation devices.

2.5 Material characterization techniques:

Characterization of a material is an essential aspect of materials science as it is crucial to identify the physical and chemical properties of the compound before using it for any application. It is well known that the performance of a material is highly dependent on its physicochemical properties. For example, optical properties are helpful in photocatalytic applications, which can be confirmed using the UV-Vis DRS technique. Electrocatalytic applications require high electrical conductivity, which can be measured using electrochemical impedance spectroscopy. Many applications depend on the material's microstructure and surface area, which FE-SEM and Brunauer-Emmett-Teller (BET) techniques can observe. Therefore, the prepared materials were characterized by XRD, FTIR, Raman, SEM, UV-Vis DRS, etc., for identifying and confirming structural, chemical, surface area, morphological and optical properties. A brief discussion of the characterization technique is given below.

2.5.1 XRD:

XRD is a powerful characterization technique primarily used to identify a material's crystal structure and phase. It works on the principle of Bragg's law, which says that the X-rays diffract from the crystallographic planes of a crystalline material. This can be mathematically represented as follows

$$2d \sin\theta = n\lambda \tag{2.1}$$

Where d is the interplanar distance, θ is the angle of diffraction, n is the order of the diffraction and λ is the X-ray's wavelength. The schematic of the X-ray diffractometer is shown in **Fig. 2.6a**.

XRD technique has a broad application as it is also used for determining lattice strain, dislocation density, lattice parameters, crystallite size and its orientations, etc. **[44-45]**. Crystallite size can be calculated using the famous Scherrer's formula as given below.

$$D = \frac{K\lambda}{\beta \cos\theta}$$ (2.2)

Where D is crystallite size, k is constant, β is full width at half maximum for the most intense peak and θ is the angle of diffraction **[46]**.

This study uses the XRD technique to confirm the phase formation of MoS_2, titanate-NS, niobate-NS and their hybrids. The photograph of the XRD instrument used for this study is shown in **Fig. 2.6b**.
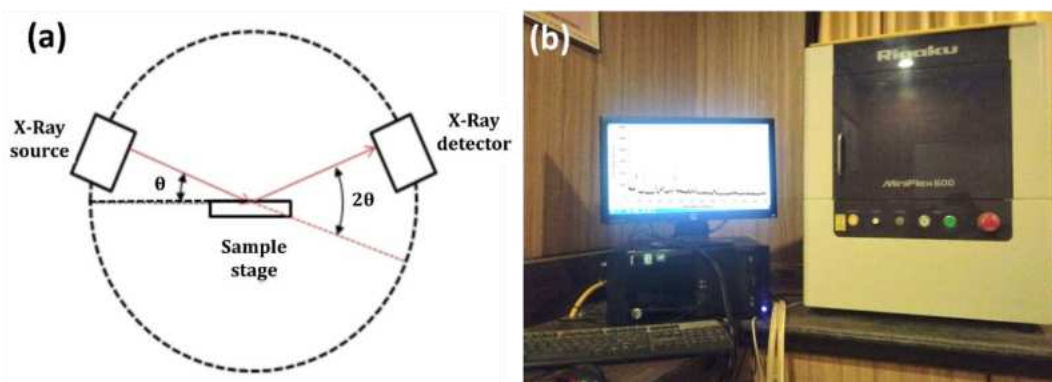
Figure 2.6: (a) Schematic representation of XRD and (b) photograph of XRD instrument (Rigaku Miniflex 600).

2.5.2 FTIR:

FTIR technique is widely used to identify the presence of functional groups and understand the chemical nature of a compound. FTIR works on the principle that when infrared radiations are passed through a sample, they get absorbed by the sample. The absorption spectra are then recorded with respect to the wavenumber. As every molecule possesses distinct absorption spectra, one can identify the unknown material by recording its FTIR spectra, which can act as a fingerprint of that material.

It is well known that atoms can vibrate in six different ways, viz. rocking, wagging, scissoring, symmetrical and anti-symmetrical stretching, and twisting **[47]**. A molecule bond will absorb distinct wavelengths depending on the type of vibration (stretching or bending) **[48]**. Different bonds and functional groups absorb different wavelengths; a distinct absorption spectrum is obtained for different samples. A ray diagram of the FTIR instrument is shown in **Fig. 2.7**. This study uses the FTIR technique

to identify the nature of the chemical bonding of MoS_2, titanate-NS, niobate-NS and their hybrids.
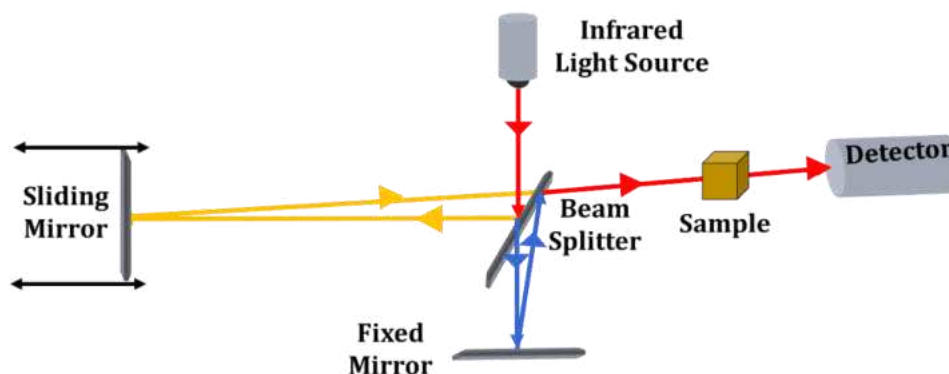
Figure 2.7: Ray diagram of FTIR spectrometer [49].

2.5.3 Raman spectroscopy:

It is an analytical technique used to identify the vibrational modes of a molecule. Other low-frequency modes and rotational modes can also be observed using this technique. This technique provides structural fingerprints of the molecule to be identified.

This technique principally works on the inelastic scattering of light. A monochromatic light source is used for this purpose. When photons interact with phonons, vibrations or excitons in the system, the energy of photons gets shifted up or down, thereby giving information about the presence of vibrational modes. The ray diagram of the Raman spectrometer is shown in **Fig.2.8**.

When a molecule absorbs the energy of a photon, it excites to a virtual state. After some time, it returns to its original position by losing energy equal to the incident photon. However, if the energy lost by an electron is not equal to the photon energy, the electron reaches different vibrational energy levels, giving rise to Raman scattering [50-53].

In this study, Raman spectroscopy is used to confirm the formation of pristine MoS_2 and identify the nature of chemical bonding in all samples. As the formation of MoS_2 can be confirmed from phonon modes of Raman spectroscopy, it provides strong evidence for the formation of MoS_2.
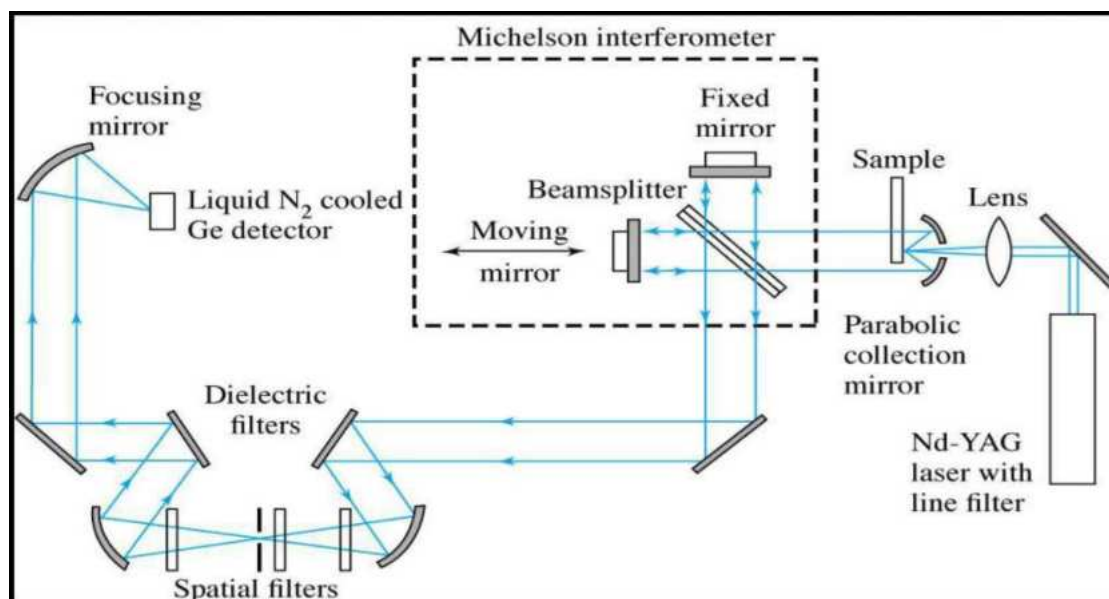
Figure 2.8: Ray diagram of Raman spectrometer **[54]**.

2.5.4 FE-SEM:

The FE-SEM technique is widely employed in material science for a material's morphological and surface inspection at a higher magnification. The EDS attached to the FE-SEM instrument is used for the qualitative and quantitative analysis of the elements present in the material.

In this technique, a beam of highly energetic electrons is generated by thermionic emission from a cathode (generally tungsten filament) and directed towards the sample placed in the sample chamber using condenser lenses **[55]**. These electrons are made to strike the samples with high kinetic energy. The schematic of the FE-SEM instrument is shown in **Fig. 2.9**. Before performing sample analysis, the chamber is closed and a high vacuum is created to increase the mean free path **[56]**.

When energetic electrons strike the sample surface, various radiations result from electron interaction with the sample surface. The different types of radiations are depicted in **Fig. 2.10** and noted in **Table 2.1**. These different radiations provide different information about the material as follows.

Table 2.1: Various types of radiations and information obtained from them.

Radiation	Information
Backscattered and secondary electrons	Creation of a sample image
Characteristic X-rays	Elemental composition
Auger electron	Composition information in the near-surface environment of a material
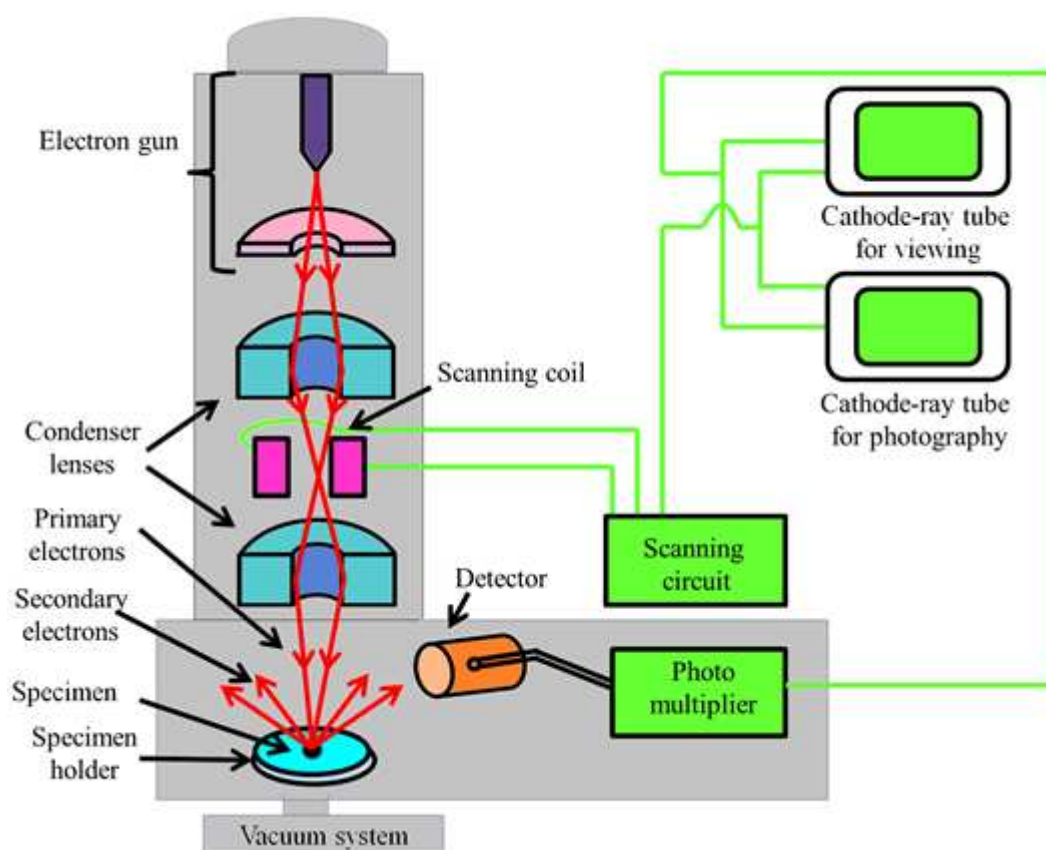
Figure 2.9: Ray diagram of FE-SEM **[57]**.
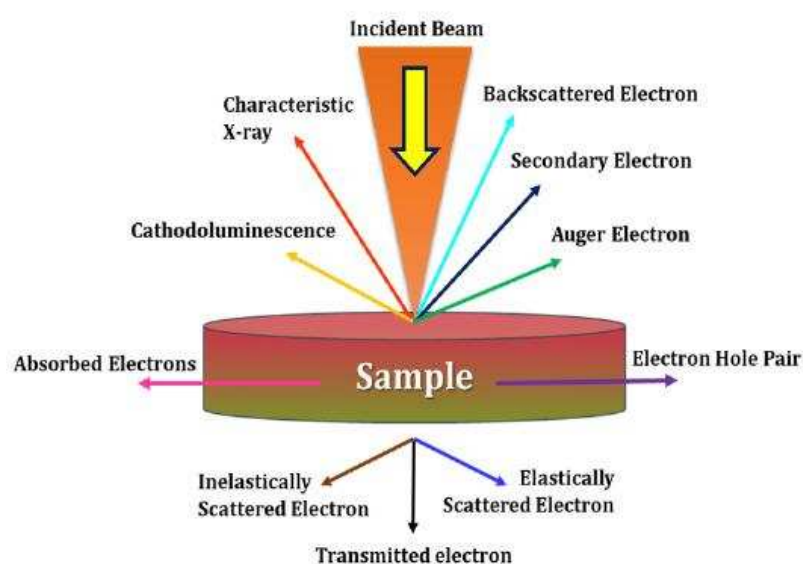
Figure 2.10: Ray diagram of the emission of diverse forms of electrons during scanning **[58]**.

This study uses the FE-SEM technique to study the surface morphology and determine the nanosheet sizes of prepared samples. Cross-section FE-SEM was also used to measure the film thickness. An EDS study was carried out to understand the elemental composition of thin deposited films.

2.5.5 XPS:
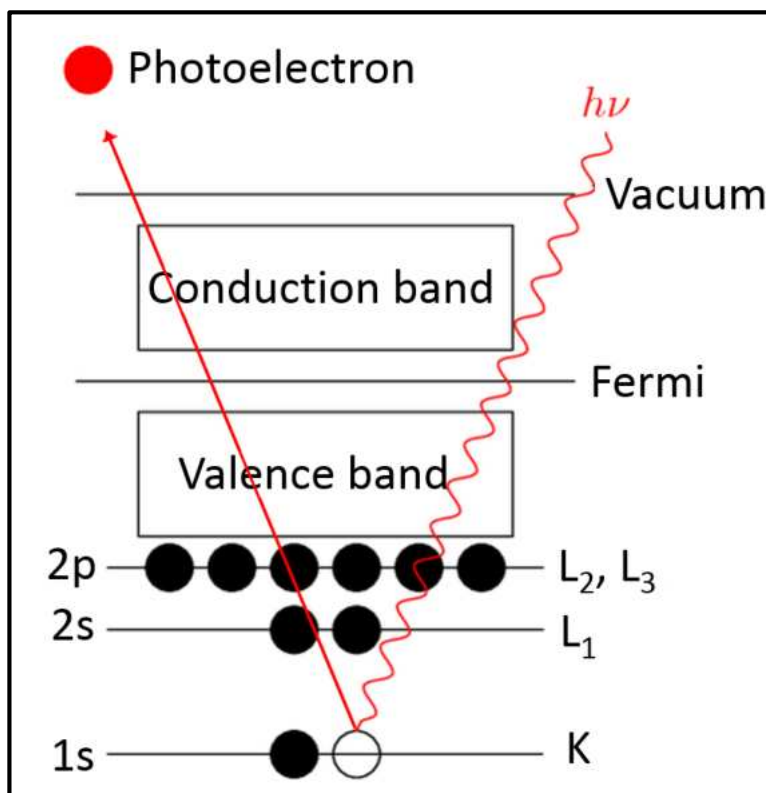
Figure 2.11: Energy diagram of XPS **[60]**.

XPS technique is a powerful tool for identifying the presence of elements in a compound and their oxidation states. It is based on the photoelectric effect. Also, it helps determine the density of electronic states and calculate work functions and chemical states. Therefore, XPS has gained enormous research attention.

In this technique, X-rays are bombarded on the sample surface, which causes a photoelectric effect and ejects an inner shell electron. This electron carries some kinetic energy with it. The kinetic energy associated with the ejected electron is recorded and presented in the form of a spectrum where the energy of the ejected electron provides information about the elements present in the sample **[59].** The binding energy (BE) is calculated using the following formula.

$$\text{E}_{binding} = \text{E}_{photon} - (\text{E}_{kinetic} + \varphi) \tag{2.3}$$

The schematic of the XPS technique is shown in **Fig.2.11**.

The count of photoelectrons as a function of BE can be used to examine the sample's composition and the different oxidation states of the elements present in the sample.

This study uses the XPS technique to study the presence of elements and to determine their oxidation states in the MoS_2, titanate-NS, niobate-NS and their hybrids.

2.5.6 UV-Vis:

The UV-Vis spectrophotometer is a vital characterization technique widely used in many science disciplines, such as physics, chemistry, microbiology and nanotechnology. This technique is used to record the absorbance of light by a sample. In this technique, UV, Visible and IR radiations are passed through the sample of interest and its absorbance is recorded and compared with the original light intensity. The ratio of I/I_0 calculates the percentage of transmittance. The absorption A is based on the transmittance

$$A = -\log T = -\log \frac{I}{I_0} \tag{2.4}$$

The wide range of wavelengths is generated using a deuterium lamp for UV light and a tungsten lamp for visible light. Another important application of the UV-Vis technique is the estimation of the bandgap energies of a material. The energy band gap of the material is found from the absorbance spectra by using the relation **[61]**

$$E_g = \frac{h_c}{\lambda_g} = \frac{1240}{\lambda_g} \ (eV) \tag{2.5}$$

Where 'λg' is the wavelength of the intercept. The schematic representing the principle of UV-Vis is shown in **Fig. 2.12**.

In this work, the UV-Vis technique is used to measure the absorbance and calculate the bandgap energies of the deposited thin films. Most importantly, dye degradation studies have been thoroughly performed on UV-Vis spectroscopy by measuring the decrease in absorption intensity at the characteristics wavelength of dye with respect to irradiation time.
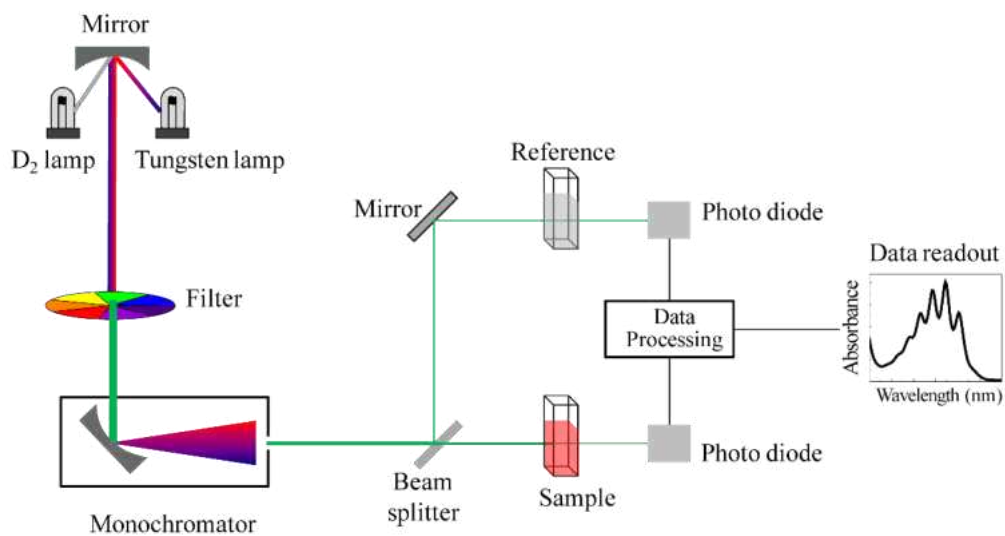
Fig. 2.12: Schematic of reflected and specular light **[62]**.

2.6 References

[1] M. T. Yagub, T. K. Sen, S. Afroze, H. M. Ang, Adv. Colloid Interface Sci., 209 (2014) 172.

[2] M. Rafatullaha, O. Sulaimana, R. Hashima, A. Ahmad, J. Hazard. Mater., 177 (2010) 70.

[3] M. A. Hassaan, A. E. Nemr, Am. J. Environ. Sci., 1 (2017) 64.

[4] I. K. Konstantinou and T. A. Albanis, Appl. Catal. B, 49 (2004) 1.

[5] V. Nicolosi, M. Chhowalla, M. G. Kanatzidis, M. S. Strano, J. N. Coleman, Science, 340 (2013) 1226419.

[6] W. Teng, Y. Wang, Q. Lin, H. Zhu, Y. Tang, X. Li, J. Nanosci. Nanotechnol., 19 (2019) 3519.

[7] I. Tacchini, E. Terrado, A. Anso´n, M. T. Martı´nez, Micro Nano Lett., 6 (2011) 932.

[8] F. Xu, B. Zhu, B. Cheng, J. Yu, J. Xu, Adv. Optical Mater., 6 (2018) 1800911.

[9] J. L. Gunjakar, T. W. Kim, H. N. Kim, I. Y. Kim, S.-J. Hwang, J. Am. Chem. Soc., 133 (2011) 14998.

[10] D. Merki and X. Hu, Energy Environ. Sci., 4 (2011) 3878.

[11] R. B. Shinde, N. S. Padalkar, S. V. Sadavar, S. B. Kale, V. V. Magdum, Y. M. Chitare, S. P. Kulkarni, U. M. Patil, V. G. Parale, H.-H. Park, J. L. Gunjakar, J. Hazard. Mater., 432 (2022) 128734.

[12] S. P. Kulkarni, V. V. Magdum, Y. M. Chitare, D. B. Malavekar, J. H. Kim, S. Alshehri, J. L. Gunjakar, S. P. Patole, Heliyon, 10 (2024) e39235.

[13] V. V. Magdum, Y. M. Chitare, S. P. Kulkarni, D. B. Malavekar, J. H. Kim, J. L. Gunjakar, Mater. Sci. Eng. B, 313 (2025) 117892.

[14] S. P. Kulkarni, Y. M. Chitare, V. V. Magdum, P. D. Sawant, S. V. Talekar, S. A. Pawar, D. B. Malavekar, S. Ansar, J. H. Kim, J. L. Gunjakar, ACS Appl. Nano Mater., 7 (2024) 11411.

[15] R. S. Mane and C. D. Lokhande, Mater. Chem. Phys., 65 (2000) 1.

[16] S. Sengupta, R. Aggarwal, M. Raula, J. Mater. Res., 38 (2023) 142.

[17] B. Sinha, R. H. Muller, J. P. Möschwitzer, Int. J. Pharm., 453 (2013) 126.

[18] F. G. Hone and T. Abza, Int. J. Thin. Fil. Sci. Tec., 8 (2019) 43.

[19] H. Soonmin, Appl. Sci., 12 (2022) 8184.

[20] H. M. Pathan and C. D. Lokhande, Bull. Mater. Sci., 27 (2004) 85.

[21] B. R. Sankapal, R. S. Mane, C. D. Lokhande, Mater. Res. Bull., 35 (2000) 2027.

[22] S. John and V. Geetha, AIP Conf. Proc., 2162 (2019) 020138.

[23] P. P. Bagwade, D. B. Malavekar, S. B. Ubale, R. N. Bulakhe, I. In, U. M. Patil, C. D. Lokhande, Electrochim. Acta, 408 (2022) 139933.

[24] M. A. M. Patwary, M. A. Hossain, B. C. Ghos, J. Chakrabarty, S. R. Haque, S. A. Rupa, J. Uddin, T. Tanaka, RSC Adv., 12 (2022) 32853.

[25] M. Shandilya, R. Rai, J. Singh, Adv. Appl. Ceram., 115 (2016) 354.

[26] Y. X. Gan, A. H. Jayatissa, Z. Yu, X. Chen, M. Li, J. Nanomater., 2020 (2020) 8917013.

[27] S. Kharbanda, N. Dhanda, A.-C. A. Sun, A. Thakur, P. Thakur, J. Magn. Magn. Mater., 572 (2023) 170569.

[28] P. B. Patil, S. S. Mali, V. V. Kondalkar, N. B. Pawar, K. V. Khot, C. K. Hong, P. S. Patil, P. N. Bhosale, RSC Adv., 4 (2014) 47278.

[29] G. Yang and S.-J. Park, Materials, 12 (2019) 1177.

[30] F. Basile, P. Benito, G. Fornasari, M. Monti, E. Scavetta, D. Tonelli, A. Vaccari, Stud. Surf. Sci. Catal., 175 (2010) 51.

[31] S. A. M. Al-Bathi. PhD thesis. Malaya University; 2007.

[32] M. Miao, H. Duan, J. Luo, X. Wang, Mater. Adv., 3 (2022) 6968.

[33] S. Saha, M. Johnson, F. Altayaran, Y. Wang, D. Wang, Q. Zhang, Electrochem., 1 (2020) 286.

[34] I. M. Dharmadasa and J. Haigh, J. Electrochem. Soc., 153 (2006) G47.

[35] L. E. Scriven, MRS Online Proceedings Library, 121 (1988) 717.

[36] M. Shigrekar and V. Amdoskar, RSC Adv., 14 (2024) 32668.

[37] M. A. Butt, Coatings, 12 (2022) 1115.

[38] X. Tang and X. Yan, J. Sol-Gel Sci. Technol., 81 (2017) 378.

[39] Solid State Chemistry and its Applications", Anthony R. West, Wiley and Sons, 2005.

[40] https://en.wikipedia.org/wiki/Solid-state_reaction_route

[41] M. Velicky and P. Toth, Appl. Mater. Today, 8 (2017) 68.

[42] G. Salussolia, E. Barbieri, N. Pugno, L. Botto, J Mech. Phys. Solids., 134 (2020) 103764.

[43] Y. Lei, T. Zhang, Y.-C. Lin, T. Granzier-Nakajima, G. Bepete, D. Kowalczyk, Z. Lin, D. Zhou, T. F. Schranghamer, A. Dodda, A. A. Sebastian, Y. Chen, Y. Liu, G. Pourtois, T. Kempa, B. Schuler, M. Edmonds, S. Quek, U. Wurstbauer, S. Wu, N. Glavin, S. Das, S. Dash, J. Redwing, J. Robinson, M. Terrones, ACS Nanosci. Au, 2 (2022) 450.

[44] G. Hodes, Marcel Dekker Inc., New York, 2001, pp. 64.

[45] B. Cullity, S. Stock, 3rd Edn., Prentice Hall, New York, 2001.

[46] B. D. Cullity, 2nd Edn., Addison- Wesley, London, 1978.

[47] R. Vilar, Woodhead Publishing, 2016.

[48] R. Nyquist, R. Kagel, Academic Press INC, New York, 2-6, 1971.

[49] https://en.wikipedia.org/wiki/Fourier-transform_infrared_spectroscopy.

[50] M. Vallikkodi, Ph. D. thesis, Alagappa University, Karaikudi, India 2018.

[51] R. A. Nyquist, R. O. Kagel, Academic press, inc., 111 Fifth Avenue, New York, 10003, 1971.

[52] G. S. Bumbrah and R. M. Sharma, Egypt. J. Forensic Sci., 6 (2016) 209.

[53] R. S. Das and Y. K. Agrawal, Vib. Spectrosc., 57 (2011) 163.

[54] R. R. Jones, D. C. Hooper, L. Zhang, D. Wolverson, V. K. Valev, Nanoscale Res. Lett., 14 (2019) 231.

[55] M. d. Assumpção, P.-d.-Silva, F. A. Ferri, Nanocharacterization Techniques, William Andrew Publishing, 2017, 1.

[56] P. Mura, J. Pharm. Biomed. Anal., 113 (2015) 226.

[57] B.J. Inkson, Materials Characterization Using Nondestructive Evaluation (NDE) Methods, (2016) 17.

[58] https://www.azom.com/article.aspx?ArticleID=16146, Interaction electron beam with sample.

[59] E. P. Barrett, L. G. Joyner, P. P. Halenda, J. Am. Chem. Soc., 73 (1951) 373.

[60] https://texample.net/tikz/examples/principle-of-x-ray-photoelectron-spectroscopy-xps/.

[61] R. Sathyamoorthy, K. Mageshwari, Sawanta, Ceram. Int., 39 (2013) 323.

[62] R. A. Soni, R. S. Rana, S. S. Godara, Nanomaterials and Nanocomposites: Characterization, Processing, and Application, (1st ed.). CRC Press. (2021) 62.

3.1 Introduction

Rapid industrialization and urbanization have led to numerous ways of causing pollution, severely degrading the ecosystem. Among various types of pollution, water pollution has been considered a severe type because of its harsh effect on living things **[1-7]**. The brief details of water pollution are given in **Chapter 1, section 1.1.**

A photocatalytic dye degradation via an advanced oxidation process is a potential way to treat dye-contaminated water. Photocatalytic dye degradation comprises a photon-assisted catalytic reaction that breaks down larger dye molecules into smaller constituents that are not harmful **[8]**. This process requires a photo-responsive catalyst that initiates a catalytic reaction when photons fall on it. Among many explored photocatalysts, MoS_2 has shown promising application as an effective photocatalyst due to its narrow bandgap and layered structure that facilitates photocatalytic performance **[9]**. MoS_2 belongs to the transition metal chalcogenide group with the general formula MX_2, where M is a transition metal and X is a chalcogen **[10, 11]**. Its layered structure provides higher access to dye molecules for adsorption, enhancing degradation efficiency. In addition, the sulfur sites in the MoS_2 are catalytically active sites that enhance the degradation performance **[12, 13]**.

As described in **Chapter 2, section 2.2**, among many thin film deposition methods, the MCSD method, also known as modified successive ionic layer adsorption and reaction (modified SILAR), offers numerous advantages, such as low-cost, large area deposition, excellent control over thickness and no requirement of conducting substrate. Most importantly, the deposition rate can be controlled using the MCSD method. It is well known that catalysis is a surface phenomenon for which optimized film properties are essential to increase the efficiency of the catalysis process. Therefore, the MCSD method is highly applicable for depositing materials with controlled deposition thickness **[14]**. Moreover, thin film photocatalysts found advantages compared to bulk photocatalysts due to the easy separation of the catalyst from the reaction. Thus, additional centrifugation or filtration steps are not required **[15]**. Though various thin film materials have been employed for photocatalytic dye degradation, MoS_2 thin films are not explored for photocatalytic dye degradation.

This chapter includes the synthesis of nanospherical-shaped MoS_2 thin films using the MCSD method and its application for photocatalytic dye degradation. The

photocatalytic performance of MoS$_2$ thin film is examined by degrading RhB and MB dyes. The degradation performance is evaluated by calculating the rate constant and applying a pseudo-first-order kinetic model.

3.2 Synthesis and characterization of MoS₂ thin film by MCSD method

3.2.1 Experimental details

3.2.1.1 Chemicals

Ammonium molybdate ($(NH_4)_2Mo_7O_{24}.4H_2O$), thioacetamide (C_2H_5NS) and sulfuric acid (H_2SO_4) were purchased from SD Fine chemicals. RhB ($C_{28}H_{31}ClN_2O_3$) and MB ($C_{16}H_{18}ClN_3S$) were purchased from Sigma Aldrich chemicals and used without further purification. Double distilled water (DDW) was used as a solvent throughout the experiment and glass slides were used as a substrate.

3.2.1.2 Synthesis of MoS₂ thin film

The glass substrates were cleaned with labolene detergent, DDW, acetone, and ethanol in an ultrasonic bath before deposition and then again in DDW. Before being used, thoroughly cleaned glass substrates were kept in deionized water.

The MCSD method was used to deposit MoS$_2$ thin films with different deposition cycles on thoroughly cleaned glass substrates. The deposition of MoS$_2$ thin films on glass substrate comprises dipping glass substrates into separately placed adsorption and reaction baths. The adsorption bath for the deposition of MoS$_2$ thin films comprised 5 mM $(NH_4)_2Mo_7O_{24}.4H_2O$ aqueous solution. The pH of the adsorption bath was adjusted at 2 using 1 M H_2SO_4. The reaction bath was prepared by ultrasonicating 100 mM of C_2H_5NS in DDW. The adsorption and reaction baths were kept at 27 and 70°C, respectively. A single deposition cycle of MCSD was completed by successive immersion of well-cleaned glass substrates into an adsorption bath for 20 seconds and a reaction bath for 20 seconds. Different thicknesses of MoS$_2$ thin films were achieved by varying numbers of MCSD deposition cycles. After the deposition, the films were washed with DDW and dried in air. Subsequently, the films are annealed in an H$_2$ atmosphere at 400°C for 2 hours for better crystallinity. The schematic representation of MoS$_2$ thin film deposition using the MCSD method is shown in **Fig. 3.1**. The MoS$_2$ thin films deposited at 200, 300 and 400 deposition cycles are denoted as MS-200, MS-300 and MS-400, respectively.
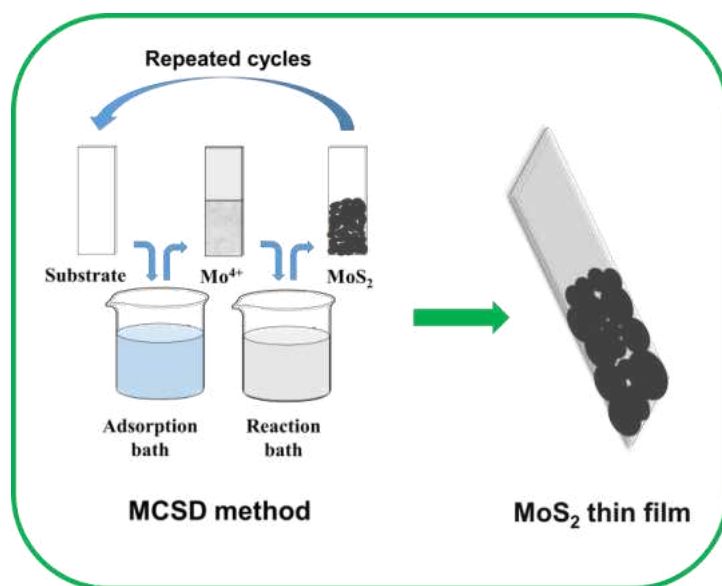
Figure 3.1: Schematic representation of the synthesis process of MoS₂ thin films by MCSD method.

3.2.1.3 Material characterization

The structural analysis of the MoS$_2$ thin films was carried out by XRD using a Rigaku Miniflex 600 Diffractometer with Ni-filtered Cu Kα radiations (l=0.15406 nm), operated at 30 kV and scanning rate of 1 degree/minute. The microscopic structural features were examined by Raman spectroscopic analysis using Thermo Scientific DXR with 532 nm laser with excitation energy of 5 mW power. The chemical bonding was studied by FTIR spectroscopy in a frequency range of 400 cm^{-1} to 4000 cm^{-1} using Bruker Alpha T. The surface morphology and spatial elemental distribution were probed by FE-SEM equipped with EDS for elemental analysis using JEOL, JSM-7900 F. The oxidation states of elements present on the surface of stated materials were investigated with XPS recorded on Thermo Scientific using Al Kα (1486.6 eV) X-ray source. The optical properties were investigated by UV-Vis DRS using a Jasco V-770 spectrophotometer in the 200-800 nm wavelength range. The UV-Vis absorption spectra of dye molecules were recorded by UV-Vis spectrophotometer using a Cary-60 spectrophotometer.

3.2.2 Results and Discussion

3.2.2.1 XRD study
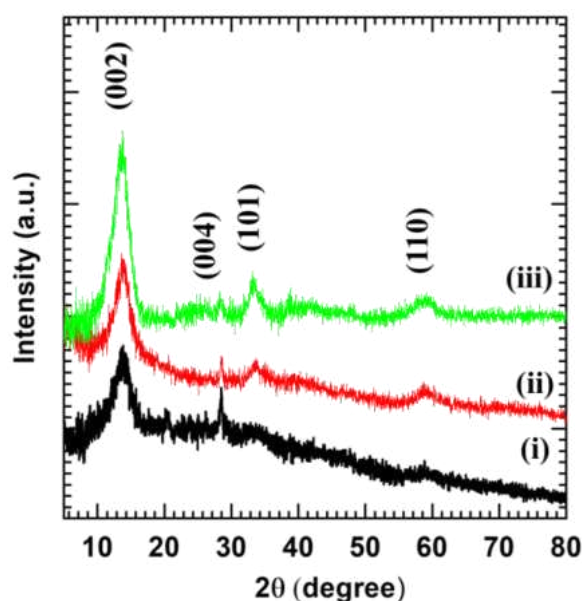
Figure 3.2: XRD patterns of (i) MS-200, (ii) MS-300 and (iii) MS-400 thin films.

The structural study of MCSD-deposited MoS₂ thin films was investigated using the XRD technique, as shown in **Fig. 3.2**. The MoS₂ thin films deposited at different deposition cycles show typical Braggs reflections that are well matched with (002), (004), (101) and (110) planes of layered hexagonal phase of MoS₂ (2H-MoS₂, JCPDS card number: 37-1492) **[16]**. The calculated lattice parameters a=b=0.313 and c=0.659 nm are in good agreement with the layered 2H-MoS₂ phase **[17-18]**. The absence of peaks other than the hexagonal phase shows the formation of phase pure MoS₂ using the MCSD method. The crystallite size was calculated for the most intense (002) plane from the Scherrer formula **(Chapter 2, section 2.5.1)**. The MS-200, MS-300 and MS-400 thin films display 57, 60 and 56 nm crystallite sizes, respectively.

3.2.2.2 Raman study

The formation of MoS₂ was further verified by Raman spectroscopy. As shown in **Fig. 3.3**, MoS₂ thin film displays characteristic Raman peaks P1 (230 cm⁻¹), P2 (384 cm⁻¹), P3 (407 cm⁻¹) and P4 (444 cm⁻¹) corresponding to longitudinal acoustic (LA(M)), in-plane (E^1_{2g}), out-of-plane (A_{1g}) vibrational and first-order optical phonon (A_{2u}) modes of MoS₂, respectively [**19**]. The origin of these peaks indicates the deposition of layered 2H-MoS₂ [**20**]. These phonon modes are separated by the Raman shift (P2-P3), which

is associated with the number of stacked MoS$_2$ layers in MoS$_2$ crystallites **[19]**. The Raman shift for the MoS$_2$ thin films is 23 cm^{-1}, confirming multi-layered MoS$_2$ thin film formation on a glass substrate **[19, 21]**. Similar correspondence between the Raman shift and the number of stacked MoS$_2$ layers has been previously reported **[20, 23]**. These spectral features associated with the chemical bonding of layered MoS$_2$ indicate the formation of layered 2H-MoS$_2$ thin films.
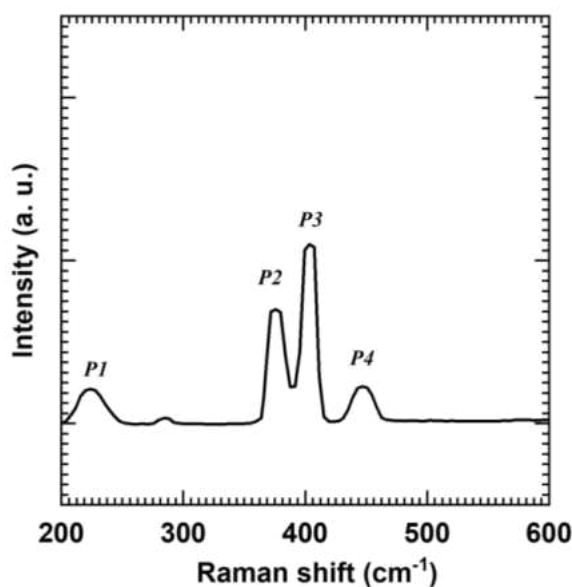
Figure 3.3: Raman spectrum of MS-300 thin film.

3.2.2.3 FTIR study
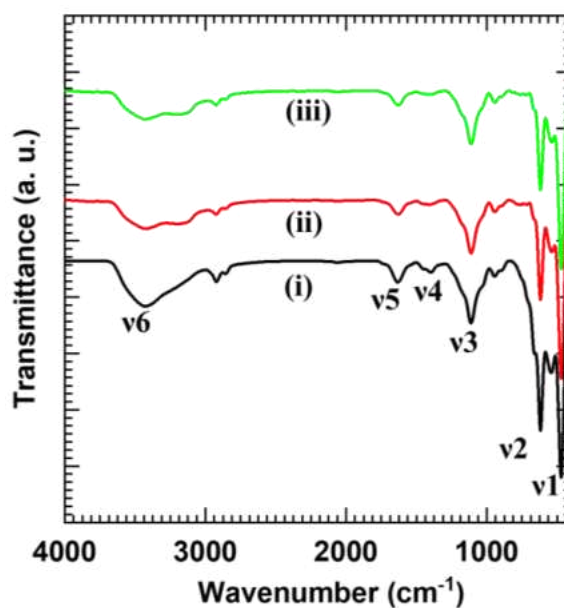
Figure 3.4: FTIR spectra of (i) MS-200, (ii) MS-300 and (iii) MS-400 thin films.

The nature of the chemical bonding of MoS$_2$ thin films was studied by FTIR spectroscopy. As shown in **Fig. 3.4**, MS-200, MS-300 and MS-400 thin films display high-intensity bands ν1 (480 cm^{-1}) and ν2 (623 cm^{-1}) ascribed to the Mo-S stretching vibrations **[24-26]**. The bands ν3 (1117 cm^{-1}) and ν4 (1411 cm^{-1}) correspond to the sulfur-related stretching vibration of S-Mo-S **[27]**. The characteristic bands ν5 (1637 cm^{-1}) and ν6 (3431 cm^{-1}) are ascribed to the bending vibrational modes of water molecules and stretching vibrations of the O-H groups, respectively **[25]**. Similar IR signatures were observed for the chemically deposited MoS$_2$ thin films **[24-27]**. These spectral features are closely related to the chemical bonding of the layered 2H-MoS$_2$ phase, indicating the formation of layered MoS$_2$ thin films.

3.2.2.4 FE-SEM study
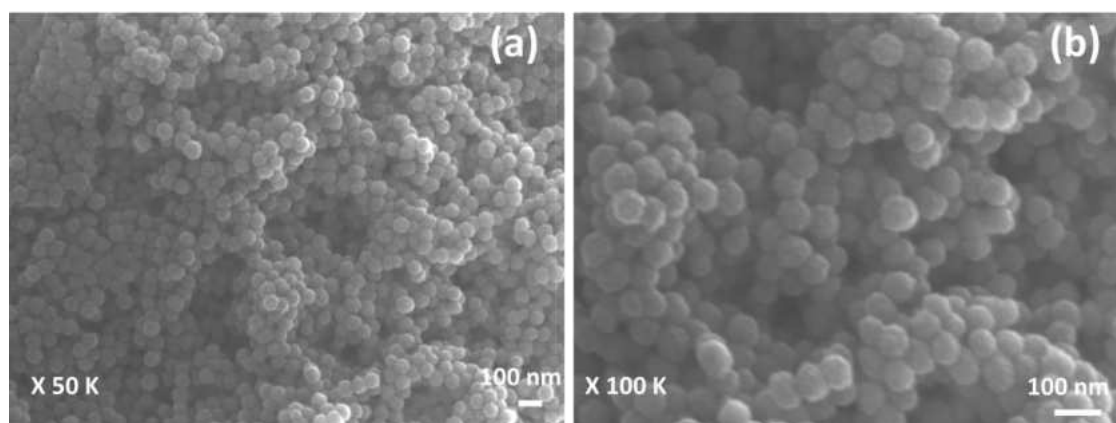
Figure 3.5: FE-SEM images of MS-300 thin film at (a) ×50K and (b) ×100K magnification.

The microstructural surface features of MoS$_2$ thin film were investigated by FE-SEM analysis. As shown in **Fig. 3.5**, MS-300 thin film shows uniform deposition of MoS$_2$ with porous morphology. The MS-300 thin film shows nano-sized spherical particles aggregated onto each other to form an interconnected network architecture. The careful observation reveals that the MoS$_2$ thin films are composed of spherical particles with sizes ranging from 40-60 nm. At high magnification, porous nature is visible for MS-300 thin film, which is beneficial for photocatalytic applications **[28-29]**. A similar morphology is observable for the MoS$_2$ thin films deposited by chemical methods **[30-32]**.

The presence of constituent elements in MS-300 thin film was investigated using EDS elemental mapping analysis. As shown in **Fig. 3.6** and **Fig. 3.7**, Mo and S are

uniformly distributed over the entire mapping area with a Mo:S ratio of ~1:2, confirming the uniform deposition of MoS_2 thin films using the MCSD method.
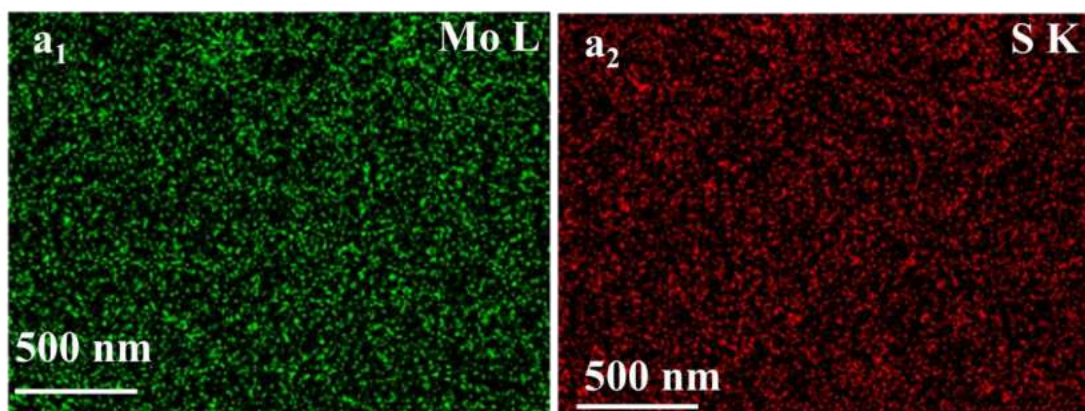
Figure 3.6: EDS elemental mapping of MS-300 thin film.
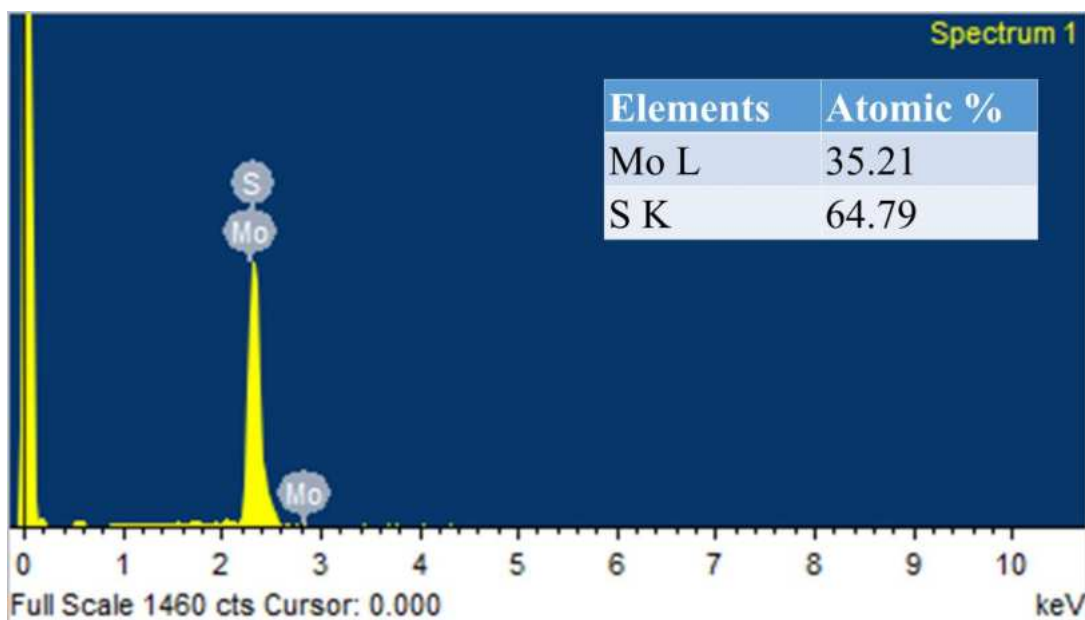
Figure 3.7: EDS spectrum of MS-300 thin film.

3.2.2.5 XPS study

The presence of elements and their oxidation states in the MoS_2 thin film were determined by XPS analysis. As shown in **Fig. 3.8**, the survey XPS spectrum of the MoS_2 thin film exhibits characteristics XPS features at BE of Mo and S elements, indicating the presence of stated elements in MoS_2 thin film.
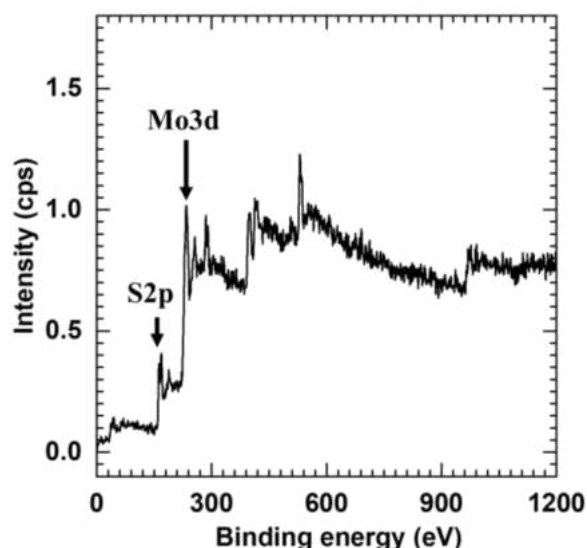
Figure 3.8: XPS survey spectrum of MS-300 thin film.

The high-resolution Mo 3d and S 2p core-level XPS spectra are plotted in **Fig. 3.9 (a** and **b)**, respectively. As shown in **Fig. 3.9a**, the high-resolution Mo 3d spectrum of MoS₂ thin film displays two spectral features, A (229.5 eV) and B (232.7 eV), corresponding to the spin-orbit splitting of Mo $3d_{5/2}$ and Mo $3d_{3/2}$, respectively. The BE difference of 3.2 eV indicates the presence of Mo^{4+} in MoS₂ thin film [33]. As displayed in **Fig. 3.9b**, the high-resolution S 2p spectrum of MoS₂ thin film shows a broad peak C (162 eV) ascribed to the spin-orbit splitting of S^{2-} [34]. These XPS features show the characteristic Mo^{4+} and S^{2-} elemental signatures required to form MoS₂ thin film, indicating the deposition of MoS₂ using the MCSD method.
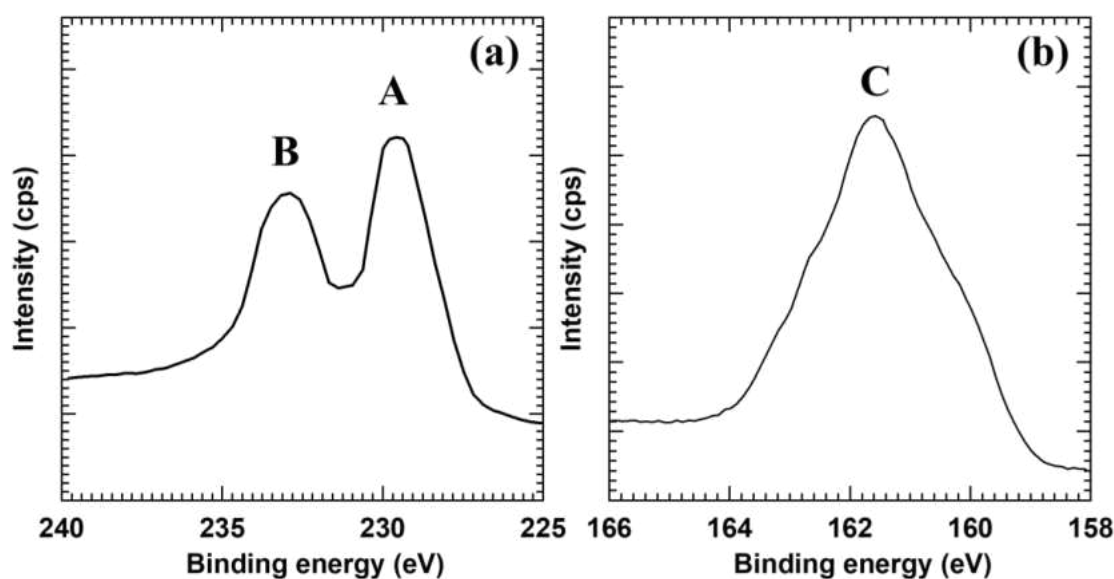
Figure 3.9: a) Mo 3d and b) S 2p Core-level XPS spectra of MS-300 thin film.

3.2.2.6 UV-Vis DRS study and band positions determination
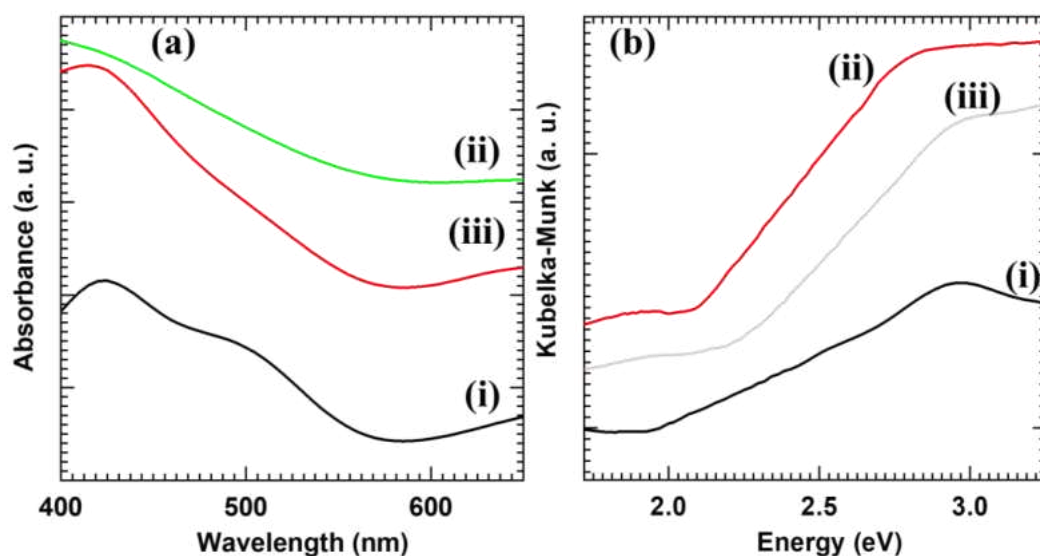
Figure 3.10: a) UV-Vis DRS absorbance spectra and b) Diffuse reflectance UV–Vis spectra (plotted as the Kubelka–Munk function of the reflectance, R) of (i) MS-200, (ii) MS-300 and (iii) MS-400 thin films.

The band structure and optical properties of the MoS_2 thin films were studied using UV-Vis DRS spectroscopy. As shown in **Fig. 3.10a**, all MoS_2 thin films exhibit significant absorption in the visible regions of the electromagnetic spectrum, displaying the visible light harvesting ability of MoS_2 thin films with an optical band gap of 1.6 eV. MoS_2 is an indirect band gap material with an electronic structure comprising a VB and CB mainly composed of Mo 4d and S 3p orbitals, respectively **[35-36]**. The band gap energies determined from the Kubelka-Munk function are displayed in **Fig 3.10b** and noted in **Table 3.1**.

Table 3.1: Bandgap energies of MoS_2 thin films.

Thin film	Bandgap (eV)
MS-200	1.45
MS-300	1.60
MS-400	1.78
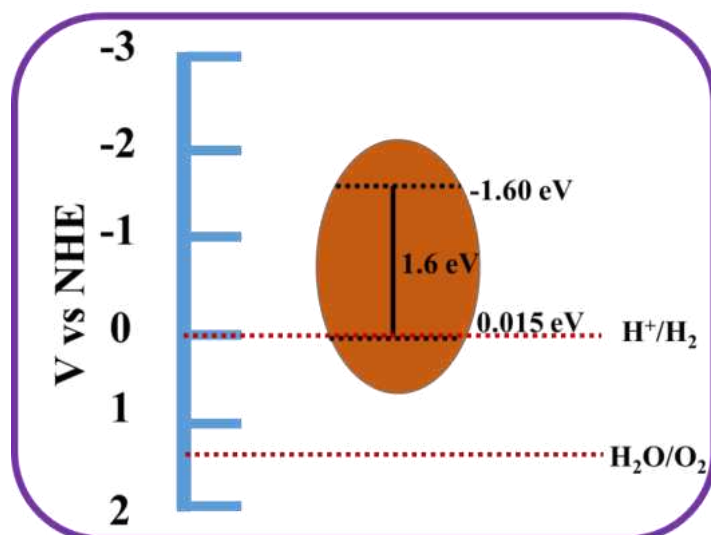
Figure 3.11: Band positions of MoS₂ thin film estimated from an empirical formula.

The VB and CB positions of MoS₂ thin films were estimated using an empirical formula.

$$E_{VB} = X - E_e + 0.5E_g \tag{3.1}$$

$$E_{CB} = E_{VB} - E_g \tag{3.2}$$

Where X is the electronegativity of the material and E_e is the energy of free electrons on the hydrogen scale. The electronegativity of MoS₂ is 5.32 eV, and the energy of free electrons on the hydrogen scale is 4.5 eV vs. normal hydrogen electrode (NHE) **[30, 37]**. Accordingly, VB and CB positions are estimated at 0.015 eV and -1.60 eV vs. NHE, respectively. The estimated band positions of MoS₂ vs. NHE are shown in **Fig. 3.11**. These values are well matched with previously reported MoS₂-based photocatalysts **[38, 39]**.

3.3 Dye Degradation Studies

3.3.1 Experimental Setup for Dye Degradation Studies

The visible light (λ>420 nm, light intensity=100 mW cm⁻²) induced photocatalytic degradation activities of MoS₂ thin films were studied by measuring the time-dependent photodegradation of RhB and MB. The initial concentration of RhB and MB was 10 µM. MoS₂ thin film was vertically placed in a square-shaped quartz reactor filled with 3 ml of target dye solution for the photocatalytic experiment. Before

irradiation by light, the dye solution was allowed to be equilibrated with target molecules in the dark for 30 minutes to ensure adsorption/desorption equilibrium of the dye molecules on the catalyst surface. All the photocatalytic measurements were performed at ambient conditions. During the photocatalytic experiments, the light was calibrated by passing through the infrared water filter followed by AM 1.5 G and optical cutoff (420 nm) filters. The calibrated light was focused on the square-shaped quartz photoreactor. The MoS₂ thin film was withdrawn intermittently during the illumination, and the change in the concentration of the dye solution was analyzed using a UV-Vis spectrophotometer. The concentration change in RhB and MB was monitored by measuring the absorbance at characteristic wavelengths of 554 and 664 nm, respectively. From the analysis of absorption spectra, photocatalytic degradation efficiency was determined using the following equation **[40]**:

$$\% \; degradation = \frac{C_0 - C_t}{C_0} * 100 \tag{3.3}$$

where C_0 is the initial concentration of the dye molecules and C_t is the concentration of the dye molecules at time t. Furthermore, the degradation kinetics were studied by employing a pseudo-first-order reaction using the following equation **[40]**:

$$\ln\left(\frac{C_0}{C_t}\right) = kt \tag{3.4}$$

where k is the pseudo-first-order rate constant and t is irradiation time.

3.3.2 Results and Discussion

The photocatalytic degradation performance of MoS₂ thin films deposited at different MCSD cycles was initially assessed by monitoring the time-dependent absorption spectra of RhB under visible light irradiation in the presence of photocatalysts. **Fig. 3.12 (a-c)** displays time-dependent UV-Vis absorption spectra of RhB dye in the presence of MS-200, MS-300 and MS-400 thin films under visible light illumination, respectively. The pristine MoS₂ displays superior visible-light photocatalytic activity for photodegradation due to its narrow band gap (1.6 eV). The decrease in intensity at the characteristic wavelength of 554 nm with respect to irradiation time indicates the degradation of RhB. **Fig. 3.12d** shows variation of RhB concentration as a function of irradiation time for MS-200, MS-300 and MS-400 thin films. Among MoS₂ thin films deposited at different MCSD cycles, MS-300 displays a

maximum RhB degradation of 73 % in 90 minutes. This study shows that MoS$_2$ thin films are photocatalytically active under visible light.
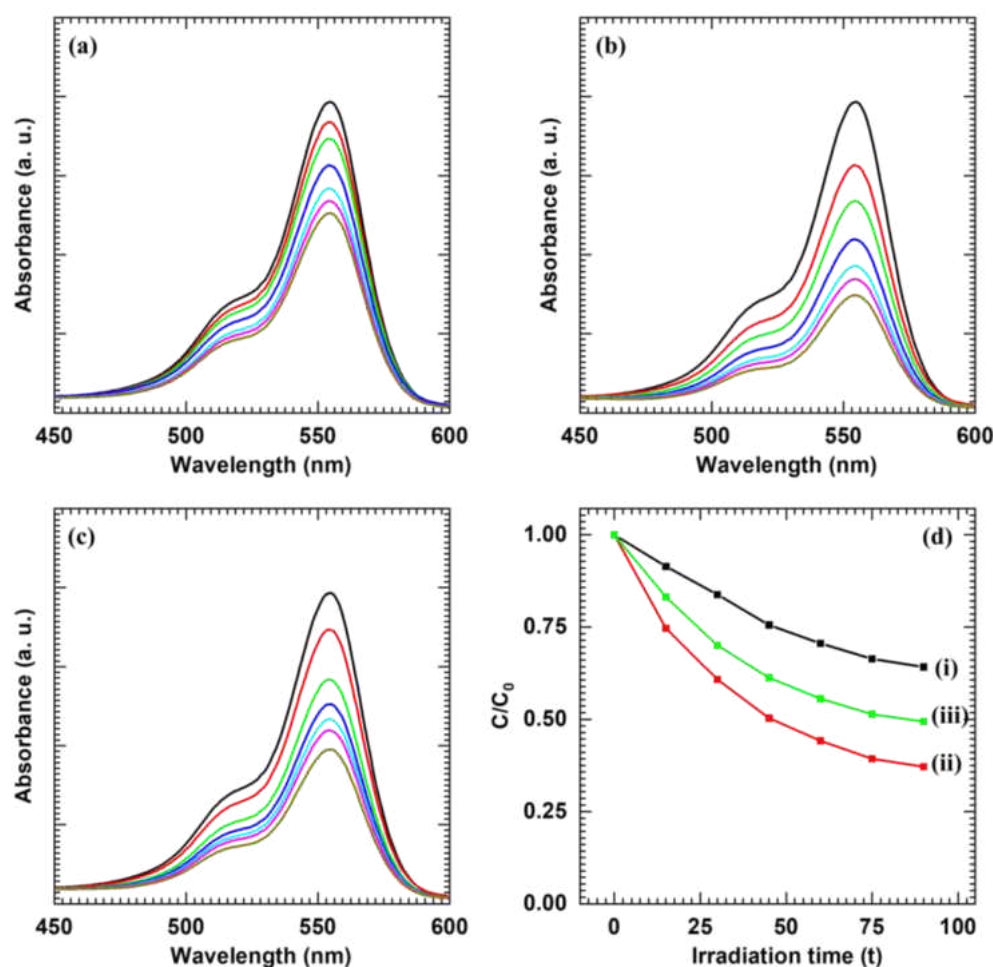
Figure 3.12: UV-Vis absorption spectra of RhB in the presence of (a) MS-200, (b) MS-300, (c) MS-400 thin films under visible-light irradiation and (d) variation of RhB concentration as a function of irradiation time for (i) MS-200, (ii) MS-300 and (iii) MS-400 thin films.

Similarly, the photocatalytic degradation performance of MoS$_2$ thin films was assessed by observing the time-dependent UV-Vis absorption spectra of MB under visible-light illumination in the presence of photocatalysts. **Fig. 3.13 (a-c)** displays time-dependent UV-Vis absorption spectra of MB in the presence of MS-200, MS-300 and MS-400 thin films, respectively. The pristine MoS$_2$ displays superior visible-light photocatalytic activity for photodegradation due to its narrow band gap (1.6 eV). The decrease in intensity at the characteristic wavelength of 665 nm with respect to irradiation time indicates the degradation of MB. **Fig. 3.13d** shows the variation of MB

concentration as a function of irradiation time for MS-200, MS-300 and MS-400 thin films. Among MoS$_2$ thin films deposited at different MCSD cycles, MS-300 displays a maximum MB degradation of 70 % in 90 minutes.

The excellent photocatalytic performance of MoS$_2$ thin films is attributed to the narrow bandgap, porous morphology and high surface area **[41, 42].**
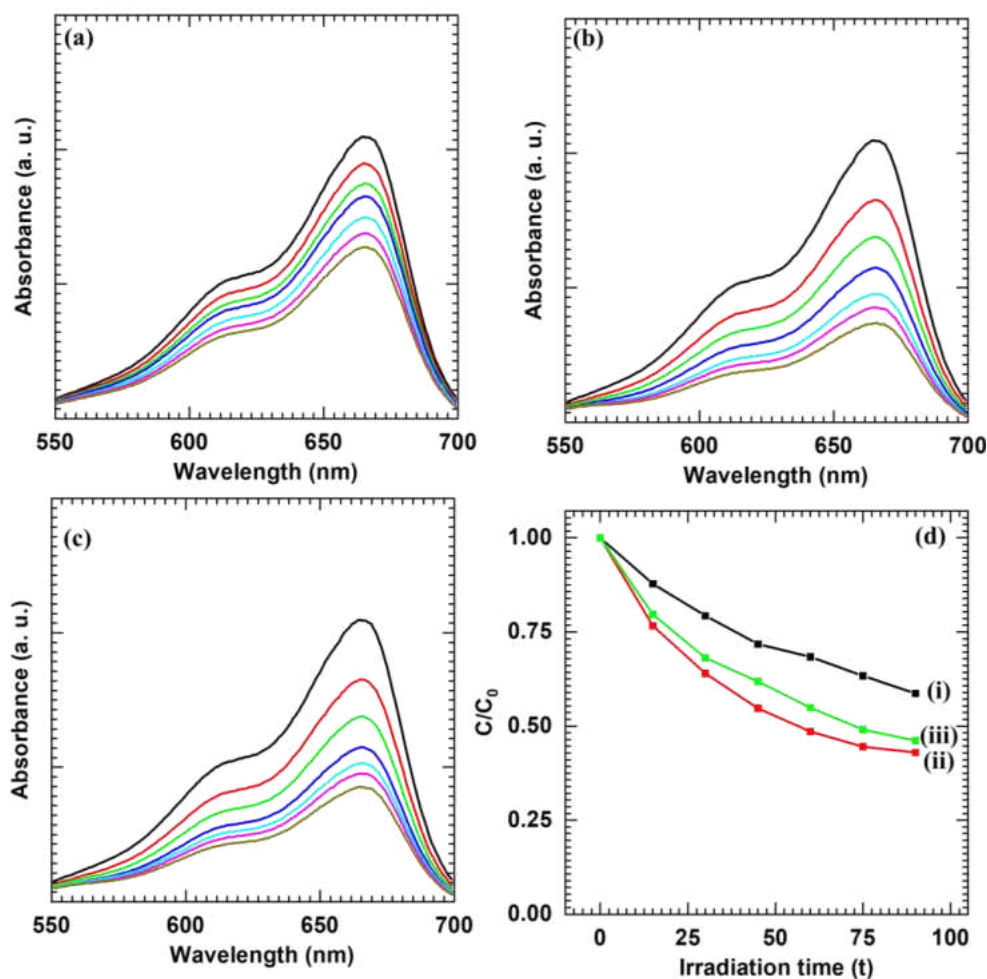
Figure 3.13: UV-Vis absorption spectra of MB in the presence of (a) MS-200, (b) MS-300, (c) MS-400 thin films under visible-light irradiation and (d) variation of MB concentration as a function of irradiation time for (i) MS-200, (ii) MS-300 and (iii) MS-400 thin films.

3.3.3 Kinetic study

The degradation kinetics of RhB and MB dyes using MoS$_2$ thin films were probed by a pseudo-first-order rate kinetic model by plotting $\ln(C_0/C_t)$ vs irradiation time as shown in **Fig. 3.14 (a-b)**. The rate constant (k) and linear correlation coefficient (R^2) values are given in **Table 3.2**. All the MoS$_2$ thin films show high k-values, confirming

the faster reaction kinetics. The MS-300 thin film exhibits the highest k value of 0.016 min^{-1} than that of MS-200 and MS-400 thin films for RhB. These k values reveal the excellent photocatalytic performance of MoS_2 thin films. The excellent photocatalytic performance of MoS_2 thin films is attributed to the porous morphology and higher surface area, which provides abundant catalytically active sites for the degradation of target molecules **[43-47]**.
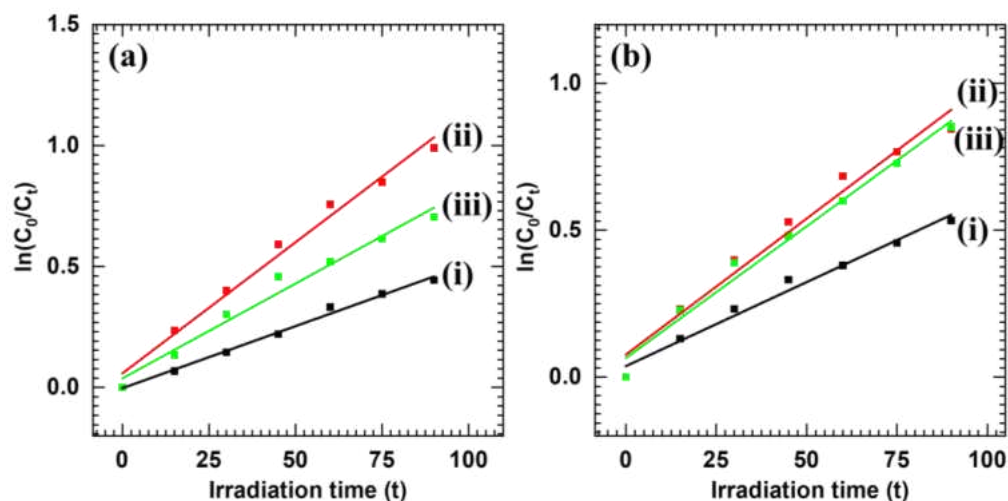
Figure 3.14: Pseudo-first-order kinetics of a) RhB and b) MB dyes using i) MS-200, ii) MS-300 and iii) MS-400 thin films.

Table 3.2: Photocatalytic dye degradation performance of MoS_2 thin films.

Target molecule	Photocatalyst	Degradation (%)	Rate constant k (min^{-1})	Correlation coefficient (R^2)
RhB	MS-200	65	0.012	0.9890
	MS-300	73	0.016	0.9720
	MS-400	68	0.015	0.9675
MB	MS-200	63	0.010	0.9844
	MS-300	70	0.014	0.9952
	MS-400	67	0.013	0.9941

3.3.4 Recycling study
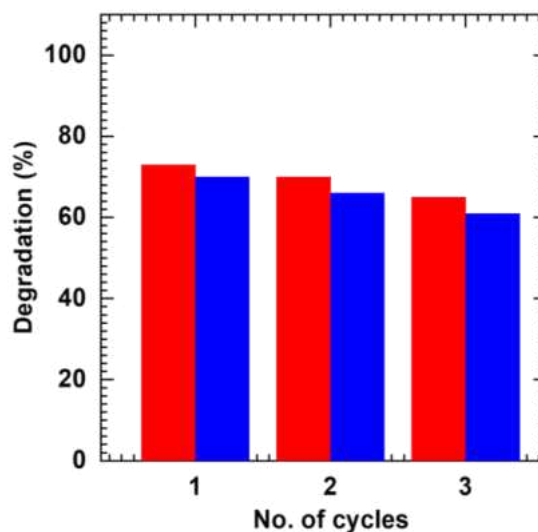
Figure 3.15: Recyclability of optimized MS-300 thin films for RhB (Red) and MB (blue) degradation for 3 cycles.

Furthermore, the stability of the optimized MS-300 thin films for the degradation of RhB and MB is studied for three consecutive cycles, as shown in **Fig. 3.15**. The MoS_2 thin film is recovered from the dye solution, washed with DDW, dried at room temperature and then used for the subsequent photocatalytic degradation tests. After three consecutive cycles, MS-300 retains 89 and 87 % degradation performance for MB and RhB, respectively. After each cycle, the slight decrement in the photocatalytic performance is attributed to the inactivity of active material due to the adsorption of target molecules on the surface of the photocatalyst **[48]**.

3.3.5 Plausible dye degradation mechanism

The schematic representation of the plausible degradation pathway using MoS_2 thin film is shown in **Fig. 3.16**. The photocatalytic dye degradation reaction occurs when a photon with energy greater than that of the bandgap energy is incident on the semiconducting photocatalyst, followed by electron-hole pair generation **[44]**. As the VB of MoS_2 is not positive enough to produce hydroxyl radicals (OH^{*-}), holes present in the VB of MoS_2 will not participate in the reaction directly. Meanwhile, superoxide radicals (O_2^{*-}) are generated when electrons in the CB of MoS_2 react with O_2. Further, hydroperoxyl radicals (HOO^*) are generated from the protonation of superoxide radicals. Finally, H_2O_2 dissociates into OH^{*-} radicals, which can break the chain of target

organic molecules **[49-50]**. The chemical reactions describing plausible dye degradation mechanism are represented in **Chapter 1, section 1.1.7.1 (b)**.
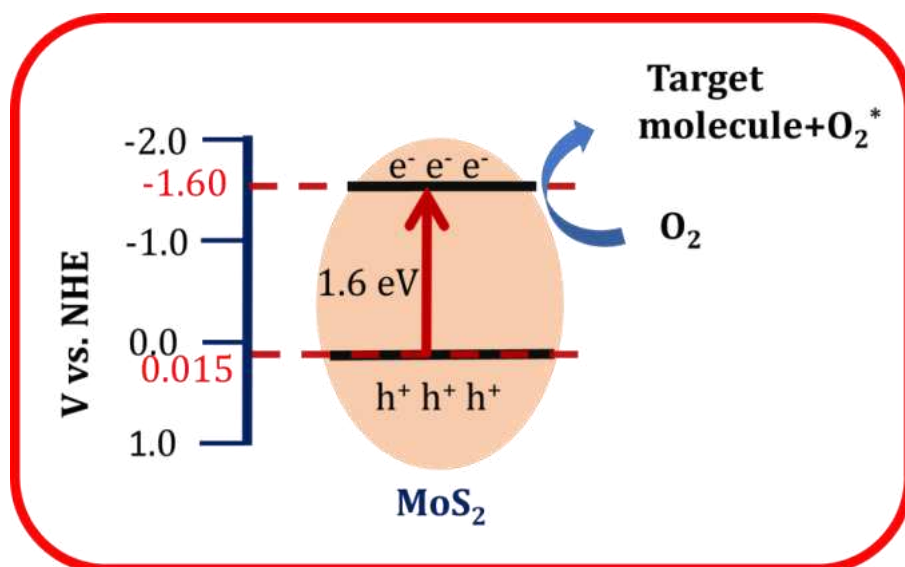
Figure 3.16: Schematic of plausible degradation mechanism of target molecules under visible-light irradiation using MoS₂ thin films.

3.4 Conclusion

In this chapter, MoS₂ thin films are deposited using the MCSD method at different deposition cycles. Structural and morphological study confirms the formation of layered 2H-MoS₂ with an interconnected network architecture composed of spherical nanoparticles. The Raman study suggests the formation of multi-layered MoS₂. The importance of optimum film thickness for photocatalytic dye degradation is examined using MoS₂ thin film with different film thicknesses. The MoS₂ thin film deposited at 300 deposition cycles shows excellent photocatalytic performance by degrading 73% and 70 % of RhB and MB dye in 90 minutes of visible light irradiation. The higher photocatalytic performance of MS-300 thin film is attributed to the porous morphology and higher surface area of MoS₂ thin film, which facilitate the photocatalytic activity by providing more photocatalytically active sites. The present finding highlights the effectiveness of optimized thickness for the photocatalytic degradation of target molecules. This strategy can be effectively used to deposit various semiconducting thin films in the future.

3.5 References

[1] S. Ledakowicz and K. Pa´zdzior, Molecules, 26 (2021) 870.

[2] L. Chen, Y. Chuang, T. B. Nguyen, J.-H. Chang, S. S. Lam, C.-W. Chen, C.-D. Dong, J. Alloys Compd., 848 (2020) 156448.

[3] S. Yi, S. Sun, Y. Zhang, Y. Zou, F. Dai, Y. Si, J. Colloid Interface Sci., 559 (2020) 134.

[4] M. M. Hassan and C. M. Carr, Chemosphere, 209 (2018) 201.

[5] X. Wei, Y. Wang, Y. Feng, X. Xie, X. Li, S. Yang, Sci. Rep., 9 (2019) 4964.

[6] Z. Zhang, I. M. O'Hara, G. A. Kent, W. O. S. Doherty, Ind. Crops Prod., 42 (2013) 41.

[7] J. Piriyanon, T. Chankhanittha, S. Youngme, K. Hemavibool, S. Nijpanich, S. Juabrum, N. Chanlek, S. Nanan, J. Mater. Sci: Mater. Electron., 32 (2021) 19798.

[8] B. Viswanathan, Current Catalysis, 7 (2018) 99.

[9] J. Ji, Y. Bao, X. Liu, J. Zhang, M. Xing, EcoMat., 3 (2021) e12155.

[10] A. Splendiani, L. Sun, Y. Zhang, T. Li, J. Kim, C.-Y. Chim, G. Galli, F. Wang, Nano Lett., 10 (2010) 1271.

[11] V. V. Magdum, Y. M. Chitare, S. P. Kulkarni, P. D. Sawant, S. A. Pawar, S. V. Talekar, C. D. Lokhande, U. M. Patil, S. B. Patil, J. L. Gunjakar, J. Mater. Chem. C, 11 (2023) 9768.

[12] Y. Jiang, D. Wang, Z. Pan, H. Ma, M. Li, J. Li, A. Zheng, G. Lv, Z. Tian, Front. Chem. Sci. Eng., 12 (2018) 32.

[13] V. Etacheri, C. D. Valentin, J. Schneider, D. Bahnemann, S. C. Pillai, J. Photochem. Photobiol. C, 25 (2015) 1.

[14] H. M. Pathan and C. D. Lokhande, Bull. Mater. Sci., 27 (2004) 85.

[15] S. Huang, C. Chen, H. Tsai, J. Shaya, C. Lu, Sep. Purif. Technol., 1997 (2018) 147.

[16] Y. Tan, K. Yu, T. Yang, Q. Zhang, W. Cong, H. Yin, Z. Zhang, Y. Chen, Z. Zhu, J. Mater. Chem. C, 2 (2014) 5422.

[17] X. Sun, J. Dai, Y. Guo, C. Wu, F. Hu, J. Zhao, X. Zeng, Y. Xie, Nanoscale, 6 (2014) 8359.

[18] I. A. Rahman and A. Purqon, J. Phys.: Conf. Ser., 877 (2017) 012026.

[19] H. Li, Q. Zhang, C. C. R. Yap, B. K. Tay, T. H. T. Edwin, A. Olivier, D. Baillargeat, Adv. Funct. Mater., 22 (2012) 1385.

[20] M. Park, J. S. Choi, L. Yang, H. Lee, Sci. Rep., 9 (2019) 19826.

[21] Y.-H. Lee, L. Yu, H. Wang, W. Fang, X. Ling, Y. Shi, C.-T. Lin, J.-K. Huang, M.-T. Chang, C.-S. Chang, M. Dresselhaus, T. Palacios, L.-J. Li, J. Kong, Nano Lett., 136 (2013) 1852.

[22] D. Vikraman, K. Akbar, S. Hussain, G. Yoo, J.-Y. Jang, S.-H. Chun, J. Jung, H. J. Park, Nano Energy, 35 (2017) 101.

[23] R. T. Sam, T. Umakoshi, P. Verma, Sci. Rep., 10 (2020) 21227.

[24] S. Patil, A. Harle, S. Sathaye, K. Patil, CystEngComm., 16 (2014) 10845.

[25] G. A. M. Ali, M. R. Thalji, W. C. Soh, H. Algarni, K. F. Chong, J. Solid State Electrochem., 24 (2020) 25.

[26] X. Wang, Y. Liu, J. Zeng, C. Peng, R. Wang, Ionics, 25 (2019) 437.

[27] M. Yi, C. Zhang, RSC Adv., 8 (2018) 9564.

[28] S. Wang, L. Li, H. Wu, Z. H. Zhu, J. Colloid Interface Sci., 292 (2005) 336.

[29] L. Meng, X. Zhang, Y. Tang, K. Su, J. Kong, Sci. Rep., 21 (2015) 7910.

[30] Y.-Y. Chen, P. Dhaiveegan, M. Michalska, J.-Y. Lin, Electrochim. Acta, 274 (2018) 208.

[31] Y. Wang, W. Lu, D. Yue, M. Wang, B. Tian, Q. Li, B. Hu, Z. Wang, Y. Zhang, CrystEngComm, 23 (2021) 935.

[32] Z. Li, J. Ma, Y. Zhou, Z. Yin, Y. Tang, Y. Ma, D. Wang, Electrochim. Acta, 283 (2018) 306.

[33] I. A. de Castro, R. S. Datta, J. Z. Ou, A. Castellanos-Gomez, S. Sriram, T. Daeneke, K. Kalantar-zadeh, Adv. Mater., 29 (2017) 1701619.

[34] N. P. Kondekar, M. G. Boebinger, E. V. Woods, M. T. McDowell, ACS Appl. Mater. Interfaces, 9 (2017) 32394.

[35] S. C. Lu, J.-P. Leburton, Nanoscale Res. Lett., 9 (2014) 676.

[36] D. Dumcenco, D. Ovchinnikov, K. Marinov, P. Lazic, M. Gibertini, N. Marzari, O. L. Sanchez, Y.-C. Kung, D. Krasnozhon, M.-W. Chen, S. Bertolazzi, P. Gillet, A. F. Morral, A. Radenovic, A. Kis, ACS Nano, 9 (2015) 4611.

[37] X. Bai, Y. Du, X. Hu, Y. He, C. He, E. Liu, J. Fan, Appl. Catal. B, 239 (2018) 204.

[38] D. Singh, P. K. Panda, N. Khossossi, Y. K. Mishra, A. Ainane, R. Ahuja, Catal. Sci. Technol., 10 (2020) 3279.

[39] R. A. El-Gendy, H. M. El-Bery, M. Farrag, D. M. Fouad, Sci Rep., 13 (2023) 7994.

[40] P. P. Bagwade, V. V. Magdum, D. B. Malavekar, Y. M. Chitare, J. L. Gunjakar, U. M. Patil, C. D. Lokhande, J. Mater. Sci: Mater. Electron., 33 (2022) 24646.

[41] V. V. Magdum, Y. M. Chitare, S. P. Kulkarni, D. B. Malavekar, A. U. Pawar, R. N. Bulakhe, C. D. Lokhande, U. M. Patil, S. B. Patil, J. L. Gunjakar, J. Mater. Sci.: Mater. Electron., 35 (2024) 1433.

[42] Y. M. Chitare, V. V. Magdum, S. P. Kulkarni, S. V. Talekar, S. A. Pawar, P. D. Sawant, D. B. Malavekar, U. M. Patil, C. D. Lokhande, J. L. Gunjakar, Appl. Surf. Sci. Adv., 19 (2024) 100573.

[43] S. Acharya, G. Swain, K. M. Parida, Int. J. Hydrog. Energy, 45 (2020) 11502.

[44] S. Chakrabarty, A. Mukherjee, S. Basu, ACS Sustainable Chem. Eng., 6 (2018) 5238.

[45] J. Chen, Y. Liao, X. Wan, S. Tie, B. Zhang, S. Lan, X. Gao, J. Solid State Chem., 291 (2020) 121652.

[46] D. Monga, D. Ilager, N. P. Shetti, S. Basu, T. M. Aminabhavi, J. Environ. Manage., 274 (2020) 111208.

[47] M. R. Abhilash, G. Akshatha, S. Srikantaswamy, RSC Adv., 9 (2019) 8557.

[48] N. K. Gupta, Y. Ghafari, S. Kim, J. Bae, K. S. Kim, M. Saifuddin, Sci. Rep., 10 (2020) 4942.

[49] P. Guo, F. Zhao, X. Hu, J. Alloys Compd., 867 (2021) 159044.

[50] W.-Q. Chen, L.-Y. Li, L. Li, W.-H. Qiu, L. Tang, L. Xu, K.-J. Xu, M.-H. Wu, Engineering, 5 (2019) 755.

4.1 Introduction

Layered materials have attracted significant attention owing to their anisotropic crystal structure, exfoliable nature, surface charge and anion intercalative property **[1-4]**. Numerous materials, such as graphite, layered double hydroxide (LDH), black phosphorous, and metal oxides, exhibit layered crystal structures **[5-6]**. Among these materials, titanium oxide and niobium oxide have attracted high research attention due to their photofunctional applications, such as photocatalytic dye degradation, solar cells, and photoelectrochemical cells **[7-8]**.

The 2D monolayers of titanate and niobate derived by the exfoliation of their host crystals have shown huge potential for various applications due to their unique physicochemical properties. These 2D nanosheets display a highly anisotropic structure, ultrathin thickness, electrostatic surface charge and flexible chemical composition. Therefore, much effort was put into synthesizing monolayered titanate-NS and niobate-NS by soft chemical exfoliation methods using organic solvents **[9-11]**. Many applications like sensors, photocatalysis and high-k dielectrics require materials in thin film form; thus, several efforts were made to deposit titanate-NS and niobate-NS thin films from the exfoliated nanosheet suspension **[12-13]**.

Various deposition methods were employed for the deposition of titanate-NS and niobate-NS thin films. LbL, Langmuir–Blodgett (LB) and electrophoretic Deposition (EPD) methods were explored for the deposition of titanate-NS and niobate-NS from their colloidal suspensions **[14-19]**. Several reports show the effectiveness of these methods for depositing titanate-NS and niobate-NS. However, these methods suffer from certain limitations, such as the requirement of oppositely charged polymer in LbL and conducting substrate in EPD with extremely high time consumption. In the LbL method, an additional step is required to remove the oppositely charged polymer layer to obtain pure material. Thus, in many instances, these limitations restrict their use in practical applications. The dip-coating technique is an excellent alternative for depositing titanate-NS and niobate-NS thin films. Dip-coating offers numerous advantages, such as large-area deposition, the possibility of deposition on any substrate shape and size, excellent control over deposited film thickness and high uniformity in deposition [**5**].

In this chapter, titanate-NS and niobate-NS are deposited on a glass substrate using the dip-coating method with variations in the number of dip cycles. Their physicochemical properties are investigated using various characterization techniques. The photocatalytic application of these films is explored for photocatalytic MB and RhB dye degradation under visible light.

4.2 Synthesis and characterization of titanate-NS

4.2.1 Experimental details

4.2.1.1 Chemicals

Titanium oxide (TiO_2), caesium carbonate (Cs_2CO_3), hydrochloric acid (HCl) and tetrabutylammonium hydroxide (TBA-OH) were purchased from Sigma-Aldrich and used without further purification. A dialysis tube (Dialysis Membrane-135, Av. flat width-33.12 mm, Av. diameter-23.8 mm, Capacity approx.-4.45 ml cm^{-1}) is used to dialysis exfoliated titanate solution. All experiments were performed in DDW.

4.2.1.2 Preparation of colloidal titanate-NS suspension

a) Synthesis of caesium titanate by solid-state reaction

The host crystal of $Cs_{0.7}Ti_{1.825}\square_{0.175}O_4$, ($\square$=vacancy) was prepared by conventional solid-state reaction in which TiO_2 and Cs_2CO_3 were taken in mortar pestle in stoichiometric ratio and ground thoroughly in N_2 atmosphere. The mixture was then heated in a furnace at 800°C for 20 hours and cooled naturally. The prepared material was thoroughly grounded to become fine particles and again heated in a furnace for calcination at 800°C for 20 hours. This process is repeated three times to obtain highly crystalline $Cs_{0.7}Ti_{1.825}\square_{0.175}O_4$ layered host crystals **[20]**.

b) Protonation of $Cs_{0.7}Ti_{1.825}\square_{0.175}O_4$

The protonated derivative of calcinated $Cs_{0.7}Ti_{1.825}\square_{0.175}O_4$ powder was achieved by proton exchange reaction of highly crystalline $Cs_{0.7}Ti_{1.825}\square_{0.175}O_4$ powder in 1 M HCl solution and constant stirring for 24 hours. The HCl solution was replaced with a fresh one every 24 hours. This process was repeated three times to complete the proton exchange reaction. Finally, the $H_xTi_{1.825}\square_{0.175}O_4.H_2O$ product was collected by centrifugation, dried at room temperature, and used for further processing **[21]**.

c) Exfoliation of protonated $H_xTi_{1.825}\square_{0.175}O_4.H_2O$

The exfoliation process comprised the dispersion of protonated $H_xTi_{1.825}\square_{0.175}O_4.H_2O$ crystals in TBA-OH solution under constant shaking for 15 days. In this process, TBA-OH ions were intercalated in layered $H_xTi_{1.825}\square_{0.175}O_4.H_2O$ crystals, leading to the swelling of layer crystals. Swollen TBA-intercalated layered crystals get exfoliated into monolayers to form a stable colloidal solution upon shaking or sonication.

d) Dialysis of titanate-NS colloidal suspension

The exfoliated titanate-NS colloidal suspension possesses a highly basic pH (~12.5). At such a high pH, the deposition of titanate-NS thin films was not possible. Thus, to obtain processable titanate-NS colloidal suspension and deposition of titanate-NS, the pH of titanate-NS colloidal suspension was reduced by the dialysis against DDW. For the dialysis process, the exfoliated colloidal suspension of titanate-NS (with a pH of 12.5) was dialyzed using a dialysis membrane in DDW. The DDW is changed after every hour in order to bring the pH of the colloidal suspension in the range of 8.

The schematic representation of titanate-NS preparation is shown in **Fig. 4.1**.
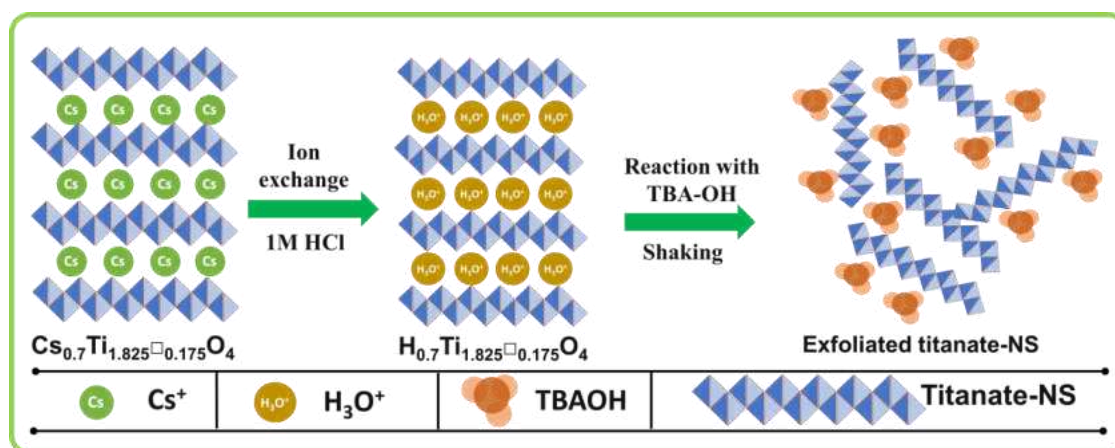
Figure 4.1: Schematic representation of the synthesis of exfoliated titanate-NS colloidal suspension.

4.2.1.3 Deposition of titanate-NS thin films by Dip-Coating

Titanate-NS thin film deposition was carried out on well-cleaned glass substrates. The glass substrate cleaning process is described in **Chapter 3, section 3.2.1.2**.

Titanate-NS thin films by the dip-coating method were obtained by dialyzing titanate-NS colloidal suspension (pH=12.5) for 10 hours using a dialysis membrane in DDW to attain a pH of 8. The dialyzed titanate-NS suspension was used as a precursor for the dip-coating method. A microprocessor-controlled dip-coating unit was used to deposit titanate-NS thin films. The titanate-NS thin films were deposited at the dipping and retrieval speed of 1000 microns sec^{-1}. One dip and consecutive retrieval of substrate comprised one dip cycle. Such 50-100 dip cycles were executed to vary the deposition thickness of the titanate-NS thin films. After each cycle, the film is dried in the infrared chamber coupled to the dip-coating unit. The titanate-NS films deposited at 50, 75 and 100 dip cycles were labeled T-1, T-2 and T-3, respectively. The schematic representation of titanate-NS thin film deposition using the dip-coating method is shown in **Fig. 4.2**.
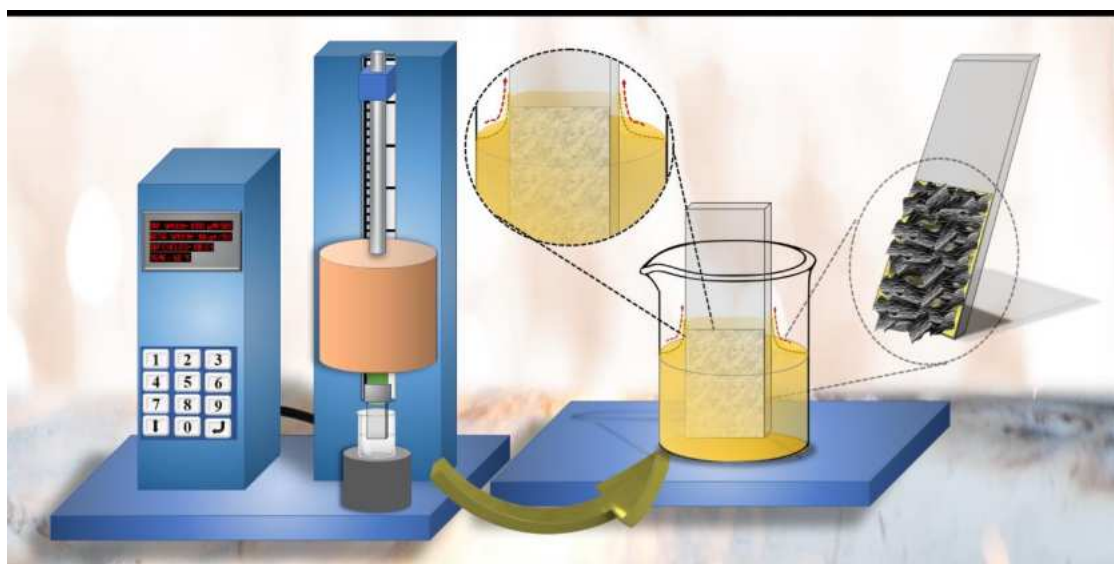
Figure 4.2: Schematic representation of the synthesis process of titanate-NS thin films.

4.2.1.4 Material characterization

The titanate-NS thin films were characterized by various physicochemical characterization techniques, as described in **Chapter 3, section 3.2.1.3**.

4.2.2 Results and Discussion

4.2.2.1 XRD study

The structural study of dip-coated titanate-NS thin films was confirmed by XRD analysis. The XRD patterns of caesium titanate ($Cs_{0.7}Ti_{1.825}\square_{0.175}O_4$) and its protonated derivative ($H_{0.7}Ti_{1.825}\square_{0.175}O_4$) are shown in **Fig. 4.3 (a-b)**, respectively.
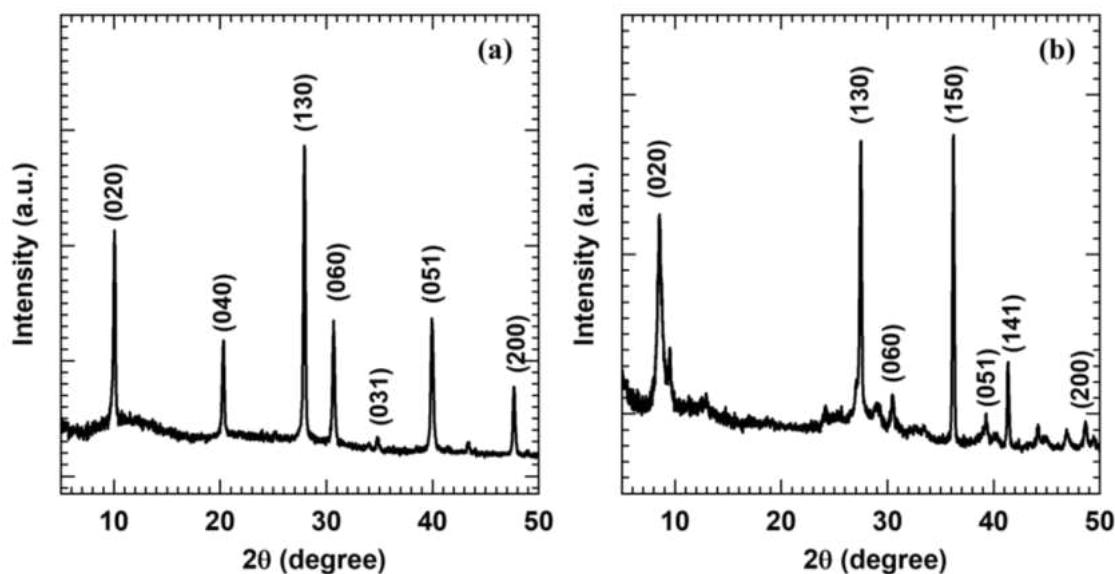
Figure 4.3: XRD patterns of a) calcinated $Cs_{0.7}Ti_{1.825}\square_{0.175}O_4$ and b) protonated $H_{0.7}Ti_{1.825}\square_{0.175}O_4$.

The pristine caesium titanate ($Cs_{0.7}Ti_{1.825}\square_{0.175}O_4$) displays intense (020), (040), (130), (060), (031), (051) and (200) diffraction peaks, indicating the formation of a lepidocrocite-type layered structure with orthorhombic symmetry (JCPDS card number: 84-1226) **[22-23]**. Its protonated derivative ($H_{0.7}Ti_{1.825}\square_{0.175}O_4$) also displays characteristic (020) and (060) diffraction peaks, which are slightly shifted towards a lower diffraction angle, signifying expanded interlayer distance due to the intercalation of water molecules into inter-gallery space of the layered crystals **[24]**. Additionally, signature (hkl) peaks (130) and (051) matching with the in-plane host structure are present, demonstrating that the in-plane host structure remains intact after acid treatment **[25]**.

The XRD patterns of dip-coated titanate-NS thin films are shown in **Fig. 4.4**. All titanate-NS thin films show a series of Braggs reflections (020), (040), and (060) corresponding to layered lepidocrocite type-layered titanate-NS with turbostratic structure having orthorhombic symmetry (JCPDS card number: 84-1226) **[26]**. The estimated basal spacing from the Braggs reflection (020) for T-1, T-2 and T-3 is 0.87, 0.88 and 0.89 nm, respectively **[27]**. The XRD study indicates the layer-by-layer stacking of deposited titanate-NS on the glass substrate.
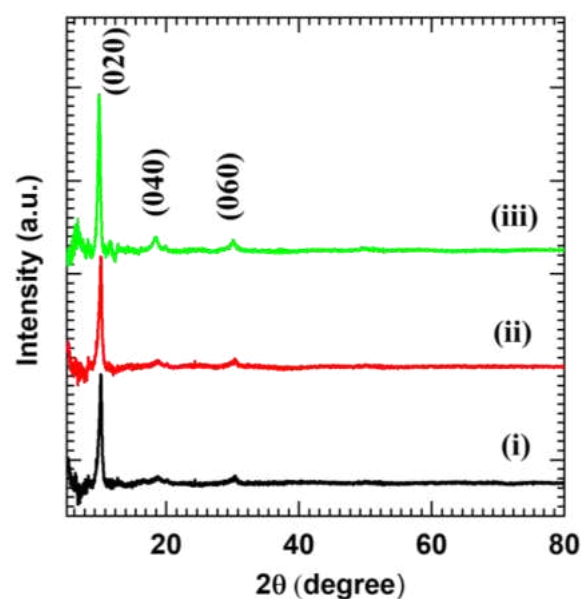
Figure 4.4: XRD patterns of i) T-1, ii) T-2 and iii) T-3 thin films.

4.2.2.2 Raman study
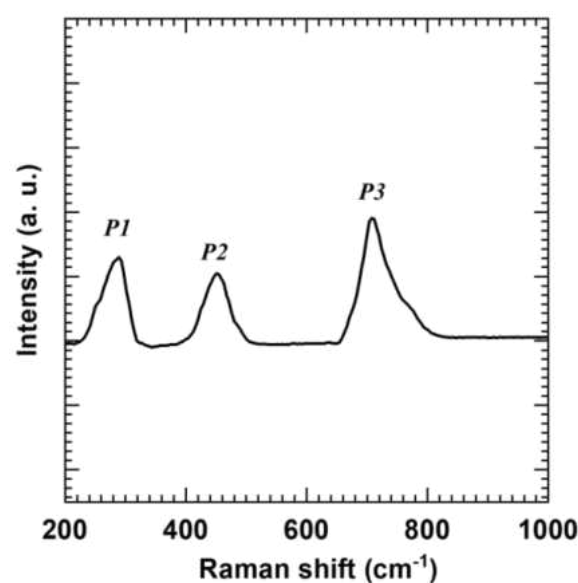
Figure 4.5: Raman spectrum of T-2 thin film.

The nature of chemical bonding and microscopic structural features of titanate-NS thin film were investigated by Raman spectroscopy, as shown in **Fig. 4.5**. Titanate-NS thin film exhibits several Raman peaks. The peaks P1 (291 cm^{-1}) and P2 (450 cm^{-1}) are assigned to the degenerate modes of the TiO$_6$ octahedron with Ag symmetry. The peak P3 (710 cm^{-1}) is attributed to the totally symmetric Ti-O vibrations **[28-30]**. These characteristic Raman peaks confirm the layer-by-layer deposition of well-developed titanate-NS thin film.

4.2.2.3 FTIR study
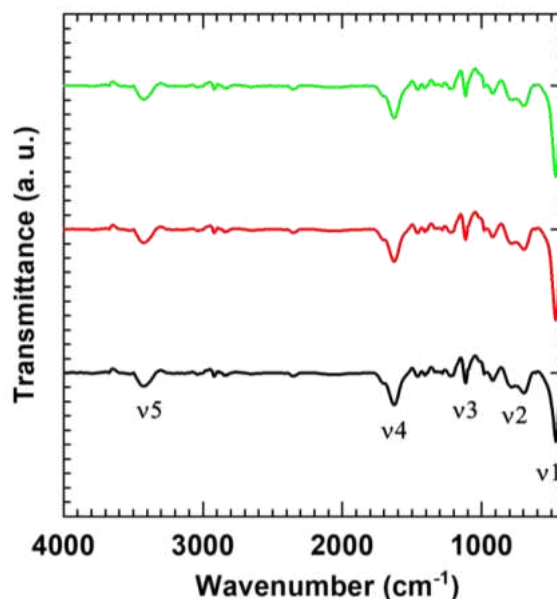
Figure 4.6: FTIR spectra of i) T-1, ii) T-2 and iii) T-3 thin films.

The chemical bonding nature of titanate-NS thin films was studied using FTIR spectroscopy. **Fig. 4.6** shows the FTIR spectra of titanate-NS thin films deposited at different dipping cycles. All titanate-NS thin films show similar IR features with absorption bands ν1 (474) and ν2 (697) corresponding to tetrahedrally and octahedrally coordinated Ti-O bonds in deposited titanate-NS **[31]**. The weak intensity band ν3 (1118 cm^{-1}) originated due to N-H stretching vibration in adsorbed TBA. The peaks ν4 (1632) and ν5 (3436 cm^{-1}) correspond to the bending vibrational modes of water molecules and stretching vibrations of the O-H groups, respectively **[32, 33]**. The FTIR study displays IR features meticulously related to the titanate-NS, which indicates the deposition of titanate-NS using the dip-coating method.

4.2.2.4 FE-SEM study

The surface morphology and microstructural features of the titanate-NS thin film were analyzed by the FE-SEM technique, as shown in **Fig. 4.7**. As shown in **Fig. 4.7a**, the titanate-NS thin film displays titanate-NS arranged parallel to the glass substrate. The titanate-NS have covered the entire substrate surface, showing high deposition uniformity. As shown in **Fig. 4.7b**, the cross-section view of the titanate-NS thin film shows stacked titanate-NS parallel to the glass substrate. The thickness of the T-2 thin film is around 0.51 µm.
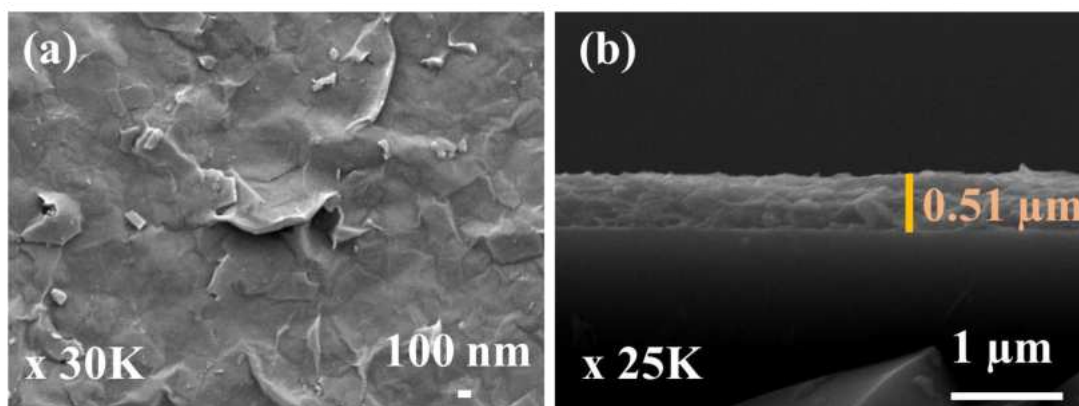
Figure 4.7: a) Top view and b) cross-section FE-SEM images of T-2 thin film.

The presence of constituent elements in titanate-NS thin film was investigated using EDS elemental mapping analysis. As shown in **Fig. 4.8** and **Fig. 4.9**, Ti and O elements are uniformly distributed over the entire mapping area, showing the uniform distribution of the constituent elements in the titanate-NS thin films deposited using the dip-coating method. This study underscores the usefulness of the dip-coating method for the uniform deposition of titanate-NS thin film.
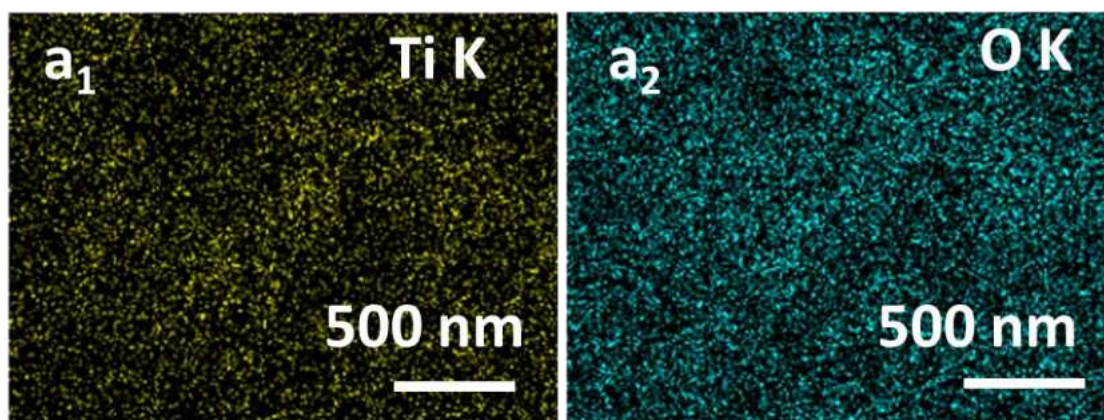
Figure 4.8: EDS elemental mapping of T-2 thin film.
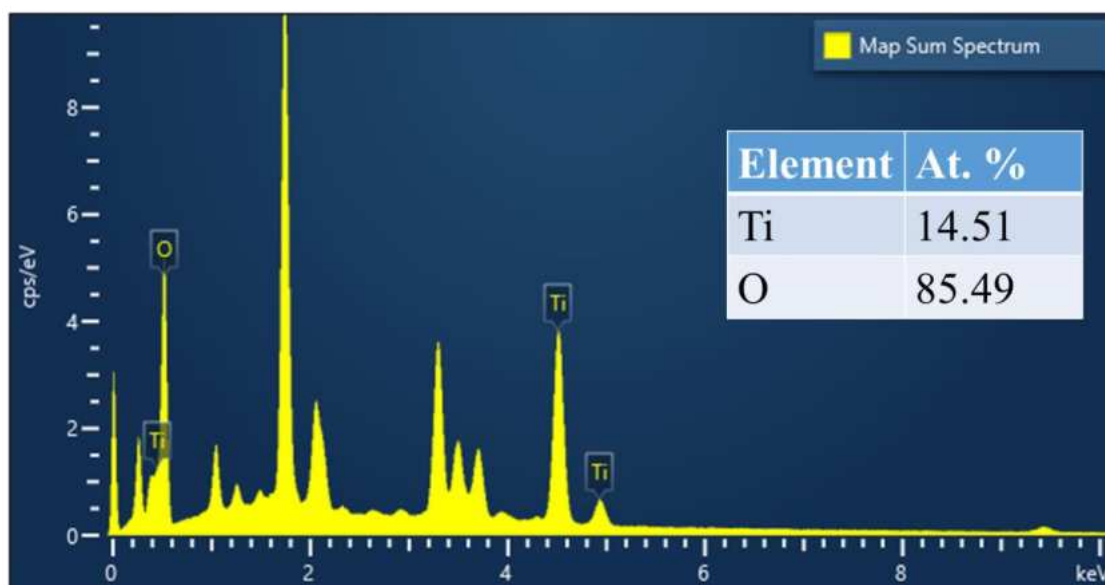
Figure 4.9: EDS spectrum of T-2 thin film.

4.2.2.5 XPS study

The presence of elements and their oxidation states in the titanate-NS thin film were determined by XPS analysis. As shown in **Fig. 4.10**, the survey spectrum of the T-2 thin film exhibits characteristic XPS features at BE of Ti and O elements, representing the presence of stated elements in the above thin film.
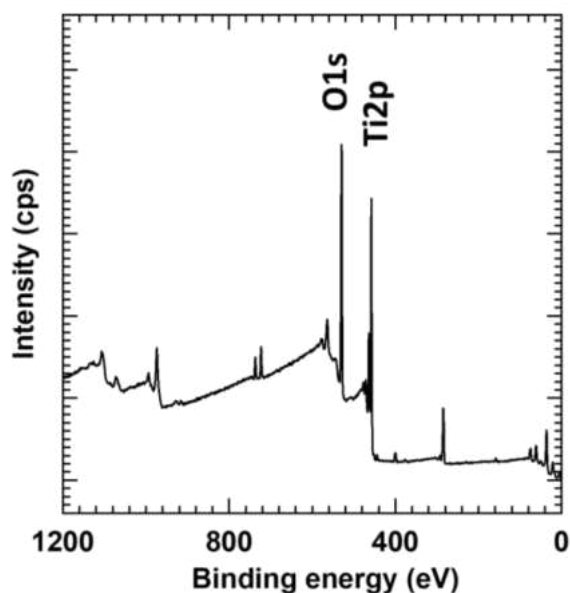
Figure 4.10: XPS survey spectrum of T-2 thin film.
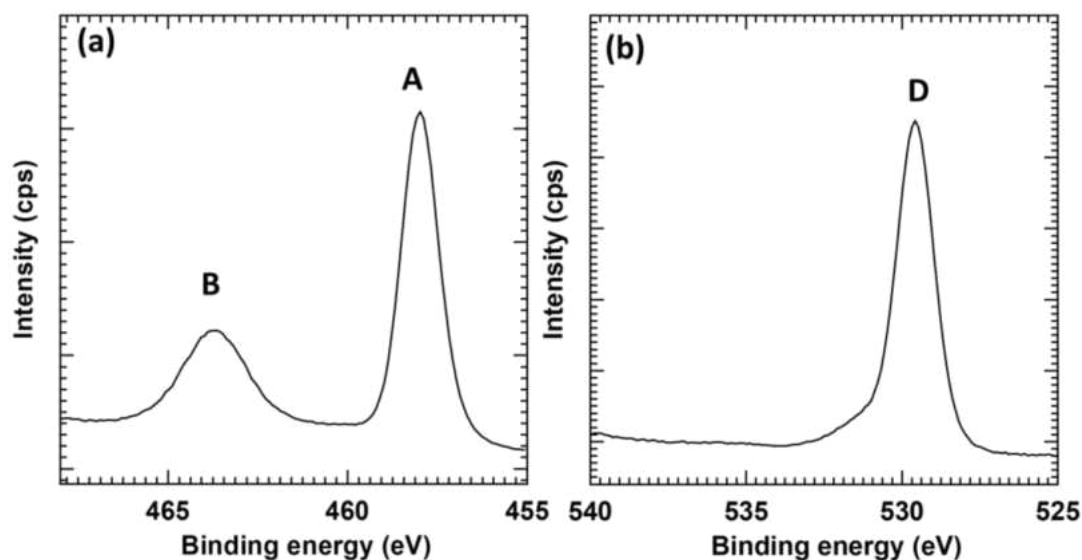
Figure 4.11: a) Ti 2p and b) O 1s core-level XPS spectra of T-2 thin film.

The high-resolution Ti 2p and O 1s core-level XPS spectra are plotted in **Fig. 4.11 (a** and **b)**, respectively. As shown in **Fig. 4.11a**, Ti exhibits two peaks, A (458 eV) and B (463.7 eV), corresponding to the spin-orbit splitting of Ti into Ti $2p_{3/2}$ and Ti $2p_{1/2}$, respectively **[23]**. The BE difference of 5.7 eV indicates the presence of Ti in the +4 state **[34]**. As shown in **Fig. 4.11b,** the high-resolution O 1s spectrum of titanate-NS thin film shows a single peak C (529.6 eV), indicating the presence of oxygen from metal oxide **[35]**. The observed XPS features underscore strong evidence of Ti^{4+} and O^{2-} states of Ti and O, respectively, confirming the titanate-NS deposition on the glass substrate.

4.2.2.6 UV-Vis DRS study and band positions determination

The optical properties and band positions of pristine titanate-NS thin film were examined using the UV-Vis DRS technique, as shown in **Fig. 4.12**. The titanate-NS thin film shows strong absorption in the UV region with no absorption in the visible region due to its wide band gap (3.34 eV), as shown in **Fig. 4.12a**. The electronic structure of titanate-NS comprises a VB and CB mainly composed of O 2p and Ti 3d orbitals, respectively **[36]**. Further, the band gap energy of titanate-NS thin film determined from the Kubelka-Munk function is shown in **Fig. 4.12b**. The band gap energy determined from the Kubelka-Munk function is 3.34 eV for T-2 thin film. The present study highlights the significant absorption of titanate-NS thin film in the UV region of the electromagnetic spectrum.
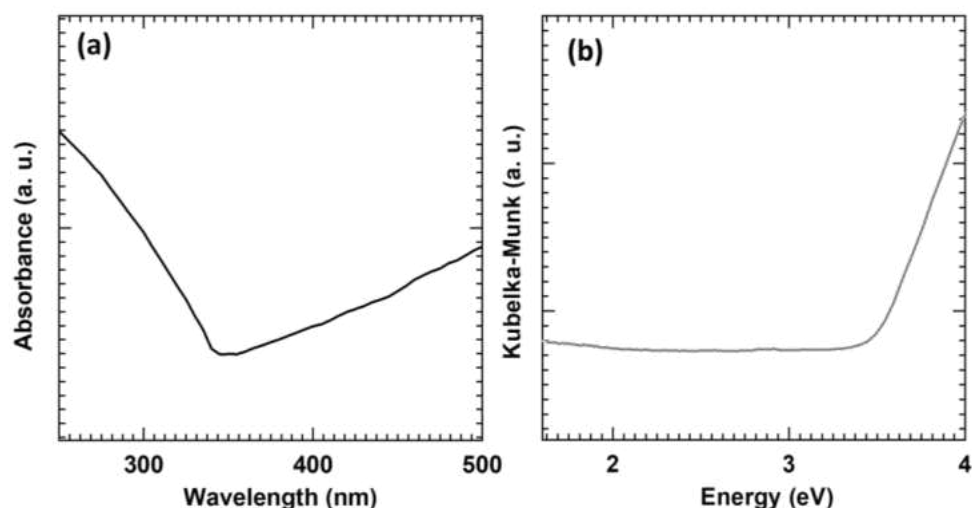
Figure 4.12: a) UV-Vis DRS absorbance spectrum and b) Diffuse reflectance UV–Vis spectrum (plotted as the Kubelka–Munk function of the reflectance, R) of T-2 thin film.

The band positions of titanate-NS thin film were estimated using an empirical formula, as described in **Chapter 3, section 3.2.2.6**. The estimated VB and CB positions of titanate-NS thin film are at 2.23 and -1.11 eV vs NHE, respectively, as shown in **Fig. 4.13**. These estimated band positions are well-matched with previously reported values **[37, 38]**.
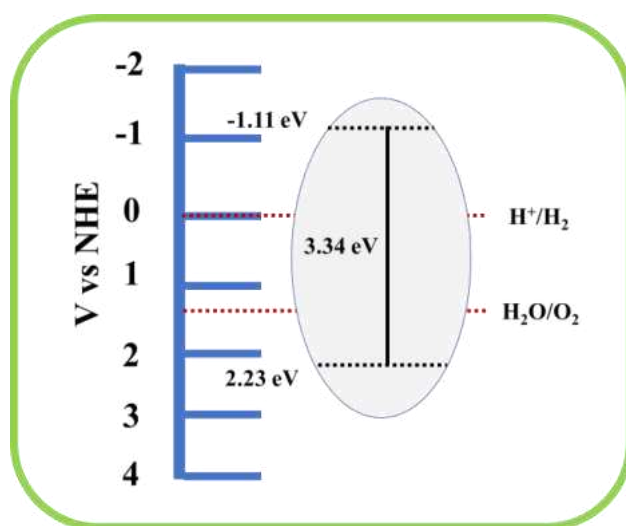
Figure 4.13: Band positions of titanate-NS thin film vs NHE.

4.3 Dye Degradation Studies

4.3.1 Results and Discussion
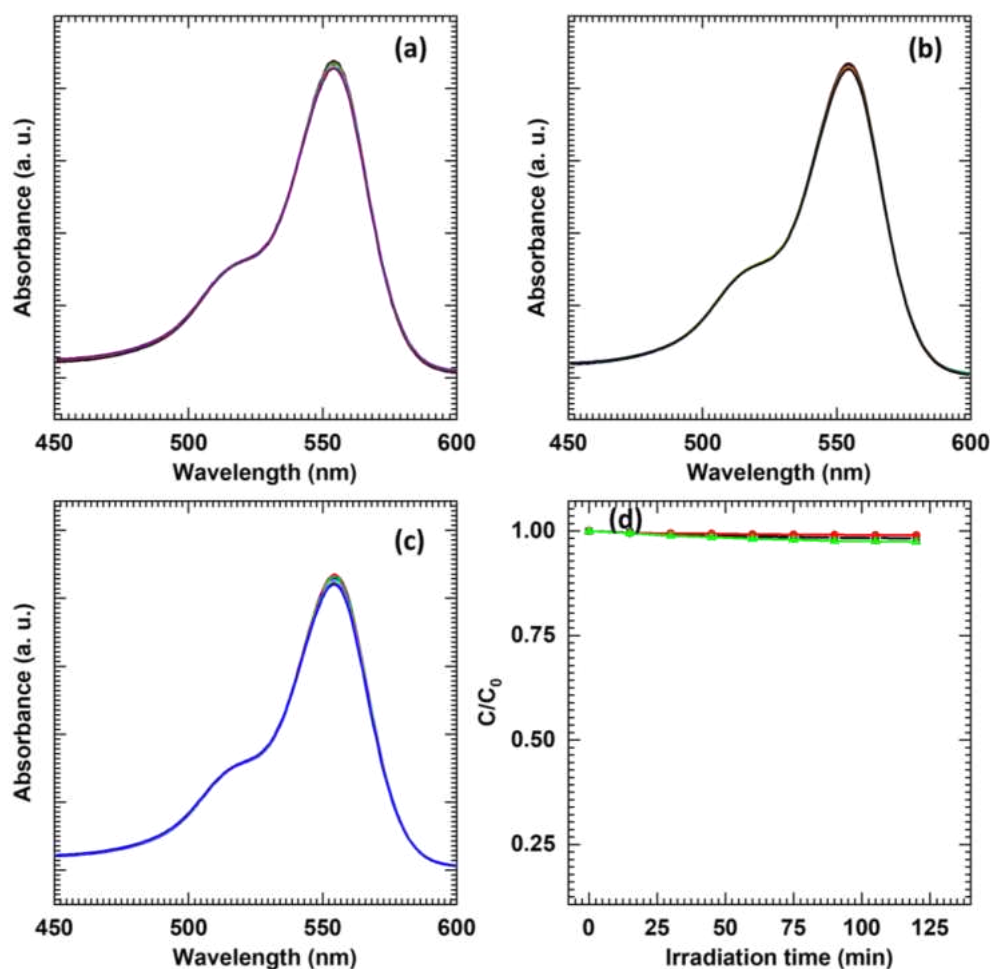
Figure 4.14: UV-Vis absorption spectra of RhB in the presence of (a) T-1, (b) T-2, (c) T-3 thin films under visible-light irradiation and (d) variation of RhB concentration as a function of irradiation time for T-1 (black), T-2 (Red) and T-3 (green) thin films.

The photocatalytic degradation performance of titanate-NS thin films was assessed by monitoring the time-dependent UV-Vis absorption spectra of RhB under visible-light illumination in the presence of photocatalysts. **Fig. 4.14 (a-c)** displays time-dependent UV-Vis absorption spectra of RhB dye in the presence of T-1, T-2 and T-3 thin films under visible-light irradiation, respectively. No decrease in the intensity at the characteristic wavelength of 554 nm with respect to irradiation time indicates that the titanate-NS does not show visible light activity due to its wide band gap (3.34 eV). **Fig. 4.14d** shows the variation of RhB concentration as a function of irradiation time for T-1, T-2 and T-3 thin films. The titanate-NS do not degrade RhB dye. The visible light

inactivity of titanate-NS is ascribed to the wide bandgap of titanate-NS (3.34 eV) thin films.
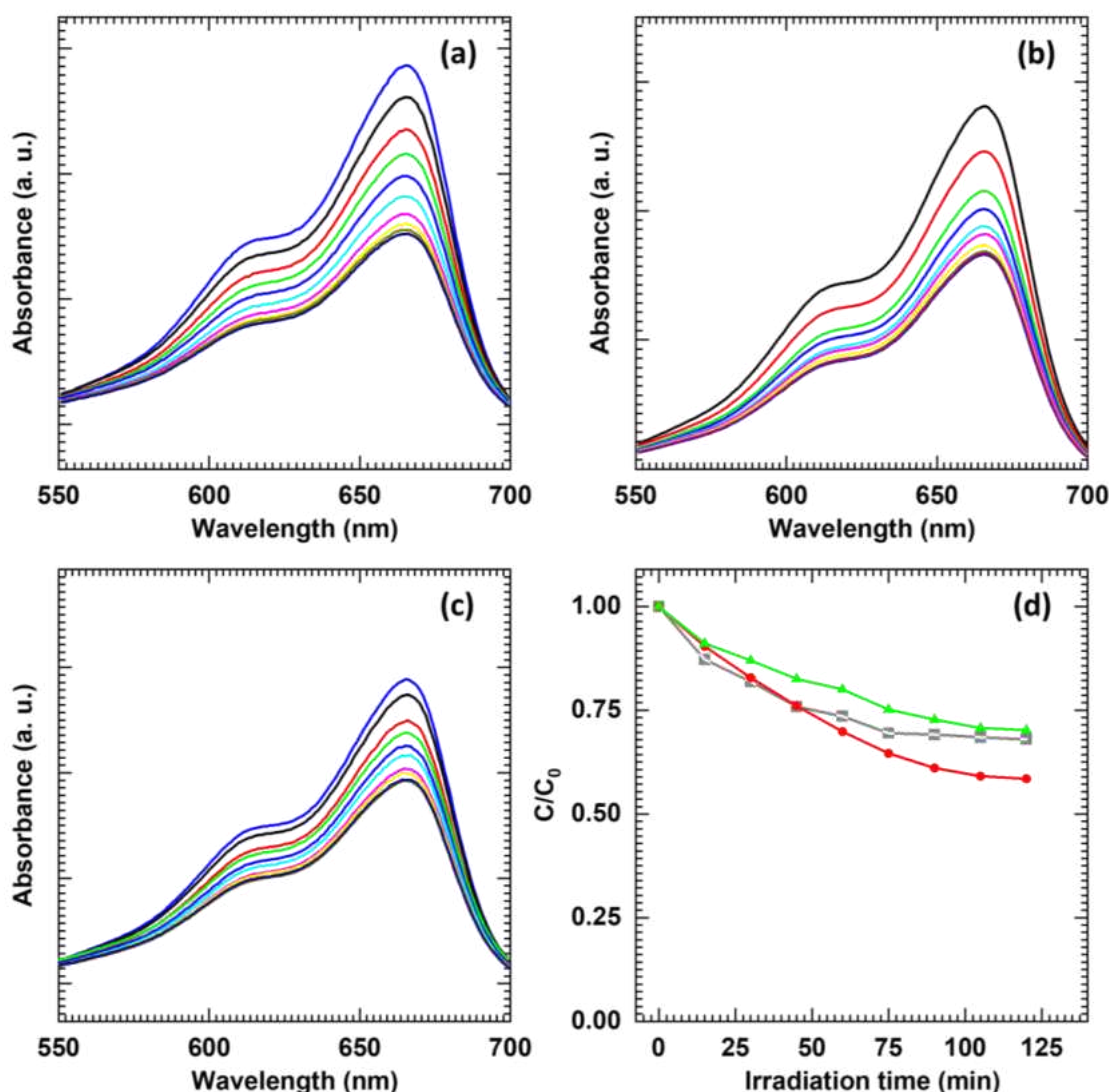
Figure 4.15: UV-Vis absorption spectra of MB in the presence of (a) T-1, (b) T-2, (c) T-3 thin films under visible light irradiation and (d) variation of MB concentration as a function of irradiation time for T-1 (black), T-2 (Red) and T-3 (green) thin films.

Similarly, the photocatalytic degradation performance of titanate-NS thin films for MB was assessed by observing the time-dependent UV-Vis absorption spectra of MB under visible-light illumination in the presence of photocatalysts. **Fig. 4.15 (a-c)** displays time-dependent UV-Vis absorption spectra of MB dye in the presence of T-1, T-2 and T-3 thin films under visible light illumination, respectively. The decrease in intensity at the characteristic wavelength of 665 nm with respect to irradiation time indicates the degradation of MB. However, this decrease in MB absorbance occurred

due to self-degradation via sensitization **[39-40]**. **Fig. 4.15d** shows the variation of MB concentration as a function of irradiation time for T-1, T-2 and T-3 thin films.

4.3.2 Kinetic study
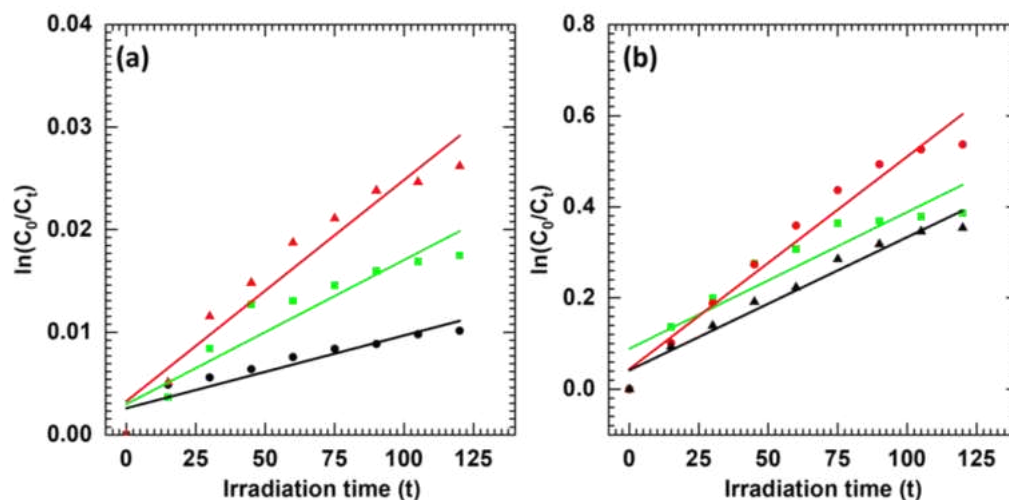
Figure 4.16: Pseudo-first-order kinetics of a) RhB and b) MB dyes using i) T-1 (black), ii) T-2 (red) and iii) T-3 (green) thin films.

The degradation kinetics of RhB and MB dyes using titanate-NS thin films were probed by a pseudo-first-order kinetic model by plotting $\ln(C_0/C_t)$ vs irradiation time as shown in **Fig. 4.16 (a-b) [41]**. The rate constant (k) and linear correlation coefficient (R^2) values are given in **Table 4.1**. T-2 showed a rate constant of 0.0007 and 0.004 min^{-1} for RhB and MB dyes, respectively. These values are inferior due to the inactivity of titanate-NS thin films under visible light irradiation.

Table 4.1: Photocatalytic dye degradation performance of titanate-NS thin films.

Target molecule	Photocatalyst	Degradation (%)	Rate constant k (min^{-1})	Correlation coefficient (R^2)
RhB	T-1	0.02	0.00007	0.8394
	T-2	0.08	0.0007	0.9316
	T-3	0.04	0.0001	0.8705
MB	T-1	30	0.002	0.9566
	T-2	41	0.007	0.9587
	T-3	36	0.003	0.8395

4.4 Synthesis and characterization of niobate-NS

4.4.1 Experimental details

4.4.1.1 Chemicals

Niobium oxide (Nb_2O_5), potassium carbonate (K_2CO_3), HCl and TBA-OH were purchased from Sigma-Aldrich and used without further purification. A dialysis tube (Dialysis Membrane-135, Av. flat width-33.12 mm, Av. diameter-23.8 mm, capacity approx.-4.45 ml cm^{-1}) is used for the dialysis of exfoliated niobate-NS solution. All experiments were performed in DDW.

4.4.1.2 Preparation of colloidal niobate-NS suspension

a) Synthesis of potassium niobate by solid-state reaction

The host crystal of $K_4Nb_6O_{17}$ was prepared by conventional solid-state reaction in which K_2CO_3 and Nb_2O_5 were taken in mortar pestle in stoichiometric ratio and ground thoroughly in a mini glove-box under N_2 atmosphere. The mixture was then heated in a furnace at 1050°C for 20 hours and allowed to cool naturally. The prepared material is thoroughly grounded to become fine particles **[42-43]**.

b) Protonation of $K_4Nb_6O_{17}$

The protonated derivative of calcinated $K_4Nb_6O_{17}$ powder was achieved by proton exchange reaction of highly crystalline $K_4Nb_6O_{17}$ powder in 1 M HCl solution and constant stirring for 24 hours. The HCl solution was replaced with a fresh one every 24 hours. This process was repeated three times to complete the proton exchange reaction. Finally, the solution was centrifuged, and the $H_xK_{4-x}Nb_6O_{17}$ product collected was freeze-dried and used for further processing **[44]**.

c) Exfoliation of protonated $H_xK_{4-x}Nb_6O_{17}$

The exfoliation process comprised the dispersion of protonated $H_xK_{4-x}Nb_6O_{17}$ crystals in TBA-OH solution under constant shaking for 24 hours. In this process, TBA-OH ions were intercalated in $H_xK_{4-x}Nb_6O_{17}$ crystals and further shaking or ultrasonication led to exfoliating $H_xK_{4-x}Nb_6O_{17}$ crystals into their monolayers to form a stable colloidal solution.

d) Dialysis of niobate-NS colloidal suspension

The exfoliated niobate-NS colloidal suspension possesses a highly basic pH (~12.5). At such a high pH, the deposition of niobate-NS thin films was not possible. Thus, to obtain processable niobate-NS colloidal suspension and deposition of niobate-NS, the pH of niobate-NS colloidal suspension was reduced by the dialysis against DDW. For the dialysis process, the exfoliated colloidal suspension of niobate-NS (with a pH of 12.5) was dialyzed using a dialysis membrane in DDW. The DDW is changed after every hour in order to bring the pH of the colloidal suspension in the range of 8.

The schematic representation of niobate-NS preparation is displayed in **Fig. 4.17**.
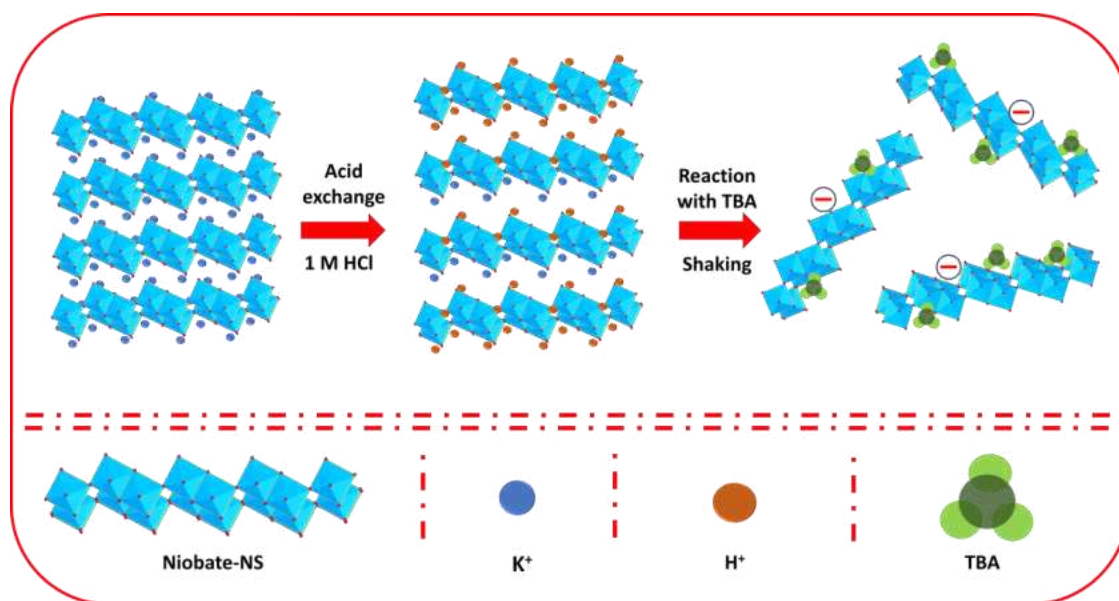
Figure 4.17: Schematic representation of synthesis of exfoliated niobate-NS.

4.4.1.3 Deposition of niobate-NS thin films by Dip-Coating

Niobate-NS thin film deposition was carried out on well-cleaned glass substrates. The glass substrate cleaning process is described in **Chapter 3, section 3.2.1.2**.

Niobate-NS thin films by the dip-coating method were obtained by dialyzing niobate-NS colloidal suspension (pH=12.5) for 14 hours using a dialysis membrane in DDW to attain a pH of 8. The dialyzed niobate-NS suspension was directly used as a precursor for depositing niobate-NS thin films. A microprocessor-controlled dip coating unit is used to deposit niobate-NS thin films. The niobate-NS thin films were deposited at the dipping and retrieval rate of 1000 microns sec^{-1}. One dip and consecutive retrieval of substrate completed one dip cycle. Such 50-100 cycles were executed to vary the deposition thickness of niobate-NS. After each cycle, the film is dried in the infrared

chamber coupled to a dip-coating unit. The films deposited at 50, 75 and 100 dip cycles were labelled N-1, N-2 and N-3, respectively. The schematic representation of niobate-NS thin film deposition using the dip-coating method is shown in **Fig. 4.18**.
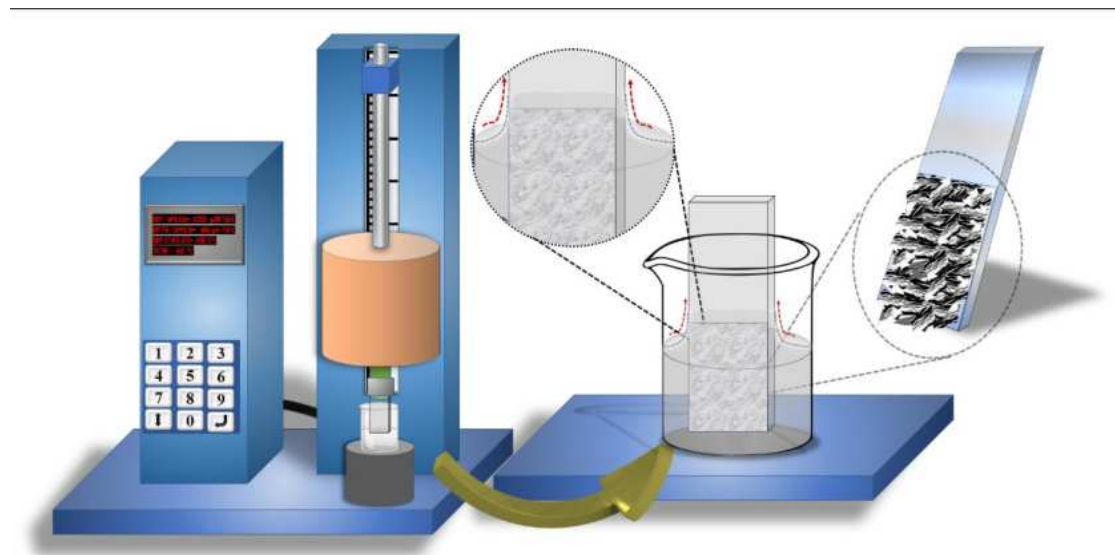
Figure 4.18: Schematic representation of the synthesis process of niobate-NS thin films.

4.4.1.4 Materials characterization

The details of material characterizations are similar to those described in **Chapter 3, section 3.2.1.3**.

4.4.2 Results and Discussion

4.4.2.1 XRD study

The structural study of the niobate-NS thin films was probed using the XRD technique. The XRD patterns of potassium niobate ($K_4Nb_6O_{17}$) and its protonated derivative ($H_xK_{4-x}Nb_6O_{17}$) are shown in **Fig. 4.19 (a and b)**, respectively. The potassium hexaniobate ($K_4Nb_6O_{17}$) displays a highly intense series of (040), (021), (220), (002), (061), (072) and (153) diffraction peaks matching with the highly crystalline well-ordered layered orthorhombic structure of layered $K_4Nb_6O_{17}$ (JCPDS: 76-0977) **[44]**. Its protonated product ($H_xK_{4-x}Nb_6O_{17}$) also shows an intense series of (040), (220), (002), (061) and (153) diffraction peaks, as shown in **Fig. 4.19b**. These diffraction peaks matching with the in-plane host structure are discernible, demonstrating that the in-plane host structure remains intact after the proton-exchange process **[44-46]**.
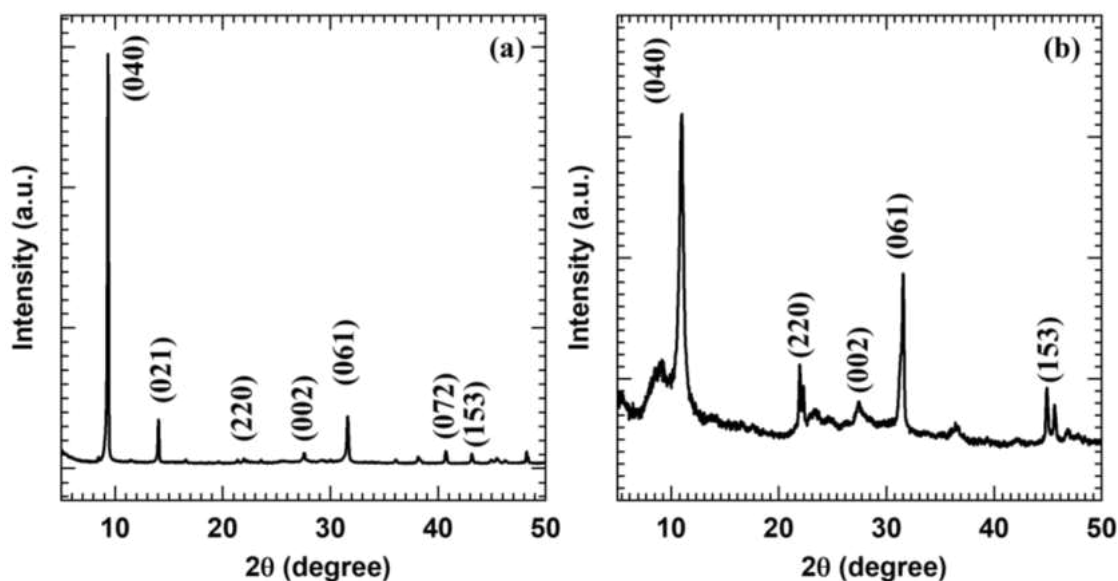
Figure 4.19: XRD patterns of a) calcinated $K_4Nb_6O_{17}$ and b) protonated $H_xK_{4-x}Nb_6O_{17}$.

The XRD patterns of dip-coated niobate-NS thin films are shown in **Fig. 4.20**. All niobate-NS thin films exhibit a broad diffraction peak at 11.2°, which is assigned to the (040) plane corresponding to the well-ordered stacking of lamellar hexaniobate nanosheets with the orthorhombic structure **[44]**. The interplanar distance for N-1, N-2 and N-3 is 0.96, 0.94 and 0.91 nm, respectively. Thus, the XRD study confirms the formation of niobate-NS deposition using the dip-coating method.
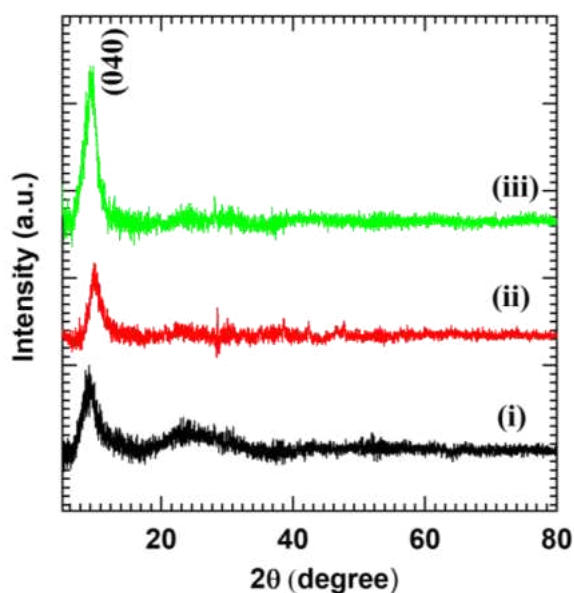
Figure 4.20: XRD patterns of i) N-1, ii) N-2 and iii) N-3 thin films.

4.4.2.2 Raman study

The nature of chemical bonding and microscopic structural features of niobate-NS thin film were studied using Raman spectroscopy, as shown in **Fig. 4.21**. The N-2 thin film shows characteristic Raman features related to niobate-NS, which confirms the deposition of niobate-NS on the glass substrate. The peak P1 (230 cm^{-1}) corresponds to the internal bending mode of O-Nb-O. The high-intensity broad peak P2 (620 cm^{-1}) corresponds to the stretching mode of Nb-O in NbO_6 octahedra. The peak P3 (884 cm^{-1}) originated due to the Nb-O terminal stretching mode of highly distorted NbO_6 octahedra [47-49]. The present Raman features confirm the deposition of niobate-NS thin film using the dip-coating method.
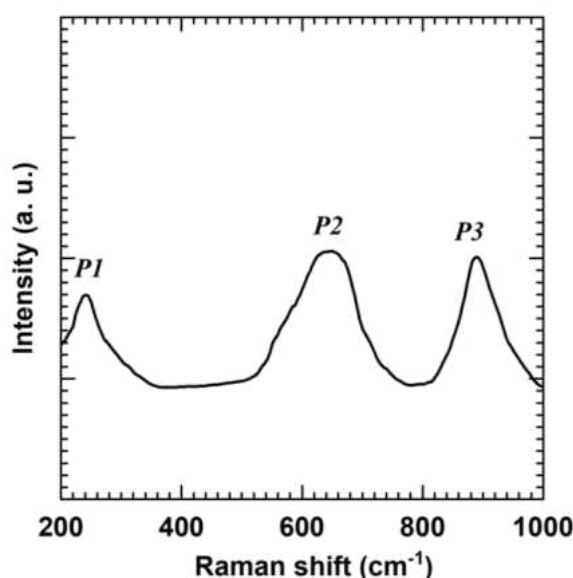
Figure 4.21: Raman spectrum of N-2 thin film.

4.4.2.3 FTIR study

Further, the chemical bonding nature of niobate-NS thin films was studied by FTIR spectroscopy. As shown in **Fig. 4.22**, all the samples exhibit similar IR spectra with several absorption bands. The absorption band v1 (540 cm^{-1}) is assigned to the stretching vibrations of O-Nb-O. The absorption band v2 (910 cm^{-1}) is assigned to the stretching vibration of Nb=O in NbO_6 octahedra [8]. The weak band v3 (1118 cm^{-1}) is ascribed to the N-H stretching vibration in TBA [48]. The absorption bands v4 (1630 cm^{-1}) and v5 (3415 cm^{-1}) correspond to the bending vibrational modes of water molecules and stretching vibration of the hydroxyl groups, respectively [32-33]. Thus,

the IR features related to niobate-NS confirm the deposition of niobate-NS using the dip-coating technique.
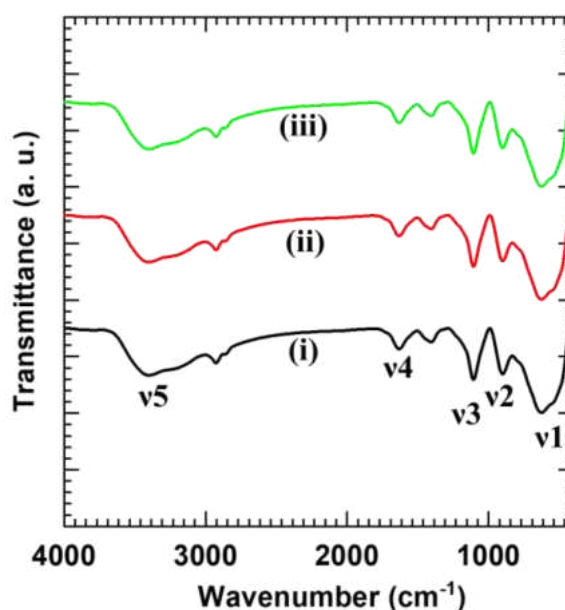
Figure 4.22: FTIR spectra of i) N-1, ii) N-2 and iii) N-3 thin films.

4.4.2.4 FE-SEM study
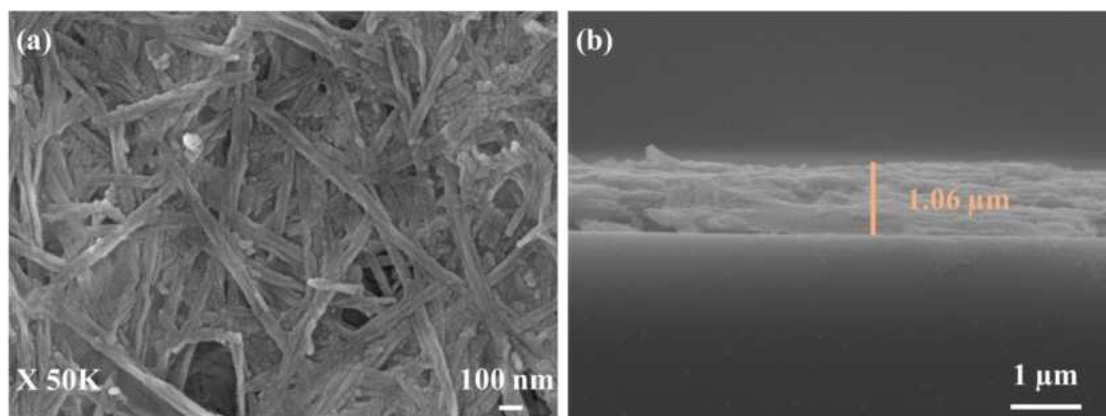
Figure 4.23: a) Top view and b) cross-section FE-SEM images of N-2 thin film.

The microstructural surface features of dip-coated niobate-NS thin film were investigated by FE-SEM analysis, as shown in **Fig. 4.23**. The anisotropic growth of niobate nanoscrolls is evidenced from the FE-SEM images, where nanoscrolls have a length ranging from 500 nm to 1 µM and a width of around 50 nm. The deposited nanoscrolls are randomly aggregated on the surface of the substrate, creating a porous structure of niobate-NS. As shown in **Fig. 4.23b**, the cross-section FE-SEM image

reveals niobate nanoscrolls are deposited on a glass substrate parallel to the substrate surface with a film thickness of 1.06 µm.

The presence of constituent elements in niobate-NS thin film was investigated using EDS elemental mapping analysis. As shown in **Fig. 4.24** and **Fig. 4.25**, Nb and O elements are uniformly distributed over the entire mapping area, showing the uniform deposition of niobate-NS thin film. This study shows the usefulness of the dip-coating method for the deposition of highly uniform thin films.
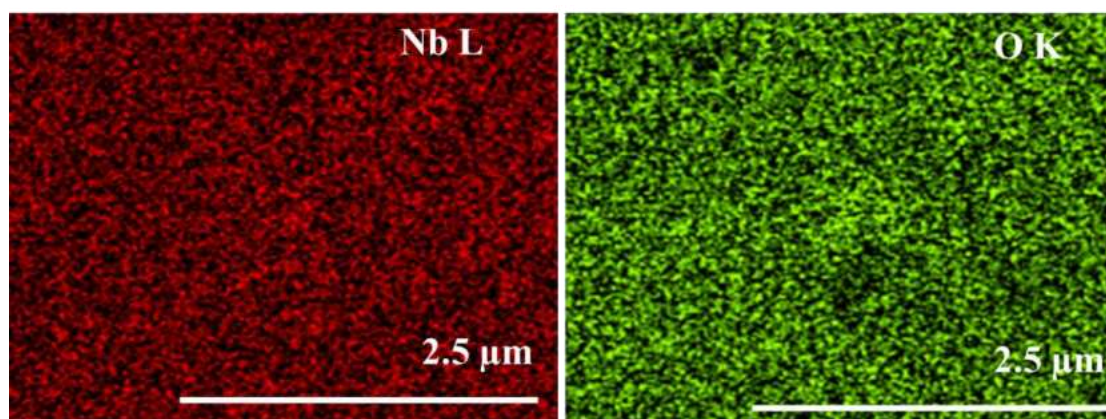
Figure 4.24: EDS elemental mapping of N-2 thin film.
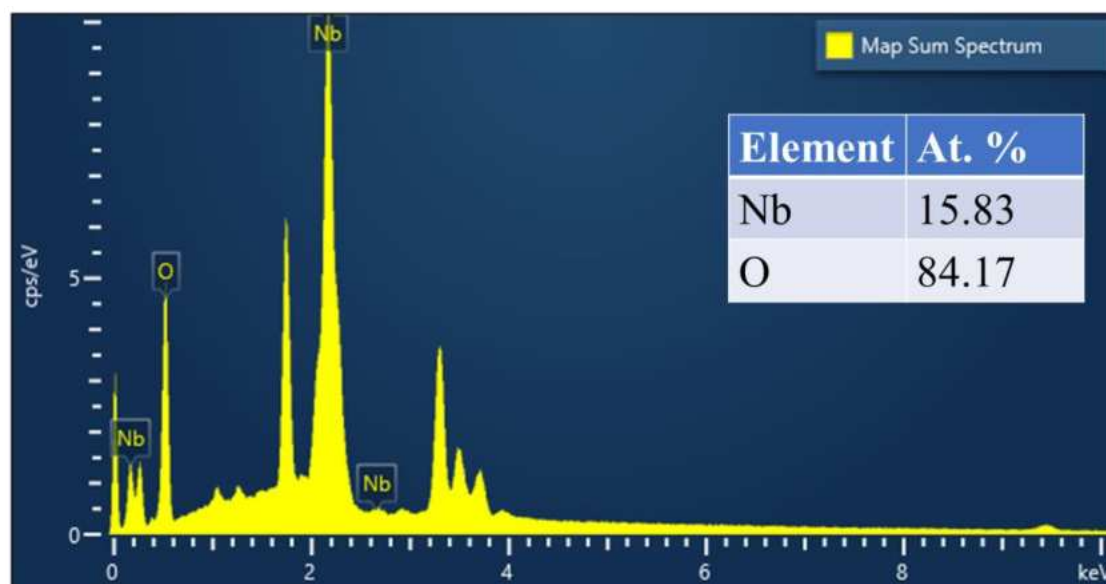
Figure 4.25: EDS spectrum of N-2 thin film.

4.4.2.5 XPS study

The presence of elements and their oxidation states in the niobate-NS thin film were determined by XPS analysis. As shown in **Fig. 4.26**, the survey XPS spectrum of the niobate-NS thin film exhibits characteristic XPS features at BE of Nb and O elements, representing the presence of stated elements in the above thin film.
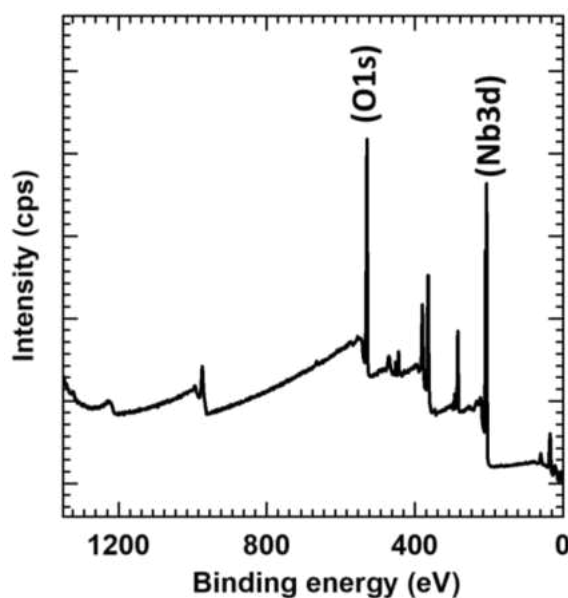
Figure 4.26: XPS survey spectrum of N-2 thin film.
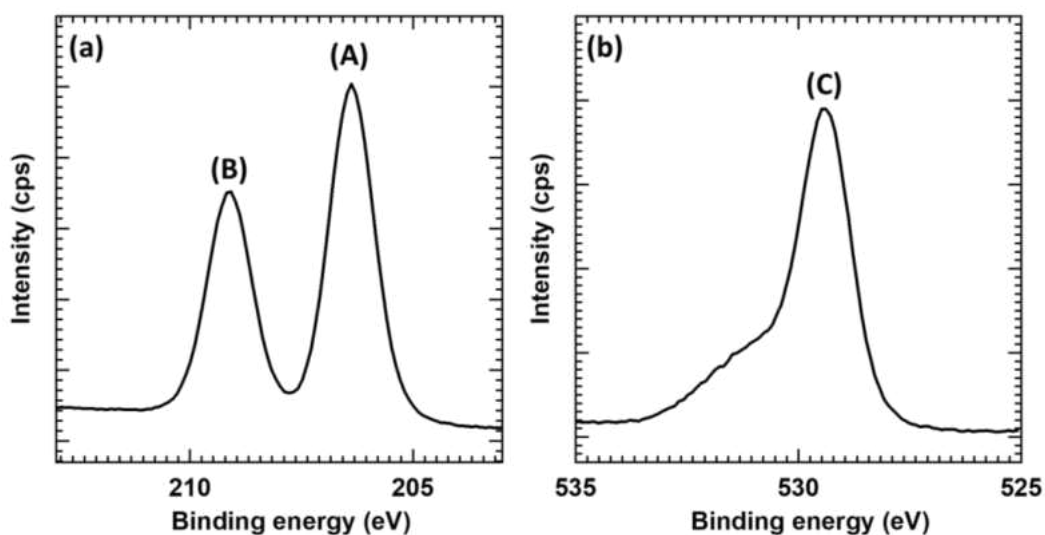
Figure 4.27: a) Nb 3d and b) O 1s Core-level XPS spectra of N-2 thin film.

The high-resolution Nb 3d and O 1s core-level XPS spectra are plotted in **Fig. 4.27 (a and b),** respectively. As shown in **Fig. 4.27a**, the high-resolution Nb 3d spectrum exhibits a doublet A (206.3) and B (209.1 eV) associated with spin-orbit splitting of Nb

$3d_{5/2}$ and Nb $3d_{3/2}$, respectively, which is characteristic of Nb^{5+} in niobate-NS thin film. As displayed in **Fig. 4.27b**, the high-resolution O 1s spectrum shows a single peak C (529.5 eV), indicating the presence of oxygen from metal oxide **[48]**. The observed XPS features underscore strong evidence of Nb^{5+} and O^{2-} states of Nb and O, respectively, which confirms the deposition of niobate-NS on the glass substrate.

4.4.2.6 UV-Vis DRS study and band structure determination
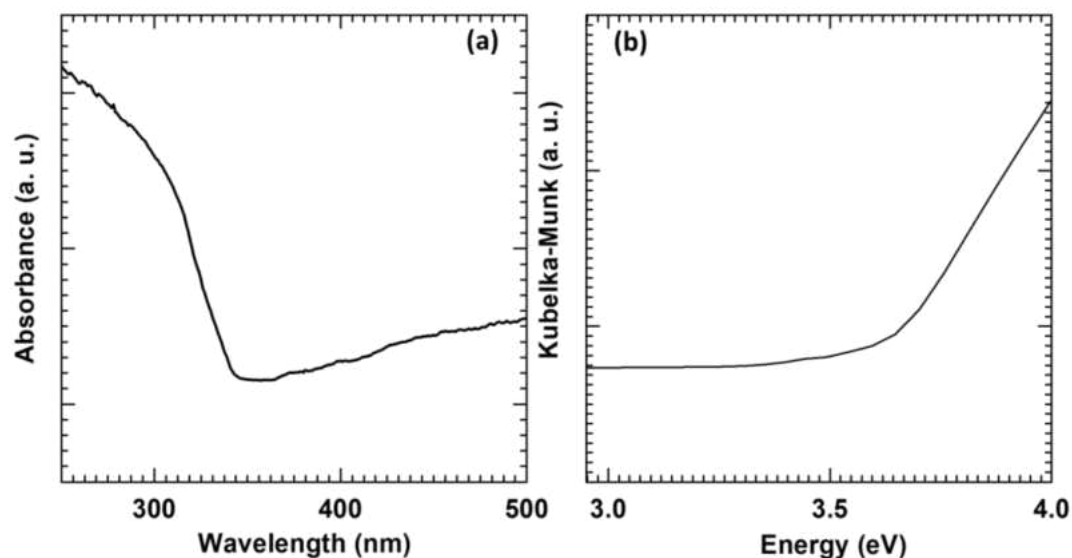
Figure 4.28: a) UV-Vis DRS absorbance spectrum and b) Diffuse reflectance UV–Vis spectrum (plotted as the Kubelka–Munk function of the reflectance, R) of N-2 thin film.

The band structure and optical properties of the niobate-NS thin film were studied using the UV-Vis DRS technique. As shown in **Fig. 4.28a**, the absorption edge of niobate-NS thin film occurs in the UV region of the solar spectrum, demonstrating the capability of niobate-NS thin film to harvest UV light. The niobate-NS thin film is an indirect band gap material with a VB and CB mainly composed of O 2p and Nb 4d orbitals, respectively **[49]**. The niobate-NS thin film absorbs UV light with a wavelength greater than 360 nm. The band gap energy determined from the Kubelka-Munk function is shown in **Fig. 4.28b**. The energy band gap value derived from the Kubelka-Munk function is 3.45 eV for niobate-NS thin film. The present study highlights the significant absorption of niobate-NS thin film in the UV region of the electromagnetic spectrum.

The VB and CB positions of niobate-NS were determined by empirical formula as described in **Chapter 3, section 3.2.2.6**. The estimated VB and CB positions for

niobate-NS are 2.69 and -0.76 eV vs NHE, respectively, as shown in **Fig. 4.29**. These band positions are well-matched with previously reported values **[50]**.
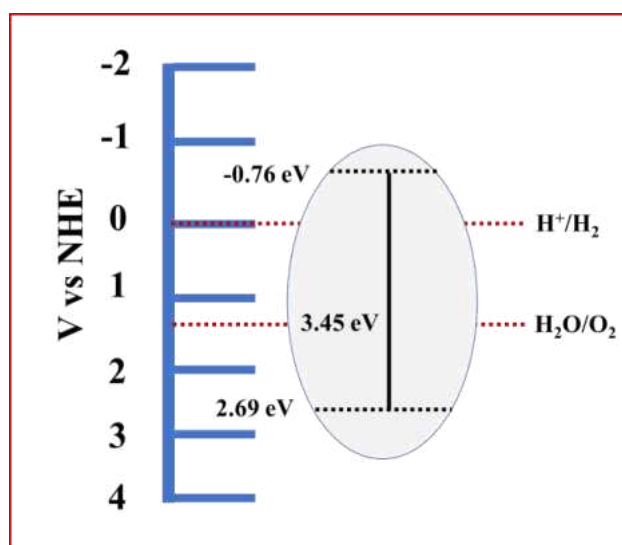
Figure 4.29: Band positions of niobate-NS thin film vs NHE.

4.5 Dye degradation studies

4.5.1 Results and Discussion

The photocatalytic degradation performance of niobate-NS thin films was assessed by observing the time-dependent UV-Vis absorption spectra of RhB under visible-light illumination in the presence of photocatalysts. **Fig. 4.30 (a-c)** displays time-dependent UV-Vis absorption spectra of RhB dye in the presence of N-1, N-2 and N-3 thin films under visible-light illumination, respectively. No decrease in the intensity at the characteristic wavelength of 554 nm with respect to irradiation time indicates that the Niobate-NS does not show visible-light activity due to its wide band gap (3.45 eV). **Fig. 4.30d** shows the variation of RhB concentration as a function of irradiation time for N-1, N-2 and N-3 thin films. The niobate-NS does not degrade RhB dye. The visible light inactivity of niobate-NS is ascribed to the wide bandgap of niobate-NS (3.45 eV) thin films.
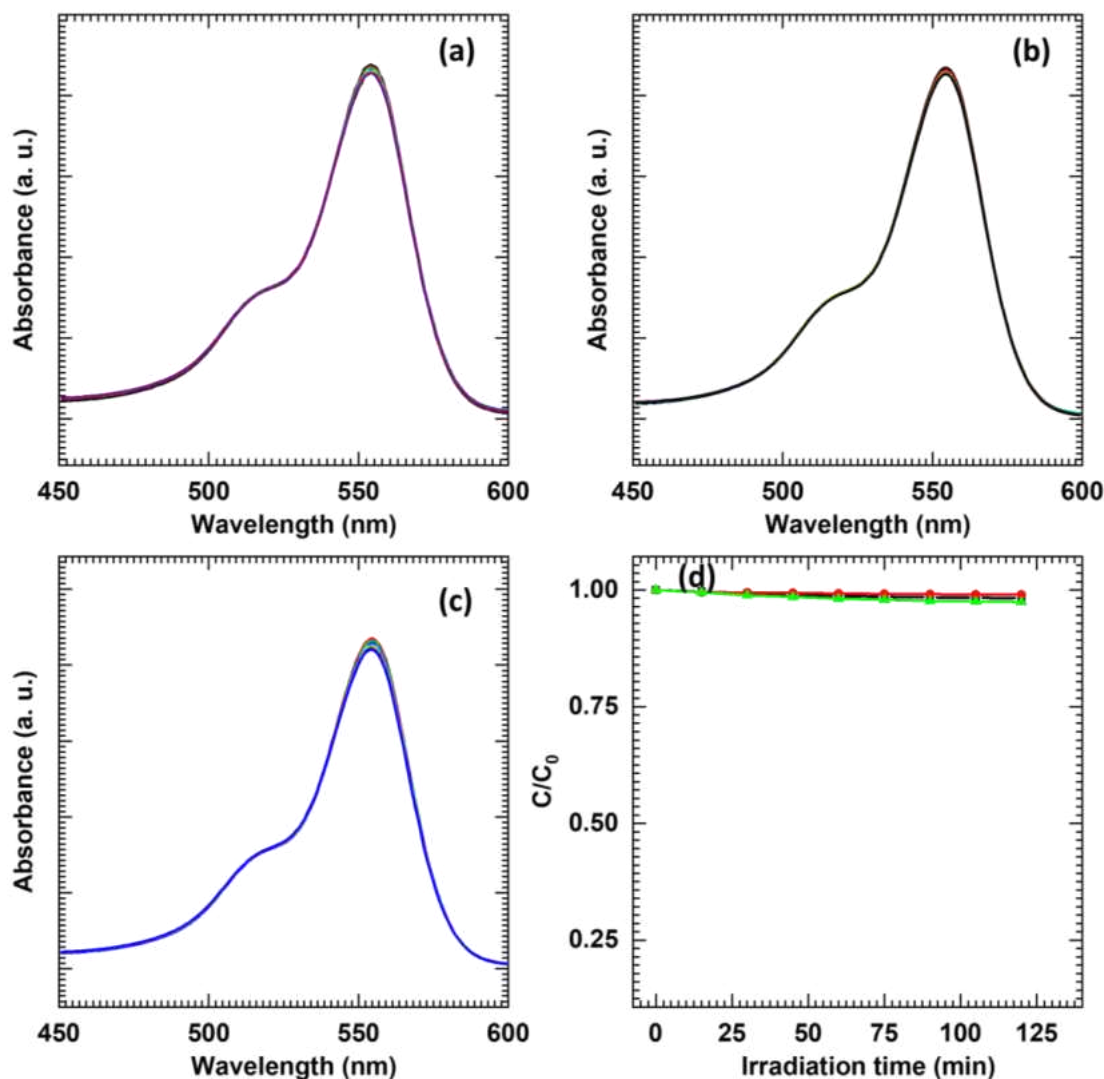
Figure 4.30: UV-Vis absorption spectra of RhB in the presence of (a) N-1, (b) N-2, (c) N-3 thin films under visible-light irradiation and (d) variation of RhB concentration as a function of irradiation time for N-1 (black), N-2 (Red) and N-3 (green) thin films.

Similarly, the photocatalytic degradation performance of niobate-NS thin films was assessed by observing the time-dependent UV-Vis absorption spectra of MB under visible-light illumination in the presence of photocatalysts. **Fig. 4.31 (a-c)** displays time-dependent absorption spectra of MB dye for N-1, N-2 and N-3 thin films, respectively. The decrease in intensity at the characteristic wavelength of 665 nm with respect to irradiation time indicates the degradation of MB. However, this decrease in MB absorbance occurred due to self-degradation via sensitization [39-40]. **Fig. 4.31d** shows the variation of MB concentration as a function of irradiation time for N-1, N-2 and N-3 thin films.
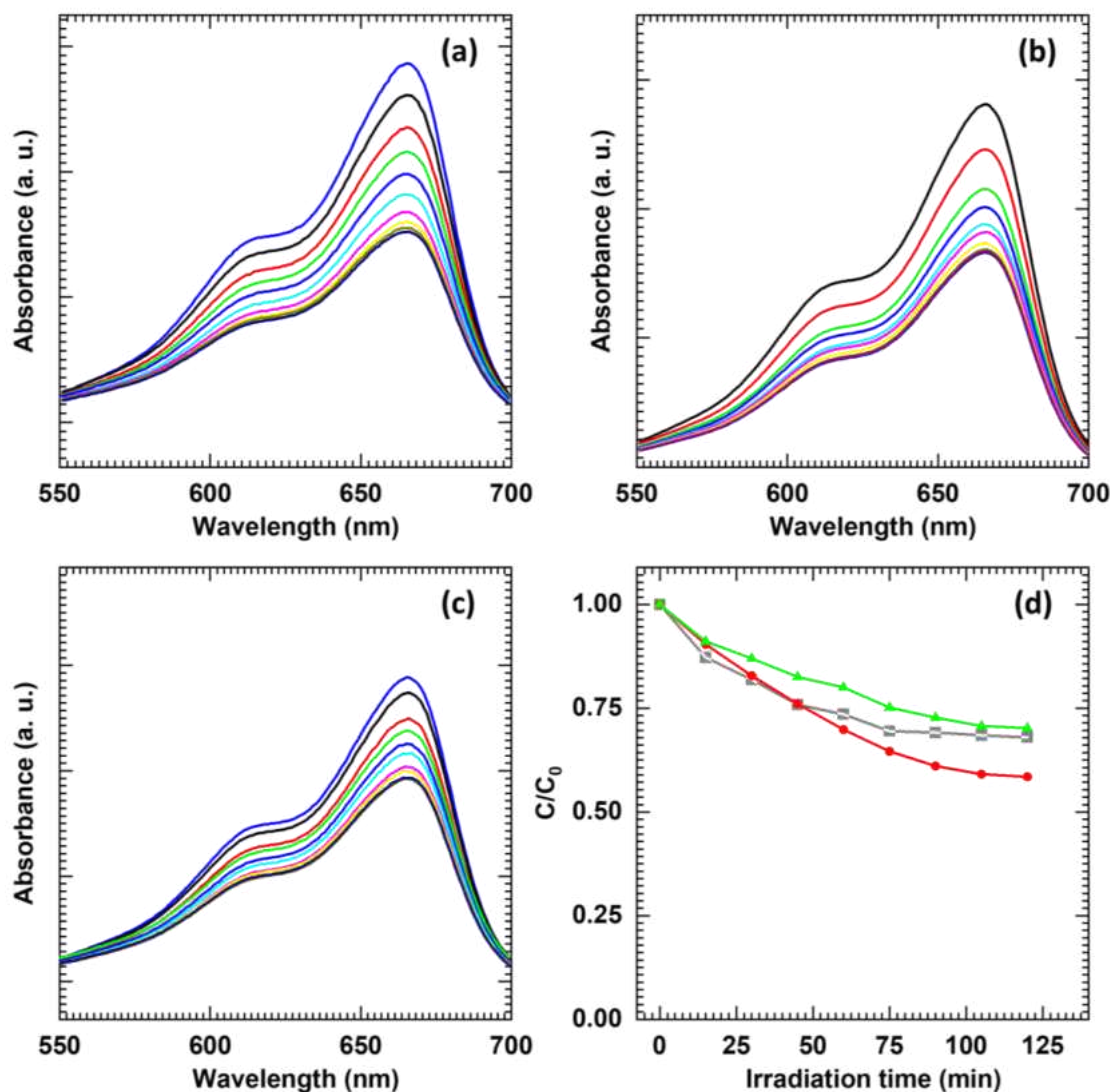
Figure 4.31: UV-Vis absorption spectra of MB in the presence of (a) N-1, (b) N-2, (c) N-3 thin films under visible-light irradiation and (d) variation of MB concentration as a function of irradiation time for N-1 (black), N-2 (Red) and N-3 (green) thin films.

4.5.2 Kinetic study

The degradation kinetics of RhB and MB dyes using niobate-NS thin films were probed by pseudo-first-order rate kinetic model by plotting $\ln(C_0/C_t)$ vs irradiation time as shown in **Fig. 4.32 [41]**. The rate constant (k) and linear correlation coefficient (R^2) values are given in **Table 4.2**. Among niobate-NS thin films, N-2 showed a better rate constant of 0.0002 and 0.004 min^{-1} for RhB and MB dyes, respectively. These values are very poor due to the inactivity of niobate-NS thin films in visible light irradiation.
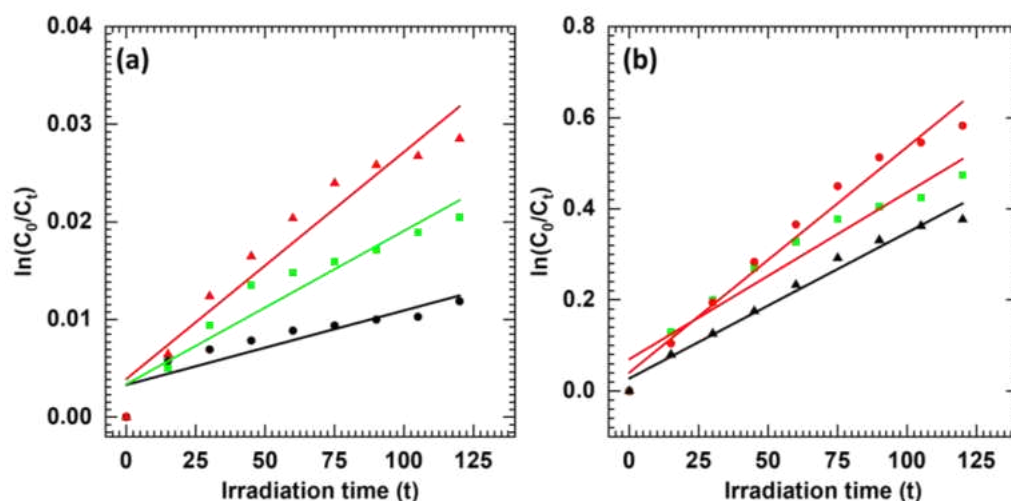
Figure 4.32: Pseudo-first-order kinetics of a) RhB and b) MB dyes using i) N-1 (black), ii) N-2 (red) and iii) N-3 (green) thin films.

Table 4.2: Photocatalytic dye degradation performance of niobate-NS thin films.

Target molecule	Photocatalyst	Degradation (%)	Rate constant k (min^{-1})	Correlation coefficient (R^2)
RhB	N-1	0.5	0.00007	0.7848
	N-2	1.7	0.0002	0.9264
	N-3	1.1	0.0001	0.9004
MB	N-1	32	0.00032	0.9754
	N-2	44	0.00049	0.9728
	N-3	40	0.00036	0.9334

4.6 Conclusions

In conclusion, a solid-state method was used to synthesize highly crystalline layered caesium titanate ($Cs_{0.7}Ti_{1.825}\square_{0.175}O_4$, $\square$=vacancy) and potassium hexaniobate ($K_4Nb_6O_{17}$). An effective route of preparing precursor solution for the deposition of titanate-NS and niobate-NS is optimized, which can be further employed for the

deposition of the exfoliated colloidal solutions. The exfoliated titanate-NS and niobate-NS solutions were directly used for the deposition of titanate-NS and niobate-NS thin films, respectively, using the dip-coating method. XRD study confirms deposition of layered titanate-NS and niobate-NS thin films with interlayer distances of 0.88 and 0.94 nm, respectively. The surface morphological analysis of titanate-NS shows titanate nanosheet deposition parallel to the substrate. Conversely, niobate-NS shows the deposition of anisotropic niobate nanoscrolls. Optical study shows the UV absorption capability of titanate-NS and niobate-NS thin films with band gaps of 3.34 and 3.45 eV, respectively. The degradation study reveals that the deposited titanate-NS and niobate-NS are photocatalytically inactive under visible light irradiation because of their wide bandgap. Titanate-NS shows a rate constant of 0.0007 and 0.007 min^{-1} for RhB and MB dyes, whereas niobate-NS shows a rate constant of 0.0002 and 0.0004 min^{-1} for RhB and MB dyes, respectively. However, due to their high anisotropy, wide band gap, high surface area and 2D structure, these films can be highly suitable for hybridization with narrow bandgap materials.

4.7 References

[1] J. Zhao, D. Ma, C. Wang, Z. Guo, B. Zhang, J. Li, G. Nie, N. Xie, H. Zhang, Nano Res., 14 (2021) 897.

[2] A. B. Kaul, J. Mater. Res., 29 (2014) 348.

[3] T. Tan, X. Jiang, C. Wang, B. Yao, H. Zhang, Adv. Sci., 7 (2020) 2000058.

[4] Y. Wu, D. Li, C.-L. Wu, H. Y. Hwang, Y. Cui, Nat. Rev. Mater., 8 (2023) 41.

[5] V. V. Magdum, Y. M. Chitare, S. P. Kulkarni, P. D. Sawant, S. A. Pawar, S. V. Talekar, C. D. Lokhande, U. M. Patil, S. B. Patil, J. L. Gunjakar, J. Mater. Chem. C, 11 (2023) 9768.

[6] G. S. Shanker, A. Biswas, S. Ogale, J. Phys. Energy, 3 (2021) 022003.

[7] M. A. Timmerman, R. Xia, P. T. P. Le, Y. Wang, J. E. T. Elshof, Chem. Eur. J., 26 (2020) 9084.

[8] R. B. Shinde, N. S. Padalkar, S. V. Sadavar, S. B. Kale, V. V. Magdum, Y. M. Chitare, S. P. Kulkarni, U. M. Patil, V. G. Parale, H.-H. Park, J. L. Gunjakar, J. Hazard. Mater., 432 (2022) 128734.

[9] T. Sasaki, M. Watanabe, Y. Michiue, Y. Komatsu, F. Izumi, S. Takenouchi, Chem. Mater., 7 (1995) 1001.

[10] T. Sasaki, M. Watanabe, H. Hashizume, H. Yamada, H. Nakazawa, J. Am. Chem. Soc., 118 (1996) 8329.

[11] K. Maeda, M. Eguchi, W. J. Youngblood, T. E. Mallouk, Chem. Mater., 20 (2008) 6770.

[12] Z. Zhang, D. Wang, M. Yang, L. Liu, J. Ma, M. Wang, C. Zhang, D. Zhang, Z. Tong, Chem. Lett., 46 (2017) 506.

[13] C. H. B. Silva, N. A. Galiote, F. Huguenin, E. Teixeira-Neto, V. R. L. Constantino, and M. L. A. Temperini, J. Mater. Chem., 22 (2012) 14052.

[14] H. Yuan, R. Lubbers, R. Besselink, M. Nijland, J. E. Elshof, ACS Appl. Mater. Interfaces, 6 (2014) 8567.

[15] H. Tokudome and M. Miyauchi, Chem. Commun., 8 (2004) 958.

[16] S. Kulkarni, Y. Chitare, V. Magdum, P. Sawant, S. Talekar, S. Pawar, D. Malavekar, S. Ansar, J. Kim, J. Gunjakar, ACS Appl. Nano Mater., 7 (2024) 11411.

[17] J.-H. Kim, J.-U. Woo, Y.-J. Yee, I.-S. Kim, H.-S. Shin, H.-G. Hwang, S. H. Kweon, H.-J. Choi, S. Nahm, Appl Surf Sci., 537 (2021) 147871.

[18] M. Fang, C. H. Kim, G. B. Saupe, H.-N. Kim, C. C. Waraksa, T. Miwa, A. Fujishima, T. E. Mallouk, Chem. Mater., 11 (1999) 1526.

[19] S. P. Kulkarni, V. V. Magdum, Y. M. Chitare, D. B. Malavekar, J. H. Kim, S. Alshehri, J. L. Gunjakar, S. P. Patole, 10 (2024) e39235.

[20] T. Sasaki, Y. Komatsu, Y. Fujiki, J. Chem. Soc., Chem. Commun., 12 (1991) 817.

[21] T. Sasaki, M. Watanabe, J. Am. Chem. Soc., 120 (1998) 4682.

[22] J. L. Gunjakar, T. W. Kim, H. N. Kim, I. Y. Kim, S.-J. Hwang, J. Am. Chem. Soc., 133 (2011) 14998.

[23] S. B. Patil, H. J. Kim, H.-K. Lim, S. M. Oh, J. Kim, J. Shin, H. Kim, J. W. Choi, S.-J. Hwang, ACS Energy Lett., 3 (2018) 412.

[24] J.-H. Choy, H.-C. Lee, H. Jung, H. Kim, H. Boo, Chem. Mater., 14 (2002) 2486.

[25] Y. Matsumoto, A. Funatsu, D. Matsuo, U. Unal, K. Ozawa, J. Phys. Chem. B, 105 (2001) 10893.

[26] J. Luo, Q. Chen, X. Dong, Powder Technol., 275 (2015) 284.

[27] J.-H. Choy, H.-C. Lee, H. Jung, S.-J. Hwang, J. Mater. Chem., 11 (2001) 2232.

[28] R. Ma, K. Fukuda, T. Sasaki, M. Osada, Y. Bando, J. Phys. Chem. B, 109 (2005) 6210.

[29] Y. Mao, S. S. Wong, J. Am. Chem. Soc., 128 (2006) 8217.

[30] A. Gajovic', I. Frišcˇic', M. Plodinec, D. Ivekovic, J. Mol. Struct., 924-926 (2009) 183.

[31] M. Milanović, I. Stijepović, L. M. Nikolić, process. Appl. Ceram., 4 (2010) 69.

[32] R. B. Shinde, A. S. Patil, S. V. Sadavar, Y. M. Chitare, V. V. Magdum, N. S. Padalkar, U. M. Patil, S. T. Kochuveedu, V. G. Parale, H. H. Park, C. D. Lokhande, J. L. Gunjakar, Sens. Actuators B Chem., 352 (2022) 131046.

[33] S. V. Sadavar, N. S. Padalkar, R. B. Shinde, S. T. Kochuveedu, U. M. Patil, A. S. Patil, R. N. Bulakhe, C. D. Lokhande, I. In, R. R. Salunkhe, J. L. Gunjakar, J. Power Sources, 524 (2022) 231065.

[34] B. Bharti, S. Kumar, H.-N. Lee, R. Kumar, Sci. Rep., 6 (2016) 32355.

[35] A. Wiatrowski, M. Mazur, A. Obstarczyk, D. Wojcieszak, D. Kaczmarek, J. Morgiel, D. Gibson, Coatings, 8 (2018) 412.

[36] X. Sun, S. Wang, C. Shen, X. Xu, ChemCatChem. 8 (2016) 2289.

[37] A. Karvounis, F. Timpu, V. V. Vogler-Neuling, R. Savo, R. Grange, Adv. Optical Mater., 8 (2020) 2001249.

[38] S. Simeonov, A. Szekeres, M. Covei, H. Stroescu, M. Nicolescu, P. Chesler, C. Hornoiu, M. Gartner, Materials, 17 (2024) 1923.

[39] M. Kotal, A. Sharma, S. Jakhar, V. Mishra, S. Roy, S. C. Sahoo, H. K. Sharma, S. K. Mehta, Cryst. Growth Des., 20 (2020) 4627.

[40] R. Abe, K. Shinohara, A. Tanaka, M. Hara, J. N. Kondo, K. Domen, Journal of Materials Research, 13 (1998) 861.

[41] G. B. Saupe, C. C. Waraksa, H.-N. Kim, Y. J. Han, D. M. Kaschak, D. M. Skinner, T. E. Mallouk, Chem. Mater., 12 (2000) 1556.

[42] R. Ma, Y. Kobayashi, W. J. Youngblood, T. E. Mallouk, J. Mater. Chem., 18 (2008) 5982.

[43] H. Hayashi, Y. Hakuta, Y. Kurata, J. Mater. Chem., 14 (2004) 2046.

[44] K. Maeda, M. Eguchi, W. J. Youngblood, T. E. Mallouk, Chem. Mater., 20 (2008) 6770.

[45] M. A. Bizeto, F. Leroux, A. L. Shiguihara, M. L. A. Temperini, O. Sala, V. R. L. Constantino, J. Phys. Chem. Solids, 71 (2010) 560.

[46] B. N. Nunes, C. Haisch, A. V. Emeline, D. W. Bahnemann, A.O.T. Patrocinio, Catal. Today, 326 (2019) 60.

[47] R. Chroma, M. Vilkova, I. Shepa, P. Makos-Chełstowska, V. Andruch, J. Mol. Liq., 330 (2021) 115617.

[47] E. A. Skryleva, I. V. Kubasov, P. V. Kiryukhantsev-Korneev, B. R. Senatulin, R. N. Zhukov, K. V. Zakutailov, M. D. Malinkovich, Y. N. Parkhomenko, Appl. Surf. Sci., 389 (2016) 387.

[49] Y. Li, G. Chen, H. Zhang, Z. Lv, Int. J. Hydrog. Energy, 35 (2010) 2652.

[50] Y. I. Kim, S. J. Atherton, E. S. Brigham, T. E. Mallouk, J. Phys. Chem., 97 (1993) 11802.

5.1 Introduction

Harmful side effects of water pollution on humans and aquatic life have emerged as a global issue **[1-2]**. The reasons, side effects and significant influence of industrial dyes on water pollution are discussed in detail in **Chapter 1, section 1.1**. Various nanostructured photocatalyst materials can effectively degrade dye molecules without creating secondary pollution to tackle water pollution due to industrial dyes. Various wide bandgap semiconducting materials (TiO_2, ZnO, Nb_2O_5) are explored as UV-active photocatalysts with excellent photostability and a suitable electronic band structure for oxidizing oxide and reducing protons. However, due to their wide bandgap, they are active only in the UV region of the electromagnetic spectrum (absorbs only 4 % of the solar spectrum) and display limited efficiency **[3]**. Therefore, hybridizing wide bandgap semiconducting materials with visible-light-active narrow bandgap photocatalysts can effectively absorb the maximum solar spectrum and depress electron-hole recombination to enhance photocatalytic performance **[4]**.

MoS_2 has been considered an effective photocatalyst due to its narrow bandgap, unique layered structure, and exfoliable nature, which result in higher photocatalytic performance **[5-6]**. The beneficial photocatalytic properties of MoS_2 are discussed in **Chapter 3, section 3.1**. As described in **Chapter 4, section 4.1**, considering the expanded surface area, ultrathin thickness, wide band gap, electrostatic surface charge, macromolecular nature and electronic structure of titanate-NS, the titanate-NS are reflected as the best choice for the hybridization with narrow band gap MoS_2 photocatalysts. The resultant hybrid can effectively absorb a wide solar spectrum. Such hybridization can result in intimate electronic coupling, which leads to enhanced photocatalytic activity via decreased electron-hole recombination **[7-8]**. Also, hybridizing titanate-NS with MoS_2 can improve photostability for long-term use of photocatalysts. The 2D titanate-NS benefits over 3D TiO_2 due to its unique 2D structure, negative surface charge, high chemical stability, high thermal stability and increased surface area [**9, 10**]. Various deposition methods, such as EPD, LbL, and LB, have been employed for the deposition of exfoliated titanate-NS **[4, 11-12]**. The dip-coating method for depositing colloidal nanoparticles from colloidal suspension offers advantages such as cost-effectiveness, excellent control over thickness and high uniformity. Thus, the dip-coating method can be advantageous for the deposition of

exfoliated titanate-NS. Moreover, chemical solution methods, such as CBD, hydrothermal, SILAR and electrodeposition, are available for the deposition of nanocrystalline MoS_2. Among them, the SILAR and MCSD methods are unique approaches to depositing the nanocrystalline MoS_2 layer. The advantages of MCSD are described in **Chapter 3, section 3.1**.

In this chapter, MoS_2 thin films are deposited on dip-coated titanate-NS layers using the MCSD method and applied for photocatalytic degradation of RhB and MB dyes. The obtained nanohybrid thin films are named $MoS_2@TiO_2$ hybrid thin films. The physicochemical properties of the $MoS_2@TiO_2$ hybrid thin films are investigated using different characterization techniques.

5.2 Synthesis and Characterization of MoS₂@TiO₂ hybrid thin film

5.2.1 Experimental details

5.2.1.1 Chemicals

The details of chemicals required for the deposition of MoS_2 and titanate-NS are given in **Chapter 3, section 3.2.1.1** and **Chapter 4, section 4.2.1.1**, respectively.

5.2.1.2 Synthesis of MoS₂@TiO₂ hybrid thin films by MCSD

a) Preparation of colloidal titanate-NS suspension:

The synthesis protocol for preparing colloidal titanate-NS suspension is given in **Chapter 4, section 4.2.1.2**.

b) Deposition of titanate-NS thin films:

Details of titanate-NS thin film deposition by dip-coating are given in **Chapter 4, section 4.2.1.3**. To achieve the dip-coated titanate-NS thin films with various thicknesses, 50, 75 and 100 dip cycles were performed, and the obtained dip-coated titanate-NS thin films are named T-1, T-2 and T-3, respectively.

c) Deposition of MoS₂ thin films by MCSD:

The procedure for depositing MoS_2 thin films on glass substrates is given in **Chapter 3, section 3.2.1.2**.

d) Deposition of MoS₂@TiO₂ hybrid thin films:

The visible light active MoS_2 thin film was deposited over dip-coated titanate-NS thin films using the MCSD method. The experimental conditions and parameters for

preparing adsorption and reaction baths for MoS_2 thin film deposition were similar to those discussed in **Chapter 3, section 3.2.1.2**. The deposition of MoS_2 thin film by the MCSD method comprised successive immersion of dip-coated titanate-NS thin films into separately placed adsorption and reaction baths. A single deposition cycle of MCSD was completed by successive immersion of dip-coated titanate-NS into an adsorption bath for 20 seconds and a reaction bath for the next 20 seconds. Such 50 deposition cycles were performed to deposit MoS_2 on dip-coated titanate-NS thin film. After the deposition, the $MoS_2@TiO_2$ hybrid thin films were washed with DDW and dried in air. Subsequently, the hybrid films were annealed in an H_2 atmosphere at 400°C for 2 hours for better crystallinity. The schematic representation of $MoS_2@TiO_2$ hybrid thin film deposition using the MCSD method is shown in **Fig. 5.1**. The $MoS_2@TiO_2$ hybrid thin films deposited on T-1, T-2 and T-3 thin films are denoted as $MoS_2@TiO_2$-1, $MoS_2@TiO_2$-2 and $MoS_2@TiO_2$-3 hybrid thin films, respectively.
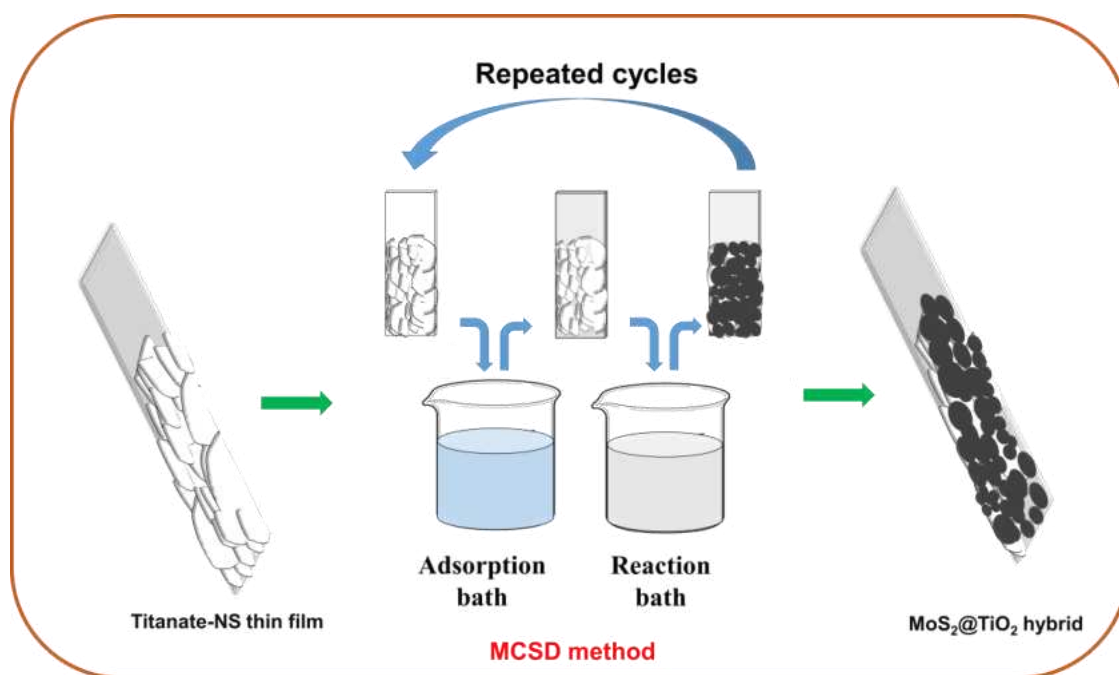
Figure 5.1: Schematic representation of the synthesis process of $MoS_2@TiO_2$ hybrid thin films.

5.2.1.3 Material characterization

The $MoS_2@TiO_2$ hybrid thin films were characterized by various physicochemical characterization techniques, as described in **Chapter 3, section 3.2.1.3.**

5.2.2 Results and Discussion

5.2.2.1 XRD study
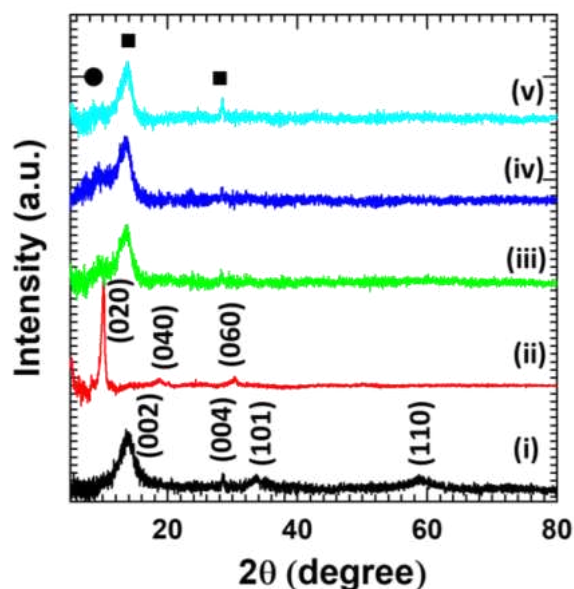
Figure 5.2: XRD patterns of i) MoS$_2$, ii) Titanate-NS, iii) MoS$_2$@TiO$_2$-1, iv) MoS$_2$@TiO$_2$-2 and v) MoS$_2$@TiO$_2$-3 hybrid thin films (The circle and square symbols represent the peaks from titanate-NS and MoS$_2$, respectively).

The structural study of MoS$_2$@TiO$_2$ hybrid thin films was examined by the XRD technique, as shown in **Fig. 5.2**. For comparison, the XRD patterns of pristine MoS$_2$ (**Chapter 3, section 3.2.2.1**) and dip-coated titanate-NS (**Chapter 4, section 4.2.2.1**) thin films are also plotted in **Fig. 5.2**. The pristine MoS$_2$ exhibits typical Braggs reflection indexed as (002), (004), (101) and (110) which confirms the formation of layered 2H-MoS$_2$ [**13-14**]. The pristine dip-coated titanate-NS thin film exhibits Braggs reflections corresponding to (020), (040) and (060) planes, indicating the deposition of layered titanate-NS thin film with lepidocrocite structure [**7, 15**]. The estimated basal spacing from the (020) Braggs reflection for titanate-NS is 0.88 nm. The detailed XRD analysis of MCSD deposited MoS$_2$ and dip-coated titanate-NS thin films are discussed in **Chapter 3, section 3.2.2.1** and **Chapter 4, section 4.2.2.1**, respectively.

Interestingly, the XRD patterns of MoS$_2$@TiO$_2$ hybrid thin film display several Bragg reflections corresponding to both titanate-NS (denoted by circles) and MoS$_2$ (denoted by squares). The low-intensity broad signature peak at 10° in MoS$_2$@TiO$_2$ hybrid thin film originated due to (020) Braggs reflection of the dip-coated inner layer

titanate-NS thin films [**16**]. On the other hand, diffraction peaks centered at 14° and 28° in MoS$_2$@TiO$_2$ hybrid thin film corresponding to the (002) and (004) planes of hexagonal layered MoS$_2$ (2H-MoS$_2$) (JCPDS card number: 37-1492) [**13-14**]. The presence of characteristic Bragg reflections corresponding to titanate-NS and MoS$_2$ in MoS$_2$@TiO$_2$ hybrid thin film confirms the deposition of layered MoS$_2$ over dip-coated titanate-NS thin films. The presence of these peaks reveals the structural intactness and mechanical stability of titanate-NS during the hybrid thin film deposition.

5.2.2.2 Raman study
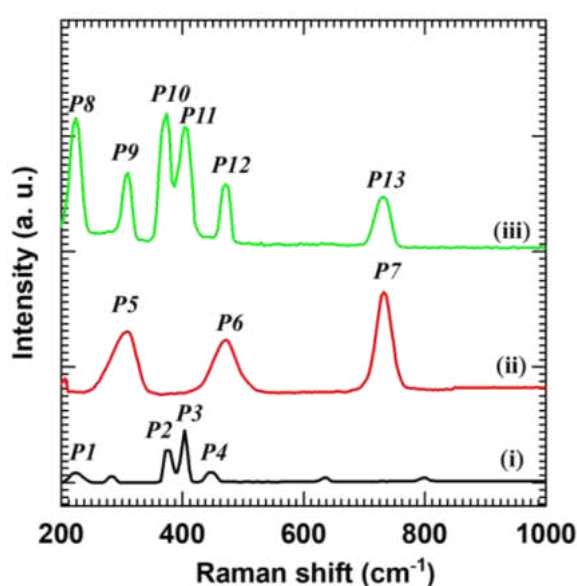
Figure 5.3: Raman spectra of i) MoS$_2$, ii) titanate-NS and iii) MoS$_2$@TiO$_2$ hybrid thin film.

The nature of chemical bonding and microscopic structural features of MoS$_2$@TiO$_2$ hybrid thin film were studied using Raman spectroscopy, as shown in **Fig. 5.3**. For comparison, the Raman spectra of pristine MoS$_2$ (**Chapter 3, section 3.2.2.2**) and dip-coated titanate-NS (**Chapter 4, section 4.2.2.2**) thin films are also plotted in **Fig. 5.3**. The pristine MoS$_2$ thin film shows characteristic Raman peaks P1 (230 cm^{-1}), P2 (384 cm^{-1}), P3 (407 cm^{-1}) and P4 (444 cm^{-1}) corresponding to longitudinal acoustic (LA(M)), in-plane (E$^1_{2g}$), out-of-plane (A$_{1g}$) vibrational and first-order optical phonon (A$_{2u}$) modes of MoS$_2$, respectively [**17**]. The origin of these peaks indicates the deposition of layered 2H-MoS$_2$ [**18-19**]. On the other hand, the titanate-NS thin film exhibits several Raman peaks denoted by P5 (291 cm^{-1}) and P6 (450 cm^{-1}) assigned to

the degenerate modes of the TiO_6 octahedron with Ag symmetry [20]. The sharp and intense Raman peak P7 (710 cm^{-1}) is attributed to the totally symmetric Ti-O vibrations [21-22]. These characteristic Raman peaks confirm the layer-by-layer deposition of well-developed titanate-NS thin film. The detailed Raman spectroscopic analysis of MoS_2 and titanate-NS thin film is described in **Chapter 3, Section 3.2.2.2** and **Chapter 4, section 4.2.2.2,** respectively.

Moreover, the $MoS_2@TiO_2$ hybrid thin film displays the characteristic Raman peaks corresponding to titanate-NS (P9, P12 and P13) and MoS_2 (P8, P10 and P11) layers. The characteristic Raman peaks P8 (230 cm^{-1}), P10 (385 cm^{-1}) and P11 (410 cm^{-1}) are ascribed to the longitudinal acoustic (LA(M)), in-plane (E^1_{2g}) and out-of-plane (A_{1g}) vibrational phonon modes of MoS_2, respectively in the deposited MoS_2 layer. The Raman peaks P9 (291 cm^{-1}) and P12 (450 cm^{-1}) correspond to the degenerate modes of the TiO_6 octahedron with Ag symmetry. The peak P13 (710 cm^{-1}) corresponds to the totally symmetric Ti-O vibrations. The observed Raman features provide strong evidence of the deposition of layered 2H-MoS_2 over dip-coated titanate-NS thin films.

5.2.2.3 FTIR study
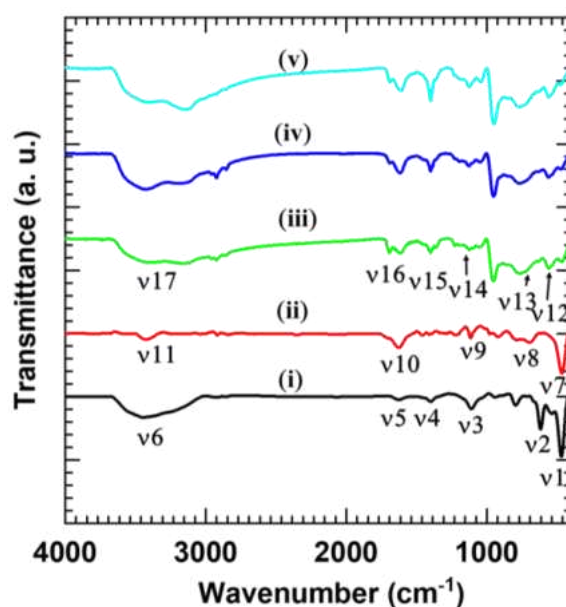
Figure 5.4: FTIR spectra of i) MoS_2, ii) Titanate-NS, iii) $MoS_2@TiO_2$-1, iv) $MoS_2@TiO_2$-2 and v) $MoS_2@TiO_2$-3 hybrid thin films.

The chemical bonding nature of $MoS_2@TiO_2$ hybrid thin films was probed with FTIR spectroscopy. For comparison, the FTIR spectra of pristine MoS_2 (**Chapter 3,**

section 3.2.2.3) and dip-coated titanate-NS (**Chapter 4, section 4.2.2.3**) thin films are also plotted in **Fig. 5.4**. As shown in **Fig. 5.4**, FTIR spectra of pristine MoS₂ show absorption bands ν1 (469 cm⁻¹) and ν2 (617 cm⁻¹) corresponding to the stretching vibrations of Mo-S bonding [**23**]. The bands ν3 (1115 cm⁻¹) and ν4 (1411 cm⁻¹) are attributed to the sulfur-related stretching vibration of S-Mo-S [**24**]. The bands ν5 (1632 cm⁻¹) and ν6 (3436 cm⁻¹) are assigned to the vibrations of adsorbed water molecules [**25**]. Pristine titanate-NS also demonstrates absorption bands ν7 (474 cm⁻¹) and ν8 (697 cm⁻¹) corresponding to tetrahedrally and octahedrally coordinated Ti-O bonds. The band ν9 (1118 cm⁻¹) originated due to N-H stretching vibration in adsorbed TBA [**26**]. The bands ν10 (1632 cm⁻¹) and ν11 (3436 cm⁻¹) are assigned to the bending vibrational modes of water molecules and stretching vibrations of the O-H groups, respectively [**25**]. The detailed FTIR analysis of MoS₂ and titanate-NS thin film is described in **Chapter 3, Section 3.2.2.3** and **Chapter 4, section 4.2.2.3,** respectively. Moreover, all the MoS₂@TiO₂ hybrid thin films commonly display several absorption bands associated with pristine MoS₂ and titanate-NS (ν12-ν17). The absorption band ν12 (617 cm⁻¹) is ascribed to the Mo-S stretching vibration. The absorption bands ν14 (1115 cm⁻¹) and ν15 (1411 cm⁻¹) are related to S-Mo-S stretching vibrations [**23-24**]. Moreover, absorption band ν13 (696 cm⁻¹) is ascribed to octahedrally coordinated Ti-O bonds [**26**]. The absorption bands ν16 (1632 cm⁻¹) and ν17 (3436 cm⁻¹) are linked with the bending vibrations of water molecules and stretching vibrations of hydroxyl groups, respectively. The characteristic IR features related to both MoS₂ and titanate-NS indicate the formation of the MoS₂@TiO₂ hybrid thin film using the MCSD method.

5.2.2.4 FE-SEM study

The microstructural surface features and stacking patterns of MoS₂@TiO₂-2 hybrid thin film were investigated by FE-SEM analysis, as shown in **Fig. 5.5**. The surface microscopic analysis of pristine MoS₂ and titanate-NS thin films is described in **Chapter 3, section 3.2.2.4** and **Chapter 4, section 4.2.2.4**, respectively. As described in **Chapter 3, section 3.2.2.4**, the pristine MoS₂ thin film shows the nanoclusters composed of spherical MoS₂ nanoparticles with particle sizes ranging from 40 to 60 nm. As described in **Chapter 4, section 4.2.2.4**, the dip-coated titanate-NS thin film displays nanosheets lying parallel to the substrate surface, with the entire substrate surface covered with titanate-NS, showing high deposition uniformity.

On the other hand, $MoS_2@TiO_2$-2 hybrid thin film shows clusters of spherical MoS_2 nanoparticles anchored on parallelly stacked titanate-NS. The MoS_2 nanoparticles are interconnected, creating a highly porous cluster architecture morphology. The cross-section of $MoS_2@TiO_2$-2 hybrid thin film shows an increased thickness of 0.81 µm after hybridization with titanate-NS. The formation of interconnected spherical MoS_2 nanoparticle clusters gives rise to a high surface area architecture, which enables expanded surface area with an open framework. A similar type of morphology is generally observed for 2D nanosheet-based heterostructures, which is advantageous for various catalytic applications [**7-8, 27**].
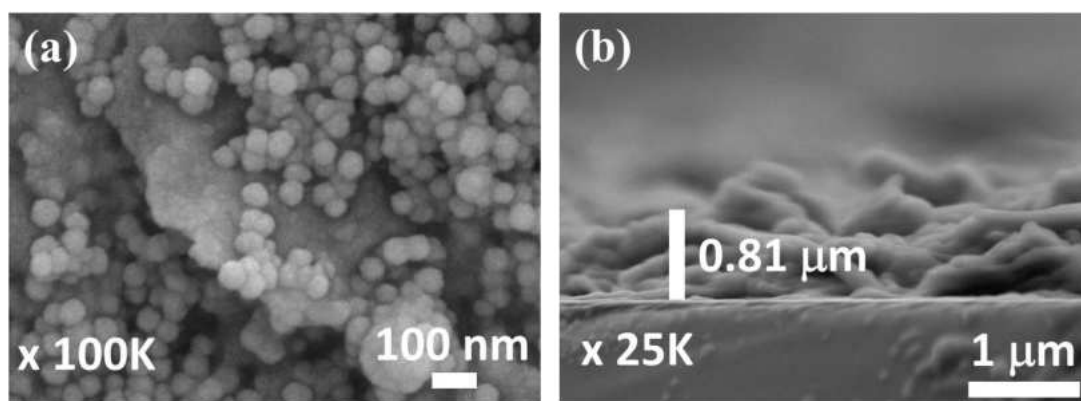
Figure 5.5: (a) Top view and (b) cross-section FE-SEM images of $MoS_2@TiO_2$-2 hybrid thin film.

The presence of constituent elements in $MoS_2@TiO_2$-2 hybrid thin film was investigated using EDS elemental mapping analysis. As shown in **Fig. 5.6** and **Fig. 5.7**, Ti, O, Mo and S elements are uniformly distributed over the entire mapping area, confirming the uniform deposition of MoS_2 on the surface of titanate-NS thin film using the MCSD method without any phase separation.
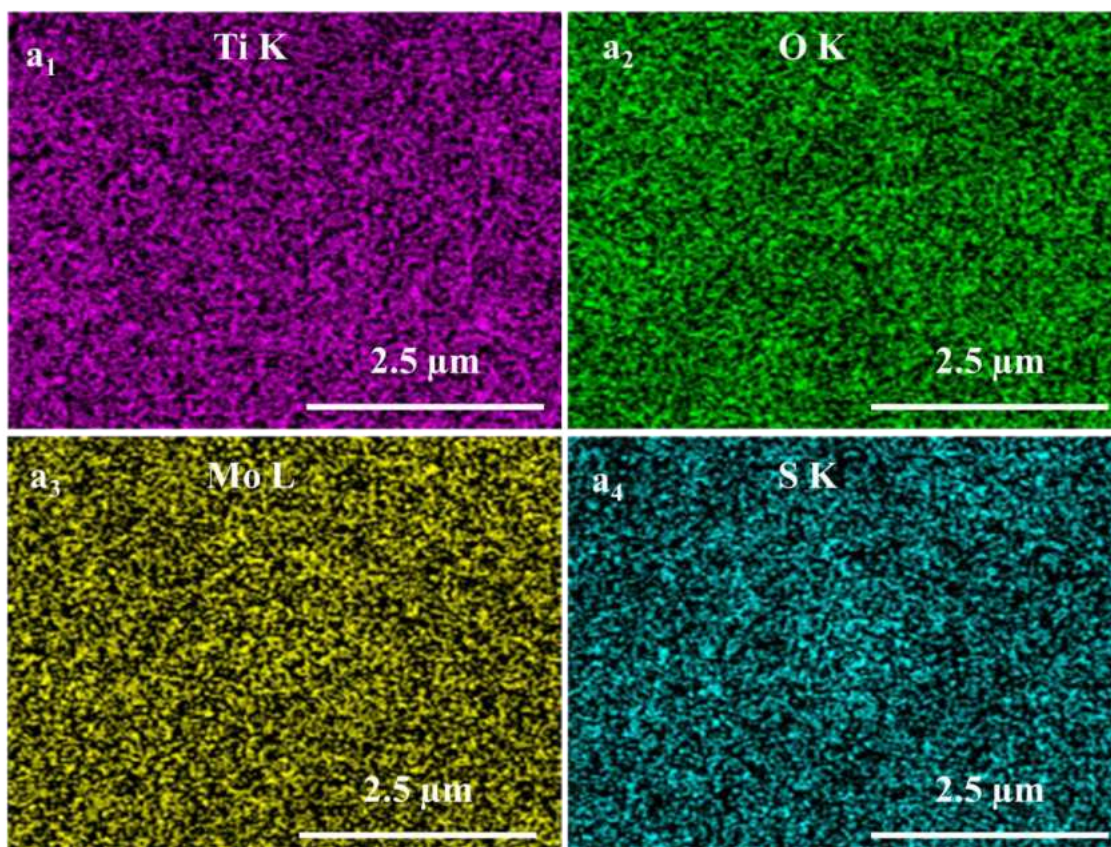
Figure 5.6: EDS elemental mapping of MoS$_2$@TiO$_2$ hybrid thin film.
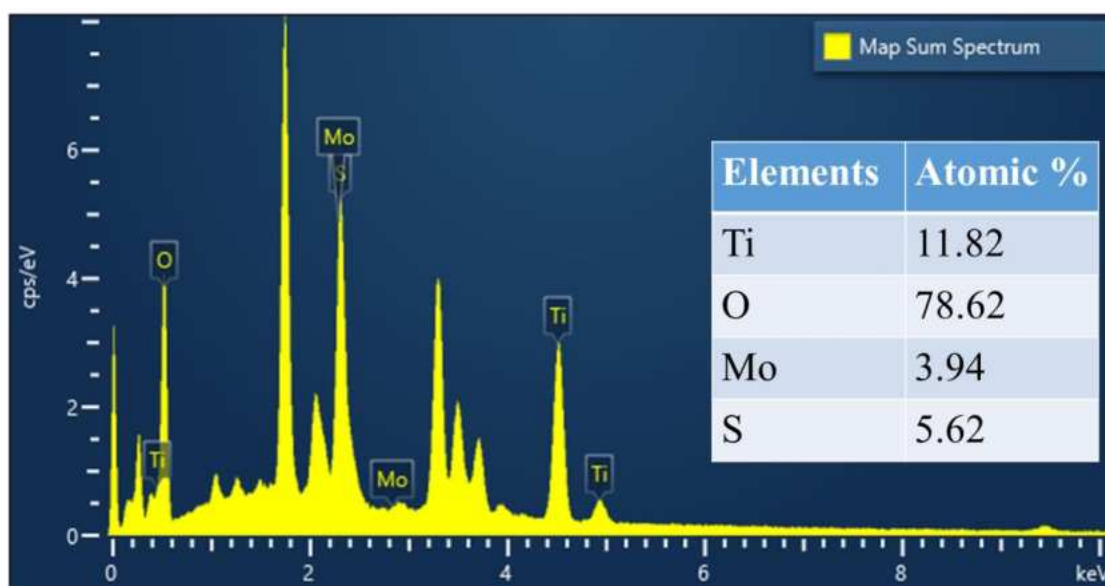
Figure 5.7: EDS spectrum of MoS$_2$@TiO$_2$ hybrid thin film.

5.2.2.5 XPS study

The presence of elements and their oxidation states in the MoS_2@TiO_2-2 hybrid thin film was determined by XPS analysis as shown in **Fig. 5.8**. For comparison, the XPS survey spectra of pristine MoS_2 (**Chapter 3, section 3.2.2.5**) and dip-coated titanate-NS (**Chapter 4, section 4.2.2.5**) thin films are also plotted in **Fig. 5.8**. The survey XPS spectra of pristine MoS_2, titanate-NS thin film and MoS_2@TiO_2-2 hybrid thin films exhibit characteristic XPS features at BE of Mo, S, Ti and O elements, representing the presence of stated elements in above thin films.
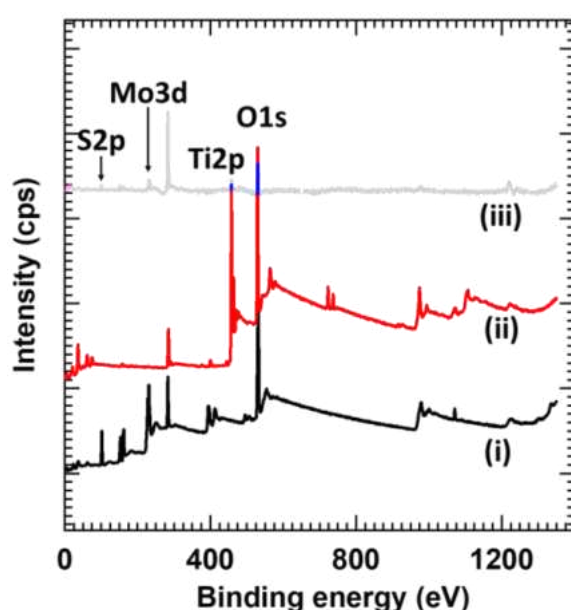
Figure 5.8: XPS survey spectra of (i) MoS_2, (ii) titanate-NS and (iii) MoS_2@TiO_2-2 hybrid thin film.

The high-resolution Mo 3d, S 2p, Ti 2p, and O 1s core-level XPS spectra are plotted in **Fig. 5.9 (a-d)**, respectively. The core-level XPS spectra of Mo 3d and S 2p are discussed in **Chapter 3, section 3.2.2.5**. As shown in **Fig. 5.9a**, the high-resolution Mo 3d spectra of MoS_2 and MoS_2@TiO_2-2 hybrid thin films commonly display two spectral features, A (229.5 eV) and B (232.7 eV) corresponding to the spin-orbit splitting of Mo $3d_{5/2}$ and Mo $3d_{3/2}$, respectively. The BE difference of 3.2 eV indicates the presence of Mo^{4+} in both films [**28**]. As displayed in **Fig. 5.9b**, the high-resolution S 2p spectra of MoS_2 and MoS_2@TiO_2-2 hybrid thin films show a broad peak C (162 eV), corresponding to the spin-orbit splitting of S^{2-} [**29**]. The core-level XPS spectra of Ti 2p and O 1s are discussed in **Chapter 4, section 4.2.2.5.** As shown in **Fig. 5.9c**, the high-

resolution Ti 2p spectra of titanate-NS thin film and MoS_2@TiO_2-2 hybrid thin films show two peaks, D (458 eV) and E (463.7 eV), which are ascribed to spin-orbit splitting of Ti $2p_{3/2}$ and Ti $2p_{1/2}$, respectively. The BE difference of 5.7 eV indicates the presence of Ti in the +4 state [24]. As displayed in **Fig. 5.9d**, the high-resolution O 1s spectra of titanate-NS and MoS_2@TiO_2-2 hybrid thin films show a single broad peak F (529.5 eV), showing the presence of oxygen from metal oxide. The O 1s spectra broadened after hybridization due to the surface hydroxyl group or adsorbed water [30]. The XPS analysis evidences the presence of Mo^{4+} and Ti^{4+} states of Mo and Ti, respectively, which confirms the formation of the MoS_2@TiO_2 hybrid thin film.
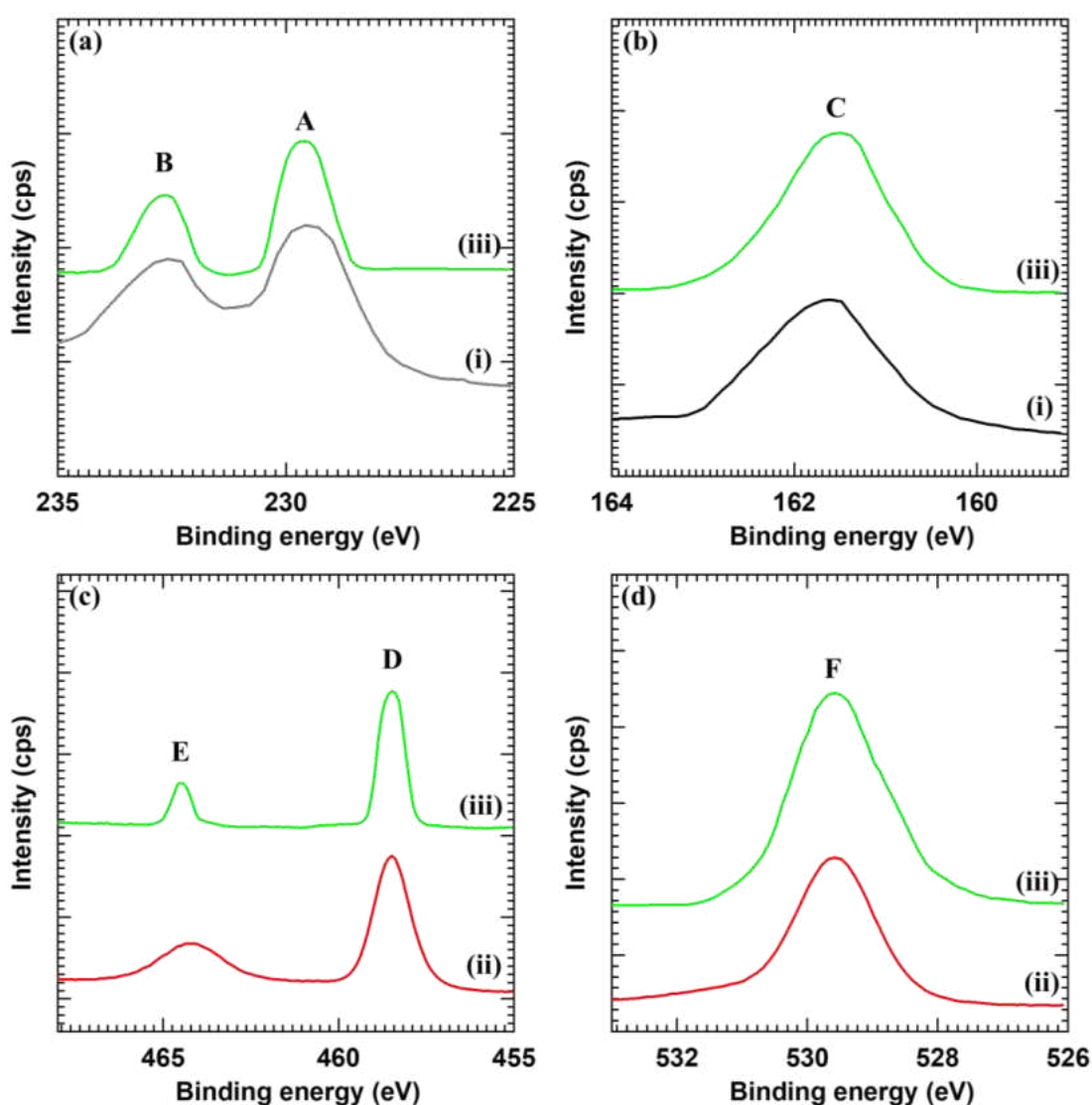
Figure 5.9: a) Mo 3d b) S 2p, c) Ti 2p and d) O 1s core-level XPS spectra of i) pristine MoS_2, ii) titanate-NS and iii) MoS_2@TiO_2-2 hybrid thin films.

5.2.2.6 UV-Vis DRS study and band positions determination
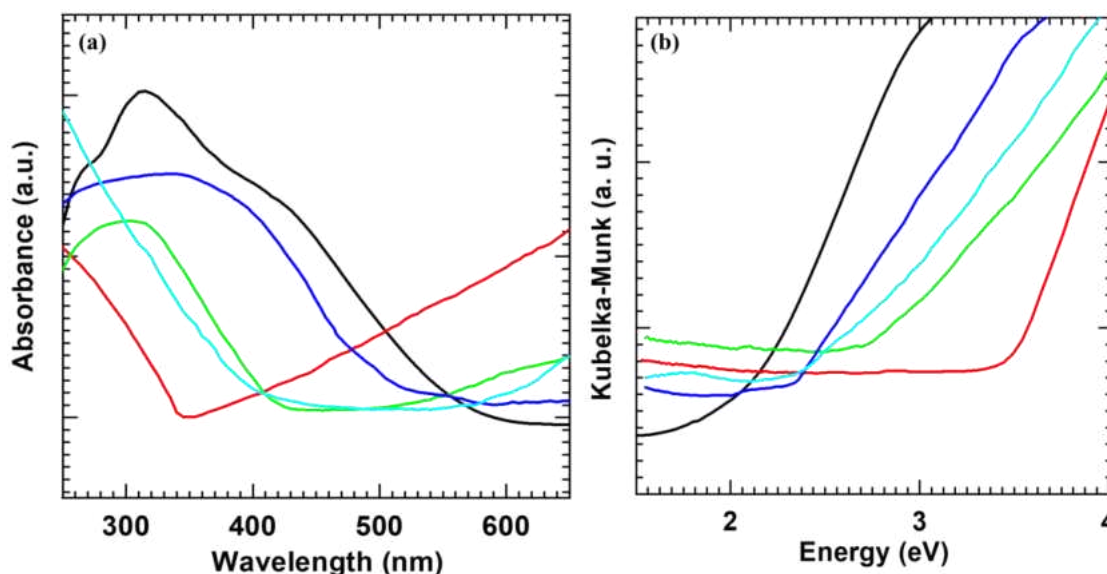
Figure 5.10: a) UV-Vis DRS absorbance spectra and b) Diffuse reflectance UV–Vis spectra (plotted as the Kubelka–Munk function of the reflectance, R) of (i) MoS$_2$ (black), (ii) titanate-NS (red), (iii) MoS$_2$@TiO$_2$-1 (green), (iv) MoS$_2$@TiO$_2$-2 (blue) and (v) MoS$_2$@TiO$_2$-3 (cyan) hybrid thin films.

The band structure and optical properties of MoS$_2$@TiO$_2$ hybrid thin films were studied using the UV-Vis DRS technique. For comparison, the UV-Vis DRS absorbance spectrum of pristine MoS$_2$ (**Chapter 3, section 3.2.2.6**) and dip-coated titanate-NS (**Chapter 4, section 4.2.2.6**) thin films are also plotted in **Fig. 5.10a**. As plotted in **Fig. 5.10a**, pristine MoS$_2$ shows significant absorption in the visible region with an optical band gap of 1.6 eV. MoS$_2$ is an indirect band gap material with an electronic structure comprising a VB and CB mainly composed of Mo 4d and S 3p orbitals, respectively [**31-32**]. On the other hand, titanate-NS thin film shows strong absorption in the UV region with no absorption in the visible region due to its wide band gap (3.34 eV). The electronic structure of titanate-NS comprises a VB and CB mainly composed of O 2p and Ti 3d orbitals, respectively [**33**]. The detailed analysis of UV-Vis DRS spectra of pristine MoS$_2$ and titanate-NS thin films are discussed in **Chapter 3, section 3.2.2.6** and **Chapter 4, section 4.2.2.6**, respectively.

Interestingly, MoS$_2$@TiO$_2$ hybrid thin films show considerable absorption in the visible region, indicating effective electronic coupling between wide band gap titanate-NS and narrow band gap MoS$_2$ thin films. The variation of dip cycles of titanate-NS thin film results in the variation of absorbance and band gap of MoS$_2$@TiO$_2$ hybrid thin

films. The MoS$_2$@TiO$_2$ hybrid thin films absorb visible light in the 540-590 nm wavelength range, corresponding to band gap energies between 2.1-2.3 eV. Increased composition of wide band gap titanate-NS in MoS$_2$@TiO$_2$-1 to MoS$_2$@TiO$_2$-3 is responsible for the increased band gap. The band gap energies determined from the Kubelka-Munk function are shown in **Fig. 5.10b** and noted in **Table 5.1**. The increased visible light absorption capacity illustrates the application of MoS$_2$@TiO$_2$ hybrid thin films for visible-light-driven photocatalytic applications.

Table 5.1: Band gap energies of MoS$_2$, titanate-NS and MoS$_2$@TiO$_2$ hybrid thin films.

Thin film	Band gap (eV)
MoS$_2$	1.6
Titanate-NS	3.34
MoS$_2$@TiO$_2$-1	2.1
MoS$_2$@TiO$_2$-2	2.18
MoS$_2$@TiO$_2$-3	2.3

The band position of MoS$_2$ and titanate-NS thin films were estimated using an empirical formula, as described in **Chapter 3, section 3.2.2.6** and **Chapter 4, section 4.2.2.6**, respectively. The estimated VB and CB positions for MoS$_2$ are 0.015 and -1.60 eV, respectively, whereas those for titanate-NS are 2.23 and -1.11 eV, respectively, as shown in **Fig. 5.11**.
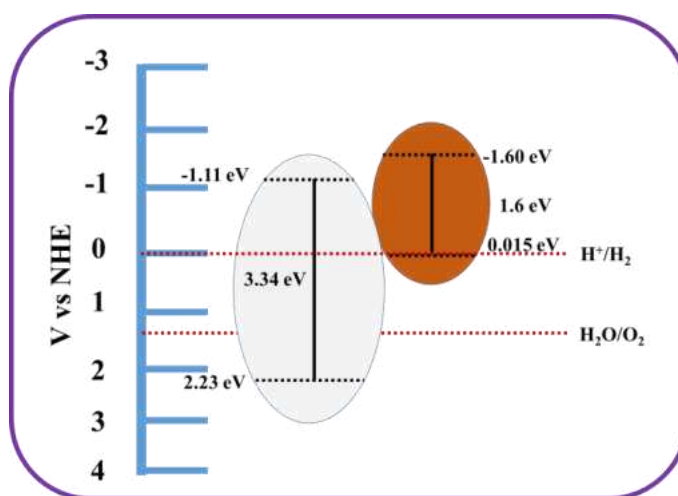
Figure 5.11: Band positions of MoS$_2$@TiO$_2$ hybrid thin films vs NHE.

5.3 Dye Degradation Studies

5.3.1 Results and Discussion
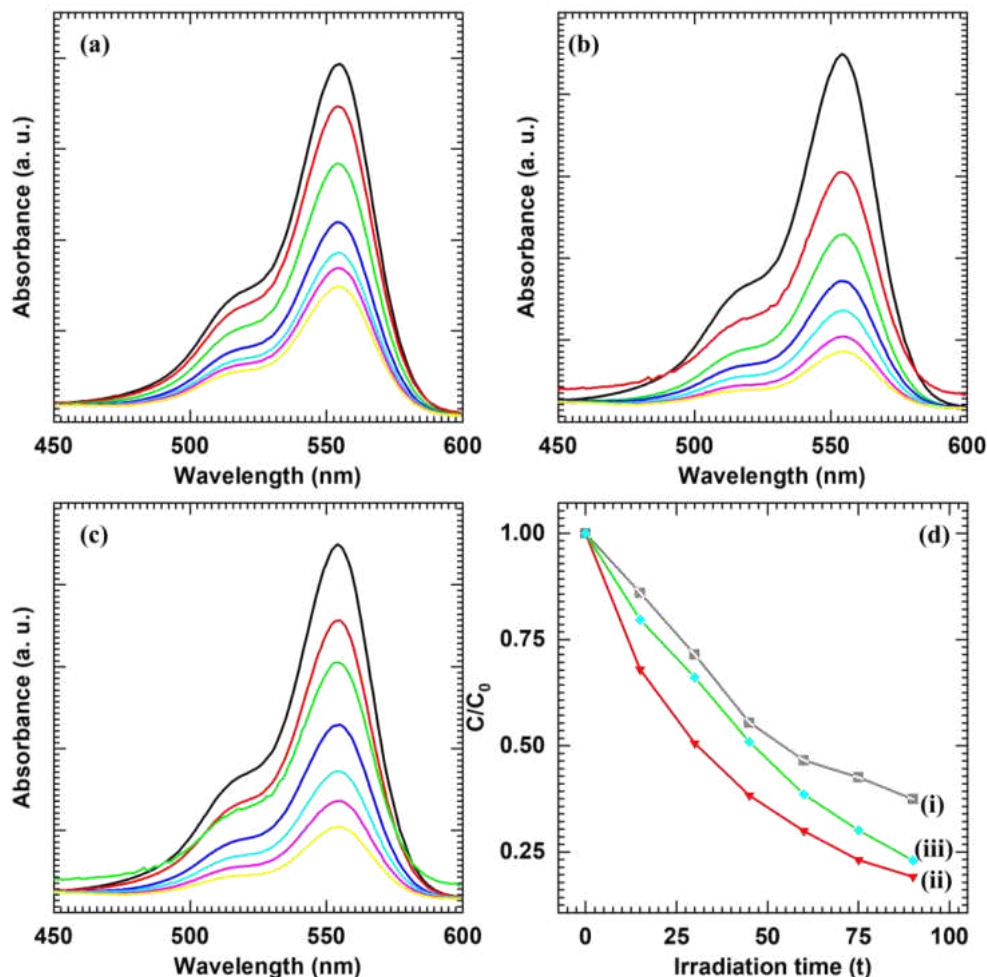
Figure 5.12: UV-Vis absorption spectra of RhB in the presence of (a) MoS$_2$@TiO$_2$-1, (b) MoS$_2$@TiO$_2$-2, (c) MoS$_2$@TiO$_2$-3 hybrid thin films under visible-light irradiation and (d) variation of RhB concentration as a function of irradiation time for (i) MoS$_2$@TiO$_2$-1, (ii) MoS$_2$@TiO$_2$-2 and (iii) MoS$_2$@TiO$_2$-3 hybrid thin films.

The photocatalytic degradation performance of MoS$_2$@TiO$_2$ hybrid thin films was assessed by observing the time-dependent UV-Vis absorption spectra of RhB under visible-light illumination in the presence of photocatalysts. The results were compared with those of pristine MoS$_2$ and titanate-NS thin film. **Fig. 5.12 (a-c)** displays time-dependent UV-Vis absorption spectra of RhB dye in the presence of MoS$_2$@TiO$_2$-1, MoS$_2$@TiO$_2$-2 and MoS$_2$@TiO$_2$-3 hybrid photocatalyst under visible-light illumination, respectively. The UV-Vis absorption spectra of RhB in the presence of MoS$_2$ and

titanate-NS thin-film photocatalysts are shown in **Chapter 3, section 3.3.2** and **Chapter 4, section 4.3.1**, respectively. The pristine MoS$_2$ displays superior visible-light photocatalytic activity for photodegradation due to its narrow band gap (1.6 eV), whereas titanate-NS does not show visible light activity due to its wide band gap (3.34 eV). On the other hand, the photocatalytic activity of MoS$_2$ remarkably improved upon hybridization with titanate-NS. The decrease in intensity at the characteristic wavelength of 554 nm with respect to irradiation time indicates the degradation of RhB. **Fig. 5.12d** shows the variation of RhB concentration as a function of irradiation time for MoS$_2$@TiO$_2$-1, MoS$_2$@TiO$_2$-2 and MoS$_2$@TiO$_2$-3 hybrids. The photocatalytic degradation performance of pristine MoS$_2$ and titanate-NS are represented in **Chapter 3, section 3.3.2** and **Chapter 4, section 4.3.1**, respectively. Among MoS$_2$@TiO$_2$ hybrid thin films deposited at various titanate-NS thicknesses, the MoS$_2$@TiO$_2$-2 displays maximum photocatalytic RhB degradation of 81 % in 90 minutes, which shows 1.2-fold increased photocatalytic degradation performance to that of pristine MoS$_2$.

Similarly, the photocatalytic degradation performance of MoS$_2$@TiO$_2$ hybrid thin films was assessed by observing the time-dependent UV-Vis absorption spectra of MB under visible-light illumination in the presence of photocatalysts. The results were compared with those of pristine MoS$_2$ and titanate-NS thin film. **Fig. 5.13 (a-c)** displays time-dependent UV-Vis absorption spectra of MB dye in the presence of MoS$_2$@TiO$_2$-1, MoS$_2$@TiO$_2$-2 and MoS$_2$@TiO$_2$-3 hybrid photocatalyst under visible-light illumination, respectively. The UV-Vis absorption spectra of MB in the presence of MoS$_2$ and titanate-NS thin film are shown in **Chapter 3, section 3.3.2** and **Chapter 4, section 4.3.1**, respectively. The pristine MoS$_2$ displays superior visible-light photocatalytic activity for photodegradation due to its narrow band gap (1.6 eV), whereas titanate-NS does not show visible-light activity due to its wide band gap (3.34 eV). On the other hand, the photocatalytic activity of MoS$_2$ remarkably improved upon hybridization with titanate-NS. The decrease in intensity at the characteristic wavelength of 665 nm with respect to irradiation time indicates the degradation of MB. **Fig. 5.13d** shows the variation of MB concentration as a function of irradiation time for MoS$_2$@TiO$_2$-1, MoS$_2$@TiO$_2$-2 and MoS$_2$@TiO$_2$-3 hybrids. The photocatalytic degradation performance of pristine MoS$_2$ and titanate-NS are represented in **Chapter 3, section 3.3.2** and **Chapter 4, section 4.3.1**, respectively. Among MoS$_2$@TiO$_2$ hybrid

thin films deposited at various titanate-NS thicknesses, the MoS$_2$@TiO$_2$-2 displays maximum photocatalytic MB degradation of 79 % in 90 minutes which shows 1.15-fold increased photocatalytic degradation performance to that of pristine MoS$_2$.

The remarkably enhanced performance of present nanohybrids is attributed to the strong visible light harvesting ability, high surface area morphology, and reduced electron-hole recombination via strong electronic coupling between hybridized species [34, 35].

Figure 5.13: UV-Vis absorption spectra of MB in the presence of (a) MoS$_2$@TiO$_2$-1, (b) MoS$_2$@TiO$_2$-2, (c) MoS$_2$@TiO$_2$-3 hybrid thin films under visible-light irradiation and (d) variation of MB concentration as a function of irradiation time for (i) MoS$_2$@TiO$_2$-1, (ii) MoS$_2$@TiO$_2$-2 and (iii) MoS$_2$@TiO$_2$-3 hybrid thin films.

5.3.2 Kinetic study
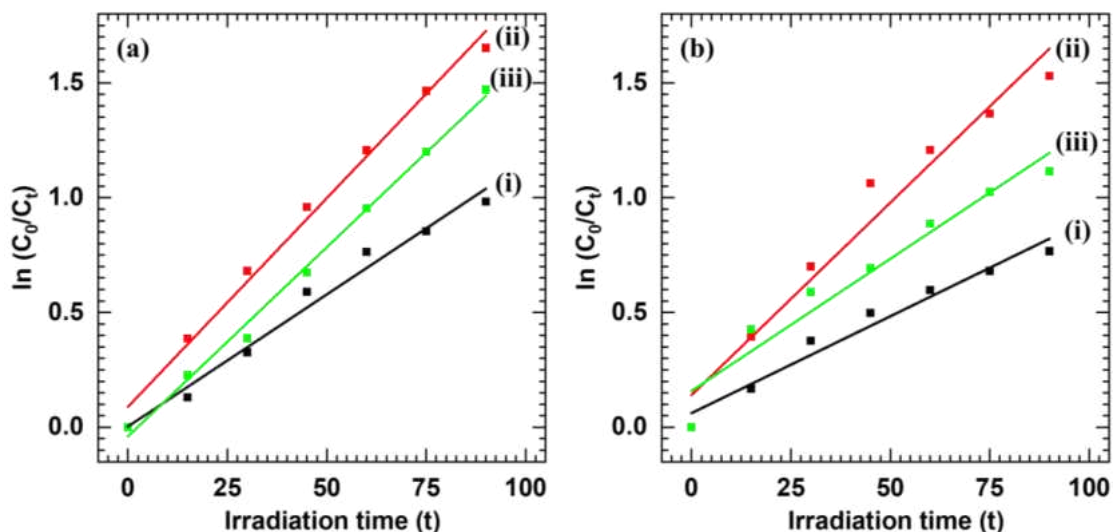
Figure 5.14: Pseudo-first-order kinetics of a) RhB and b) MB dyes using i) MoS₂@TiO₂-1, ii) MoS₂@TiO₂-2 and iii) MoS₂@TiO₂-3 hybrid thin films.

The degradation kinetics of RhB and MB dyes using MoS₂@TiO₂ hybrid thin films were probed by pseudo-first-order rate kinetic model by plotting $ln(C_0/C_t)$ vs irradiation time as shown in **Fig. 5.14 (a-b)**. The rate constant (k) and linear correlation coefficient (R^2) values are given in **Table 5.2**. All the MoS₂ thin films show high k-values, confirming the faster reaction kinetics. The MoS₂@TiO₂-2 hybrid thin film exhibits the highest k value of 0.018 min⁻¹ than that of MoS₂@TiO₂-1 and MoS₂@TiO₂-3 hybrid thin films for RhB. These k values reveal the excellent photocatalytic performance of MoS₂@TiO₂ hybrids. The excellent photocatalytic performance of MoS₂@TiO₂-2 hybrid thin films is attributed to the expanded surface area, strong electronic coupling and high photostability, which provides catalytically active sites for the degradation of target molecules **[36-41]**.

Table 5.2: Photocatalytic dye degradation performance of MoS$_2$@TiO$_2$ hybrid thin films.

Target molecule	Photocatalyst	Degradation (%)	Rate constant k (min^{-1})	Correlation coefficient (R^2)
RhB	MoS$_2$@TiO$_2$-1	63	0.011	0.98
	MoS$_2$@TiO$_2$-2	81	0.018	0.99
	MoS$_2$@TiO$_2$-3	78	0.016	0.99
MB	MoS$_2$@TiO$_2$-1	54	0.008	0.96
	MoS$_2$@TiO$_2$-2	79	0.016	0.96
	MoS$_2$@TiO$_2$-3	68	0.011	0.94

5.3.3 Recycling study
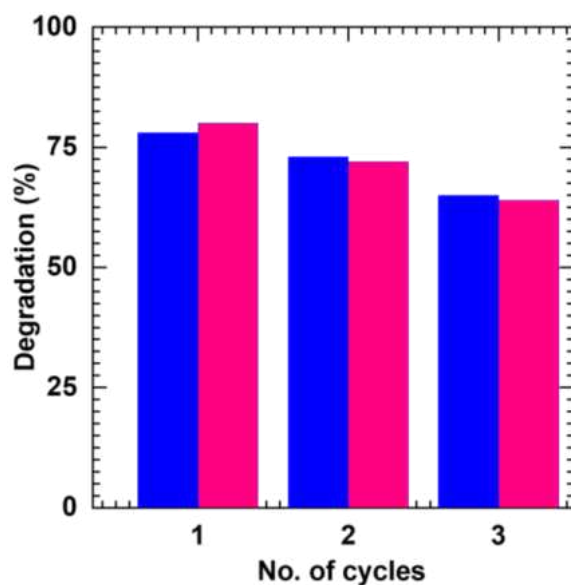
Figure 5.15: Recyclability of optimized MoS$_2$@TiO$_2$-2 hybrid thin films for RhB (pink) and MB (blue) degradation for 3 cycles.

Furthermore, the stability of the optimized MoS$_2$@TiO$_2$-2 hybrid thin films for the degradation of RhB and MB is studied for three consecutive cycles, as shown in **Fig. 5.15**. The present MoS$_2$@TiO$_2$-2 hybrid thin films display good recycling performance by retaining 80 and 83 % of the photocatalytic performance for RhB and MB, respectively. After each cycle, the slight decrement in the photocatalytic performance is attributed to the inactivity of active material due to the adsorption of target molecules on the surface of the photocatalyst **[42]**.

5.3.4 Plausible dye degradation mechanism
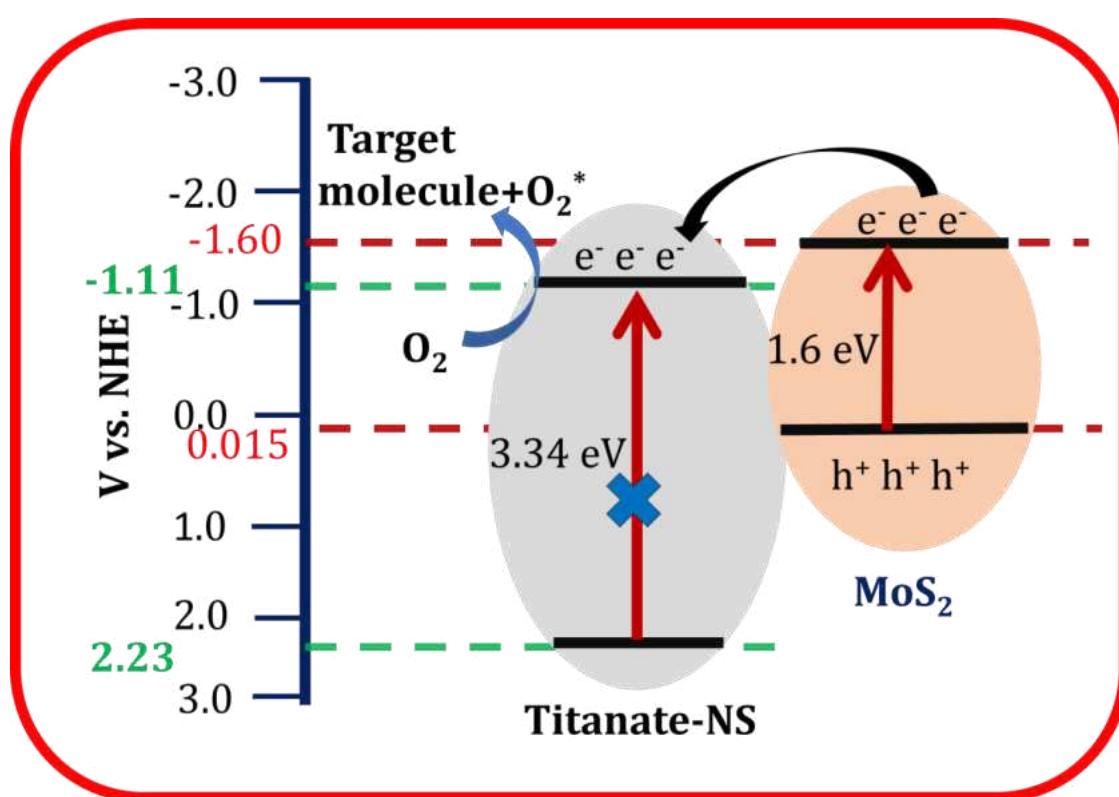
Figure 5.16: Schematic of plausible degradation mechanism of target molecules under visible-light irradiation using MoS$_2$@TiO$_2$ hybrid photocatalyst thin films.

The dye degradation mechanism is explained in **Chapter 3, section 3.3.5**. The schematic representation of the degradation pathway using the MoS$_2$@TiO$_2$ hybrid thin film is shown in **Fig. 5.16**. The CB of MoS$_2$ is more negative than that of titanate-NS and VB of titanate-NS is more positive than that of MoS$_2$ with respect to NHE. Therefore, the photo-excited electrons from the CB of MoS$_2$ can transfer to the CB of the titanate-NS, causing spatial separation of electrons and holes with a reduction in recombination rate. Thus, the lifetime of holes in the VB of MoS$_2$ increases. As the VB

of MoS$_2$ is not positive enough to produce hydroxyl radicals (OH*), holes present in the VB of MoS$_2$ will not participate in the reaction directly. Meanwhile, superoxide radicals (O$_2$*$^-$) are generated when electrons in the CB of titanate-NS react with O$_2$. Further, hydroperoxyl radicals (HOO*) are generated from the protonation of superoxide radicals. Finally, H$_2$O$_2$ dissociates into OH* radicals, which can break the chain of target organic molecules **[43-45]**. The chemical reactions describing plausible dye degradation mechanism are represented in **Chapter 1, section 1.1.7.1 (b)**.

5.4 Conclusion

In this report, MoS$_2$@TiO$_2$ hybrid thin films are synthesized using dip-coating and MCSD methods and employed to degrade dye (RhB and MB) molecules under visible light irradiation. The structural study of MoS$_2$@TiO$_2$ hybrid thin films shows characteristic features of titanate-NS and MoS$_2$, which confirms the direct growth of MoS$_2$ on titanate-NS thin film. MoS$_2$@TiO$_2$ hybrid thin films show MoS$_2$ particles randomly anchored on parallelly ordered titanate-NS thin film, demonstrating intimate contact and strong electronic coupling between the hybridized species. The optimized MoS$_2$@TiO$_2$-2 hybrid thin films exhibit enhanced visible light harvesting capacity with depressed electron-hole recombination rates, signifying effective electronic coupling between titanate-NS and MoS$_2$. The optimized MoS$_2$@TiO$_2$-2 hybrid thin film exhibits photocatalytic degradation performance of 81 % and 79 % for RhB and MB, respectively, within 90 minutes of visible light irradiation. This work demonstrates the usefulness of hybrid formation for obtaining high surface area structures. This study can be used to synthesize various hybrids based on 2D metal oxide-based exfoliated nanosheets. This study may also lead to develop the protocol for aqueous exfoliation of titanate-NS with a reduced time period.

5.5 References

[1] B. S. Rathi, P. S. Kumar, P.-L. Show, J. Hazard. Mater., 409 (2021) 124413.

[2] S. Sharma and A. Bhattacharya, Appl. Water. Sci., 7 (2017) 1043.

[3] V. Etacheri, C. D. Valentin, J. Schneider, D. Bahnemannd, S. C. Pillai, J. Photochem. Photobiol. C: Photochem. Rev., 25 (2015) 1.

[4] S. P. Kulkarni, Y. M. Chitare, V. V. Magdum, P. D. Sawant, S. V. Talekar, S. A. Pawar, D. B. Malavekar, S. Ansar, J. H. Kim, J. L. Gunjakar, ACS Appl. Nano Mater., 7, (2024) 11411.

[5] P. P. Singh, S. Sinha, G. Pandey, V. Srivastava, RSC Adv., 12 (2022) 29826.

[6] L. O. Amaral, A. L. Daniel-da-Silva, Molecules, 27 (2022) 6782.

[7] J. L. Gunjakar, T. W. Kim, H. N. Kim, I. Y. Kim, S.-J. Hwang, J. Am. Chem. Soc., 133 (2011) 14998.

[8] J. L. Gunjakar, I. Y. Kim, J. M. Lee, N.-S. Lee, S.-J. Hwang, Energy Environ. Sci., 6 (2013) 1008.

[9] T. Sasaki, Y. Komatsu, Y. Fujiki, J. Chem. Soc., Chem. Commun., (1991) 817.

[10] T. Sasaki and M. Watanabe, J. Am. Chem. Soc., 120 (1998) 4682.

[11] M. Muramatsu, K. Akatsuka, Y. Ebina, K. Wang, T. Sasaki, T. Ishida, K. Miyake, M.-A. Haga, Langmuir, 21 (2005) 6590.

[12] T. Sasaki, Y. Ebina, M. Watanabe, G. Decher, Chem. Commun., 21 (2000) 2163.

[13] Y. Tan, K. Yu, T. Yang, Q. Zhang, W. Cong, H. Yin, Z. Zhang, Y. Chen, Z. Zhu, J. Mater. Chem. C, 2 (2014) 5422.

[14] X. Sun, J. Dai, Y. Guo, C. Wu, F. Hu, J. Zhao, X. Zeng, Y. Xie, Nanoscale, 6 (2014) 8359.

[15] S. B. Patil, H. J. Kim, H.-K. Lim, S. M. Oh, J. Kim, J. Shin, H. Kim, J. W. Choi, S.-J. Hwang, ACS Energy Lett., 3 (2018) 412.

[16] J.-H. Choy, H.-C. Lee, H. Jung, S.-J. Hwang, J. Mater. Chem., 11 (2001) 2232.

[17] H. Li, Q. Zhang, C. C. R. Yap, B. K. Tay, T. H. T. Edwin, A. Olivier, D. Baillargeat, Adv. Funct. Mater., 22 (2012) 1385.

[18] M. Park, J. S. Choi, L. Yang, H. Lee, Sci. Rep., 9 (2019) 19826.

[19] Y.-H. Lee, L. Yu, H. Wang, W. Fang, X. Ling, Y. Shi, C.-T. Lin, J.-K. Huang, M.-T. Chang, C.-S. Chang, M. Dresselhaus, T. Palacios, L.-J. Li, J. Kong, Nano Lett., 136 (2013) 1852.

[20] W. Hu, L. Li, G. Li, Y. Liu, R. L. Withers, Sci. Rep., 4 (2014) 6582.

[21] Y. Mao, M. Kanungo, T. Hemraj-Benny, S. S. Wong, J. Phys. Chem. B, 110 (2006) 702.

[22] A. Kudo and T. Kondo, J. Mater. Chem., 7 (1997) 777.

[23] S. Patil, A. Harle, S. Sathaye, K. Patil, CrystEngComm., 16 (2014) 10845.

[24] S. V. Kite, A. N. Kadam, D. J. Sathe, S. Patil, S. S. Mali, C. K. Hong, S.-W. Lee, K. M. Garadkar, ACS Omega, 6 (2021) 17071.

[25] G. A. M. Ali, M. R. Thalji, W. C. Soh, H. Algarni, K. F. Chong, J. Solid State Electrochem., 24 (2020) 25.

[26] M. Milanović, I. Stijepović, L. M. Nikolić, Appl. Ceram., 4 (2010) 69.

[27] J. L. Gunjakar, T. W. Kim, I. Y. Kim, J. M. Lee, S.-J. Hwang, Sci. Rep., 3 (2013) 2080.

[28] I. A. de Castro, R. S. Datta, J. Z. Ou, A. Castellanos-Gomez, S. Sriram, T. Daeneke, K. Kalantar-zadeh, Adv. Mater., 29 (2017) 1701619.

[29] N. P. Kondekar, M. G. Boebinger, E. V. Woods, M. T. McDowell, ACS Appl. Mater. Interfaces, 9 (2017) 32394.

[30] X. Liu, Z. Xing, H. Zhang, W. Wang, Y. Zhang, Z. Li, X. Wu, X. Yu, W. Zhou, ChemSusChem, 9 (2016) 1118.

[31] X. Xiao, Y. Wang, B. Cui, X. Zhang, D. Zhang, X. Xu, New J. Chem., 44 (2020) 4558.

[32] M. H. Johari, M. S. Sirat, M. A. Mohamed, Y. Wakayama, A. R. Mohmad, Nanomater. Nanotechnol., 11 (2021) 1.

[33] X. Sun, S. Wang, C. Shen, X. Xu, ChemCatChem., 8 (2016) 2289.

[34] J. L. Gunjakar, Y. K. Jo, I. Y. Kim, J. M. Lee, S. B. Patil, J.-C. Pyun, S.-J. Hwang, J. Solid State Chem. 240 (2016) 115.

[35] M. Kotal, A. Sharma, S. Jakhar, V. Mishra, S. Roy, S. C. Sahoo, H. K. Sharma, S. K. Mehta, Cryst. Growth Des., 20 (2020) 4627.

[36] S. Acharya, G. Swain, K. M. Parida, Int. J. Hydrog. Energy, 45 (2020) 11502.

[37] S. Chakrabarty, A. Mukherjee, S. Basu, ACS Sustainable Chem. Eng., 6 (2018) 5238.

[38] J. Chen, Y. Liao, X. Wan, S. Tie, B. Zhang, S. Lan, X. Gao, J. Solid State Chem., 291 (2020) 121652.

[39] D. Monga, D. Ilager, N. P. Shetti, S. Basu, T. M. Aminabhavi, J. Environ. Manage., 274 (2020) 111208.

[40] M. R. Abhilash, G. Akshatha, S. Srikantaswamy, RSC Adv., 9 (2019) 8557.

[41] K. H. Hu, X. G. Hu, Y. F. Xu, X. Z. Pan, Reac. Kinet. Mech. Cat. 100 (2010) 153.

[42] S. Varnagiris, M. Urbonavicius, S. Tuckute, M. Lelis, D. Milcius, Vacuum 143 (2017) 28.

[43] N. K. Gupta, Y. Ghafari, S. Kim, J. Bae, K. S. Kim, M. Saifuddin, Sci. Rep., 10 (2020) 4942.

[44] P. Guo, F. Zhao, X. Hu, J. Alloys Compd., 867 (2021) 159044.

[45] W.-Q. Chen, L.-Y. Li, L. Li, W.-H. Qiu, L. Tang, L. Xu, K.-J. Xu, M.-H. Wu, Engineering, 5 (2019) 755.

6.1 Introduction:

The development of various hybrid heterostructures for the effective use of the solar spectrum is an important aspect necessary to improve photocatalytic efficiency **[1-4]**. However, selecting hybridizing species is a crucial task that decides the properties of the resultant hybrid. TiO$_2$ and Nb$_2$O$_5$ are well-known wide-band gap semiconductors applied as photocatalysts. Their exfoliated counterparts act as a building block to form various kinds of hybrids. Much of the work has been devoted to exploring hybrids based on TiO$_2$.

Chapter 4, section 4.1 describes the usefulness of niobate-NS as an efficient photocatalyst due to its highly anisotropic structure, negative surface charge, high chemical and thermal stability and high photocatalytic activity **[5-6]**. The typical layered structure provides high surface area and ease of structural modification through intercalation and nanosheets or nanoscroll formation **[7-8]**. However, due to its wide band gap, its response is only limited to the UV spectrum. Moreover, the high recombination rate of excitons restricts its efficiency. On the other hand, MoS$_2$ is one of the narrow bandgap materials with visible light activity and abundant catalytic active sites, making it suitable for the visible-light-driven photocatalyst **[9]**. However, electron-hole recombination in MoS$_2$ hinders its performance **[10-11]**. The beneficial photocatalytic properties of MoS$_2$ are discussed in **Chapter 3, section 3.1**. On the other hand, as discussed in **Chapter 4, section 4.1**, exfoliated niobate-NS, with its ultrathin thickness, flexible chemical composition, and electrostatic surface charge, makes it the best choice for hybridization with narrow band gap MoS$_2$ photocatalysts. Therefore, coupling nanostructured MoS$_2$ with exfoliated niobate-NS can expand the surface area and separate excited electron-hole pairs, enhancing photocatalytic efficiency. The CB of MoS$_2$ is more negative than that of niobate-NS, which can be helpful for the easy charge transfer process and enhance the performance of the resultant hybrid. Also, exfoliated niobate-NS can be used as a platform for the growth of MoS$_2$ nanoparticles. The hybridization could increase surface area and depressed electron-hole recombination with mesoporous morphology, which can achieve better photocatalytic performance **[12-13]**.

In this chapter, the MCSD approach is used to anchor MoS$_2$ nanoparticles on dip-coated niobate-NS thin film. The obtained nanohybrid thin films are named

$MoS_2@Nb_6O_{17}$ hybrid thin films. Their photocatalytic performance is investigated by degrading RhB and MB dyes under visible light irradiation. Also, their physicochemical characterizations have been investigated to understand the obtained properties of the hybrid thin films.

6.2 Synthesis and Characterization of MoS₂@Nb₆O₁₇ hybrid thin film

6.2.1 Experimental details:

6.2.1.1 Chemicals:

The details of chemicals required for the deposition of MoS_2 and niobate-NS are given in **Chapter 3, section 3.2.1.1** and **Chapter 4, section 4.4.1.1**, respectively.

6.2.1.2 Synthesis of MoS₂@Nb₆O₁₇ hybrid thin film by MCSD

a) Preparation of colloidal niobate-NS suspension:

The synthesis protocol for preparing colloidal niobate-NS suspension is given in **Chapter 4, section 4.4.1.2**.

b) Deposition of niobate-NS thin films:

Details of niobate-NS thin film deposition by dip-coating are given in **Chapter 4, section 4.4.1.3**. To achieve the dip-coated niobate-NS thin films with various thicknesses, 50, 75 and 100 dip cycles were performed, and the obtained dip-coated niobate-NS thin films are named N-1, N-2 and N-3, respectively.

c) Deposition of MoS₂ thin films by MCSD:

The procedure for depositing MoS_2 thin films on glass substrates is given in **Chapter 3, section 3.2.1.2**.

d) Deposition of MoS₂@Nb₆O₁₇ hybrid thin films:

The visible light active MoS_2 thin film was deposited over dip-coated niobate-NS thin films using the MCSD method. The experimental conditions and parameters for preparing adsorption and reaction baths for MoS_2 thin film deposition are similar to those discussed in **Chapter 3, section 3.2.1.2**. The deposition of MoS_2 thin film by the MCSD method comprised successive immersion of dip-coated niobate-NS thin films into separately placed adsorption and reaction baths. A single deposition cycle of MCSD was completed by successive immersion of dip-coated niobate-NS thin film into an adsorption bath for 20 seconds and a reaction bath for the next 20 seconds. Such 50 deposition cycles were performed to deposit MoS_2 on dip-coated niobate-NS thin film. After the deposition, the $MoS_2@Nb_6O_{17}$ hybrid thin films were washed with DDW and

dried in air. Subsequently, the hybrid films were annealed in an Ar (95%)+H$_2$ (5%) atmosphere at 400°C for 2 hours for better crystallinity. The schematic representation of MoS$_2$@Nb$_6$O$_{17}$ hybrid thin film deposition using the MCSD method is shown in **Fig. 6.1**. The MoS$_2$@Nb$_6$O$_{17}$ hybrid thin films deposited on N-1, N-2 and N-3 thin films are denoted as MoS$_2$@Nb$_6$O$_{17}$-1, MoS$_2$@Nb$_6$O$_{17}$-2 and MoS$_2$@Nb$_6$O$_{17}$-3 hybrid thin films, respectively.
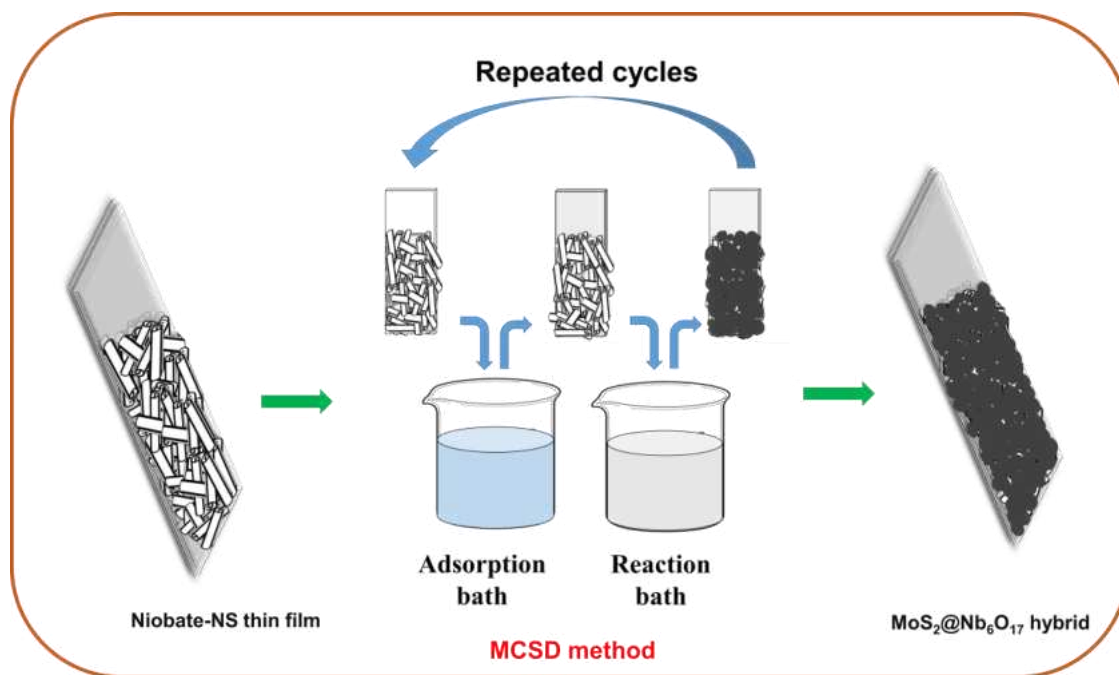
Figure 6.1: Schematic representation of the synthesis process of MoS$_2$@Nb$_6$O$_{17}$ hybrid thin films.

6.2.1.3 Material characterization

The MoS$_2$@Nb$_6$O$_{17}$ hybrid thin films were examined by various physicochemical characterization techniques, as described in **Chapter 3, section 3.2.1.3.**

6.2.2 Results and Discussion

6.2.2.1 XRD study
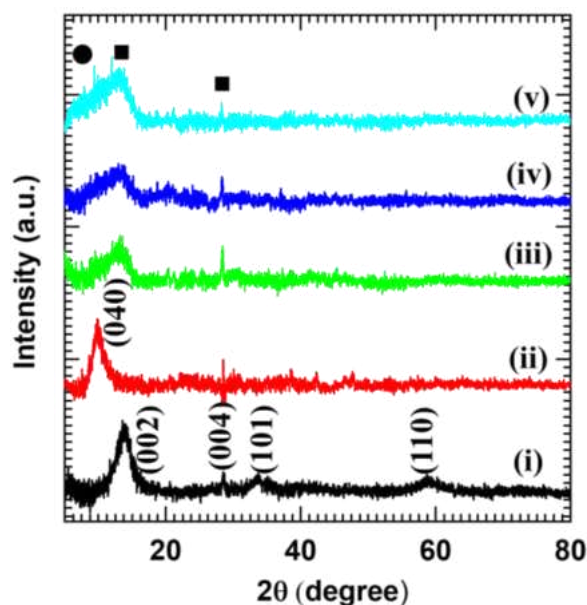
Figure 6.2: XRD patterns of i) MoS_2, ii) niobate-NS, iii) $MoS_2@Nb_6O_{17}$-1, iv) $MoS_2@Nb_6O_{17}$-2 and v) $MoS_2@Nb_6O_{17}$-3 hybrid thin films (The circle and square symbols represent the peaks from niobate-NS and MoS_2, respectively).

The structural study of $MoS_2@Nb_6O_{17}$ hybrid thin films was examined by the XRD technique, as shown in **Fig. 6.2**. For comparison, the XRD patterns of pristine MoS_2 (**Chapter 3, section 3.2.2.1**) and dip-coated niobate-NS (**Chapter 4, section 4.4.2.1**) thin films are also plotted in **Fig. 6.2**. The pristine MoS_2 exhibits typical Braggs reflection indexed as (002), (004), (101) and (110), which confirms the formation of layered 2H-MoS_2 [**14-15**]. The pristine dip-coated niobate-NS thin film exhibits a broad diffraction peak at 11.2°, which is assigned to the (040) plane corresponding to the well-ordered stacking of lamellar hexaniobate with the orthorhombic structure [**16**]. The estimated basal spacing from the (040) Braggs reflection for niobate-NS is 0.94 nm. The detailed XRD analysis of MCSD deposited MoS_2 and dip-coated niobate-NS thin films are discussed in **Chapter 3, section 3.2.2.1** and **Chapter 4, section 4.4.2.1**, respectively.

Interestingly, the XRD patterns of $MoS_2@Nb_6O_{17}$ hybrid thin film display several Bragg reflections corresponding to both niobate-NS (denoted by circles) and MoS_2 (denoted by squares). The peak centered at 14° is broadened due to the reflection of the (040) plane of niobate-NS and (002) plane of MoS_2 in the $MoS_2@Nb_6O_{17}$ hybrid,

which confirms the strong electronic coupling between them [**17**]. The diffraction peaks centered at 28° in MoS$_2$@Nb$_6$O$_{17}$ hybrid corresponds to the (004) plane of hexagonal layered MoS$_2$ (2H-MoS$_2$) (JCPDS card number: 37-1492) [**14-15**]. The presence of characteristic Bragg reflections corresponding to niobate-NS and MoS$_2$ in MoS$_2$@Nb$_6$O$_{17}$ hybrid thin film confirms the deposition of layered MoS$_2$ over dip-coated niobate-NS thin films. The present XRD features of MoS$_2$ and niobate-NS indicate the growth of MoS$_2$ over niobate-NS thin films. It also shows the structural intactness of niobate-NS with high mechanical stability during the hybrid thin film deposition.

6.2.2.2 Raman study
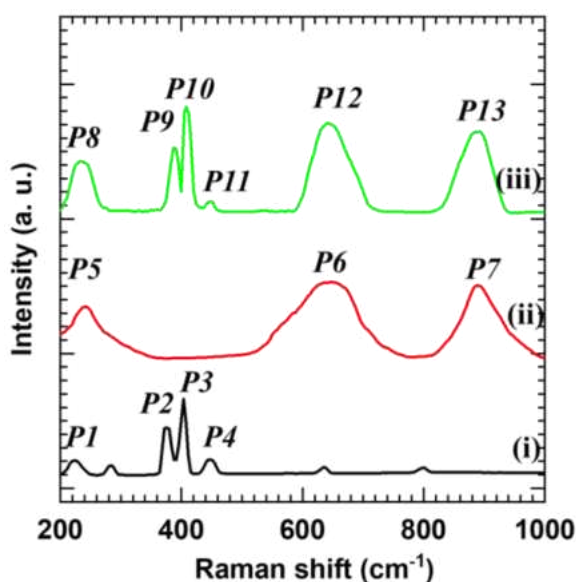
Figure 6.3: a) Raman spectra of i) MoS$_2$, ii) niobate-NS and iii) MoS$_2$@Nb$_6$O$_{17}$-2 hybrid thin film.

The nature of chemical bonding and microscopic structural features of MoS$_2$@Nb$_6$O$_{17}$ hybrid thin film were studied using Raman spectroscopy, as shown in **Fig. 6.3**. For comparison, the Raman spectra of pristine MoS$_2$ (**Chapter 3, section 3.2.2.2**) and dip-coated niobate-NS (**Chapter 4, section 4.4.2.2**) thin films are also plotted in **Fig. 6.3**. The pristine MoS$_2$ thin film shows characteristic Raman peaks P1 (230 cm^{-1}), P2 (384 cm^{-1}), P3 (407 cm^{-1}) and P4 (444 cm^{-1}) corresponding to longitudinal acoustic (LA(M)), in-plane (E$^1_{2g}$), out-of-plane (A$_{1g}$) vibrational and first-order optical phonon (A$_{2u}$) modes of MoS$_2$, respectively [**18-20**]. The origin of these peaks indicates the deposition of layered 2H-MoS$_2$ [**18**]. On the other hand, the niobate-NS thin film

exhibits several Raman peaks denoted by P5 (230 cm^{-1}), P6 (620 cm^{-1}) and P7 (884 cm^{-1}), which are ascribed to the internal bending mode of O-Nb-O, stretching mode in Nb-O in NbO$_6$ octahedra and Nb-O terminal stretching mode, respectively **[21-23]**. These characteristic Raman peaks confirm the deposition of well-developed niobate-NS thin film. The detailed Raman spectroscopic analysis of MoS$_2$ and niobate-NS thin film is described in **Chapter 3, section 3.2.2.2** and **Chapter 4, section 4.4.2.2,** respectively.

Moreover, MoS$_2$@Nb$_6$O$_{17}$ hybrid thin film displays the characteristic Raman peaks corresponding to niobate-NS (P8, P12 and P13) and MoS$_2$ (P9-P11). The characteristic Raman peaks P8 (230 cm^{-1}), P12 (620 cm^{-1}) and P13 (884 cm^{-1}) correspond to O-Nb-O internal bending mode, Nb-O in stretching mode in NbO$_6$ octahedra and Nb-O terminal stretching mode, respectively **[21-23]**. The Raman peaks P9 (384 cm^{-1}) and P10 (407 cm^{-1}) in MoS$_2$@Nb$_6$O$_{17}$ hybrid thin films are ascribed to the in-plane (E^1_{2g}) and out-of-plane (A_{1g}) vibrational phonon modes in the deposited MoS$_2$ layer. The peak P11 (444 cm^{-1}) originated due to the first-order optical phonon (A_{2u}) mode in MoS$_2$. The observed Raman features provide strong evidence of the deposition of layered 2H-MoS$_2$ over dip-coated niobate-NS thin films.

6.2.2.3 FTIR study
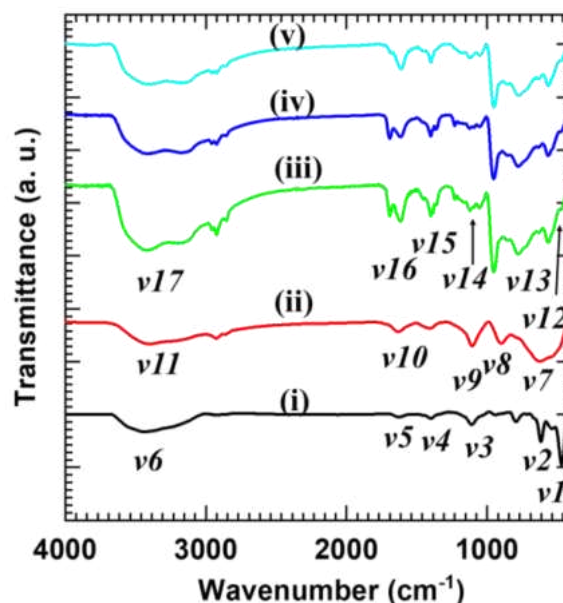
Figure 6.4: FTIR spectra of i) MoS$_2$, ii) niobate-NS, iii) MoS$_2$@Nb$_6$O$_{17}$-1, iv) MoS$_2$@Nb$_6$O$_{17}$-2 and v) MoS$_2$@Nb$_6$O$_{17}$-3 hybrid thin films.

The chemical bonding nature of $MoS_2@Nb_6O_{17}$ hybrid thin films was probed with FTIR spectroscopy. For comparison, the FTIR spectra of pristine MoS_2 (**Chapter 3, section 3.2.2.3**) and dip-coated niobate-NS (**Chapter 4, section 4.4.2.3**) thin films are also plotted in **Fig. 6.4**. As shown in **Fig. 6.4**, FTIR spectra of pristine MoS_2 show absorption bands ν1 (469 cm^{-1}) and ν2 (617 cm^{-1}) corresponding to the stretching vibration of Mo-S bonding [**24**]. The bands ν3 (1115 cm^{-1}) and ν4 (1411 cm^{-1}) are attributed to the sulfur-related stretching vibration of S-Mo-S [**25**]. The bands ν5 (1632 cm^{-1}) and ν6 (3436 cm^{-1}) are assigned to the bending vibrational modes of water molecules and stretching vibrations of the O-H groups, respectively [**26**]. Pristine niobate-NS demonstrates absorption bands ν7 (540 cm^{-1}) and ν8 (910 cm^{-1}) corresponding to the stretching vibration of O-Nb-O and stretching vibration of Nb=O in NbO_6 octahedra, respectively [**22**]. The weak band ν9 (1118 cm^{-1}) is ascribed to N-H stretching vibration in TBA [**23**]. The absorption bands ν10 (1630 cm^{-1}) and ν11 (3415 cm^{-1}) correspond to the bending vibrational modes of water molecules and stretching vibration of the hydroxyl groups, respectively [**27-28**]. The detailed FTIR analysis of MoS_2 and niobate-NS thin film is described in **Chapter 3, section 3.2.2.3** and **Chapter 4, section 4.4.2.3,** respectively. Moreover, all the $MoS_2@Nb_6O_{17}$ hybrid thin films commonly display several absorption bands associated with pristine MoS_2 and niobate-NS thin film (ν12- ν17). The absorption bands ν12 (469 cm^{-1}) and ν15 (1411 cm^{-1}) are ascribed to the Mo-S stretching vibration and S-Mo-S stretching vibrations, respectively [**24-25**]. The absorption bands ν13 (540 cm^{-1}) and ν14 (1118 cm^{-1}) correspond to the stretching vibration of O-Nb-O and N-H stretching vibration in TBA, respectively [**22**]. The absorption bands ν16 (1632 cm^{-1}) and ν17 (3436 cm^{-1}) are linked with the bending vibrations of water molecules and stretching vibrations of hydroxyl groups, respectively. The presence of IR features related to both MoS_2 and niobate-NS indicates the formation of the $MoS_2@Nb_6O_{17}$ hybrid thin film using the MCSD method.

6.2.2.4 FE-SEM study

The microstructural surface features and stacking patterns of $MoS_2@Nb_6O_{17}$-2 hybrid thin film were investigated by FE-SEM analysis as shown in **Fig. 6.5**. The surface microscopic analysis of pristine MoS_2 and niobate-NS thin film is described in **Chapter 3, section 3.2.2.4** and **Chapter 4, section 4.4.2.4**, respectively. As described in **Chapter 3, section 3.2.2.4**, pristine MoS_2 thin film shows the nanoclusters composed of spherical

MoS$_2$ nanoparticles with particle sizes ranging from 40 to 60 nm. As described in **Chapter 4, section 4.4.2.4**, the dip-coated niobate-NS thin film displays anisotropic growth of niobate nanoscrolls having a length ranging from 500 nm to 1 µM and a width of around 50 nm lying parallel to the substrate.

On the other hand, MoS$_2$@Nb$_6$O$_{17}$-2 hybrid thin film shows clusters of spherical MoS$_2$ nanoparticles anchored on parallelly stacked niobate nanoscrolls. The MoS$_2$ nanoparticles are interconnected, creating a highly porous cluster architecture morphology. The cross-section of MoS$_2$@Nb$_6$O$_{17}$-2 hybrid thin film shows an increased thickness of 1.06 µm after hybridization with niobate nanoscrolls. The anchored MoS$_2$ clusters give rise to a high surface area architecture, which enables expanded surface area with an open framework. It shows the strong electronic coupling between both hybridized species, which is highly beneficial in spatial electron-hole pair separation for solar-assisted photocatalytic applications. A similar type of morphology is generally observed for 2D nanosheet-based heterostructures, which is advantageous for various applications [**29-31**].
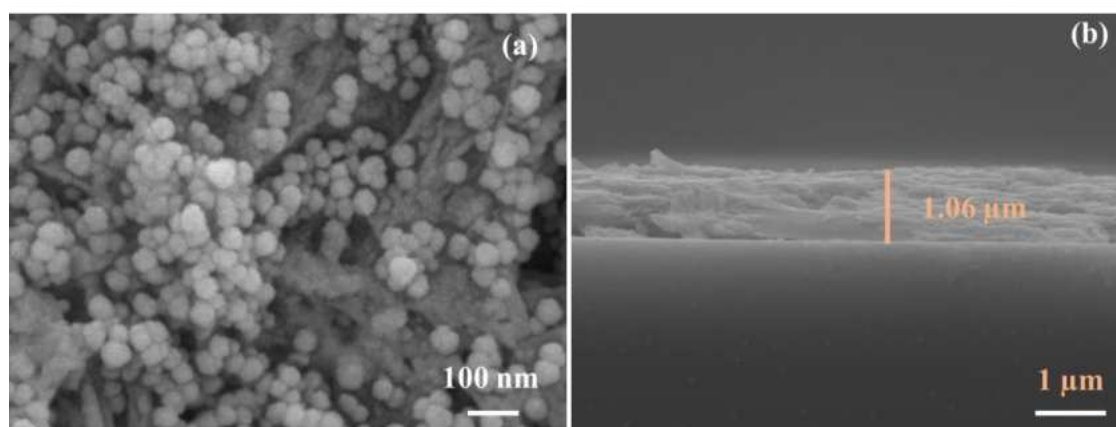
Figure 6.5: (a) Top view and (b) cross-section FE-SEM images of MoS$_2$@Nb$_6$O$_{17}$-2 hybrid thin film.

The presence of constituent elements in MoS$_2$@Nb$_6$O$_{17}$-2 hybrid thin film was investigated using EDS elemental mapping analysis. As shown in **Fig. 6.6** and **Fig. 6.7**, Nb, O, Mo and S elements are distributed uniformly over the entire mapping area, confirming the uniform deposition of MoS$_2$ on the surface of niobate nanoscrolls thin film using the MCSD method without any phase separation.
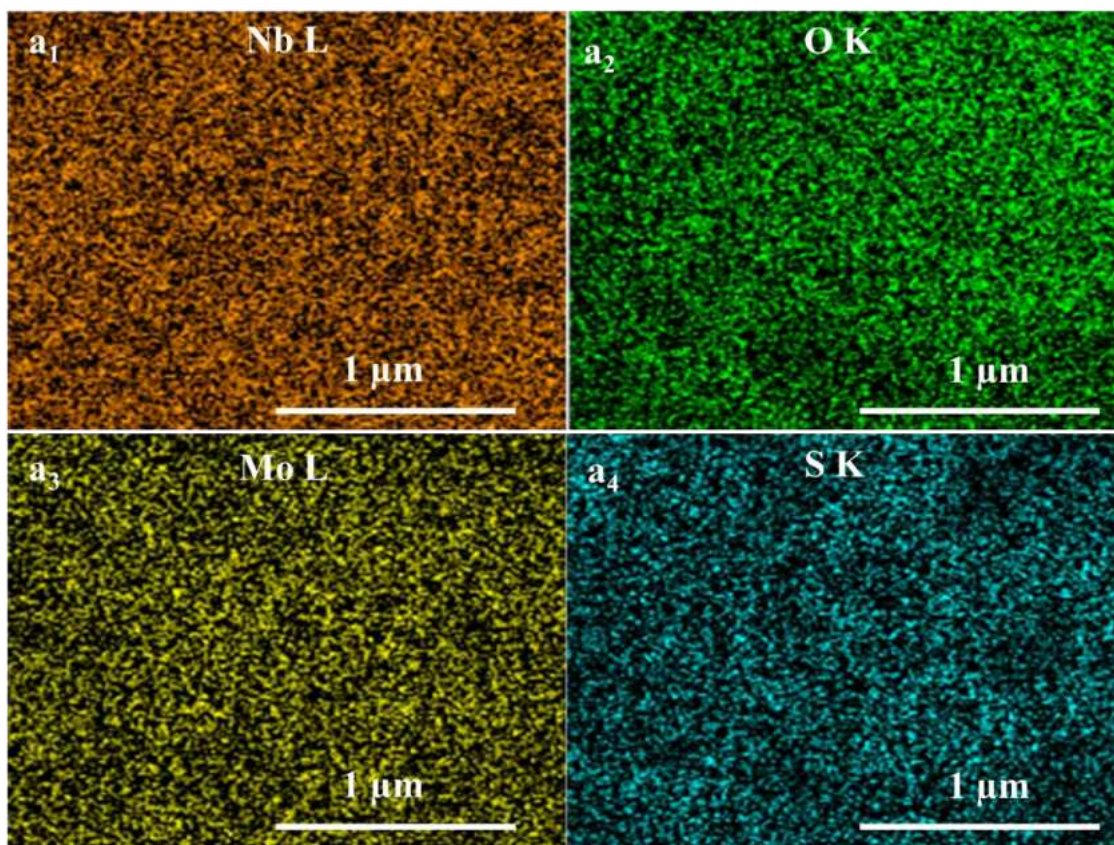
Figure 6.6: EDS elemental mapping of MoS$_2$@Nb$_6$O$_{17}$-2 hybrid thin film.

Elements	Atomic %
Nb	16.37
O	71.56
Mo	4.30
S	7.77
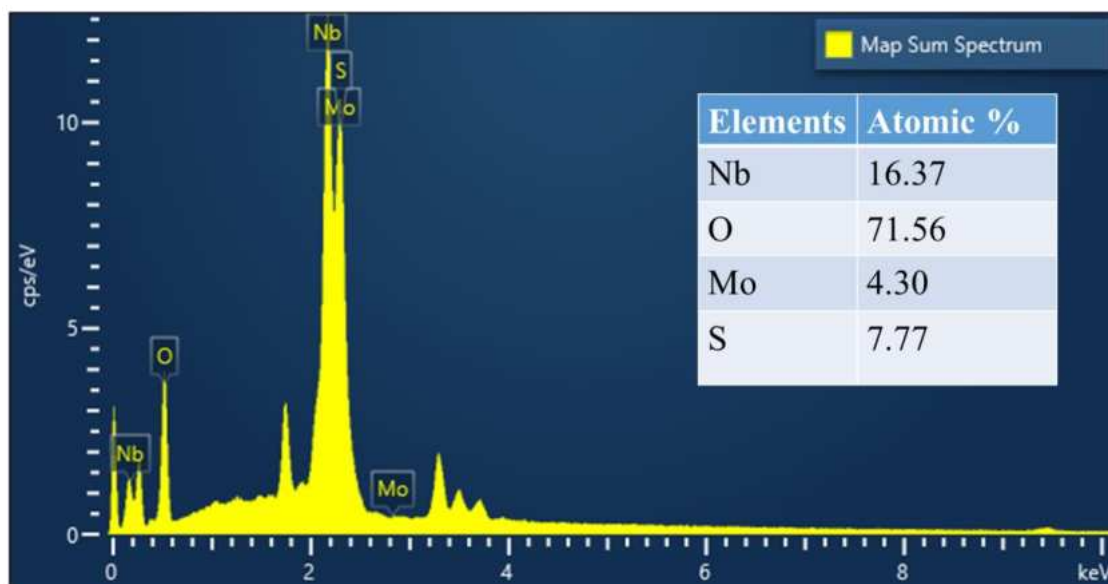
Figure 6.7: EDS spectrum of MoS$_2$@Nb$_6$O$_{17}$-2 hybrid thin film.

6.2.2.5 XPS study

The presence of elements and their oxidation states in the MoS$_2$@Nb$_6$O$_{17}$-2 hybrid thin film was determined by XPS analysis as shown in **Fig. 6.8.** For comparison,

the XPS survey spectra of pristine MoS$_2$ (**Chapter 3, section 3.2.2.5**) and dip-coated niobate-NS (**Chapter 4, section 4.4.2.5**) thin films are also plotted in **Fig. 6.8**. The survey XPS spectra of pristine MoS$_2$, niobate-NS thin film and MoS$_2$@Nb$_6$O$_{17}$-2 hybrid thin films exhibit characteristic XPS features at BE of Mo, S, Nb and O elements, representing the presence of stated elements in above thin films.
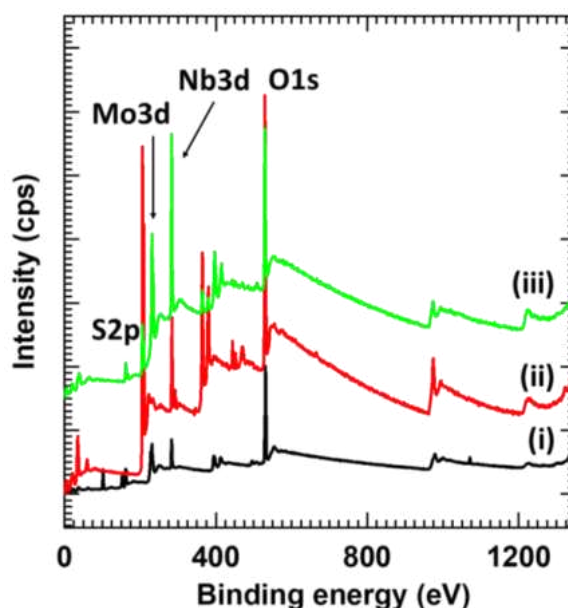
Figure 6.8: XPS survey spectra of (i) MoS$_2$, (ii) niobate-NS and (iii) MoS$_2$@Nb$_6$O$_{17}$-2 hybrid thin films.

The high-resolution Mo 3d, S 2p, Nb 3d, and O 1s XPS spectra are plotted in **Fig. 6.9 (a-d)**, respectively. The high-resolution XPS spectra of Mo 3d and S 2p are discussed in **Chapter 3, section 3.2.2.5**. As shown in **Fig. 6.9a**, high-resolution Mo 3d spectra of MoS$_2$ and MoS$_2$@Nb$_6$O$_{17}$-2 hybrid thin films commonly display two spectral features, A (229.5 eV) and B (232.7 eV) corresponding to the spin-orbit splitting of Mo 3d$_{5/2}$ and Mo 3d$_{3/2}$, respectively. The BE difference of 3.2 eV indicates the presence of Mo^{4+} in both films [**32**]. As displayed in **Fig. 6.9b**, the high-resolution S 2p spectra of MoS$_2$ and MoS$_2$@Nb$_6$O$_{17}$-2 hybrid thin films show a broad peak C (162 eV), corresponding to the spin-orbit splitting of S^{2-} [**33**]. The high-resolution XPS spectra of Nb 3d and O 1s are discussed in **Chapter 4, section 4.4.2.5**. As shown in **Fig. 6.9c**, the high-resolution Nb 3d spectra of niobate-NS thin film and MoS$_2$@Nb$_6$O$_{17}$-2 hybrid thin films commonly exhibit a doublet D (206.3) and E (209.1 eV) related with spin-orbit splitting of Nb 3d$_{5/2}$ and Nb 3d$_{3/2}$, respectively, which is characteristic of Nb^{5+} in niobate-NS and MoS$_2$@Nb$_6$O$_{17}$-2 hybrid thin film [**34-35**]. As displayed in **Fig. 6.9d**, the high-

resolution O 1s spectra of niobate-NS and $MoS_2@Nb_6O_{17}$-2 hybrid thin films show a single broad peak F (529.5 eV), showing the presence of oxygen from metal oxide. The O 1s spectra is broadened after hybridization due to the surface hydroxyl group or adsorbed water [**35**]. The XPS analysis evidences the presence of Mo^{4+} and Nb^{5+} states of Mo and Nb, respectively, which confirms the formation of $MoS_2@Nb_6O_{17}$ hybrid thin film.
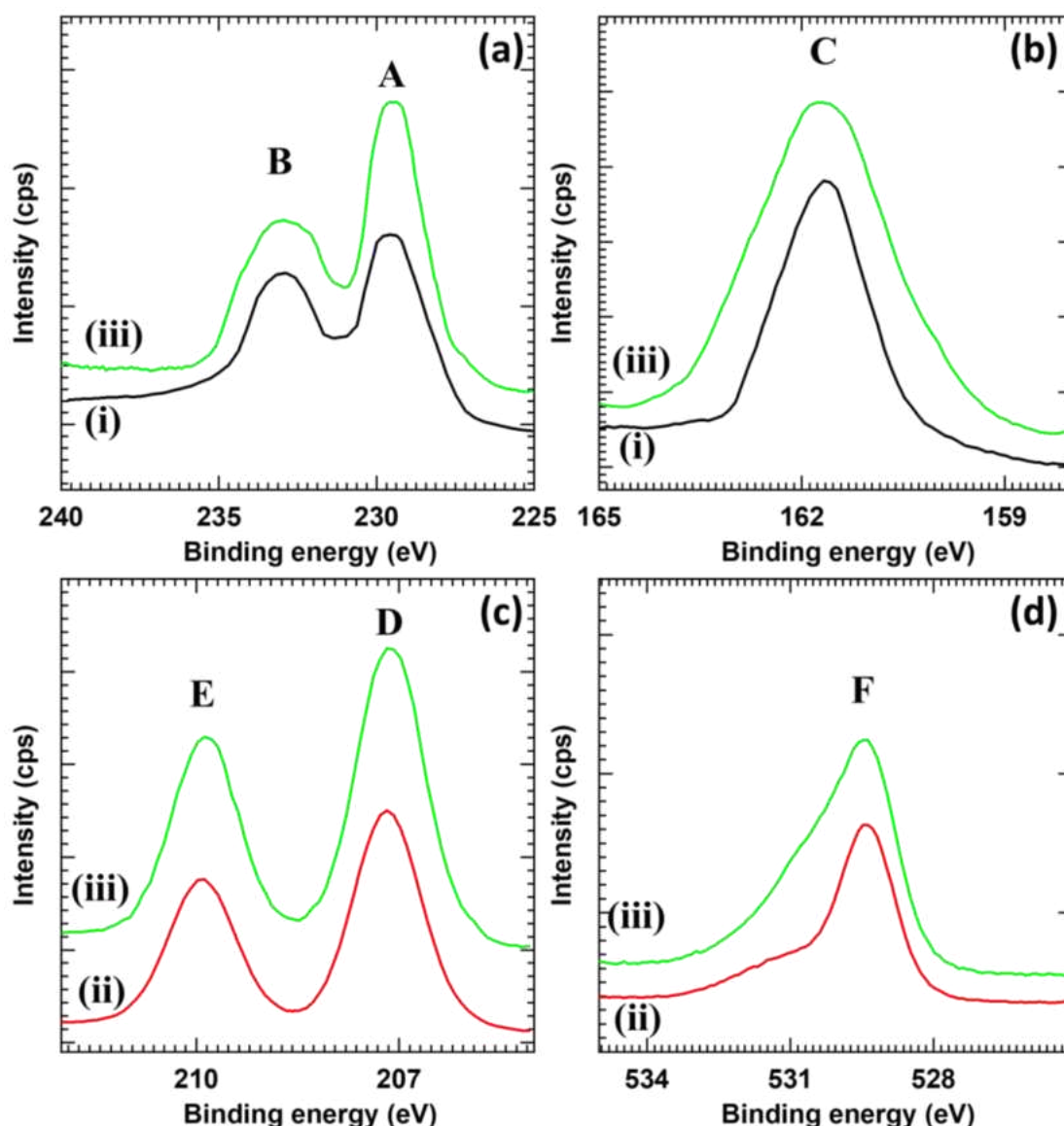
Figure 6.9: a) Mo 3d b) S 2p, c) Nb 3d and d) O 1s core-level XPS spectra of i) pristine MoS_2, ii) niobate-NS and iii) $MoS_2@Nb_6O_{17}$-2 hybrid thin film.

6.2.2.6 UV-Vis DRS study and band positions determination
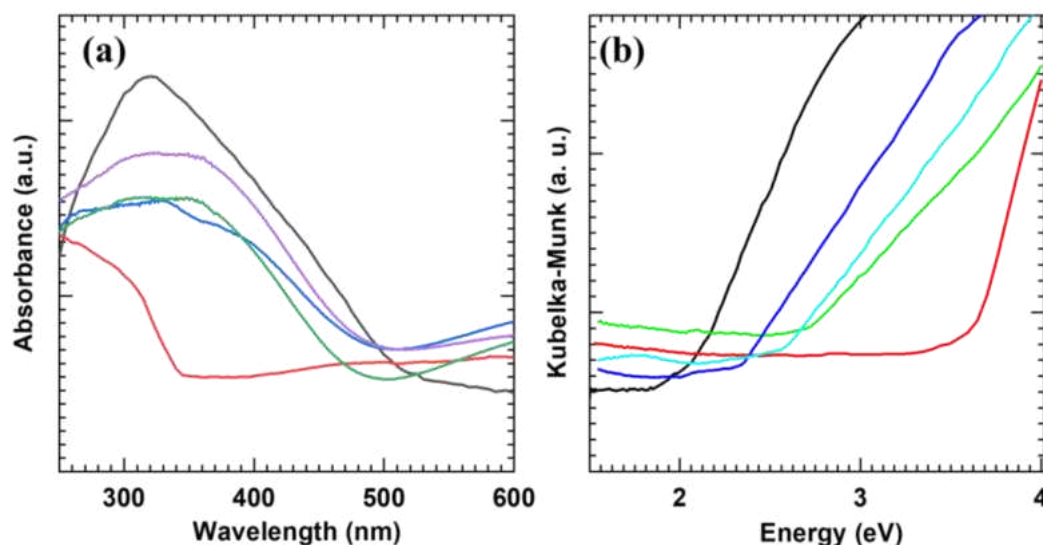
Figure 6.10: a) UV-Vis DRS absorbance spectra and b) Diffuse reflectance UV–Vis spectra (plotted as the Kubelka–Munk function of the reflectance, R) of (i) MoS₂ (black), (ii) niobate-NS (red), (iii) MoS₂@Nb₆O₁₇-1 (green), (iv) MoS₂@Nb₆O₁₇-2 (blue) and (v) MoS₂@Nb₆O₁₇-3 (cyan) hybrid thin films.

The band structure and optical properties of MoS₂@Nb₆O₁₇ hybrid thin films were evaluated using the UV-Vis DRS technique. For comparison, the UV-Vis DRS absorption spectrum of pristine MoS₂ (**Chapter 3, section 3.2.2.6**) and dip-coated niobate-NS (**Chapter 4, section 4.4.2.6**) are plotted again in **Fig. 6.10a**. As plotted in **Fig. 6.10a**, pristine MoS₂ shows significant absorption in the visible region with an optical band gap of 1.6 eV. MoS₂ is an indirect band gap material with an electronic structure comprising a VB and CB, mainly composed of Mo 4d and S 3p orbitals, respectively **[36-37]**. On the other hand, niobate-NS thin film shows strong absorption in the UV region with no absorption in the visible region due to its wide band gap (3.45 eV). The electronic structure of niobate-NS comprises a VB and CB mainly composed of O 2p and Nb 4d orbitals, respectively **[38]**. The detailed analysis of UV-Vis DRS spectra of pristine MoS₂ and titanate-NS thin films are discussed in **Chapter 3, section 3.2.2.6** and **Chapter 4, section 4.4.2.6**, respectively.

Interestingly, MoS₂@Nb₆O₁₇ hybrid thin films show considerable absorption in the visible region, indicating effective electronic coupling between wide band gap niobate-NS and narrow band gap MoS₂ thin films. The variation of dip cycles of niobate-NS thin film results in a variation of absorbance and band gap of MoS₂@Nb₆O₁₇ hybrid

thin films. The MoS$_2$@Nb$_6$O$_{17}$ hybrid thin films absorb visible light in the 590-640 nm wavelength range, corresponding to band gap energies between 1.95-2.10 eV. Increased composition of wide band gap niobate-NS in MoS$_2$@Nb$_6$O$_{17}$-1 to MoS$_2$@Nb$_6$O$_{17}$-3 is responsible for the increased band gap. The band gap energies determined from the Kubelka-Munk function and their values are shown in **Fig. 6.10b** and noted in **Table 6.1**. The increased visible light absorption capacity illustrates the application of the MoS$_2$@Nb$_6$O$_{17}$ hybrid for visible-light-driven photocatalytic applications.

Table 6.1: Band gap energies of MoS$_2$, niobate-NS and MoS$_2$@Nb$_6$O$_{17}$ hybrid thin films.

Thin film	Band gap (eV)
MoS$_2$	1.6
Niobate-NS	3.45
MoS$_2$@Nb$_6$O$_{17}$-1	1.95
MoS$_2$@Nb$_6$O$_{17}$-2	1.98
MoS$_2$@Nb$_6$O$_{17}$-3	2.1

The band position of MoS$_2$ and niobate-NS are calculated from the empirical formula described in **Chapter 3, section 3.2.2.6** and **Chapter 4, section 4.4.2.6**, respectively. The estimated VB and CB positions for MoS$_2$ are 0.015 and -1.60 eV, respectively, whereas those for niobate-NS are 2.69 and -0.76 eV, respectively, as shown in **Fig. 6.11**.
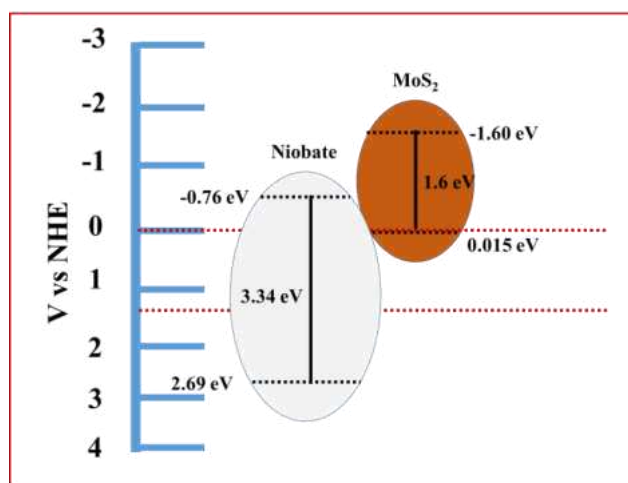
Figure 6.11: Band positions of MoS$_2$@Nb$_6$O$_{17}$ hybrid thin film vs NHE.

6.3 Dye Degradation Studies

6.3.1 Results and Discussion
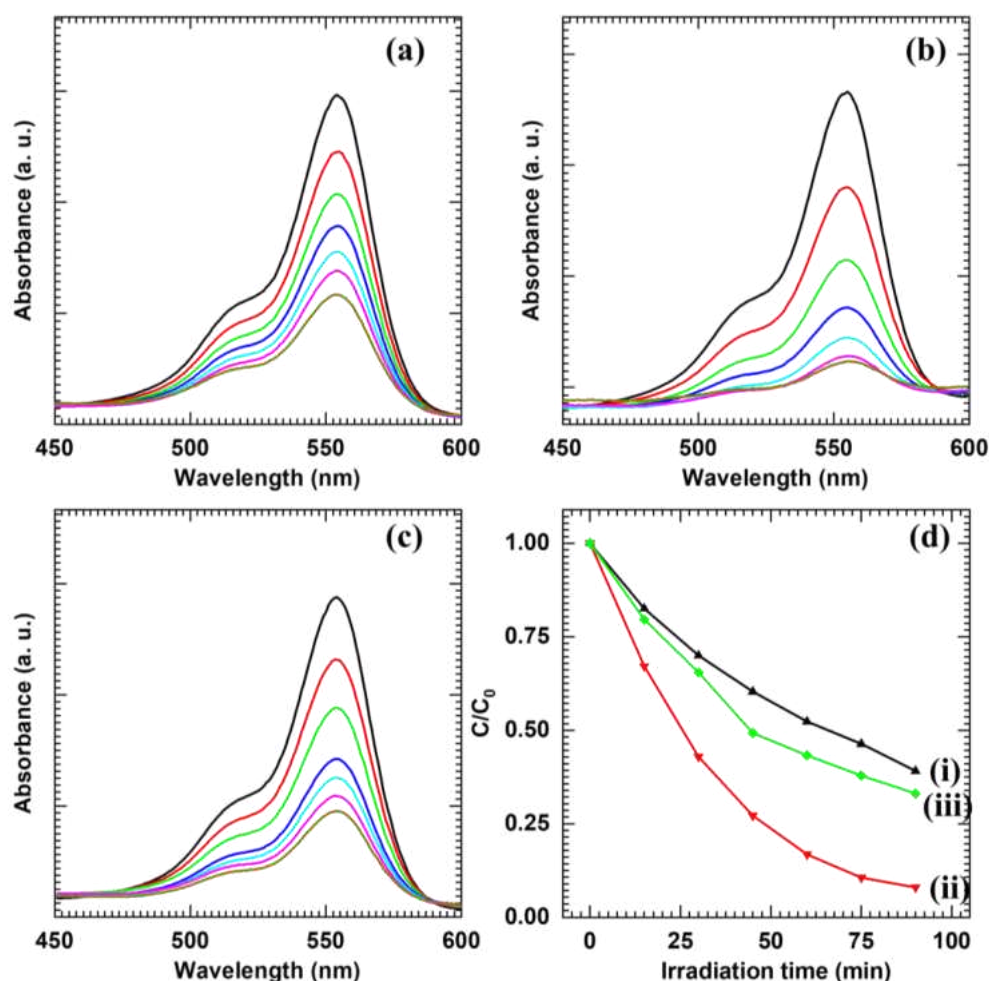
Figure 6.12: Time dependant UV-Vis absorption spectra of RhB in the presence of (a) MoS$_2$@Nb$_6$O$_{17}$-1, (b) MoS$_2$@Nb$_6$O$_{17}$-2, (c) MoS$_2$@Nb$_6$O$_{17}$-3 hybrid thin films under visible-light irradiation and (d) variation of RhB concentration as a function of irradiation time for (i) MoS$_2$@Nb$_6$O$_{17}$-1, (ii) MoS$_2$@Nb$_6$O$_{17}$-2 and (iii) MoS$_2$@Nb$_6$O$_{17}$-3 hybrid thin films.

The photocatalytic degradation performance of MoS$_2$@Nb$_6$O$_{17}$ hybrid thin films was assessed by observing the time-dependent UV-Vis absorption spectra of RhB under visible-light illumination in the presence of photocatalysts. The results were compared with those of pristine MoS$_2$ and niobate-NS thin films. **Fig. 6.12 (a-c)** displays time-dependent absorption spectra of RhB dye in the presence of MoS$_2$@Nb$_6$O$_{17}$-1, MoS$_2$@Nb$_6$O$_{17}$-2 and MoS$_2$@Nb$_6$O$_{17}$-3, hybrid photocatalyst under visible-light illumination, respectively. The UV-Vis absorption spectra of RhB in the presence of

MoS$_2$ and niobate-NS are shown in **Chapter 3, section 3.3.2** and **Chapter 4, section 4.5.1**, respectively. The pristine MoS$_2$ displays superior visible-light photocatalytic activity for photodegradation due to its narrow band gap (1.6 eV), whereas niobate-NS does not show visible light activity due to its wide band gap (3.45 eV). On the other hand, the photocatalytic activity of MoS$_2$ remarkably improved upon hybridization with niobate- NS. The decrease in intensity at the characteristic wavelength of 554 nm with respect to irradiation time indicates the degradation of RhB. **Fig. 6.12d** shows the variation of RhB concentration as a function of irradiation time for MoS$_2$@Nb$_6$O$_{17}$-1, MoS$_2$@Nb$_6$O$_{17}$-2 and MoS$_2$@Nb$_6$O$_{17}$-3 hybrid thin films. The photocatalytic degradation performance of pristine MoS$_2$ and niobate-NS are represented in **Chapter 3, section 3.3.2** and **Chapter 4, section 4.5.1**, respectively. Among MoS$_2$@Nb$_6$O$_{17}$ hybrid thin films deposited at various niobate-NS thicknesses, the MoS$_2$@Nb$_6$O$_{17}$-2 displays maximum photocatalytic RhB degradation of 92 % in 90 minutes which shows 1.30-fold increased photocatalytic degradation performance to that of pristine MoS$_2$.

Similarly, the photocatalytic degradation performance of MoS$_2$@Nb$_6$O$_{17}$ hybrid thin films was assessed by observing the time-dependent UV-Vis absorption spectra of MB under visible-light illumination in the presence of photocatalysts. The results were compared with those of pristine MoS$_2$ and niobate-NS thin film. **Fig. 6.13 (a-c)** displays time-dependent UV-Vis absorption spectra of MB dye in the presence of MoS$_2$@Nb$_6$O$_{17}$-1, MoS$_2$@Nb$_6$O$_{17}$-2 and MoS$_2$@Nb$_6$O$_{17}$-3 hybrids, respectively. The UV-Vis absorption spectra of MB in the presence of MoS$_2$ and niobate-NS are shown in **Chapter 3, section 3.3.2** and **Chapter 4, section 4.5.1**, respectively. The pristine MoS$_2$ displays superior visible-light photocatalytic activity for photodegradation due to its narrow band gap (1.6 eV), whereas niobate-NS does not show visible-light activity due to its wide bandgap (3.45 eV). On the other hand, the photocatalytic activity of MoS$_2$ remarkably improved upon hybridization with niobate-NS. The decrease in intensity at the characteristic wavelength of 665 nm with respect to irradiation time indicates the degradation of MB. **Fig. 6.13d** shows the variation of MB concentration as a function of irradiation time for MoS$_2$@Nb$_6$O$_{17}$-1, MoS$_2$@Nb$_6$O$_{17}$-2 and MoS$_2$@Nb$_6$O$_{17}$-3 hybrid thin films. The photocatalytic degradation performance of pristine MoS$_2$ and niobate-NS are represented in **Chapter 3, section 3.3.2** and **Chapter 4, section 4.5.1**, respectively. Among MoS$_2$@Nb$_6$O$_{17}$ hybrid thin films deposited at various niobate-NS thicknesses, the MoS$_2$@Nb$_6$O$_{17}$-2 displays maximum photocatalytic MB degradation of

79 % in 90 minutes, which shows 1.15 fold increased photocatalytic degradation performance to that of pristine MoS_2.

The remarkably enhanced performance of present nanohybrids is attributed to the strong visible light harvesting ability, high surface area morphology, and reduced electron-hole recombination via strong electronic coupling between hybridized species [39].

Figure 6.13: Time dependant UV-Vis absorption spectra of MB in the presence of (a) $MoS_2@Nb_6O_{17}$-1, (b) $MoS_2@Nb_6O_{17}$-2, (c) $MoS_2@Nb_6O_{17}$-3 hybrid thin films under visible-light irradiation and (d) variation of MB concentration as a function of irradiation time for (i) $MoS_2@Nb_6O_{17}$-1, (ii) $MoS_2@Nb_6O_{17}$-2 and (iii) $MoS_2@Nb_6O_{17}$-3 hybrid thin films.

6.3.2 Kinetic study
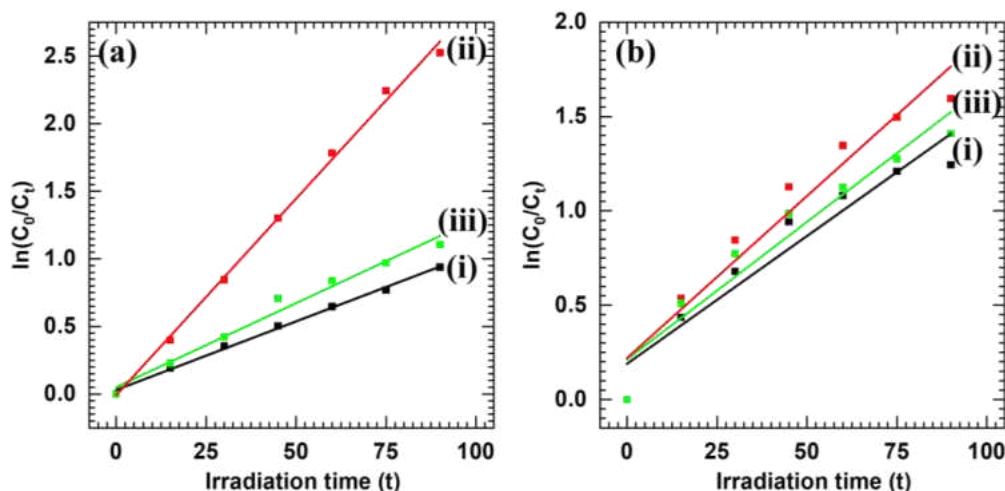
Figure 6.14: Pseudo-first-order kinetics of a) RhB and b) MB dyes using i) MoS$_2$@Nb$_6$O$_{17}$-1, ii) MoS$_2$@Nb$_6$O$_{17}$-2 and iii) MoS$_2$@Nb$_6$O$_{17}$-3 hybrid thin films.

The degradation kinetics of RhB and MB dyes using MoS$_2$@Nb$_6$O$_{17}$ hybrid thin films were probed by a pseudo-first-order rate kinetic model by plotting ln(C$_0$/C$_t$) vs irradiation time as shown in **Fig. 6.14 (a-b)**. The rate constant (k) and linear correlation coefficient (R^2) values are given in **Table 6.2**. All the MoS$_2$ thin films show high k-values, confirming the faster reaction kinetics. The MoS$_2$@Nb$_6$O$_{17}$-2 hybrid thin film exhibits the highest k value of 0.029 min^{-1} than that of MoS$_2$@Nb$_6$O$_{17}$-1 and MoS$_2$@Nb$_6$O$_{17}$-3 hybrid thin films for RhB. These k values reveal the excellent photocatalytic performance of MoS$_2$@Nb$_6$O$_{17b}$ hybrid thin films. The excellent photocatalytic performance of MoS$_2$@Nb$_6$O$_{17}$-2 hybrid thin films is attributed to the expanded surface area, strong electronic coupling and high photostability, which provides catalytically active sites for the degradation of target molecules **[40-41]**.

Table 6.2: Photocatalytic dye degradation performance of MoS$_2$@Nb$_6$O$_{17}$ hybrid thin films.

Target molecule	Photocatalyst	Degradation (%)	Rate constant (k) (min^{-1})	Correlation coefficient (R^2)
RhB	MoS$_2$@Nb$_6$O$_{17}$-1	60	0.010	0.9962
	MoS$_2$@Nb$_6$O$_{17}$-2	92	0.029	0.9970
	MoS$_2$@Nb$_6$O$_{17}$-3	66	0.012	0.9813
MB	MoS$_2$@Nb$_6$O$_{17}$-1	71	0.013	0.9213
	MoS$_2$@Nb$_6$O$_{17}$-2	79	0.017	0.9391
	MoS$_2$@Nb$_6$O$_{17}$-3	75	0.014	0.9329

6.3.3 Recycling study
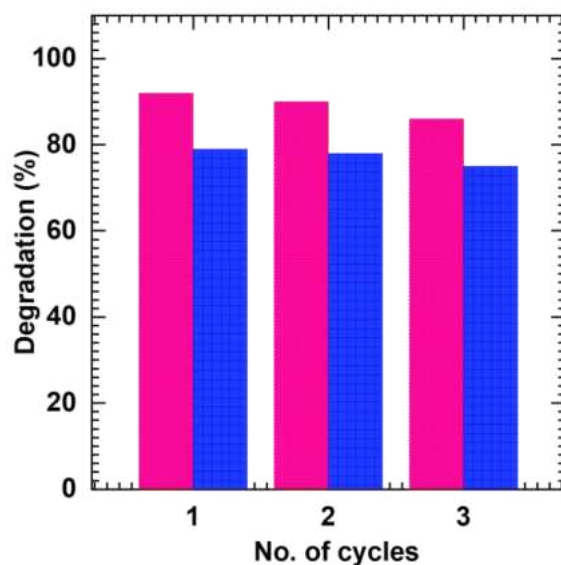
Figure 6.15: Recyclability of optimized MoS$_2$@Nb$_6$O$_{17}$-2 hybrid thin films for RhB (pink) and MB (blue) degradation for 3 cycles.

Furthermore, the stability of the optimized MoS$_2$@Nb$_6$O$_{17}$-2 hybrid thin films for the degradation of RhB and MB is studied for three consecutive cycles, as shown in

Fig. 6.15. The present MoS$_2$@Nb$_6$O$_{17}$-2 hybrid thin film displays good recycling performance by retaining 93 and 94 % of the photocatalytic performance for RhB and MB, respectively. After each cycle, the slight decrement in the photocatalytic performance is attributed to the inactivity of active material as dye molecules adsorb on the photocatalyst surface **[42]**.

6.3.4 Plausible dye degradation mechanism
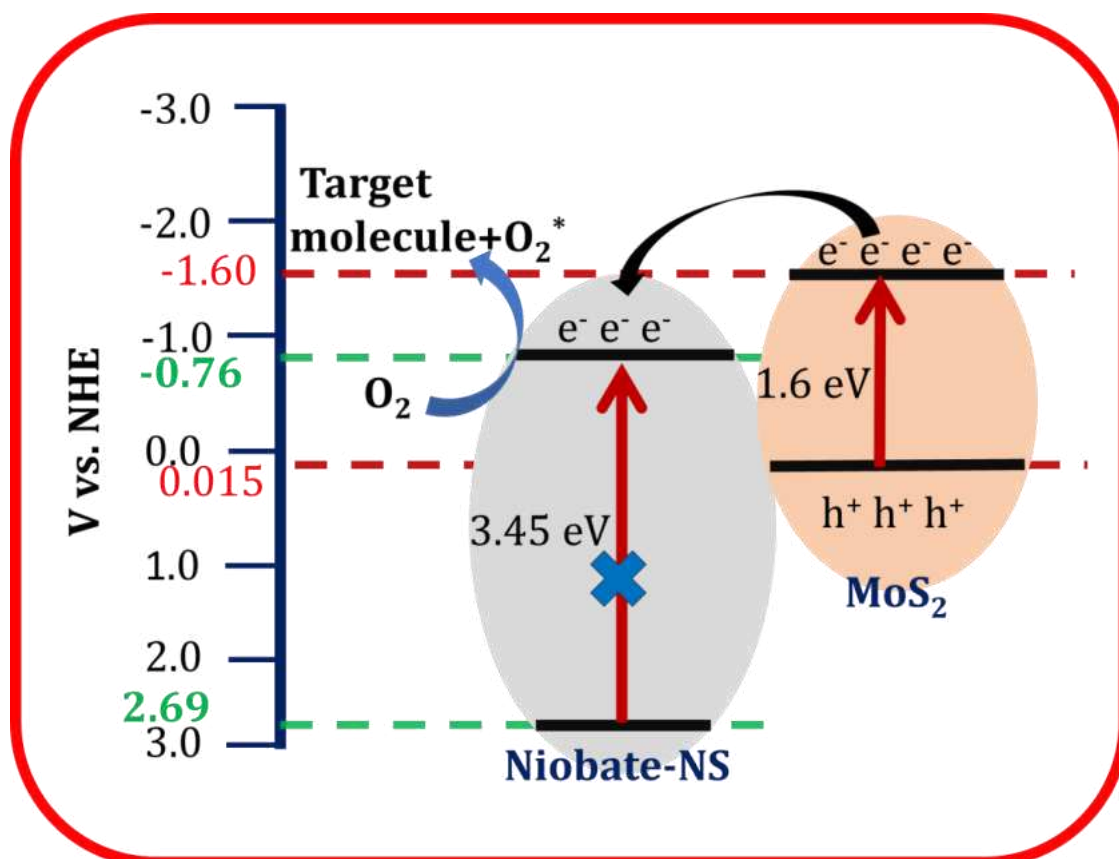
Figure 6.16: Schematic of plausible degradation mechanism of target molecules under visible-light irradiation using MoS$_2$@Nb$_6$O$_{17}$ hybrid thin films.

The dye degradation mechanism is explained in **Chapter 3, section 3.3.5**. The schematic representation of the degradation pathway using the MoS$_2$@Nb$_6$O$_{17}$ hybrid thin film is shown in **Fig. 6.16**. The CB of MoS$_2$ is more negative than that of niobate-NS and VB of niobate-NS is more positive than that of MoS$_2$ with respect to NHE. The photo-excited electrons from the CB of MoS$_2$ can transfer to the CB of the niobate-NS, causing spatial separation of electrons and holes with a reduction in recombination rate. Thus, the lifetime of holes in the VB of MoS$_2$ increases. As the VB of MoS$_2$ is not positive enough for the production of hydroxyl radicals (OH*), holes present in the VB

of MoS$_2$ will not participate in the reaction directly. Meanwhile, superoxide radicals (*O$_2^-$) are generated when electrons in the CB of niobate-NS react with O$_2$. Further, hydroperoxyl radicals (HOO*) are generated from the protonation of superoxide radicals. Finally, H$_2$O$_2$ dissociates into OH* radicals, which can break the chain of target organic molecules **[43-45]**. The chemical reactions describing plausible dye degradation mechanism are represented in **Chapter 1, section 1.1.7.1 (b)**.

6.4 Conclusion

In this report, MoS$_2$@Nb$_6$O$_{17}$ hybrid thin films are synthesized by a combination of dip-coating and MCSD methods and employed to degrade dye (RhB and MB) molecules under visible light irradiation. The structural study of MoS$_2$@Nb$_6$O$_{17}$ hybrid thin films shows characteristic features of niobate-NS and MoS$_2$, which confirms the direct growth of MoS$_2$ on niobate-NS thin film. MoS$_2$@Nb$_6$O$_{17}$ hybrid thin films show MoS$_2$ particles randomly anchored on parallel ordered niobate-NS thin film, demonstrating intimate contact and strong electronic coupling between the hybridized species. The MoS$_2$@Nb$_6$O$_{17}$-2 hybrid thin films display enhanced visible light harvesting properties with effective electron-hole separation. The optimized MoS$_2$@Nb$_6$O$_{17}$-2 hybrid thin film exhibits enhanced visible light harvesting capacity with a depressed electron-hole recombination rate. The optimized MoS$_2$@Nb$_6$O$_{17}$-2 hybrid thin film exhibits photocatalytic degradation performance of 92 % and 79 % for RhB and MB, respectively, within 90 minutes of visible light irradiation. This work demonstrates the usefulness of heterostructure formation for obtaining high surface area structures. This study can be used to synthesize various hybrids based on 2D metal oxide-based exfoliated nanosheets.

6.5 References

[1] J. Liu, N. Ma, W. Wu, Q. He, Chem. Eng. J., 393 (2020) 124719.

[2] D. Zhu, Z. Dong, F. Lv, C. Zhong, W. Huang, Cell Rep. Phys. Sci., 3 (2022) 101082.

[3] H. Li, H. Hu, C. Bao, F. Guo, X. Zhang, X. Liu, J. Hua, J. Tan, A. Wang, H. Zhou, B. Yang, Y. Qu, X. Liu, Sci. Rep., 6 (2016) 29327.

[4] Y. Wang, Z. Ding, N. Arif, W.-C. Jiang, Y.-J. Zeng, Mater. Adv., 3 (2022) 3389.

[5] F. E. Osterloh, Chem. Mater., 20 (2008) 35.

[6] M. A. Bizeto, A. L. Shiguihara, V. R. L. Constantino, J. Mater. Chem., 19 (2009) 2512.

[7] M. C. Sarahan, E. C. Carroll, M. Allen, D. S. Larsen, N. D. Browning, F. E. Osterloh, J. Solid State Chem., 181 (2008) 1678.

[8] A. L. Shiguihara, M. A. Bizeto, V. R.L. Constantino, Colloids and Surfaces A: Physicochem. Eng. Aspects, 295 (2007) 123.

[9] Z. Li, X. Meng, Z. Zhang, J. Photochem. Photobiol. C: Photochem. Rev., 35 (2018) 39.

[10] H. Deng, C. Qin, K. Pei, G. Wu, M. Wang, H. Ni, P. Ye, Mater. Chem. Phys., 270 (2021) 124796.

[11] R. A. El-Gendy, H. M. El-Bery, M. Farrag, D. M. Fouad, Sci. Rep., 13 (2023) 7994.

[12] V. G. Parale, T. Kim, V. D. Phadtare, H. M. Yadav, H.-H. Park, J. Mol. Liq., 277 (2019) 424.

[13] Q. Wang, Y. Li, F. Huang, S. Song, G. Ai, X. Xin, B. Zhao, Y. Zheng, Z. Zhang, Molecules, 28 (2023) 432.

[14] Y. Tan, K. Yu, T. Yang, Q. Zhang, W. Cong, H. Yin, Z. Zhang, Y. Chen, Z. Zhu, J. Mater. Chem. C, 2 (2014) 5422.

[15] X. Sun, J. Dai, Y. Guo, C. Wu, F. Hu, J. Zhao, X. Zeng, Y. Xie, Nanoscale, 6 (2014) 8359.

[16] R. Ma, Y. Kobayashi, W. J. Youngblood, T. E. Mallouk, J. Mater. Chem., 18 (2008) 5982.

[17] J.-H. Choy, H.-C. Lee, H. Jung, S.-J. Hwang, J. Mater. Chem., 11 (2001) 2232.

[18] H. Li, Q. Zhang, C. C. R. Yap, B. K. Tay, T. H. T. Edwin, A. Olivier, D. Baillargeat, Adv. Funct. Mater., 22 (2012) 1385.

[19] M. Park, J. S. Choi, L. Yang, H. Lee, Sci. Rep., 9 (2019) 19826.

[20] Y.-H. Lee, L. Yu, H. Wang, W. Fang, X. Ling, Y. Shi, C.-T. Lin, J.-K. Huang, M.-T. Chang, C.-S. Chang, M. Dresselhaus, T. Palacios, L.-J. Li, J. Kong, Nano Lett., 13 (2013) 1852.

[21] M. A. Bizeto, F. Leroux, A. L. Shiguihara, M. L. A. Temperini, O. Sala, V. R. L. Constantino, J. Phys. Chem. Solids, 71 (2010) 560.

[22] B. N. Nunes, C. Haisch, A. V. Emeline, D. W. Bahnemann, A. O. T. Patrocinio, Catal. Today, 326 (2019) 60.

[23] R. Chroma, M. Vilkova, I. Shepa, P. Makos-Chełstowska, V. Andruch, J. Mol. Liq., 330 (2021) 115617.

[24] S. Patil, A. Harle, S. Sathaye, K. Patil, CrystEngComm., 16 (2014) 10845.

[25] S. V. Kite, A. N. Kadam, D. J. Sathe, S. Patil, S. S. Mali, C. K. Hong, S.-W. Lee, K. M. Garadkar, ACS Omega, 6 (2021) 17071.

[26] G. A. M. Ali, M. R. Thalji, W. C. Soh, H. Algarni, K. F. Chong, J. Solid State Electrochem., 24 (2020) 25.

[27] X. Liu, Z. Xing, H. Zhang, W. Wang, Y. Zhang, Z. Li, X. Wu, X. Yu, W. Zhou, ChemSusChem, 9 (2016) 1118.

[28] X. Xiao, Y. Wang, B. Cui, X. Zhang, D. Zhang, X. Xu, New J. Chem., 44 (2020) 4558.

[29] J. L. Gunjakar, T. W. Kim, H. N. Kim, I. Y. Kim, S.-J. Hwang, J. Am. Chem. Soc., 133 (2011) 14998.

[30] J. L. Gunjakar, I. Y. Kim, J. M. Lee, N.-S. Lee, S.-J. Hwang, Energy Environ. Sci., 6 (2013) 1008.

[31] J. L. Gunjakar, T. W. Kim, I. Y. Kim, J. M. Lee and S. -J. Hwang, Sci. Rep., 3 (2013) 2080.

[32] I. A. de Castro, R. S. Datta, J. Z. Ou, A. Castellanos-Gomez, S. Sriram, T. Daeneke, K. Kalantar-zadeh, Adv. Mater., 29 (2017) 1701619.

[33] N. P. Kondekar, M. G. Boebinger, E. V. Woods, M. T. McDowell, ACS Appl. Mater. Interfaces, 9 (2017) 32394.

[34] R. B. Shinde, N. S. Padalkar, S. V. Sadavar, S. B. Kale, V. V. Magdum, Y. M. Chitare, S. P. Kulkarni, U. M. Patil, V. G. Parale, H. H. Park, J. L. Gunjakar, J. Hazard. Mater., 432 (2022) 128734.

[35] E. A. Skryleva, I. V. Kubasov, P. V. Kiryukhantsev-Korneev, B. R. Senatulin, R. N. Zhukov, K. V. Zakutailov, M. D. Malinkovich, Y. N. Parkhomenko, Appl. Surf. Sci., 389 (2016), 387.

[36] X. Xiao, Y. Wang, B. Cui, X. Zhang, D. Zhang, X. Xu, New J. Chem., 44 (2020) 4558.

[37] M. H. Johari, M. S. Sirat, M. A. Mohamed, Y. Wakayama, A. R. Mohmad, Nanomater. Nanotechnol., 11 (2021) 1.

[38] Y. Li, G. Chen, H. Zhang, Z. Lv, Int. J. Hydrog. Energy, 35 (2010) 2652.

[39] M. Kotal, A. Sharma, S. Jakhar, V. Mishra, S. Roy, S. C. Sahoo, H. K. Sharma and S. K. Mehta, Cryst. Growth Des., 20 (2020) 4627.

[40] S. Acharya, G. Swain, K. M. Parida, Int. J. Hydrog. Energy, 45 (2020) 11502.

[41] S. Chakrabarty, A. Mukherjee, S. Basu, ACS Sustainable Chem. Eng., 6 (2018) 5238.

[42] S. Varnagiris, M. Urbonavicius, S. Tuckute, M. Lelis, D. Milcius, Vacuum, 143 (2017) 28.

[43] N. K. Gupta, Y. Ghafari, S. Kim, J. Bae, K. S. Kim, M. Saifuddin, Sci. Rep., 10 (2020) 4942.

[44] P. Guo, F. Zhao, X. Hu, J. Alloys Compd., 867 (2021) 159044.

[45] W.-Q. Chen, L.-Y. Li, L. Li, W.-H. Qiu, L. Tang, L. Xu, K.-J. Xu, M.-H. Wu, Engineering, 5 (2019) 755.

Summary and conclusions:

Increasing water pollution has been considered one of the significant problems for marine life as well as human beings. There are several reasons for water pollution, out of which the toxification of water by organic dyes has a significant contribution. Various organic dyes are primarily used in textile industries for the coloring of fabrics. Also, synthetic dyes are widely used in many fields of advanced technologies, e.g., in various textile, paper, leather tanning, food processing, plastics, cosmetics, rubber, printing and dye manufacturing industries. Their discharge into the hydrosphere causes a significant source of pollution due to their recalcitrant nature. It has been reported that more than 1,00,000 dyes are available commercially and around 8,00,000 tonnes of dyes are produced annually. About 10-15% of dyes are lost during various processes in the textile industry. Many of these dyes have adverse effects on the environment. Some of them are carcinogenic and give rise to various biological disorders. These dyes can cause various biological disorders like skin irritation, contact dermatitis, chemosis, lacrimation, exophthalmos, permanent blindness, rhabdomyolysis, acute tubular necrosis supervene, vomiting gastritis, hypertension, vertigo and, upon ingestion, edema of the face, neck, pharynx, tongue and larynx along with respiratory distress. Various processes, such as adsorption on activated carbon, ultrafiltration, reverse osmosis, coagulation by chemical agents, ion exchange on synthetic adsorbent resins, etc., have been used to reduce water contamination. Nevertheless, they are non-destructive since they transfer organic compounds from water to another phase, thus causing secondary pollution. In this context, heterogeneous photocatalysis has emerged as one of the best solutions for degrading organic dye pollutants from the water using sunlight in the presence of semiconductors.

Photocatalysis includes a broad range of applications like solar-assisted H_2 production via water splitting, dye adsorption/degradation of organic dyes to reduce water pollution, and conversion of carbon dioxide into gaseous hydrocarbons using semiconductor photocatalyst. Various semiconductor materials have been exploited for photocatalysis. However, most photocatalysts ever developed are inappropriate for visible light-photocatalysis because of their wide bandgap energy, poor photostability and unsuitable band positions for reducing protons and oxidizing oxide ions. Therefore, much effort is put into hybridizing two kinds of photocatalysts with suitable band positions. Such a hybridization strategy can enable electron-hole pair separation via

strong electronic coupling between the coupled semiconductors. Especially nanostructures of wide bandgap TiO_2, Nb_2O_5 and ZnO are used for the coupling with narrow bandgap semiconductors like CdS, WO_3, $BiVO_4$, MoS_2, WS_2, etc. Recently, 2DMONs have emerged as basic building blocks for synthesizing hybrid materials. These materials are unique in terms of unusually high anisotropy in their crystal structure and morphology, large surface area and ultrathin thickness of the exfoliated nanosheets. These 2DMON can be synthesized using the soft-chemical exfoliation process of the pristine layered materials. 2DMON demonstrated the excellent photocatalytic performance when hybridized with Fe_2O_4, ZnO, CdS, MoS_2, ZnCr-LDH, WO_3 etc. Still, the hybrid photocatalyst based on 2DMON is at the nascent stage. A number of synthesis strategies, like hydrothermal, solvothermal, ultrasonication, CBD, SILAR, LbL, self-assembly, etc., were reported to hybridize narrow bandgap semiconductors with 2DMON.

Solution deposition techniques like CBD and SILAR demonstrated the advantages of extremely low-cost fabrication, large-area deposition and the better orientation of crystallites with pinhole-free homogeneous and uniform deposition. Narrow band gap tungsten and molybdenum sulfide have proved their ability to harvest visible light for photocatalytic applications with high chemical stability, non-toxicity, low cost, high optical absorption coefficient, well-suited band structure and favorable flat band potential positive to hydrogen evolution reaction.

The goal of this work is to hybridize wide bandgap materials titanate-NS and niobate-NS with narrow bandgap material MoS_2 using a cost-effective MCSD method for the effective utilization of solar spectrum, which can ultimately enhance the photocatalytic performance. For this purpose, two hybrids were prepared, and their photocatalytic performance was compared with that of their pristine counterparts. Initially, thin films of titanate-NS and niobate-NS are synthesized using the dip-coating method and used for hybridization with MoS_2. In the first hybrid, the titanate-NS is hybridized with MoS_2 nanoparticles, whereas in the second hybrid, the niobate-NS is hybridized with MoS_2 nanoparticles. Further, these hybrids were employed for the photocatalytic degradation of RhB and MB dyes.

Chapter 1 describes the current pollution statistics, causes and remedies to overcome the pollution problem. It describes the photocatalysis process, types of organic dyes and various methods employed for water purification. The chapter mainly focuses on photocatalytic dye degradation with an introduction to various photocatalysts such as

titanate-NS, niobate-NS and MoS_2. The importance of hybridization and related literature reviews have been included followed by orientation of work..

Chapter 2 contains the theoretical background of various chemical deposition techniques, characterization techniques and mechanisms of photocatalytic dye degradation. The theoretical background of the synthesis of titanate-NS and niobate-NS using the solid-state method and the steps involved, such as calcination, protonation and exfoliation, are thoroughly explained. Also, the MCSD method for depositing MoS_2 thin films is discussed. Further, XRD, Raman, FTIR, FE-SEM, XPS and UV-Vis DRS techniques are described in detail. The photocatalytic dye degradation mechanism is also explained.

Chapter 3 focuses on the synthesis of MoS_2 thin films using the MCSD method. This chapter deals with optimizing MoS_2 synthesis parameters and examining MoS_2 thin film with various physicochemical characterizations such as XRD, Raman, FTIR, FE-SEM, XPS and UV-Vis DRS. MoS_2 thin film exhibits a layered hexagonal crystal structure ($2H\text{-}MoS_2$) with spherical morphology. The porous structure of MoS_2 nanoparticles helps obtain higher photocatalytic performance.

The prepared MoS_2 thin films were employed to degrade RhB and MB dyes. MoS_2 thin films prepared at 300 cycles exhibited maximum degradation of 73 % and 70 % of RhB and MB in 90 minutes of visible light irradiation.

Chapter 4 describes the synthesis of titanate-NS and niobate-NS from their host crystals and their deposition on a glass substrate using the dip-coating method. The preparation of titanate-NS and niobate-NS involves multiple steps, including solid-state synthesis, protonation, exfoliation, dialysis and thin film deposition. The chapter includes optimizing titanate-NS and niobate-NS thin films using the dip-coating method.

The structural study confirms the formation of lepidocrocite-type layered titanate-NS with an orthorhombic crystal structure. The Raman and FTIR study provides enough evidence of the deposition of titanate-NS. The FE-SEM image shows the stacked titanate-NS parallel to the glass substrate. Similarly, the XRD study confirms the formation of the well-ordered stacking of lamellar niobate nanoscrolls with the orthorhombic structure. The FE-SEM provides evidence of niobate nanoscrolls with high anisotropic growth parallel to the glass substrate. UV-Vis DRS study shows the high optical absorption by titanate-NS and niobate-NS thin films in the UV region, signifying its wide bandgap nature.

The prepared titanate-NS and niobate-NS thin films were used for the photocatalytic degradation of RhB and MB dyes under visible light irradiation. These materials possess wide bandgap, so they do not show any photocatalytic activity under visible light irradiation.

Chapter 5 deals with the hybridization of dip-coated titanate-NS with MoS_2 nanoparticles deposited using the MCSD method and their application in photocatalytic dye degradation. In this chapter, pre-deposited titanate thin films were used as a building block for the growth of MoS_2 nanoparticles. Structural study shows the Braggs reflection corresponding to both titanate-NS and MoS_2 phases, confirming the successful hybridization between them. Further, the hybridization is confirmed by Raman spectroscopy, which shows various signatures related to titanate-NS and MoS_2. FE-SEM image shows the decoration of MoS_2 nanoparticles on titanate-NS, which shows the intimate contact between them.

Further, these hybrids were employed to degrade RhB and MB dyes. The $MoS_2@TiO_2$-2 hybrid displays higher photocatalytic activity by degrading 81 % and 79 % of RhB and MB in 90 minutes of visible light irradiation, which is superior to pristine MoS_2 thin films. The enhanced photocatalytic performance is attributed to the effective hybridization between titanate-NS and MoS_2, which depresses electron-hole recombination.

Chapter 6 describes a method to hybridize niobate-NS thin films with MoS_2 nanoparticles by combining dip-coating and MCSD methods. In this chapter, pre-deposited niobate-NS are used to grow MoS_2 nanoparticles. The resultant hybrids are characterized by various characterization techniques. The structural study shows Braggs reflections corresponding to layered niobate and $2H$-MoS_2, which shows their effective hybridization. FE-SEM analysis reveals anchoring of MoS_2 nanoparticles on niobate nanoscrolls. The optical study shows the decreased band gap energies of $MoS_2@Nb_6O_{17}$ hybrids, which are beneficial for enhanced photocatalytic activity.

These hybrids were employed for the photocatalytic degradation of RhB and MB under visible light irradiation. The $MoS_2@Nb_6O_{17}$-2 hybrid exhibits the highest photocatalytic performance by degrading 92 % and 79 % of RhB and MB in 90 minutes of visible light irradiation. The enhanced performance is attributed to the formation of porous morphology upon hybridization, increasing the surface area.

Chapter 7 summarizes the outcomes of all the above-mentioned chapters and provides conclusions based on them. It is concluded that $2H$-MoS_2 synthesized by the

MCSD method shows a layered structure with interconnected porous morphology, which is beneficial for photocatalytic activity. It is concluded that dip-coating is a potential method for the uniform deposition of titanate-NS and niobate-NS thin films with control over thickness. Titanate-NS and niobate-NS possess wide bandgap, which means they do not show any activity under visible light irradiation. Further, it is concluded that hybridization between wide bandgap titanate-NS and narrow bandgap MoS_2 results in enhanced photocatalytic performance by depressing electron-hole recombination. Also, niobate-NS hybridized with MoS_2 exhibits maximum photocatalytic degradation performance, which is attributed to the porous morphology of the resultant hybrid.

The comparative photocatalytic degradation performance of pristine MoS_2 and hybrids is presented in **Table 7.1** below. The table shows that the hybridization strategy is highly effective in obtaining enhanced photocatalytic performance. The $MoS_2@Nb_6O_{17}$-2 hybrid exhibits the highest photocatalytic degradation performance among all hybrids, with 92% and 79 % of RhB and MB degradation, respectively, under 90 minutes of visible light irradiation.

Table 7.1: Comparative photocatalytic dye degradation performance of pristine MoS_2, $MoS_2@TiO_2$ and $MoS_2@Nb_6O_{17}$ hybrids.

Target molecule	Photocatalyst	Degradation % (minutes)	Rate constant (k) (min^{-1})	Correlation coefficient (R^2)
RhB	MS-300	73 (90)	0.016	0.9720
	$MoS_2@TiO_2$-2	81 (90)	0.018	0.99
	$MoS_2@Nb_6O_{17}$-2	**92 (90)**	**0.029**	**0.9970**
MB	MS-300	70 (90)	0.014	0.9952
	$MoS_2@TiO_2$-2	79 (90)	0.016	0.96
	$MoS_2@Nb_6O_{17}$-2	**79 (90)**	**0.017**	**0.9391**

8.1 Recommendations

Drawing from the comprehensive dissertation analysis, several recommendations have emerged to advance the development in the field of photocatalysis. Firstly, MoS_2, with its superior visible light activity, can deliver excellent catalytic performance. However, a high electron-hole recombination rate hinders its performance. The physicochemical properties of MoS_2 can be altered to enhance its performance. Changes in precursor chemicals or synthesis methods could significantly affect the physicochemical properties.

Titanate-NS and niobate-NS have shown promising impacts in photocatalysis applications. However, their synthesis process is very lengthy and time-consuming. Therefore, the direct exfoliation process could make a revolutionary change in the field of LMO. The limitations of single-component photocatalysts can be effectively overcome by hybridizing multiple compounds. Selecting the appropriate compound is of utmost importance to achieve maximum performance with a hybrid material. Exfoliated titanate-NS and niobate-NS possess significant potential as a photocatalyst with its ability to couple with many other inorganic compounds. Therefore, a library of titanate-NS and niobate-NS-based hybrid materials must be explored to achieve better photocatalytic performance.

MoS_2 hybridized with titanate-NS and niobate-NS has shown enhanced photocatalytic performance compared to their pristine counterparts. These hybrids can be further employed for applications such as photocatalytic antibiotics and pesticide degradation. Hybrid materials possess large surface areas that can be used for hydrogen evolution reactions, CO_2 adsorption, etc.

The deposition of titanate-NS and niobate-NS using the dip-coating method has shown good application in developing novel hybrid materials. Therefore, it is recommended that the dip-coating method can be used to deposit various nanostructured materials with reasonable control over the deposition thickness. However, other deposition methods, such as EPD and LbL, can be used to observe the change in the obtained properties.

8.2 Future findings

The hybridization of MoS_2 with titanate-NS and niobate-NS has delivered excellent photocatalytic performance by effectively degrading RhB and MB dyes. These hybrids possess excellent physicochemical properties such as strong electronic coupling, enhanced surface area, porous morphology and layered structure. Future investigations

may use these hybrids for energy storage and conversion applications. This may involve engineering the layered structure, increasing surface area, or changing the composition of the hybrid. Efforts may also be directed towards enhancing the stability and reusability of the hybrid materials. Overall, ongoing research in this field may open up new pathways towards the multifunctional use of the obtained hybrids.

Publications

ROYAL SOCIETY OF CHEMISTRY

REVIEW

Versatility of group VI layered metal chalcogenide thin films synthesized by solution-based deposition methods

Vikas V. Magdum, [ID] Yogesh M. Chitare, [ID] Shirin P. Kulkarni, [ID] Prashant D. Sawant, [ID] Shraddha A. Pawar, [ID] Shweta V. Talekar, [ID] Chandrakant D. Lokhande, Umakant M. Patil, [ID] Sharad B. Patil [ID] and Jayavant L. Gunjakar [ID] *

Among transition metal dichalcogenides (TMDs), group VI layered metal (Mo and W) dichalcogenides (LMD) have received increased research interest for numerous applications due to their layered structure as well as interesting physicochemical properties that facilitate tunable physical, chemical, electrical and optical properties. These features extend LMDs' use in energy storage, catalysis, optoelectronics *etc.* The use of solution-based methods such as the successive ionic layer adsorption and reaction (SILAR), chemical bath deposition (CBD), electrodeposition, and hydrothermal method for the deposition of group VI LMDs over vapor-based methods such as chemical vapor deposition (CVD) and various sputtering techniques allows one to tune the physicochemical properties. With such promising features, solution-based deposited group VI LMDs possess a vast scope for their application in diverse fields. Hence, it is important to underscore the research progress in group VI LMDs and their future scope. The present study focuses on the versatility of solution-based deposited group VI LMDs in diverse fields. In addition, various solution-based deposition methods, different fascinating properties, and a thorough literature review of solution-based deposited group VI LMDs, along with the future scope, are discussed.

Centre for Interdisciplinary Research, D. Y. Patil Education Society (Deemed to be University), Kolhapur, 416 006, MS, India. E-mail: jlgunjakar@gmail.com

Vikas V. Magdum

From left- top row-S. A. Pawar, S. P. Kulkarni, S. V. Talekar, Y. M. Chitare, and P. D. Sawant. From left- bottom row- Dr. J. L. Gunjakar, V. V. Magdum, Prof. C. D. Lokhande, and Dr. S. B. Patil. Vikas V. Magdum, Yogesh M. Chitare, Shirin P. Kulkarni, Prashant D. Sawant, Shraddha A. Pawar, and Shweta V. Talekar are pursuing PhD degree at D. Y. Patil Education Society, Kolhapur (DYPES). Their research area includes the synthesis of 2D hybrids for energy storage, photocatalysis, electrocatalysis and gas sensor application. Dr. Umakant. M. Patil is currently working as an associate professor at DYPES. His research work includes the synthesis of metal phosphates for energy storage and catalysis applications. Dr. Sharad. B. Patil is currently working as an assistant professor at DYPES. His research interest lies in the synthesis of 2D hybrids for battery application. Dr. Jayavant L. Gunjakar is working as a Ramanujan Fellow at D. Y. Patil Education Society, Kolhapur. His

research interest includes the synthesis of 2D hybrids for energy storage, catalysis, and sensing applications. Prof. C. D. Lokhande is currently a Professor at D. Y. Patil Education Society, Kolhapur, India. His current research is focused on the synthesis of thin films by chemical methods for energy storage and catalysis.

Development of MoS$_2$ anchored 2D exfoliated titanate nanosheets thin film for Efficient photocatalytic degradation of organic pollutants

Vikas V. Magdum [a], Yogesh M. Chitare [a], Shirin P. Kulkarni [a], Dhanaji B. Malavekar [b], Jin H. Kim [b], Jayavant L. Gunjakar [a,*]

[a] Centre for Interdisciplinary Research, D. Y. Patil Education Society (Deemed to be University), Kolhapur, 416 006, MS, India
[b] Optoelectronic Convergence Research Centre, Department of Materials Science and Engineering, Chonnam National University, Gwangju, 61186, South Korea

ABSTRACT

A novel synthesis route is developed by combining dip-coating and chemical solution deposition methods for the synthesis of photo-functional MoS$_2$@TNS hybrid photocatalyst thin films. The MoS$_2$@TNS hybrid films display high surface area morphology of randomly anchored MoS$_2$ nanospheres on parallly ordered titanate nanosheet (TNS) thin film. An X-ray diffraction study evidences the 2H-MoS$_2$ growth on parallly stacked lepidocrocite-type TNS thin films. The MoS$_2$@TNS hybrid films exhibit a significant visible light absorption and high surface area structure, representing their visible-light harvesting capability and effective electronic coupling between TNS and MoS$_2$ nanospheres. The MoS$_2$@TNS hybrid films display enhanced visible-light-induced photocatalytic activity by degrading organic pollutants such as rhodamine B, methylene blue and tetracycline hydrochloride with degradation efficiencies of 81, 79 and 77 % in 90 min, respectively. This work demonstrates the effective synthesis route of TNS-based hybrid thin films and their application in photocatalytic organic pollutant degradation.

1. Introduction

The unprecedented growth of industrialization has led to enormous pollution around the globe. Wastewater released from various industries, such as the textile, pharmaceutical and agriculture sectors, releases numerous toxic pollutants harmful to aquatic and human life [1–4]. The effluents from these industries contain a mixture of organic dyes, antibiotics and pesticides. The dyes present in the wastewater are carcinogenic and cause unfavorable ecosystem changes. At the same time, the antibiotics released in wastewater cause mutagenic changes, leading to the growth of antibiotic-resistant bacteria [5,6]. Though many methods are used to degrade these organic pollutants, an advanced oxidation process in the presence of a photocatalyst is an effective way to degrade and remove organic pollution in water bodies. Many low-dimensional semiconducting materials have been developed and explored as photocatalysts. This process has received increased research attention due to its environmentally benign nature and dependence on renewable energy resources [7]. Earth's surface receives around 4 % of UV and 45 % of visible light, which shows the need to develop visible light-active photocatalysts to achieve maximum photocatalytic efficiency [8].

Thus, efforts were devoted to developing visible light-active photocatalysts. However, most visible light active photocatalysts possess high electron-hole recombination rates, poor photostability, low efficiency and inappropriate band positions to reduce protons and oxidize oxide ions [9,10]. Consequently, various strategies were employed to enhance the photocatalytic performance by morphology and porosity tuning, doping, nanostructure formation, structural engineering and hybridizing with suitable photocatalyst [3,11,12]. Nanostructured hybridization with strong electronic coupling can enable maximum solar spectrum absorption, thereby increasing the overall photocatalytic performance of the semiconducting material [13–17].

Recently, 2-dimensional (2D) materials have gained significant research attention owing to their obvious advantages, such as inherent surface charge, the presence of functional groups and the possibility of hybridizing with other inorganic species [18]. In particular, wide bandgap 2D exfoliated titanate nanosheets (TNS) show excellent potential for photocatalytic applications due to their large surface area, ultrathin thickness, macromolecule nature, and negative surface charge. In addition, the TNS can act as a basic building block for hybridization

* Corresponding author at: Centre for Interdisciplinary Research, D. Y. Patil Education Society (Deemed to be University), Kolhapur, 416 006 MS, India.
E-mail address: jlgunjakar@gmail.com (J.L. Gunjakar).

Tailoring the physicochemical properties of chemically deposited MoS$_2$ thin films for photocatalytic dye and TC degradation: effect of different cationic precursors

Vikas V. Magdum[1], Yogesh M. Chitare[1], Shirin P. Kulkarni[1], Dhanaji B. Malavekar[2], Amol U. Pawar[3], Ravindra N. Bulakhe[4], Chandrakant D. Lokhande[1], Umakant M. Patil[1], Sharad B. Patil[1,*], and Jayavant L. Gunjakar[1,*]

[1] *Centre for Interdisciplinary Research, D. Y. Patil Education Society (Deemed to Be University), Kolhapur, MS 416 006, India*

[2] *Department of Materials Science and Engineering, Optoelectronic Convergence Research Centre, Chonnam National University, Gwangju 61186, South Korea*

[3] *Environmental and Climate Technology, Korea Institute of Energy Technology, Naju-Si, Jeollanamdo 58219, Republic of Korea*

[4] *Department of Chemistry, Sungkyunkwan University, Suwon 16419, Republic of Korea*

ABSTRACT

Precursor chemicals significantly impact the physicochemical properties of chemically deposited thin films. Herein, different cationic precursors such as ammonium molybdate (AM), molybdenum trioxide (MO) and sodium molybdate (NM) are used to deposit MoS$_2$ thin films using chemical bath deposition (CBD). Their effect on film formation, physicochemical properties and photocatalytic performance is investigated. The MoS$_2$ thin films display a hexagonal phase of MoS$_2$ with nanocrystalline characteristics. All MoS$_2$ thin films display nanospherical morphology with an optical bandgap of 1.6 eV. The MoS$_2$ thin film deposited using NM precursor shows a higher surface area of 31 m^{2}g^{-1} than that of the MoS$_2$ thin films deposited using AM (28 m^{2}g^{-1}) and MO (22 m^{2}g^{-1}) precursors. All MoS$_2$ thin films are highly active for the photocatalytic degradation of target organic molecules like methylene blue (MB), rhodamine B (RhB) and tetracycline hydrochloride (TC) antibiotic. Among all, the MoS$_2$ thin film deposited using NM demonstrated excellent photocatalytic performance by degrading 84, 71 and 74% of RhB, MB and TC in 2 h of visible light irradiation with a pseudo-first-order rate constant of 0.038, 0.033 and 0.026 min^{-1}, respectively. This work shows that MoS$_2$ thin films deposited using NM exhibit better photocatalytic performance than those deposited using AM and MO precursors.

Address correspondence to E-mail: sbpphy@gmail.com; jlgunjakar@gmail.com

Research article

2D porous hexaniobate-bismuth vanadate hybrid photocatalyst for photodegradation of aquatic refractory pollutants

Shirin P. Kulkarni [a], Vikas V. Magdum [a], Yogesh M. Chitare [a], Dhanaji B. Malavekar [b], Jin H. Kim [b], Sultan Alshehri [c], Jayavant L. Gunjakar [a,*], Shashikant P. Patole [d,**]

[a] *Centre for Interdisciplinary Research, D. Y. Patil Education Society (Deemed to Be University), Kolhapur, 416 006, MS, India*
[b] *Optoelectronic Convergence Research Centre, Department of Materials Science and Engineering, Chonnam National University, Gwangju, 61186, South Korea*
[c] *Department of Pharmaceutics, College of Pharmacy, King Saud University, Riyadh, 11451, Saudi Arabia*
[d] *Department of Physics, Khalifa University of Science and Technology, AbuDhabi, 127788, United Arab Emirates*

A B S T R A C T

Metal oxide semiconductors are highly promising due to their excellent photocatalytic performance in the photodegradation of industrial waste containing refractory chemical compounds. A hybrid structure with other semiconductors provides improved photocatalytic performance. In this work, porous and two-dimensional (2D) hexaniobate-bismuth vanadate (Nb_6-$BiVO_4$) Z-scheme hybrid photocatalysts are synthesized by chemical solution growth (CSG) of $BiVO_4$ over electrophoretically deposited Nb_6 thin films. The structural and morphological analysis of Nb_6-$BiVO_4$ hybrid thin films evidenced the well-crystalline uniform growth of monoclinic scheelite $BiVO_4$ over lamellar Nb_6 nanosheets. The Nb_6-$BiVO_4$ hybrid thin films exhibit a highly porous randomly aggregated nanosheet network, creating the house-of-cards type morphology. The Nb_6-$BiVO_4$ hybrid thin films display a strong visible light absorption with band gap energy of 2.29 eV and highly quenched photoluminescence signal, indicating their visible light harvesting nature and intimate electronic coupling between hybridized species beneficial for photocatalytic applications. The visible-light-driven photodegradation performance of methylene blue (MB), rhodamine-B (Rh-B) dyes, and tetracycline hydrochloride (TC) antibiotic over Nb_6-$BiVO_4$ hybrid are studied. The best optimized Nb_6-$BiVO_4$ thin film shows superior photocatalytic activity for photodegradation of MB, Rh-B dyes, and TC antibiotic with photodegradation rates of 87.3, 92.8, and 64.7 %, respectively, exceptionally higher than that of pristine $BiVO_4$. Furthermore, the mineralization study of Nb_6-$BiVO_4$ thin film is conducted using chemical oxygen demand (COD) analysis. The optimized Nb_6-$BiVO_4$ thin film shows superior percentage COD removal of 83.33, 85.42, and 61.36 % for MB, Rh-B dyes and TC antibiotic, respectively. The present results highlight the expediency of hybridization in enhancing the photocatalytic activity of pristine $BiVO_4$ by minimizing its charge recombination rate and improving chemical stability.

Preferentially oriented m-tuned WO₃ thin-films photocatalysts for the multitargeted degradation of organic molecules

Yogesh M. Chitare [a], Vikas V. Magdum [a], Shirin P. Kulkarni [a], Shweta V. Talekar [a], Shraddha A. Pawar [a], Prashant D. Sawant [a], Dhanaji B. Malavekar [b], Umakant M. Patil [a], Chandrakant D. Lokhande [a], Jayavant L. Gunjakar [a,*]

[a] *Centre for Interdisciplinary Research, D. Y. Patil Education Society (Deemed to be University), Kolhapur, Maharashtra 416006, India*
[b] *Optoelectronic Convergence Research Centre, Department of Materials Science and Engineering, Chonnam National University, Gwangju 61186, South Korea*

A B S T R A C T

In this work, morphology-tuned tungsten oxide (m-tuned WO₃) thin films are deposited on a glass substrate by a simple and cost-effective chemical bath deposition (CBD) method. The deposition pH is varied to tune the physicochemical properties of m-tuned WO₃ thin films. The m-tuned WO₃ thin films show an orthorhombic crystal structure with a preferred orientation along the (020) plane. The morphological study demonstrated the conversion of 'rice hull' to 'interlocked nanosheets' to 'reticulated nanosheets composed of nanorods' upon changing pH, highlighting the significant role of pH in m-tuned WO₃ thin film synthesis. The m-tuned WO₃ thin films show good absorption in the visible-light region (390–780 nm) of the solar spectrum. The m-tuned WO₃ thin films are used for the visible light active photocatalytic degradation of organic molecules such as methylene blue (MB), rhodamine B (Rh B), and tetracycline hydrochloride (TC). The optimized m-tuned WO₃ thin film shows maximum photocatalytic performance of 95, 94, and 86 % in 180 min for MB, Rh B, and TC, respectively. The present study demonstrates the usefulness of the CBD method for the deposition of m-tuned WO₃ and improved photocatalytic performance.

1. Introduction

Globally accelerated industrial development, traditional agricultural practices, industrial emissions and excessive antibiotics usage have increased water pollution. Humans and aquatic life are now seriously threatened due to water pollution by numerous industrial dyes, antibiotics, and pesticides. Many modern sectors such as plastic, leather, textile, cosmetics, rubber, pharmaceutical, printing, food processing, etc. widely utilize synthetic dyes [1]. Currently, around 10,000 commercial dyes are available globally, and above 700,000 tonnes of dyes are manufactured and utilized in the above sectors annually [2]. In textile industries, a significant portion of these dyes (~20 %) are wasted in the manufacturing process and end up in industrial wastewater, significantly contributing to water pollution. Most industrial dyes are toxic, mutagenic, carcinogenic, and hazardous, adversely affecting human and aquatic life. Moreover, excessive usage and slow metabolism of antibiotics cause their foreseeable expulsion to aquatic environments, leading to untraceable water pollution. Such discharge of antibiotics leads to the spread of bacteria with antibiotic and multiple drug resistance, which may cause fetal diseases [3]. Thus, removing such contaminants from wastewater has garnered much research interest. In recent years, heterogeneous photocatalysis has emerged as an effective approach for degrading various organic molecules from polluted water [4]. It is considered a green process since it utilizes natural light in the presence of a semiconductor photocatalyst to decompose a range of toxic and hazardous organic water pollutants. Consequently, nanostructured semiconducting materials (TiO₂, ZnO, CuO, CoO, BiVO₄, and WO₃, etc.) with suitable composition, structure, and optical properties have been investigated as photocatalytic materials [5–12]. TiO₂ and ZnO are the most studied photocatalysts due to their good stability; however, their performance is highly limited due to their wide band gap (>3.2 eV) with only 4% solar spectrum utilization [13]. Thus, efforts are escalated to find visible light active photocatalysts such as CuO, CoO, BiVO₄, Ag₃PO₄, WO₃, etc.

However, most visible light active photocatalysts do not possess sufficiently high efficiency and stability due to their nonoptimized

---

Vertically aligned interlocked tungsten oxide nanosheet thin film for photocatalytic application: effect of deposition cycles

Yogesh M. Chitare[1], Vikas V. Magdum[1], Shirin P. Kulkarni[1], Shweta V. Talekar[1], Shraddha A. Pawar[1], Prashant D. Sawant[1], Dhanaji B. Malavekar[2], Umakant M. Patil[1], Jin H. Kim[2], Sabah Ansar[3], and Jayavant L. Gunjakar[1,*]

[1] *Centre for Interdisciplinary Research, D. Y. Patil Education Society (Deemed to Be University), Kolhapur, Maharashtra 416 006, India*

[2] *Department of Materials Science and Engineering, Optoelectronic Convergence Research Centre, Chonnam National University, Gwangju 61186, South Korea*

[3] *Department of Clinical Laboratory Sciences, College of Applied Medical Sciences, King Saud University, P.O. Box 10219, Riyadh 11433, Saudi Arabia*

ABSTRACT

In this work, vertically aligned interlocked tungsten oxide (WO_3) nanosheets are deposited on non-conducting substrates using the modified chemical solution deposition (MCSD) method. The number of deposition cycles is varied to tune the physicochemical properties of WO_3 thin films. The WO_3 thin films exhibit an orthorhombic crystal structure with a preferred orientation along the (111) plane. The WO_3 thin film shows the vertically aligned interlocked nanosheet morphology with a change in the lateral dimensions upon varying the number of deposition cycles. All the WO_3 thin films exhibited strong visible light harvesting characteristics in the 510–530 nm wavelength range. The WO_3 thin films are used for the visible-light-active photocatalytic degradation of organic molecules such as methylene blue (MB), rhodamine B (Rh B) and tetracycline hydrochloride (TC). The optimized WO_3 thin film shows maximum photocatalytic degradation performance of 92, 89 and 87% in 210 min for MB, Rh B and TC, respectively. The present study illustrates the usefulness of the MCSD approach for depositing vertically aligned interlocked WO_3 nanosheet thin films and enhancing photocatalytic performance.

1 Introduction

Rapid industrial development leads to serious environmental pollution problems. In particular, organic pollutants such as synthetic dyes, antibiotics, and pesticides have emerged as one of the most challenging problems because of their high toxicity, massive accumulation, and difficulty in degradation [1, 2]. Their excessive use and uncontrolled release into the aqueous reservoirs are highly hazardous to the

Springer

Synthesis, characterization and visible light driven dye degradation performance of one-pot synthesized amorphous CoWO₄ powder

P. P. Bagwade[1] , V. V. Magdum[1], D. B. Malavekar[1], Y. M. Chitare[1], J. L. Gunjakar[1], U. M. Patil[1], and C. D. Lokhande[1,*]

[1] *Centre for Interdisciplinary Research, D. Y. Patil Education Society, Kolhapur 416 006, India*

ABSTRACT

This study illustrates the first ever report on degradation of methylene blue (MB) and rhodamine B (RhB) within visible light using facile one-pot synthesized amorphous cobalt tungstate (a-CoWO₄) powder via wet chemical method. Various physico-chemical techniques including X-ray diffraction, field emission scanning electron microscope, X-ray photoelectron spectroscopy, and ultra-violet diffuse reflectance spectroscopy confirmed the successful formation of CoWO₄. The a-CoWO₄ exhibited spherical morphology with direct band gap of 2.51 eV, as estimated using the Kubelka Munk method. Furthermore, CoWO₄ powder used for the photocatalytic degradation of rhodamine B (RhB) and methylene blue (MB) dyes demonstrated excellent performance by degrading 94% RhB and 89% MB dye in 2 hour (h). The a-CoWO₄ demonstrates excellent recyclability as well as stability. The superior performance was ascribed to a larger surface area as well as reduced band gap due to the amorphous nature which enabled the response to the visible light. This work highlights the potential of a-CoWO₄ powder for visible light active photocatalysis.

1 Introduction

Metal tungstates exhibit a wide range of materials (AWO₄) which are disunited in two arrays; Wolframite (A = Cd, Co, Mn, Zn, and Cu) and Scheelite (A = Ca, Sr, Ba, and Pb) [1–3]. Metal tungstates are fascinating between specific transition metal oxides due to less harmfulness, rich divergence, natural kindness, and secure versatile resources. However, few reports are associated with photocatalytic studies [4–6]. CoWO₄, on the other hand, is an ultimate relevant compound, with outstanding catalytic and electrochemical properties. Various methods have been developed to synthesize CoWO₄ nanomaterials, including conventional solid-state reaction at high temperature, co-precipitation, spray pyrolysis, low temperature molten salt route and hydro/solvothermal approaches [7–13]. It is a p-type material possessing appropriate valence and conduction band
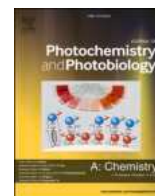
Invited paper

Modified successive ionic layer adsorption and reaction for interconnected bismuth vanadate nanograins: Highly active visible light harvesting photoanodes

Shirin P. Kulkarni [a], Vikas V. Magdum [a], Yogesh M. Chitare [a], Prashant D. Sawant [a], Shweta V. Talekar [a], Shraddha A. Pawar [a], Amol U. Pawar [b], Dhanaji B. Malavekar [c], Shrikrishna D. Sartale [d], Ayman A. Ghfar [e], Jayavant L. Gunjakar [a,*]

[a] *Centre for Interdisciplinary Research, D. Y. Patil Education Society (Deemed to be University), Kolhapur 416 006, MS, India*
[b] *Environmental and Climate Technology, Korea Institute of Energy Technology, Naju-Si, Jeollanamdo 58219, Republic of Korea*
[c] *Optoelectronic Convergence Research Centre, Department of Materials Science and Engineering, Chonnam National University, Gwangju 61186, Republic of Korea*
[d] *Department of Physics, Savitribai Phule Pune University, Pune 411 007, MS, India*
[e] *Department of Chemistry, College of Science, King Saud University, P.O. Box 2455, Riyadh 11451, Saudi Arabia*

ARTICLE INFO

ABSTRACT

A modified successive ionic layer adsorption and reaction (SILAR) method is developed for depositing interconnected bismuth vanadate (BiVO$_4$) nanoparticles with improved visible light harvesting activity. Facile control of preparative parameters like deposition cycles, anionic precursor, pH and deposition temperature significantly altered BiVO$_4$ surface morphology. BiVO$_4$ thin films prepared with Na$_3$VO$_4$ anionic precursor show dispersed nanoparticles type morphology and that deposited with NaVO$_3$ precursor displays 3D interconnected nanoparticles morphology. The BiVO$_4$ photoanodes with 3D interconnected nanoparticles morphology exhibits an excellent photocurrent density of 5.19 mA cm^{-2} at 1.23 V vs. RHE with superior photostability and improved applied bias photon to current efficiency (ABPE) (1.50 %) compared to dispersed nanostructured BiVO$_4$ photoanodes. The excellent photoelectrochemical (PEC) characteristics of BiVO$_4$ photoanodes with 3D interconnected nanoparticle morphology can be ascribed to porous morphology, optimum thickness, narrow band gap energy and favorable electronic band structure for water splitting. The current study illustrates the usefulness of the modified SILAR approach for depositing 3D interconnected BiVO$_4$ nanoparticle morphology in a single step that is superior and efficient to previously reported multistep processes.

1. Introduction

In recent years, photoelectrochemical (PEC) water splitting has attracted intense research interest for photoinduced production of H$_2$ and O$_2$ molecules using semiconductor photoelectrodes as it is one of the most environmentally friendly processes ever developed [1,2]. Overall, the PEC water-splitting process comprises electron-hole pairs generation upon light exposure; these charge carriers get separated and migrate toward the respective electrodes to perform redox reactions [3,4]. The suitable band positions and band gap energy of photocatalyst electrodes are the most crucial points for visible-light-driven PEC water-splitting applications [5]. Researchers have investigated several inorganic compounds such as transition metal oxides, carbides, nitrides, carbonitrides and chalcogenides as photocatalysts to attain greater efficiency for PEC water-splitting [6]. Compared with others, transition metal oxides are regarded as the most potential photocatalysts because of their high chemical stability and non-toxicity.

BiVO$_4$ is an n-type direct band gap semiconducting oxide, exhibited excellent properties such as suitable band positions for water splitting reactions, a narrow band gap energy (2.4 eV) with improved photostability, low photo-corrosion, low toxicity, a high optical absorption coefficient and excellent theoretical solar to hydrogen conversion efficiency [7]. Therefore, it is widely employed as a photocatalyst or photoelectrode in a wide range of photo-functional applications such as photocatalytic/photoelectrocatalytic-PEC water splitting, PEC CO$_2$ reduction, PEC glucose sensing and photocatalytic dye/antibiotic
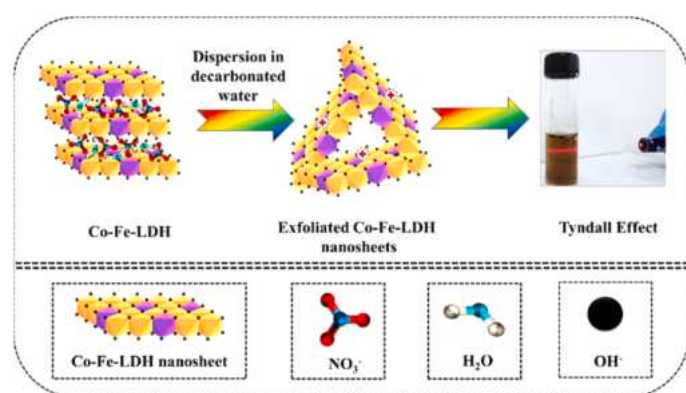

Aqueous exfoliated 2D cobalt-iron-layered double hydroxide nanosheets: Effect of Co:Fe ratio on electrocatalytic oxygen evolution reaction

Shraddha A. Pawar [a], Shweta V. Talekar [a], Prashant D. Sawant [a], Vikas V. Magdum [a],
Shirin P. Kulkarni [a], Yogesh M. Chitare [a], Chandrakant D. Lokhande [a], Hemraj M. Yadav [b,*],
Jayavant L. Gunjakar [a,*]

[a] Centre for Interdisciplinary Research, D. Y. Patil Education Society (Deemed to be University), MS, Kolhapur 416006, India
[b] School of Nanoscience and Biotechnology, Shivaji University Kolhapur, MS, Kolhapur 416004, India

GRAPHICAL ABSTRACT

ARTICLE INFO

ABSTRACT

The water exfoliation strategy is utilized to synthesize ultrathin monolayers of 2-dimensional cobalt-iron-layered double hydroxide nanosheets (CFL-NS) for application in the electrocatalytic oxygen evolution reaction (OER). These nanosheets exhibit a hexagonal crystal structure, and their zeta potential varies between $+30$ mV and $+36$ mV, depending on the Co:Fe ratio. The electron microscopy analysis reveals aggregated ultrathin nanosheets with a lateral size of $\sim$75 nm and the formation of very small nanoparticles due to the tearing of CFL-NS. The bulk CFL and CFL-NS with Co:Fe ratio of 3:1 demonstrate outstanding OER performance, with an overpotential of 305 and 299 mV at a current density of 10 and 25 mA cm^{-2}, respectively. Additionally, they exhibit a high electrochemical active surface area (ECSA) of 8.5 cm^2, a Tafel slope of 47 mV dec^{-1}, and excellent electrocatalytic stability during a chronoamperometric test of 24 h. This study underscores the benefits of an aqueous LDH exfoliation strategy for achieving enhanced electrocatalytic performance of CFL-NS.

Nanohybrids of Layered Titanate and Bismuth Vanadate as Visible-Light-Driven Photocatalysts for the Degradation of Dyes and Antibiotic

Shirin P. Kulkarni, Yogesh M. Chitare, Vikas V. Magdum, Prashant D. Sawant, Shweta V. Talekar, Shraddha A. Pawar, Dhanaji B. Malavekar, Sabah Ansar, Jin H. Kim, and Jayavant L. Gunjakar*

Read Online

ACCESS | Metrics & More | Article Recommendations | Supporting Information

ABSTRACT: The present article reports a novel approach for synthesizing two-dimensional (2D) lattice-engineered layered titanate−bismuth vanadate (NS-titanate−$BiVO_4$) nanohybrid thin films by a combination of electrophoretic deposition (EPD) and chemical solution growth (CSG) methods. The synthesized nanohybrid thin films display significant absorption of visible light and depressed electron−hole recombination, demonstrating the strong electronic coupling between the hybridized species. Upon hybridization, the chemical stability of pristine $BiVO_4$ is significantly enhanced due to the highly stable NS-titanate. The hybridization of NS-titanate with $BiVO_4$ leads to the formation of highly mesoporous house-of-cards-type morphology beneficial for improved photocatalytic activity. The resultant nanohybrids are very effective for visible-light-driven photocatalytic degradation of dyes (methylene blue (MB), rhodamine-B (Rh-B)) and tetracycline hydrochloride (TC) antibiotic with photodegradation rates of 85.1, 97, and 73%, respectively, higher than that of pristine $BiVO_4$ which is one of the most prominent visible-light-active photocatalysts. Present results underscore the superior photofunctionality of the NS-titanate−$BiVO_4$ nanohybrids as an effective visible-light-driven photocatalyst. Moreover, these findings vividly demonstrate that NS-titanate-based nanohybrids are quite effective in enhancing photocatalytic activity and developing various types of 2D nanosheet-based hybrid materials.

KEYWORDS: $BiVO_4$, nanohybrid, nanosheet, photocatalyst, thin film, titanate
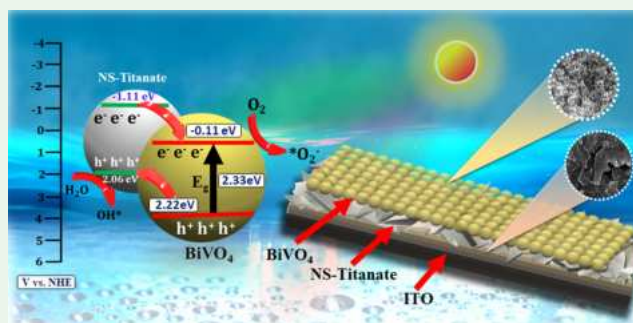
1. INTRODUCTION

The contamination of water resources due to toxic dye effluents is a significant issue in modern society.[1] Among the various techniques developed for toxic dye removal, photocatalysis has attracted considerable research attention as it is a cost-effective and environmentally friendly process.[2,3] Many low-dimensional nanostructured semiconducting materials have been designed and explored as photocatalysts. Considering the efficient use of the solar spectrum (3−5% UV light, 42−43% visible light, and 52−55% near-infrared (NIR) light), developing visible-light-active photocatalysts is highly crucial.

During the past few decades, researchers have explored a variety of inorganic materials for visible-light-driven active photocatalysis. Most visible-light photocatalysts suffer from low efficiency, high exciton recombination, poor photostability, and inappropriate band positions to reduce protons and oxidize oxide ions.[4,5] Consequently, attempts were made to enhance the photocatalytic activity by doping, nanostructuring photocatalysts, and hybridization with wide-band gap semiconductors. Nanostructure hybridization with intimate electronic coupling can enable effective electron−hole pair

separation, thus improving the photocatalytic activity of semiconducting materials.[6] Many low-dimensional wide-band gap semiconductor materials are coupled with narrow-band gap semiconductors and explored in thin film form for efficient visible-light-active photocatalysts. Such coupled thin film photocatalyst systems mainly comprise TiO_2, Nb_2O_5, ZnO, etc., as wide-band gap semiconductors and CdS, PbI, CdSe, Ag_3PO_4, etc., as narrow-band gap semiconductors.[7−10] The coupled semiconductor photocatalyst systems still suffer from limited efficiency and stability.[8] Recently, advanced two-dimensional (2D) metal oxide nanosheets (MONs) have been widely explored as basic building blocks for the development of various lattice-engineered nanohybrids owing to their fascinating characteristics.[11] These wide-band gap 2D

Sodium-Substituted Tungsten Oxide Nanoflowers: An Efficient Electrode Enhancing the Pseudocapacitive Storage in Aqueous Asymmetric Supercapacitors

Harishchandra S. Nishad,[a] Shobhnath P. Gupta,[b] Vishal Kotha,[c] Vikas V. Magdum,[d] Vinayak V. Gawade,[e] Shashikant P. Patole,[f] Ankush V. Biradar,[g] Pravin S. Walke*,[h]

[a] Mr. Harishchandra S. Nishad,
National Centre for Nanosciences and Nanotechnology,
University of Mumbai, Mumbai- 400098, India.

[b] Dr. Shobhnath P. Gupta
Department of Chemistry,
Indian Institute of Technology Bombay, Mumbai-400076, India

[c] Dr. Vishal Kotha
Department of Chemistry,
Indian Institute of Technology Bombay, Mumbai-400076, India

[d] Mr. Vikas V. Magdum
Department of Chemistry,
D. Y. Patil Education Society (Institution Deemed to be University), Kolhapur 416006, India.

[e] Mr. Vinayak V. Gawade
Shivaji University, Kolhapur, Maharashtra, 416004, India

[f] Dr. Shashikant P. Patole,
Department of Physics,
Khalifa University of Science and Technology (KU), Abu Dhabi-127788, UAE.

[g] Dr. Ankush V. Biradar
Inorganic Materials and Catalysis Division,
CSIR-Central Salt and Marine Chemicals Research Institute, G. B. Marg, Bhavnagar 364002, India.

[h] Dr. Pravin S. Walke, Corresponding Author (*)
National Centre for Nanosciences and Nanotechnology,
University of Mumbai, Mumbai- 400098, India.
Emails: shivshripsw@gmail.com

Abstract: Electrode materials engineering at the nanoscale is essential to improve the electrochemical performance for next-generation energy storage devices. Herein, a novel approach of sodium substitution in the tungsten oxide matrix is highlighting the enhancement of the pseudocapacitor performance of the electrode in an aqueous asymmetric supercapacitor. The sodium-substituted tungsten trioxide (NWO) and pristine tungsten oxide (PWO) nanoflowers prepared by a single-step hydrothermal process has presented. The tetragonal crystal structure and nanoflower morphology has maintained even after Na substitution. The electrochemical properties of PWO and NWO have investigated with three-electrode setups in 1 M H_2SO_4 aqueous electrolyte. The specific capacitance of PWO and NWO exhibits 104 F g^{-1} and 476 F g^{-1} at 1 A g^{-1}, respectively. Furthermore, an aqueous asymmetric supercapacitor (AAS) of NWO demonstrates a specific capacitance of 41 F g^{-1}, an energy density of 13 W h kg^{-1}, and a power density of 3750 W kg^{-1}. An excellent stability of AAS has achieved with 100% capacitance retention from 1000 to 5000 cycles. The sodium substitution significantly enhanced the pseudocapacitive behavior, attributed to enhanced electroactive sites, conductivity, surface area, and chemical stability. It shows the potential of NWO nanoflowers as a promising candidate for next-generation supercapacitor devices.

Introduction

Since a decade, the energy storage devices, for instance supercapacitors, are insisting a rapid development of electrode materials and its engineering considering the high power densities, excellent cycling stability, and fast charging/discharging.[1,2]

The prerequisite for supercapacitor development is abundant electrode materials selection and suitable electrolytes deliberating cost effective, ecofriendly and sustainable approach. Subsequently, aqueous electrolytes may be an excellent alternative while taking in to the account exclusive safety regulations over organic solvents, which is safety (fire/explosion) and health (toxicity/flammable) risks.[3,4] To overcome these limitations, couple of simultaneous approaches is required: an effective electrode design that promotes increased redox activity and an additional asymmetric supercapacitor arrangement.

Several efforts taken to design suitable electrode materials for the supercapacitor using transition-metal Oxides (TMOs)[5], Transition-metal dichalcogenides (TMDs)[6], Carbon based materials[7] and many more. TMO materials such as NiO, WO_3, MoO_3, Fe_3O_4, Co_3O_4 etc. are highly suitable for the supercapacitor because of their pseudocapacitive charge storage and various oxidation states.[8–12]
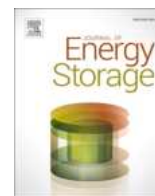
Research Papers

Self-assembled architecture of 2D layered double hydroxide pillared with 0D polyoxomolybdate anions: High-performance redox-type cathode for solid-state hybrid supercapacitor

Navnath S. Padalkar [a,b], Chae Hwan Cho [b], Vikas V. Magdum [a], Yogesh M. Chitare [a], Shirin P. Kulkarni [a], Umakant M. Patil [a], Jong Pil Park [b,*], Jayavant L. Gunjakar [a,*]

[a] *Centre for Interdisciplinary Research, D. Y. Patil Education Society, Deemed to be University, Kasaba Bawada, Kolhapur 416 006, India*
[b] *Basic Research Laboratory, Department of Food Science and Technology, Chung-Ang University, Anseong 17546, Republic of Korea*

ABSTRACT

Herein, mesoporous self-assembled architecture of two-dimensional (2D) nickel chromium-layered double hydroxide (NiCr–LDH) monolayers pillared with 0D polyoxomolybdate anions (NCMo) was prepared via a lattice engineering rapid exfoliation–restacking synthesis route. The self-assembled 2D-0D NCMo architecture exhibited expanded surface area, porous interconnected nanosheet morphology, flexible chemical composition, layer-by-layer stacking structure, and excellent electrochemical activity. The NCMo architecture exhibited promising electrochemical performance with a large specific capacity of 567 C g^{-1} at a current density of 1 A g^{-1}, and an excellent cyclic retention of 89 % after 5000 charge–discharge cycles. Additionally, an all-solid-state hybrid supercapacitor (HSC) device was assembled using NCMo architecture as the redox-type cathode, reduced graphene oxide (rGO) as the EDLC-type anode, and PVA-KOH gel as the electrolyte. The NCMo-2//PVA-KOH//rGO HSC device exhibited a high specific capacitance (171.8 F g^{-1} at 10 A g^{-1}), decent cycling stability (91 % after 10,000 cycles), and a high energy/power density (61.1 Wh kg^{-1}/6.7 W kg^{-1}). The findings of this study demonstrate that the intercalation of polyoxomolybdate is an effective lattice-engineered method for improving the electrode functionality of self-assembled LDH-based architectures.

1. Introduction

Recent years have experienced a rapid increase usage of fossil fuels and, which has triggered the need for sustainable and renewable energy resources [1,2]. Electrochemical devices such as solar cells, fuel cells, lead-acid batteries, zinc-ion batteries, lithium-ion batteries, and supercapacitors (SCs) have been used for electrochemical energy storage and conversion [3,4]. Among existing electrochemical devices, batteries exhibit the highest energy density (ED) but a low power density (PD) and long charge-discharge time [5–7]. In contrast, SCs possess high PD due to fast charge-discharge processes, but their relatively lower ED limits their practical applications [8–10]. To address these problems, among various types of SCs, hybrid supercapacitors (HSCs) have attracted increasing attention. The HSC devices, in which one electrode is a redox-type (energy source) and the other is an electric double-layer capacitor-type (EDLC) (power source), can fill the gap between the batteries and SCs [11–13]. Typically, HSCs are constructed using various

transition metal-based oxide/hydroxide (e.g., MnO_2, RuO_2, NiO, $NiCo_2O_4$, NiCoP, $Co(OH)_2$)-based electrodes with a high specific capacity, and carbon-based electrodes (e.g., activated carbon, carbon nanotube, reduced graphene oxide, carbon fabrics, and carbon aerogel) with high PD [13–20].

Among the various layered metal hydroxide, 2D layered double hydroxides (LDHs) can be applied as redox-type electrode materials for HSCs owing to their tunable interlayer chemical composition and space with unique anion-intercalated layered structure [21]. Most current research on LDH-based SCs focuses on tuning the surface area, electrical conductivity, and chemical composition and constructing composites with various conductive materials [22]. For example, a previous study demonstrated the effectiveness of LDHs-graphene composite in improving electrochemical conductivity [23]. However, the interlayer space and chemical composition of LDHs significantly affects their electrode performance. Consequently, efforts have been devoted to tuning the chemical composition and enlarging the interlayer distance of

Chemically synthesized facet-controlled visible light active BiVO₄ thin films for photoelectrochemical water splitting

Shirin P. Kulkarni[1] · Yogesh M. Chitare[1] · Vikas V. Magdum[1] · Prashant D. Sawant[1] · Shweta V. Talekar[1] ·
Shraddha A. Pawar[1] · Umakant M. Patil[1] · Kishor V. Gurav[2] · Dhanaji B. Malavekar[3] · Amol U. Pawar[4] ·
Jayavant L. Gunjakar[1]

Abstract

The facile and cost-effective chemical bath deposition (CBD) method is used to synthesize highly photoactive facet-controlled bismuth vanadate (BiVO₄) thin films on glass and stainless steel (SS) substrates. The facet-controlled BiVO₄ thin films are synthesized by variation in anionic precursor with fine tuning of chemical bath pH from alkaline to acidic media. The variation of anionic precursor evolves the morphology of BiVO₄ from dispersed nanoparticles to faceted microcrystals. Furthermore, the fine-tuning of chemical bath pH leads to the well-defined octahedral BiVO₄ microcrystals. Compared to dispersed nanoparticulate BiVO₄ photoanodes, the octahedral BiVO₄ photoanodes demonstrated superior photocurrent density of 2.75 mA cm^{-2} (at 1.23 V vs. RHE), good photostability and charge separation efficiency (45.5%) owing to their excellent PEC reaction kinetics. The present study underscores the usefulness of the CBD method for facet-controlled synthesis of semiconducting thin films for different photo-functional applications.

Keywords BiVO₄ · CBD · Microstructure · Photoanode · Photoelectrochemical performance · Water splitting

1 Introduction

In recent years, energy crises and environmental pollution have increased market demands for clean energy storage sources that can replace fossil fuels and provide energy when needed. Sustainable hydrogen (H₂) production is a key challenge for developing alternative energy systems that provide an environmentally friendly and inexpensive energy supply [1, 2]. Among the numerous renewable energy sources, solar energy has tremendous potential for energy conversion as it is one of the most abundant, cost-free and clean sources [3]. The conversion of solar energy into H₂ via the solar-assisted water-splitting process is one of the most promising technologies because of its potential for green and sustainable H₂ production [4]. Photoelectrochemical (PEC) water-splitting technology has emerged as an effective approach for producing H₂ using semiconducting photoelectrodes [5]. The PEC water-splitting is an environmentally friendly process, because it uses natural sunlight for water-splitting reactions in the presence of semiconductor photoelectrode.

During the past few decades, ZnO and TiO₂ have been extensively studied as photoelectrodes in PEC water splitting due to their high chemical stability and non-toxicity [6, 7]. However, their performance is limited owing to the wide bandgap energy (absorb only ultraviolet radiations; < 4% of solar spectrum). Hence, lots of efforts were put forward on narrow bandgap materials, such as doped-metal oxides, metal sulfides and nitrides for improved PEC water splitting [8–12]. Compared with other photocatalysts, BiVO₄ with suitable bandgap energy (~ 2.4 eV), highest photostability, high optical absorption coefficient, least photo-corrosion,

✉ Jayavant L. Gunjakar
jlgunjakar@gmail.com

1 Centre for Interdisciplinary Research, D. Y. Patil Education Society (Deemed to Be University), Kolhapur, MS 416 006, India

2 Energy Conversion and Storage Research Laboratory, Department of Physics, Devchand College, Arjunnagar, MS 591 237, India

3 Department of Materials Science and Engineering, Optoelectronic Convergence Research Centre, Chonnam National University, Gwangju 61186, South Korea

4 Environmental and Climate Technology, Korea Institute of Energy Technology, Naju-Si, Jeollanamdo 58219, Republic of Korea

Review

Doping of rare earth elements: Towards enhancing the electrochemical performance of pseudocapacitive materials

D.B. Malavekar [a,b], V.V. Magdum [a], S.D. Khot [a], J.H. Kim [b,*], C.D. Lokhande [a,*]

[a] Centre for Interdisciplinary Research, D. Y. Patil Education Society, Kolhapur 416 006, India
[b] Optoelectronic Convergence Research Center, Department of Materials Science and Engineering, Chonnam National University, Gwangju 61186, South Korea

ARTICLE INFO

ABSTRACT

The emerging challenges of global warming have instigated people to produce and store renewable energy. Among various energy storage devices, the supercapacitor is an advanced energy storage device that has been used in many crucial applications to provide the necessary power. As a result, in the last couple of decades, pseudocapacitive materials such as metal oxides and conducting polymer-based electrode materials have shown remarkable electrochemical performance. However, the performance of bare pseudocapacitive materials is hindered due to their limitations, such as low conductivity, low surface area, poor electrochemical activity, etc. These limitations can be addressed by doping as it is an effective way of altering various physicochemical properties, such as crystal structure, surface morphology, specific surface area, electronic conductivity, and chemical stability of the host material, which ultimately enhances the electrochemical performance of the doped material. Therefore, in this review, we have discussed the effect of rare earth element doping in pseudocapacitive material. The doping strategy altered the crystallographic parameters, surface morphology, specific capacitance, and cyclability. In addition, various methods employed for doping rare earth elements in pseudocapacitive materials are summarized. Finally, the prospects of rare earth element doped electrode materials in current supercapacitor development are discussed.

© 2023 Elsevier B.V. All rights reserved.

Contents

Nanocrystalline cobalt tungstate thin films prepared by SILAR method for electrocatalytic oxygen evolution reaction

P.P. Bagwade, D.B. Malavekar, V.V. Magdum, S.D. Khot, R.P. Nikam, D.J. Patil, U.M. Patil, C.D. Lokhande*

Centre for Interdisciplinary Research, D. Y. Patil Education Society, Kolhapur 416 006, India

HIGHLIGHTS

- $CoWO_4$ thin film electrocatalysts prepared by SILAR method was employed for oxygen evolution reaction.
- The $CoWO_4$ material exhibited porous morphology with specific surface area of 49.3 m^2 g^{-1}.
- $CoWO_4$ electrode exhibited excellent OER functioning with overpotential of 330 mV at a current density of 100 mA cm^{-2}.
- $CoWO_4$ thin film electrode exhibited remarkable stability (97%) after 24 h in 1 M KOH.

GRAPHICAL ABSTRACT

ABSTRACT

This study highlights on the application of nanocrystalline cobalt tungstate ($CoWO_4$) thin films as an electrocatalyst for oxygen evolution reaction (OER) prepared using successive ionic layer adsorption and reaction (SILAR) method. The X-ray diffraction, scanning electron microscopy, X-ray photoelectron spectroscopy, Fourier transform infrared spectroscopy etc. were employed for the characterization of $CoWO_4$ thin films, revealing the formation of crystalline $CoWO_4$ with spherical morphology. Furthermore, $CoWO_4$ showed excellent electrochemical performance with the overpotential of 330 mV and Tafel slope of 153 mV dec^{-1} with retaining 97% of electrochemical stability after 24 h of OER. The study confirmed the structural maintenance of $CoWO_4$ thin films after stability study.

© 2022 Hydrogen Energy Publications LLC. Published by Elsevier Ltd. All rights reserved.

2D-2D nanohybrids of Ni–Cr-layered double hydroxide and graphene oxide nanosheets: Electrode for hybrid asymmetric supercapacitors

Navnath S. Padalkar [a], Shrikant V. Sadavar [a], Rohini B. Shinde [a], Akash S. Patil [a],
Umakant M. Patil [a], Vikas V. Magdum [a], Yogesh M. Chitare [a], Shirin P. Kulkarni [a],
Ravindra N. Bulakhe [b], Vinayak G. Parale [c], Jayavant L. Gunjakar [a,*]

[a] Centre for Interdisciplinary Research, D. Y. Patil Education Society, Deemed to be University, Kasaba Bawada, Kolhapur 416006, India
[b] School of Mechanical Engineering, Chung-Ang University, Seoul, South Korea
[c] Department of Materials Science and Engineering, Yonsei University, 50 Yonsei-ro, Seodaemun-gu, Seoul 03722, South Korea

ARTICLE INFO

ABSTRACT

Nanohybrids of 2D Ni–Cr-layered double hydroxide (Ni–Cr-LDH) and graphene oxide (GO) nanosheets (Ni–Cr-LDH–GO) are prepared by electrostatic self-assembly between cationic Ni–Cr-LDH nanosheets and anionic GO nanosheets. Anionic GO nanosheets provide charge-transporting conducting channels leading to remarkably improved electrochemical activity of Ni–Cr-LDH–GO nanohybrid. The unique Ni–Cr-LDH–GO nanohybrid electrodes enable stable electrochemical structure, abundant active electrochemical sites, and fast electron-transporting channels, which play a crucial role in improving the specific capacities, cycle stability, and rate capacity. As a result, Ni–Cr-LDH–GO nanohybrid electrodes demonstrate excellent electrochemical performance with a specific capacity of 815 C g^{-1} at 1 A g^{-1}, superior to pristine Ni–Cr-LDH (354 C g^{-1}). An aqueous hybrid supercapacitor (AHS) device displays outstanding electrochemical performance with improved energy density (ED) of 51.85 Wh kg^{-1} and power density (PD) of 1.34 kW kg^{-1}. An all-solid-state hybrid supercapacitor (ASSHS) displays ED of 38.51 Wh kg^{-1} and PD of 1.33 kW kg^{-1}. Furthermore, AHS and ASSHS show excellent cycling stability of 89% and 86% capacitance retention after 10,000 galvanostatic charge/discharge (GCD) cycles, respectively. The present exfoliation-restacking strategy provides a useful method for developing a 2D-2D Ni–Cr-LDH–GO structure for a highly active hybrid-type supercapacitor structure.

1. Introduction

Energy storage via batteries and supercapacitors (SCs) focuses on an enormous amount of research activity due to their usefulness in new-generation electric automobiles, portable electronics, healthcare, and defense equipment [1–3]. SCs or electrochemical capacitors garnered colossal attention because of their advantages like high power delivery, extended cycle life, good operational safety and high rate characteristic [4]. However, the lower energy density (ED) associated with commercially available carbon-based SCs cannot meet the requirement of advanced applications, especially hybrid electric vehicles [5]. Thus, numerous efforts are put forward on the hybrid SCs (HSCs) with one pseudocapacitor or battery-type and other electrochemical double-layer capacitance (EDLC)-type electrode [6–11]. As SCs electrode materials design significantly impacts its performance, exploration of the novel

electrode materials with characteristics of high ED, power density (PD) and electrochemical stability is the key to achieving desired electrochemical performance. The expanded surface area carbon-based materials perform exceptionally well as an EDLC-type electrode in HSC [12]. However, materials like transition metal oxide, hydroxides, and conducting polymers are potential pseudocapacitive or battery-type electrode materials in HSC [13–16].

Nickel–chromium-layered double hydroxide (Ni–Cr-LDH) is a lamellar compound, which comprises stacking of positively charged brucite-like Ni–Cr-$(OH)_2$ monolayers and charge-balancing anions sandwiched between the monolayers. Ni–Cr-LDH is regarded as a high-performance battery-type SC electrode material due to its unique properties like anisotropic crystal structure, flexible chemical composition, anion intercalated layered structure, ion exchange capacity and tunable interlayer space [17,18]. Numerous research efforts have been

pH-responsive glycine functionalized magnetic iron oxide nanoparticles for SARS-CoV-2 RNA extraction from clinical sample

Rutuja Prashant Gambhir[1], Arun Kumar Parthasarathy[2], Shimpa Sharma[3], Shital Kale[4], Vikas Vijay Magdum[5], and Arpita Pandey Tiwari[1,*]

[1] Department of Stem Cell and Regenerative Medicine, Centre for Interdisciplinary Science, D.Y. Patil Education Society, Kolhapur, India

[2] Department of Microbiology, D.Y. Patil Medical College and Hospital, Kolhapur, India

[3] D.Y. Patil Medical College and Hospital, Kolhapur, India

[4] Department of Materials Science and Engineering, Chonnam National University, Gwangju, South Korea

[5] Centre for Interdisciplinary Science, D.Y. Patil Education Society, Kolhapur, India

ABSTRACT

The recent outbreak of the novel corona virus disease 2019 (COVID-19) has been made a serious global impact due to its high infectivity and severe symptoms. The Severe Acute Respiratory Syndrome (SARS-CoV-2) RNA extraction is considered as one of the most important steps in COVID-19 detection. Several commercially available kits and techniques are currently being used for specific extraction of SARS-CoV-2 RNA. However, such methods are time consuming and expensive due to the requirement of trained labors, and several chemical reagents. To overcome the mentioned limitations, magnetic RNA adsorption methodology of glycine functionalized iron oxide nanoparticles (GNPs) was established. It showed an efficient potential in SARS-CoV-2 RNA extraction due to pH responsive nature of GNPs. The highly magnetic pH responsive GNPs were synthesized by one-pot co-precipitation method. Random morphology and average 20 nm size of GNPs were denoted by Transmission Electron Microscopy (TEM). X-ray diffractometer (XRD) showed the crystalline magnetite nature. Fourier transform infrared spectroscopy (FT-IR) and UV–visible spectrometry confirmed the presence of glycine on the surface of magnetic nanoparticles. Furthermore, the magnetic nature and thermal properties of GNPs were examined by vibrating sample magnetometer (VSM) and thermogravimetric analysis (TGA), respectively. In this study, glycine performed the role of RNA adsorbent. The adsorption of RNA onto the surface of GNPs was achieved in acidic medium (pH 6). In contrary, the elution of RNA from the

Address correspondence to E-mail: arpitaptiwari@gmail.com

Research Paper

2D–2D lattice engineering route for intimately coupled nanohybrids of layered double hydroxide and potassium hexaniobate: Chemiresistive SO₂ sensor

Rohini B. Shinde [a], Navnath S. Padalkar [a], Shrikant V. Sadavar [a], Shital B. Kale [a], Vikas V. Magdum [a], Yogesh M. Chitare [a], Shirin P. Kulkarni [a], Umakant M. Patil [a], Vinayak G. Parale [b], Hyung-Ho Park [b], Jayavant L. Gunjakar [a,*]

[a] Centre for Interdisciplinary Research, D. Y. Patil Education Society (Institution Deemed to be University), Kolhapur 416 006, Maharastra, India
[b] Department of Materials Science and Engineering, Yonsei University, 50 Yonsei-ro, Seodaemun-gu, Seoul 03722, South Korea

HIGHLIGHTS

- Nanohybrids of ZC-LDH and HNb (ZCNb) nanosheets are prepared via lattice-engineered self-assembly method.
- ZCNb nanohybrids shows high surface area mesoporous structure.
- The ZCNb nanohybrids shows excellent sensitivity for the detection of SO₂ at 150 °C.
- The enhanced SO₂ sensing performance of ZCNb nanohybrids is attributed to porous microstructure and expanded surface area.

GRAPHICAL ABSTRACT
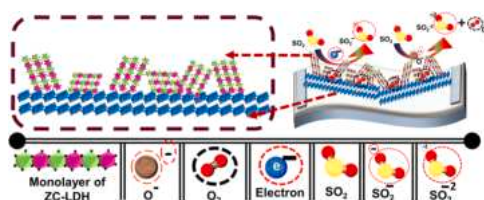
ARTICLE INFO

ABSTRACT

2D–2D lattice engineering route is used to synthesize intimately coupled nanohybrids of layered double hydroxide (LDH) and potassium hexaniobate. The 2D–2D lattice engineering route is based on the electrostatically derived self-assembly of delaminated zinc-chromium-layered double hydroxide (ZC-LDH) nanosheets and potassium hexaniobate (HNb) nanosheets (ZCNb nanohybrids). The 2D–2D lattice-engineered ZCNb nanohybrids display expanded surface area, mesoporous anchored nanosheets network morphology, and intimate coupling between nanosheets. The 2D–2D lattice engineered ZCNb nanohybrids are used for the low temperature operated gas sensor. The ZCNb nanohybrids display outstanding selectivity for the SO₂, with the high response of 61.5% compared to pristine ZC-LDH (28.08%) and potassium niobate (8%) at 150 °C. Moreover, ZCNb sensors demonstrate superior response and recovery periods of 6 and 167 s at 150 °C, respectively. This result underscores the exceptional functionality of the ZCNb nanohybrids as efficient SO₂ sensors. Moreover, these findings vividly demonstrate that the 2D–2D lattice-engineered ZCNb nanohybrids are quite effective not only in improving the gas sensor activity but also in developing of new type of intimately coupled mesoporous LDH-metal-oxide based hybrid materials.
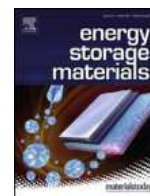
Lattice engineering exfoliation-restacking route for 2D layered double hydroxide hybridized with 0D polyoxotungstate anions: Cathode for hybrid asymmetric supercapacitors

Shrikant V. Sadavar[a], Navnath S. Padalkar[a], Rohini B. Shinde[a], Akash S. Patil[a], Umakant M. Patil[a], Vikas V. Magdum[a], Yogesh M. Chitare[a], Shirin P. Kulkarni[a], Shital B. Kale[b], Ravindra N. Bulakhe[c], Deu S. Bhange[d], Saji T. Kochuveedu[a], Jayavant L. Gunjakar[a],*

[a] *Centre for Interdisciplinary Research, D. Y. Patil Education Society, Deemed to be University, Kasaba Bawada, Kolhapur, 416 006 (India)*
[b] *Department of materials science and engineering, Chonnam National University, Gwangju, 500-757, South Korea*
[c] *School of Mechanical Engineering, Chung-Ang University, Seoul, (South Korea)*
[d] *Department of Chemistry, Shivaji University, Kolhapur, 416004, MS, India*

ARTICLE INFO

ABSTRACT

A lattice engineering exfoliation-reassembling route is used to prepare porous layer-by-layer self-assembled nanohybrids of cobalt-chromium-layered double hydroxide (Co-Cr-LDH) intercalated with 0D polyoxotungstate anions (CCW). The CCW nanohybrids provide interconnected nanosheets morphology, highly porous stacking structure, flexible chemical composition, and exceptional electrochemical activity. The self-assembled CCW nanohybrids display a high specific capacity of 1303 C g^{-1} with a capacity retention of 85.43 % over 5000 cycles. An aqueous hybrid asymmetric supercapacitor (AHAS) and all-solid-state hybrid asymmetric supercapacitor (ASHAS) devices are fabricated using CCW nanohybrids and reduced graphene oxide (rGO) as cathode and anode, respectively. The AHAS device demonstrates a high specific capacitance of 167 F g^{-1} at 0.8 A g^{-1} and specific energy (SE) of 59.37 Wh kg^{-1} at specific power (SP) of 640 W kg^{-1} with capacitance retention of 91 % after 10,000 cycles. Moreover, the ASHAS device delivers high specific capacitance of 126 F g^{-1} at 1.92 A g^{-1} and SE of 44.58 Wh kg^{-1} at SP of 1536 W kg^{-1} with capacitance retention of 87 % over 10,000 cycles. The POW intercalative hybridization significantly improves the electrode activity of the CCW nanohybrids, representing an effective method for developing LDH-based nanohybrid materials.

1. Introduction

Various energy storage technologies are emerged to address the balance between intermittent energy transformation and its utilization. Electrochemical capacitor or supercapacitor (SC) attracts enormous research attention as a pulse power source due to their high energy density, fast delivery, and extended durability. Among the various SC types, burgeoning research efforts are put forward on hybrid supercapacitors (HSCs) with one battery-type electrode (source of energy) and another electrical-double-layer-capacitors (EDLCs)-type electrode (power source). Due to their high energy and power delivery, HSCs can fulfill the gap between battery and SC. Carbon-based materials with high surface area, including activated carbon, carbon aerogels, carbon nanotubes, carbon fabrics and reduced graphene oxide (rGO), have been tested as EDLC electrodes in HSC. rGO with high conductivity and expanded surface area is one of the promising EDLC-type electrode materials that

exhibited a maximum capacity value of 127 mAh g^{-1} [1]. On the other hand, various transition metal oxides/hydroxides (RuO_2, MnO_2, Co_3O_4, NiO, $Ni(OH)_2$), conducting polymers (polyaniline, polypyrrole, and polythiophene) and metal chalcogenides (MnS, NiS, CoS, CuS, $NiCo_2S_4$) have been developed as a potential pseudocapacitive- or redox-type electrode material [2–5].

Among the various metal hydroxides, layer-double-hydroxide (LDHs) has emerged as a promising redox-type SC electrode material due to their special anion intercalated layered structure with tunable interlayer chemical composition and space. However, most of LDH-based supercapacitor state of the art is devoted to tuning the high surface area, chemical composition, electrical conductivity and making composites with various conducting carbonaceous nanostructures [6]. Electrode functionality of LDHs is significantly influenced by the chemical composition as well as interlayer space [7]. Consequently, the research efforts were put forward to tune the LDH chemical composition

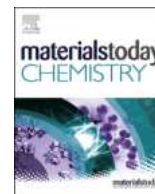# Lattice engineering route for self-assembled nanohybrids of 2D layered double hydroxide with 0D isopolyoxovanadate: chemiresistive SO$_2$ sensor

R.B. Shinde [a], N.S. Padalkar [a], S.V. Sadavar [a], A.S. Patil [a], S.B. Kale [a], V.V. Magdum [a], Y.M. Chitare [a], S.P. Kulkarni [a], U.M. Patil [a], V.G. Parale [b], J.L. Gunjakar [a, *]

[a] Centre for Interdisciplinary Research, D. Y. Patil Education Society (Institution Deemed to Be University), Kolhapur, 416 006, MS, India
[b] Department of Materials Science and Engineering, Yonsei University, 50 Yonsei-ro, Seodaemun-gu, Seoul, 03722, South Korea

ABSTRACT

Tuning the interior chemical composition of layered double hydroxides (LDHs) via lattice engineering route is a unique approach to enable multifunctional applications of LDHs. In this regard, the exfoliated 2D LDH nanosheets coupled with various guest species lead to the lattice-engineered LDH-based multifunctional self-assembly with precisely tuned chemical composition. This article reports the synthesis and characterization of mesoporous zinc–chromium-LDH (ZC-LDH) hybridized with iso-polyoxovanadate nanohybrids (ZCiV) via lattice-engineered self-assembly between delaminated ZC-LDH nanosheets and isopolyoxovanadate (iPOV) anions. Electrostatic self-assembly between 2D ZC-LDH monolayers and 0D iPOV significantly altered structural, morphological, and surface properties of ZC-LDH. The structural and morphological study demonstrated the formation of mesoporous inter-connected sheet-like architectures composed of restacked ZCiV nanosheets with expanded surface area and interlayer spacing. In addition, the ZCiV nanohybrid resistive elements were used as a room-temperature gas sensor. The selectivity of ZCiV nanohybrid was tested for various oxidizing (SO$_2$, Cl$_2$, and NO$_2$) gases and reducing (LPG, CO, H$_2$, H$_2$S, and NH$_3$) gases. The optimized ZCiV nanohybrid demonstrated highly selective SO$_2$ detection with the maximum SO$_2$ response (72%), the fast response time (20 s), low detection limit (0.1 ppm), and long-term stability at room temperature (27 ± 2 °C). Of prime importance, ZCiV nanohybrids exhibited moderately affected SO$_2$ sensing responses with high relative humidity conditions (80%–95%). The outstanding SO$_2$ sensing performance of ZCiV is attributed to the active surface gas adsorptive sites via plenty of mesopores induced by a unique lattice-engineered interconnected sheet-like microstructure and expanded interlayer spacing.

© 2022 Elsevier Ltd. All rights reserved.

1. Introduction

In the modern era of worldwide industrialization and urbanization, the air quality inhaled is a foremost important concern due to the continuously increasing concentration of numerous toxic and harmful gases [1]. The quality of the air we inhale, which is a prime health concern in this era, is degrading day by day due to increased emissions of these gases. The prime contribution to this degradation is different pollutant emitting centers such as modern industries, automobiles, houses, etc. Numerous hazardous pollutants such as oxides of carbon, sulfur and nitrogen, numerous miscible vapors such as NH$_3$ and HCl above their threshold values are hazardous to the ecosystem [2–4]. Along with human health hazards, these pollutants are also responsible for ecological imbalances like global warming, ozone depletion, acid rain, and greenhouse effects. Thus, reliable sensing of these polluting gases is of utmost necessity in various applications. Out of various pollutants, oxides of sulfur (SO$_x$) are a highly poisonous and devastating family of pollutants that adversely affects human health (skin and eye irritation, human respiratory, nervous system malfunction, lung failure, and death in acute conditions) [5]. It is also a significant contributor to acid rain, soil acidification, and climate change. Among the SO$_x$ family (SO, SO$_2$, and SO$_3$), sulfur dioxide (SO$_2$) is a significant automobile and industrial emission component and is considered a highly

Graphene Oxide as an Efficient Hybridization Matrix for Exploring Electrochemical Activity of Two-Dimensional Cobalt-Chromium-Layered Double Hydroxide-Based Nanohybrids

Shrikant V. Sadavar, Navnath S. Padalkar, Rohini B. Shinde, Akash S. Patil, Umakant M. Patil,
Vikas V. Magdum, Yogesh M. Chitare, Shirin P. Kulkarni, Ravindra N. Bulakhe, Vinayak G. Parale,
and Jayavant L. Gunjakar*

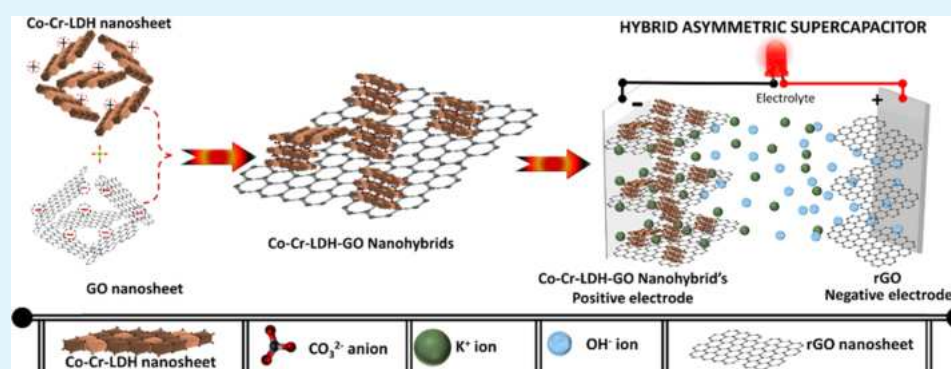Cite This: https://doi.org/10.1021/acsaem.1c03619

Read Online

| ACCESS | Metrics & More | Article Recommendations | Supporting Information |

ABSTRACT: Two-dimensional graphene oxide (GO) nanosheets with high electrical conductivity and electrochemical stability are employed as a hybridization matrix to improve the electrode performance of layered double hydroxides (LDHs). A cobalt-chromium-LDH hybridized with a GO matrix leads to anchored Co-Cr-LDH-GO (CCG) self-assembly with a high surface area, mesoporous morphology, high electrical conductivity, and high charge transfer kinetics. The CCG nanohybrids display enhanced specific capacity (1502 C g^{-1}) with high-rate characteristics compared to pristine Co-Cr-LDH (591 C g^{-1}), signifying the crucial role of GO as a hybridization matrix for improving the electrode performance of LDH materials. Aqueous and all-solid-state hybrid supercapacitors are fabricated using the best-optimized CCG nanohybrid and reduced graphene oxide as an anode and a cathode, respectively. The aqueous device delivers a specific capacitance of 181 F g^{-1}, a specific energy (SE) of 56.66 Wh kg^{-1}, and a specific power (SP) of 600 W kg^{-1} at 0.8 A g^{-1}. Moreover, the solid-state device delivers a specific capacitance of 130.8 F g^{-1}, a SE of 46.50 Wh kg^{-1}, and a SP of 1536 W kg^{-1} at 1.92 A g^{-1}. The present study clearly demonstrates the usefulness of conducting GO as an efficient hybridization matrix to improve the electrode performance of LDHs.

KEYWORDS: *anchor assembly, graphene oxide, layered double hydroxide, nanosheets, hybrid asymmetric supercapacitor*

1. INTRODUCTION

At present, considerable research has been focused on portable energy storage devices that can deliver a high energy and power density. Hybrid supercapacitors (HSCs) with one battery- or pseudocapacitive (PC)-type anode and other electrical double-layered capacitor (EDLC)-type cathodes are the most promising devices to fulfill this demand.[1] Carbon-based electrode materials like reduced graphene oxide (rGO) and activated carbon are the most suitable EDLC-type electrode materials for HSCs because of their high surface area, high conductivity, and excellent chemical stability. On the other hand, several layered inorganic materials (transition metal oxides/hydroxides/carbides/nitrides/carbonitrides/chalcogenides) have been tested as PC- or battery-type electrodes

because of their distinctive electrochemical properties.[1,2] In this regard, layered double hydroxides (LDHs) have garnered special attention because of their unique anion-intercalated layered crystal structure, tunable interlayer space, and chemical composition, thus enabling highly flexible electrochemical properties. However, the electrochemical activity of LDH-based electrodes is primarily limited by the highly compact

Polyoxotungstate intercalated self-assembled nanohybrids of Zn-Cr-LDH for room temperature Cl_2 sensing

Rohini B. Shinde [a], Akash S. Patil [a], Shrikant V. Sadavar [a], Yogesh M. Chitare [a], Vikas V. Magdum [a], Navnath S. Padalkar [a], Umakant M. Patil [a], Saji T. Kochuveedu [a], Vinayak G. Parale [b], Hyung-Ho Park [b], Chandrakant D. Lokhande [a], Jayavant L. Gunjakar [a],[*]

[a] Centre for Interdisciplinary Research, D. Y. Patil Education Society (Institution Deemed to be University), Kolhapur 416006, MS, India
[b] Department of Materials Science and Engineering, Yonsei University, 50 Yonsei-ro, Seodaemun-gu, Seoul 03722, South Korea

A B S T R A C T

This article reports the preparation of mesoporous layered nanohybrids of zinc chromium layered double hydroxide (Zn-Cr-LDH) and polyoxotungstate (POW) anions via an exfoliation-reassembling process. The hybridization of Zn-Cr-LDH and POW anions leads to forming a layer-by-layer intercalated structure with a randomly interconnected mesoporous nanoplate network composed of 'restacked POW intercalated Zn-Cr-LDH nanosheets' (Zn-Cr-WO). The gas-sensing performance of the pristine Zn-Cr-LDH and Zn-Cr-WO was investigated for oxidizing (NO_2 and Cl_2), and reducing (LPG, H_2, H_2S, CO and NH_3) gases at room temperature. The Zn-Cr-WO nanohybrids displayed the highest selectivity towards Cl_2. The Cl_2 gas response for the pristine Zn-Cr-LDH is 25.2% which further increased to 66.8% after hybridization with POW anions. The Zn-Cr-WO nanohybrids showed fastest response and recovery times of 5 and 133 s, respectively, at room temperature.

1. Introduction

Technology development, ongoing industrialization, and rapid urbanization resulted in substantial consumption of fossil fuels and organic chemical compounds that lead to ambient air pollution worldwide. Air pollution, produced by toxic and combustible gases, such as Cl_2, SO_2, NH_3, NO_2, and H_2 is responsible for global warming, climate change and is harmful to human health [1–5]. Nowadays, due to cognizance about environmental pollution, climate mitigation, ever-changing sociology, hygiene, human health, etc., and adverse outcomes due to excessive consumption of potentially harmful gases, gas sensors received considerable attention for their development. Until now, various techniques have been explored for effective sensing of these gases. The quantitative evaluation of harmful gases can be done by optochemical sensors, gas chromatography, resistive gas sensors, impedance sensors, conductometric gas sensors, etc. [6]. In addition, the chemiresistive gas sensors based on semiconducting materials are widely used for gas sensing applications due to their inherent characteristics, such as excellent sensitivity, superior selectivity, ease of fabrication, compactness and mobility, and low power consumption during real-time applications [7]. Considerable efforts have been taken

to develop chemiresistive gas sensors based on metal oxides such as SnO_2, ZnO, TiO_2, WO_3, etc. However, lack of stability and sensitivity, the influence of changing ambient atmosphere, and higher operating temperatures are some of the concerned challenges with such gas sensors [8,9]. Thus, significant and imperative efforts must be taken for developing a room temperature operated gas sensor with high sensitivity, superior selectivity, long-time stability and low detection limit (DL).

Layered double hydroxides (LDHs) are being explored nowadays to design and fabricate gas sensors that exhibit a larger surface area and produce excellent sensing performance [10]. LDHs are the class of two-dimensional (2D) layered inorganic matrices having hydrotalcite-like structure belonging to the group of layered anionic clays. It can be generalize by formula, $[M^{2+}_{1-x}M^{3+}_x(OH)_2]^{x+}(A^{n-})_{x/n}\cdot mH_2O$, in which M^{2+} (Ni^{2+}, Mg^{2+}, Co^{2+}, Zn^{2+} etc.), M^{3+} (Fe^{3+}, Al^{3+}, Cr^{3+}, Ga^{3+} etc.), and A^{n-} (Cl^-, OH^-, NO_3^-, SO_4^{2-} etc.) denote divalent metal cations, trivalent metal cations, and intercalated charge balancing anions, respectively [11,12]. This class of materials attracted attention in the field of gas sensors due to their inherent characteristics such as hierarchical structure, significantly higher stability over a prolonged period, larger specific surface area, compositional flexibility, anion exchangeability, etc. [13]. Of prime

---

Metal Oxide-Based Composites in Nonenzymatic Electrochemical Glucose Sensors

Yogesh M. Chitare,[†] Satish B. Jadhav,[†] Padamaja N. Pawaskar,[*] Vikas V. Magdum, Jayavant L. Gunjakar, and Chandrakant D. Lokhande

Cite This: https://doi.org/10.1021/acs.iecr.1c03662

Read Online

ACCESS | Metrics & More | Article Recommendations | Supporting Information

ABSTRACT: The new generation of glucose biosensors has gained immense research interest owing to its cost effectiveness, quick response, good stability, reproducibility, and low detection limit. The enzymatic glucose sensor suffers from numerous intrinsic disadvantages; therefore, there is a need to develop a new biosensor which can overcome the disadvantages of enzymatic glucose biosensors. In that context, metal oxide-based nanostructures and their compostites exhibit properties that can overcome the drawbacks of enzymatic glucose sensors. This review discusses recent developments in some of the metal oxides (CoO, NiO, CuO, and ZnO) along with their composites as well as their applications toward nonenzymatic glucose sensors. The metal oxide composites possess excellent features which signify the potential commercial applications of metal oxide-based composites for nonenzymatic electrochemical glucose sensing.
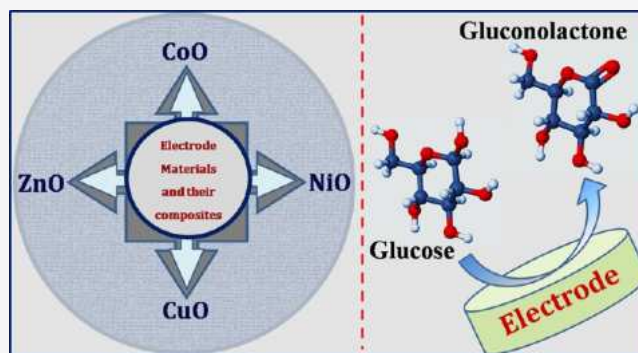
1. INTRODUCTION

Diabetes has emerged as a severe threat to public health problems worldwide. Today about 9.5% of the world population is suffering from diabetes. It can lead to various health problems such as heart disease, kidney failure, strokes, eye diseases, gum and other dental diseases, and so on.[1] The International Diabetes Federation (IDF) reported that due to diabetes 5 million deaths occurred in 2015, equivalent to a death every six seconds.[2] A decade ago, in 2010, around 438 million people were thought to be diagnosed with diabetes. According to IDF, by 2030, diabetes will affect 578 million adults and 700 million by 2045. Figure 1 shows projected and estimate number of adults with diabetes.

As per the World Health Organization, diabetes will become the seventh leading cause of death by 2030. Insufficient production of insulin in the body (called as type 1 diabetes) or incapability to use produce insulin (called as type 2 diabetes) can be treated effectively by supplying requisite insulin to the body. Otherwise, the glucose level in the blood reaches a point where it affects human health and causes several problems.[3] Regular measurement of glucose concentrations level in blood samples is required to check whether treatment works effectively or not.[4] Due to the large number of applications in the field of medicine, food, pharmaceuticals, biotechnology, environmental industry, and more, quantitative and qualitative analyses of glucose has gained great attention. Specifically, to avoid challenges initiated by diabetes diseases, very fast and trustworthy diagnoses of glucose levels in the blood samples

are required to give determine the right treatment and strict control. Therefore, for clinical diagnostics, development of highly sensitive, precise, fast, and quick sensing devices to check glucose concentrations in human blood samples possess intense challenges in the present scenario.[1,5]

Various methods including colorimetry, conductometry, electrochemical, optical, and fluorescent spectroscopy have been employed for glucose sensing. Out of theses, for the last four decades, the glucose sensing domain was dominated by electrochemical glucose sensors due to their fast response, simple instrumentation, sensitivity, excellent stability, low cost, high specificity, and low detection limit (LOD). Within the electrochemical method, two specific methods, viz., potentiometric and amperometric methods, are used mostly in monitoring glucose concentration. In the potentiometric method, the potential difference between the working electrode and reference electrode is measured at zero applied current. It is commonly used to measure glucose concentration on the order of few μM. As the concentration of glucose changes, the potential of the working electrode also changes.[6,7] In the amperometric method, constant bias potential is

High-performance supercapacitor electrode and photocatalytic dye degradation of mixed-phase WO_3 nanoplates

Shobhnath P. Gupta, Harishchandra Nishad, Vikas Magdum, Pravin S. Walke *

National Centre for Nanosciences and Nanotechnology, University of Mumbai, Mumbai 400098, India

ARTICLE INFO

ABSTRACT

We report a single-step synthesis of mixed-phase WO_3 nanoplates by a rapid and cost-effective wet chemical method. The excellent electrochemical performance of WO_3 nanoplate attributed to the proton insertion supported pseudocapacitive charge storage with a superior specific capacitance of 471 Fg^{-1} and greater stability. Additionally, the WO_3 nanoplate shows better methylene blue (MB) dye degrading performance of 87% in 105 min. Thus the bi-functional activity of the WO_3 nanoplates has the potential to employ in the integrated devices for further applications.

© 2020 Elsevier B.V. All rights reserved.

1. Introduction

The development of green energy solutions and environmentally clean technology would be an appropriate approach to satisfy the energy demand of the next-generation without impairing the environment [1]. Furthermore, water pollution is directly detrimental to human health and aquatic life, therefore it has attracted extensive consideration of the scientific society [2]. The supercapacitor is a promising electrochemical energy storage device owing to high power density, fast charge–discharge process, and superior cyclic stability with environmental friendliness [3]. Moreover, the photocatalytic dye degradation has emerged as an efficient way for the remediation of this environmental problem especially water pollution [4].

There are a variety of materials mainly transition metal oxides such as RuO_2, MnO_2, NiO, Co_3O_4, ZnO, and TiO_2 are extensively used for supercapacitor electrode and dye-degradation purpose exclusively. However, they are restricted by their cost, toxic nature, low-conductivity, stability, and wide bandgap etc. The WO_3 is highly preferred as a potential multifunctional candidate due to various oxidation states (W^{+2} to W^{+6}), high conductivity and high intrinsic density ensure the suitable electrode material for supercapacitor as well as the narrow band-gap supports photocatalytic applications [4]. Nevertheless, the WO_3 structure shows polymorphic nature with tunnel/cavity and hydrate WO_3 structure confirm

the rapid transformation of electrolyte ions in sub-seconds and improve the energy storage capability owing to insertion of H^+ into a layered structure [5]. Further, the nanomaterials have shown huge potential in all the applications due to superior activity, large surface to volume ratio, and fast surface mechanism.

Herein, we report the preparation of the WO_3 nanoplate via a simple, wet chemical method. The WO_3 nanoplate shows outstanding electrochemical performance attributed to pseudocapacitive charge storage. Simultaneously, it exhibits efficient photocatalytic performance. Thus bifunctional nature of WO_3 nanoplates is favorable to future applications.

2. Preparation of WO_3 nanoplates

Typically, 500 mg of $Na_2WO_4 \cdot 2H_2O$ was dissolved in 100 ml of double-distilled water (DDW) and a further 100 ml of 1 M H_2SO_4 solutions was added drop-wise while stirring. The solution was stirred at room temperature for 1 h and then heated at temperature 90 °C for 2 h. Finally; the obtained yellow precipitate was washed by DDW and ethanol several times, followed by annealing it at temperature 200 °C for 2 h. See Supporting Information for more details characterization and measurements.

3. Results and discussion

The XRD spectra (Fig. 1(a)) shows the combined phases of the tetragonal and monoclinic crystal structure [6–7]. The diffraction peaks at angles 24.18° and 34.10° are corresponding to planes (110) and (220) of tetragonal structure and remaining diffraction

* Corresponding author.
E-mail addresses: shivshripsw@gmail.com, pravin.w@nano.mu.ac.in (P.S. Walke).

Book chapters

Rare Earth Element-Based Nonenzymatic Glucose Sensor

Check for updates

Yogesh M. Chitare, Vikas V. Magdum, Satish B. Jadhav, Shirin P. Kulkarni, Chandrakant D. Lokhande, and Jayavant L. Gunjakar

Abbreviations

AA	Ascorbic acid
ACM	Activated chemisorption model
CV	Cyclic voltammetry
DA	Dopamine
FE-SEM	Field emission scanning electron microscope
Fru	Fructose
GCE	Glassy carbon electrode
IHOAM	Incipient hydrous oxide adatom mediator model
Lac	Lactose
LOD	Limit of detection
MOH	Metal hydroxide
PBS	Phosphate buffer solution
PVP	Polyvinyl pyrrolidone
REEs	Rare earth elements
RGO	Reduced graphene oxide
RSD	Relative standard deviation
SWV	Square wave voltammetry
UA	Uric acid

Y. M. Chitare · V. V. Magdum · S. B. Jadhav · S. P. Kulkarni · C. D. Lokhande (✉) ·
J. L. Gunjakar (✉)
Centre for Interdisciplinary Research, D. Y. Patil Education Society (Institution Deemed to be University), Kolhapur, India

Patents

INTELLECTUAL PROPERTY INDIA
PATENTS | DESIGNS | TRADE MARKS
GEOGRAPHICAL INDICATIONS

सत्यमेव जयते

पेटेंट कार्यालय,भारत सरकार | The Patent Office, Government Of India

पेटेंट प्रमाण पत्र | Patent Certificate

(पेटेंट नियमावली का नियम 74) | (Rule 74 of The Patents Rules)

पेटेंट सं. / Patent No.	:	501334
आवेदन सं. / Application No.	:	202121000897
फाइल करने की तारीख / Date of Filing	:	08/01/2021
पेटेंटी / Patentee	:	Dr. Jayavant Laxman Gunjakar.
आविष्कारक (जहां लागू हो)/ Inventor(s)	:	1.Dr. Jayavant Laxman Gunjakar 2.Mr. Akash Shashikant Patil 3.Mr. Vikas Vijay Magdum 4.Mr. Yogesh Murlidhar Chitare 5.Miss. Abhaya Shashikant Patil

प्रमाणित किया जाता है कि पेटेंटी को, उपरोक्त आवेदन में यथाप्रकटित *LIQUID COLUMN BASED OPTICAL INFRARED FILTER* नामक आविष्कार के लिए, पेटेंट अधिनियम, 1970 के उपबंधों के अनुसार आज तारीख जनवरी 2023 के आठवें दिन से बीस वर्ष की अवधि के लिए पेटेंट अनुदत्त किया गया है।

It is hereby certified that a patent has been granted to the patentee for an invention entitled *LIQUID COLUMN BASED OPTICAL INFRARED FILTER* as disclosed in the above mentioned application for the term of 20 years from the 8th day of January 2023 in accordance with the provisions of the Patents Act,1970.

अनुदान की तारीख : 19/01/2024
Date of Grant :

पेटेंट नियंत्रक
Controller of Patent

टिप्पणी – इस पेटेंट के नवीकरण के लिए फीस, यदि इसे बनाए रखा जाना है, जनवरी 2023 के आठवें दिन को और उसके पश्चात प्रत्येक वर्ष मे उसी दिन देय होगी।

Note. - The fees for renewal of this patent, if it is to be maintained will fall / has fallen due on 8th day of January 2023 and on the same day in every year thereafter.

INTELLECTUAL PROPERTY INDIA
PATENTS | DESIGNS | TRADE MARKS
GEOGRAPHICAL INDICATIONS

सत्यमेव जयते

पेटेंट कार्यालय, भारत सरकार | The Patent Office, Government Of India

डिजाइन के पंजीकरण का प्रमाण पत्र | Certificate of Registration of Design

डिजाइन सं. / Design No.	:	407337-001
तारीख / Date	:	12/02/2024
पारस्परिकता तारीख / Reciprocity Date*	:	
देश / Country	:	

प्रमाणित किया जाता है कि संलग्न प्रति में वर्णित डिजाइन जो *INFRARED (IR) CUT-OFF WATER FILTER ASSEMBLY* से संबंधित है, का पंजीकरण, श्रेणी 23-01 में 1.D. Y. Patil Education Society Kolhapur 2. Dr. Jayavant L. Gunjakar 3.Mr. Yogesh M. Chitare 4.Mr. Vikas V. Magdum 5.Miss. Shirin P. Kulkarni 6.Mr. Akash S. Patil 7.Miss Abhaya S. Patil के नाम में उपर्युक्त संख्या और तारीख में कर लिया गया है।

Certified that the design of which a copy is annexed hereto has been registered as of the number and date given above in class 23-01 in respect of the application of such design to *INFRARED (IR) CUT-OFF WATER FILTER ASSEMBLY* in the name of 1.D. Y. Patil Education Society Kolhapur 2. Dr. Jayavant L. Gunjakar 3.Mr. Yogesh M. Chitare 4.Mr. Vikas V. Magdum 5.Miss. Shirin P. Kulkarni 6.Mr. Akash S. Patil 7.Miss Abhaya S. Patil.

डिजाइन अधिनियम, 2000 तथा डिजाइन नियम, 2001 के अध्यधीन प्रावधानों के अनुसरण में।

In pursuance of and subject to the provisions of the Designs Act, 2000 and the Designs Rules, 2001.

जारी करने की तिथि :
Date of Issue : 10/04/2024

महानियंत्रक पेटेंट, डिजाइन और व्यापार चिह्न
Controller General of Patents, Designs and Trade Marks

Copyrights

दिनांक/Dated:23/04/2024

1.	पंजीकरण संख्या/Registration Number	:	**L-147009/2024**
2.	आवेदक का नाम, पता तथा राष्ट्रीयता Name, address and nationality of the applicant	:	THE REGISTRAR , D. Y. PATIL EDUCATION SOCIETY, DEEMED TO BE UNIVERSITY, KASABA BAWADA, KOLHAPUR-416006 INDIAN
3.	कृति के प्रतिलिप्यधिकार में आवेदक के हित की प्रकृति Nature of the applicant's interest in the copyright of the work	:	PUBLISHER
4.	कृति का वर्ग और वर्णन Class and description of the work	:	LITERARY/ DRAMATIC WORK
5.	कृति का शीर्षक Title of the work	:	FIGURE REPRESENTING SCHEMATIC OF MICROPROCESSOR-CONTROLLED DIP-COATING INSTRUMENT
6.	कृति की भाषा Language of the work	:	ENGLISH
7.	रचयिता का नाम, पता और राष्ट्रीयता तथा यदि रचयिता की मृत्यु हो गई है, तो मृत्यु की तिथि Name, address and nationality of the author and if the author is deceased, date of his decease	:	DR. JAYAVANT L. GUNJAKAR, ASSOCIATE PROFESSOR , CENTRE FOR INTERDISCIPLINARY RESEARCH, D. Y. PATIL EDUCATION SOCIETY, DEEMED TO BE UNIVERSITY, KOLHAPUR-416006 INDIAN MR. VIKAS V. MAGDUM, PH.D. SCHOLAR , CENTRE FOR INTERDISCIPLINARY RESEARCH, D. Y. PATIL EDUCATION SOCIETY, DEEMED TO BE UNIVERSITY, KOLHAPUR-416006 INDIAN MR. YOGESH M. CHITARE, PH.D. SCHOLAR , CENTRE FOR INTERDISCIPLINARY RESEARCH, D. Y. PATIL EDUCATION SOCIETY, DEEMED TO BE UNIVERSITY, KOLHAPUR-416006 INDIAN
8.	कृति प्रकाशित है या अप्रकाशित Whether the work is published or unpublished	:	PUBLISHED
9.	प्रथम प्रकाशन का वर्ष और देश तथा प्रकाशक का नाम, पता और राष्ट्रीयता Year and country of first publication and name, address and nationality of the publisher	:	2024 INDIA THE REGISTRAR , D. Y. PATIL EDUCATION SOCIETY, DEEMED TO BE UNIVERSITY, KASABA BAWADA, KOLHAPUR-416006 INDIAN
10.	बाद के प्रकाशनों के वर्ष और देश, यदि कोई हों, और प्रकाशकों के नाम, पते और राष्ट्रीयताएँ Years and countries of subsequent publications, if any, and names, addresses and nationalities of the publishers	:	N.A.
11.	कृति में प्रतिलिप्यधिकार सहित विभिन्न अधिकारों के स्वामियों के नाम, पते और राष्ट्रीयताएं और समनुदेशन और अनुज्ञप्तियों के विवरण के साथ प्रत्येक के अधिकार का विस्तार, यदि कोई हो। Names, addresses and nationalities of the owners of various rights comprising the copyright in the work and the extent of rights held by each, together with particulars of assignments and licences, if any	:	THE REGISTRAR , D. Y. PATIL EDUCATION SOCIETY, DEEMED TO BE UNIVERSITY, KASABA BAWADA, KOLHAPUR-416006 INDIAN
12.	अन्य व्यक्तियों के नाम, पते और राष्ट्रीयताएं, यदि कोई हों, जो प्रतिलिप्यधिकार वाले अधिकारों को समनुदेशित करने या अनुज्ञप्ति देने के लिए अधिकृत हों Names, addresses and nationalities of other persons, if any, authorised to assign or licence of rights comprising the copyright	:	N.A.
13.	यदि कृति एक 'कलात्मक कृति' है, तो कृति पर अधिकार रखने वाले व्यक्ति का नाम, पता और राष्ट्रीयता सहित मूल कृति का स्थान। (एक वास्तुशिल्प कृति के मामले में कृति पूरी होने का वर्ष भी दिखाया जाना चाहिए) If the work is an 'Artistic work', the location of the original work, including name, address and nationality of the person in possession of the work. (In the case of an architectural work, the year of completion of the work should also be shown).	:	N.A.
14.	यदि कृति एक 'कलात्मक कृति' है जो किसी भी माल या सेवाओं के संबंध में उपयोग की जाती है या उपयोग किए जाने में सक्षम है, तो आवेदन में प्रतिलिप्यधिकार अधिनियम, 1957 की धारा 45 की उप–धारा (i) के प्रावधान के अनुसार व्यापार चिह्न रजिस्ट्रार से प्रमाणन शामिल होना चाहिए। If the work is an 'Artistic work' which is used or capable of being used in relation to any goods or services, the application should include a certification from the Registrar of Trade Marks in terms of the provision to Sub-Section (i) of Section 45 of the Copyright Act, 1957.	:	N.A.
15.	यदि कृति एक 'कलात्मक कृति' है, तो क्या यह डिजाइन अधिनियम 2000 के अंतर्गत पंजीकृत है? यदि हां, तो विवरण दें। If the work is an 'Artistic work', whether it is registered under the Designs Act 2000, if yes give details.	:	N.A.
16.	यदि कृति एक 'कलात्मक कृति' है, जो डिजाइन अधिनियम 2000 के तहत एक डिजाइन के रूप में पंजीकृत होने में सक्षम है, तो क्या यह औद्योगिक प्रक्रिया के माध्यम से किसी वस्तु पर प्रयुक्त की गई है और यदि हाँ, तो कितनी बार पुनरुत्पादित किया गया है? If the work is an 'Artistic work', capable of being registered as a design under the Designs Act 2000.whether it has been applied to an article though an industrial process and ,if yes ,the number of times it is reproduced.	:	N.A.

Registrar of Copyrights

17. टिप्पणी, यदि कोई हो/Remarks, if any   :

डायरी संख्या/Diary Number: 8371/2024-CO/L

आवेदन की तिथि/Date of Application: 18/03/2024

प्राप्ति की तिथि/Date of Receipt: 18/03/2024

Registrar of Copyrights

Extracts from the Register of Copyrights

प्रतिलिप्यधिकार कार्यालय, भारत सरकार | Copyright Office, Government Of India
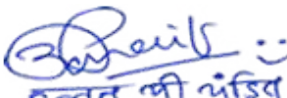
दिनांक/Dated:27/02/2024

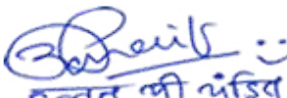|			
1.	पंजीकरण संख्या/Registration Number	:	L-144382/2024
2.	आवेदक का नाम, पता तथा राष्ट्रीयता Name, address and nationality of the applicant	:	THE REGISTRAR , D. Y. PATIL EDUCATION SOCIETY, DEEMED TO BE UNIVERSITY, KASABA BAWADA, KOLHAPUR-416006 INDIAN
3.	कृति के प्रतिलिप्यधिकार में आवेदक के हित की प्रकृति Nature of the applicant's interest in the copyright of the work	:	PUBLISHER
4.	कृति का वर्ग और वर्णन Class and description of the work	:	LITERARY/ DRAMATIC WORK
5.	कृति का शीर्षक Title of the work	:	THIN FILM PHOTOCATALYST SETUP FOR DYE DEGRADATION
6.	कृति की भाषा Language of the work	:	ENGLISH
7.	रचयिता का नाम, पता और राष्ट्रीयता तथा यदि रचयिता की मृत्यु हो गई है, तो मृत्यु की तिथि Name, address and nationality of the author and if the author is deceased, date of his decease	:	DR. JAYAVANT L. GUNJAKAR , ASSOCIATE PROFESSOR , CENTRE FOR INTERDISCIPLINARY RESEARCH, D. Y. PATIL EDUCATION SOCIETY, DEEMED TO BE UNIVERSITY, KASABA BAWADA, KOLHAPUR-416006 INDIAN MR. YOGESH M. CHITARE, PH.D. SCHOLAR , CENTRE FOR INTERDISCIPLINARY RESEARCH, D. Y. PATIL EDUCATION SOCIETY, DEEMED TO BE UNIVERSITY, KASABA BAWADA, KOLHAPUR-416006 INDIAN MR. VIKAS V. MAGDUM, PH.D. SCHOLAR, , CENTRE FOR INTERDISCIPLINARY RESEARCH, D. Y. PATIL EDUCATION SOCIETY, DEEMED TO BE UNIVERSITY, KASABA BAWADA, KOLHAPUR-416006 INDIAN
8.	कृति प्रकाशित है या अप्रकाशित Whether the work is published or unpublished	:	PUBLISHED
9.	प्रथम प्रकाशन का वर्ष और देश तथा प्रकाशक का नाम, पता और राष्ट्रीयता Year and country of first publication and name, address and nationality of the publisher	:	2024 INDIA THE REGISTRAR , D. Y. PATIL EDUCATION SOCIETY, DEEMED TO BE UNIVERSITY, KASABA BAWADA, KOLHAPUR-416006 INDIAN
10.	बाद के प्रकाशनों के वर्ष और देश, यदि कोई हों, और प्रकाशकों के नाम, पते और राष्ट्रीयताएं Years and countries of subsequent publications, if any, and names, addresses and nationalities of the publishers	:	N.A.
11.	कृति में प्रतिलिप्यधिकार सहित विभिन्न अधिकारों के स्वामियों के नाम, पते और राष्ट्रीयताएं और समनुदेशन और अनुज्ञप्तियों के विवरण के साथ प्रत्येक के अधिकार का विस्तार, यदि कोई हो। Names, addresses and nationalities of the owners of various rights comprising the copyright in the work and the extent of rights held by each, together with particulars of assignments and licences, if any	:	THE REGISTRAR , D. Y. PATIL EDUCATION SOCIETY, DEEMED TO BE UNIVERSITY, KASABA BAWADA, KOLHAPUR-416006 INDIAN
12.	अन्य व्यक्तियों के नाम, पते और राष्ट्रीयताएं, यदि कोई हों, जो प्रतिलिप्यधिकार वाले अधिकारों को समनुदेशित करने या अनुज्ञप्ति देने के लिए अधिकृत हों Names, addresses and nationalities of other persons, if any, authorised to assign or licence of rights comprising the copyright	:	N.A.
13.	यदि कृति एक 'कलात्मक कृति' है, तो कृति पर अधिकार रखने वाले व्यक्ति का नाम, पता और राष्ट्रीयता सहित मूल कृति का स्थान। (एक वास्तुशिल्प कृति के मामले में कृति पूरी होने का वर्ष भी दिखाया जाना चाहिए) If the work is an 'Artistic work', the location of the original work, including name, address and nationality of the person in possession of the work. (In the case of an architectural work, the year of completion of the work should also be shown).	:	N.A.
14.	यदि कृति एक 'कलात्मक कृति' है जो किसी भी माल या सेवाओं के संबंध में उपयोग की जाती है या उपयोग किए जाने में सक्षम है, तो आवेदन में प्रतिलिप्यधिकार अधिनियम, 1957 की धारा 45 की उप–धारा (i) के प्रावधान के अनुसार व्यापार चिह्न रजिस्ट्रार से प्रमाणन शामिल होना चाहिए। If the work is an 'Artistic work' which is used or capable of being used in relation to any goods or services, the application should include a certification from the Registrar of Trade Marks in terms of the provision to Sub-Section (i) of Section 45 of the Copyright Act, 1957.	:	N.A.
15.	यदि कृति एक 'कलात्मक कृति' है, तो क्या यह डिजाइन अधिनियम 2000 के अंतर्गत पंजीकृत है? यदि हां, तो विवरण दें। If the work is an 'Artistic work', whether it is registered under the Designs Act 2000, if yes give details.	:	N.A.
16.	यदि कृति एक 'कलात्मक कृति' है, जो डिजाइन अधिनियम 2000 के तहत एक डिजाइन के रूप में पंजीकृत होने में सक्षम है, तो क्या यह औद्योगिक प्रक्रिया के माध्यम से किसी वस्तु पर प्रयुक्त की गई है और यदि हाँ, तो कितनी बार पुनरुत्पादित किया गया है? If the work is an 'Artistic work', capable of being registered as a design under the Designs Act 2000.whether it has been applied to an article though an industrial process and ,if yes ,the number of times it is reproduced.	:	N.A.

Registrar of Copyrights

17. टिप्पणी, यदि कोई हो/Remarks, if any :

    डायरी संख्या/Diary Number: 3072/2024-CO/L

    आवेदन की तिथि/Date of Application: 27/01/2024

    प्राप्ति की तिथि/Date of Receipt: 27/01/2024

उन्नत श्री पंडित

Registrar of Copyrights

Conferences, Workshops, Seminar

2nd Asian e-Conference on Engineered Science

CERTIFICATE

This is to certify that **Mr** **Vikas** **Magdum**

of **D. Y. Patil Education Society, Kolhapur**

has Participated in 2nd Asian e-Conference on Engineered Science jointly organized by Prof. C. D. Lokhande Endowment Charitable Trust and Engineered Science Publisher, USA held during 5-6 December 2021.

Prin. Dr. J. D. Desai
President, Prof. CDLET, Pune

Prof. John Zhanhu Guo,
ES Publisher, USA

CERTIFICATE OF PARTICIPATION

This is to certify that Mr. Vikas Magdum has attended the Asian e-Conference on 'Engineered Science' 2020 which was held online on 5-6 December 2020.

Organizer
ES Publisher, USA
Prof. C. D. Lokhande Endowment Charitable Trust

In association with P. S. G. V. P. Mandal's Arts, Commerce and Science college Shahada, Dist. Nandurbar, India

D. Y. PATIL EDUCATION SOCIETY

(Institution Deemed to be University), Kolhapur

Re-Accredited by NAAC with 'A' Grade

Workshop on

CERTIFICATE

GOOD LABORATORY PRACTICES

Successfully attended by *Vikas Vijay Magdum*
on Saturday 06 February 2021

Organized By

Department of Stem Cell and Regenerative Medicine and Department of
Medical Physics, Centre for Interdisciplinary Research

Prof. Dr. C. D. Lokhande
Chairman

Prof. Dr. S. Mohan Karuppayil
Convener

Dr Shivaji Kashte
Organising Secretary

D.Y. PATIL EDUCATION SOCIETY

DEEMED TO BE UNIVERSITY

KOLHAPUR, MAHARASHTRA, INDIA

Reaccredited by NAAC with 'A' Grade

Certificate

This is to certify that Mr./ Ms./Dr. **Vikas Vijay Magdum** ....,

Of .... **D. Y. Patil Education Society, Kolhapur** ....has

participated in webinar on *"International Seminar Series on Nanotechnology for Environment and Sustainability"* organized by Department of Medical Physics, Centre for Interdisciplinary Research, D. Y. Patil Education Society (Deemed to be University), Kolhapur held on **12th and 13th January 2021.**

Dr. V. M. Khot
Organizing Secretary

Prof. C. D. Lokhande
Convenor

SHIVAJI UNIVERSITY, KOLHAPUR

SOPHISTICATED ANALYTICAL INSTRUMENT FACILITY (SAIF) – COMMON FACILITY CENTRE (CFC)

WORKSHOP & HANDS-ON TRAINING ON XRD ORGANISED BY SAIF-CFC UNDER STRIDE PROGRAMME

Certificate of Participation

This is certify that Mr. *Magdum Vikas Vijay* has successfully participated in the workshop & hands-on training on XRD organised by SAIF (CFC), Shivaji University, Kolhapur held during 11-12 Nov, 2021 under the STRIDE (Scheme for Trans-disciplinary Research for India's Developing Economy) programme.

Prof. R. G. Sonkawade
Co-ordinator : SAIF, Head (i/c) : CFC
Shivaji University, Kolhapur.
Chairman

Organiser   Co-Host

60th ACC 2023
Annual Convention of Chemists

20th-21st Dec 2023 | IIT Delhi Campus, Hauz Khas, New Delhi

— THEME —

NET ZERO GOAL & SUSTAINABILITY: ROLE OF CHEMICAL SCIENCES IN GREEN ENERGY, CIRCULAR ECONOMY AND PROSPERITY OF INDIA

CERTIFICATE OF PARTICIPATION

THIS CERTIFICATE IS PROUDLY PRESENTED TO

MR.VIKAS MAGDUM

FOR PARTICIPATING
AT 60TH ANNUAL CONVENTION OF CHEMISTS

CENTENNIAL JUBILEE CELEBRATION
★ ★ ★

Prof. Akhilesh K. Verma
Convenor, 60th ACC 2023
Department of Chemistry, University of Delhi

Prof. G. D. Yadav
Chairman, 60th ACC
President, Indian Chemical Society

PUNYASHLOK AHILYADEVI HOLKAR SOLAPUR UNIVERSITY, SOLAPUR

National e-Conference on Materials for Emerging Technologies (MET) - 2021

Organized by School of Physical Sciences
In collaboration with Internal Quality Assurance Cell

CERTIFICATE

This is to certify that, **Vikas Vijay Magdum** of **D. Y. Patil Education Society, Kolhapur** has actively **Participated/Presented** a Paper in the "National e-Conference on Materials for Emerging Technologies- 2021"(MET-2021) organized by School of Physical Sciences, P.A.H. Solapur University, Solapur on 22nd March 2021.

Prof. Vikas Patil
(Convener)

Certificate Of Participation

This is to certify that

VIKAS MAGDUM

For his/her participation in

"WORKSHOP ON AWARENESS ABOUT SHARING R&D RESOURCES THROUGH I-STEM PORTAL"

on 05th August 2022

Organized by SAIF-DST centre, Shivaji University, Kolhapur

Prof R.G.Sonkawade
Head(i/c)SAIF-DST
Shivaji University,Kolhapur

Date:05/08/2022

"Dissemination of Education for Knowledge, Science and Culture"
- Shikshanmaharshi Dr. Bapuji Salunkhe

Shri Swami Vivekanand Shikshan Sanstha's

Raje Ramrao Mahavidyalaya, Jath

Dist – Sangli, Maharashtra, India

(Affiliated to Shivaji University, Kolhapur)

"One Day International Symposium on Advances in Photocatalysis"(Virtual Mode)

on Wednesday, 13th April 2022

Organized by Department of Physics, Research and Innovation Committee and IQAC

CERTIFICATE

This is to certify that Mr./Miss./Dr./Prof. ***Mr. Vikas Vijay Magdum*** of D. Y. Patil Education Society, Kolhapur has **participated** in the "One Day International Symposium on Advances in Photocatalysis" (Virtual Mode) organized by Department of Physics, Research and Innovation Committee and IQAC of Raje Ramrao Mahavidyalaya, Jath-416 404, Dist – Sangli, Maharashtra, India on Wednesday, 13th April 2022.

E-Certificate Id: 60

Dr. S. S. Latthe	Dr. A. K. Bhosale	Dr. R. S. Sutar	Dr. S. R. Kulal	Prof. (Dr.) S. S. Patil
Organizing Secretary	Convenor	Co-convenor	Coordinator, IQAC	I/C Principal

International Conference on Nanomaterials & Nanotechnology

ICONN-2021

CERTIFICATE

This is to certify that Mr./Ms./Dr. _Vikas Magdum_ has participated in the Golden Jubilee "International Conference on Nonmaterial's & Nanotechnology" held on 25 th to 27th March, 2021 organized by Department of Physics, University of Mumbai.

Dr. Pradip Sarawade

Convener ICONN-2021

Prof. Anuradha Misra

Coordinator ICONN-2021

Head, Department of Physics